STUDIES IN NON-NEUTRAL PLASMAS USING PARTICLE-IN-CELL SIMULATIONS

By
MEGHRAJ SENGUPTA

PHYS06201104012

Institute for Plasma Research, Gandhinagar

A thesis submitted to the

Board of Studies in Physical Sciences

In partial fulfillment of requirements

for the Degree of

DOCTOR OF PHILOSOPHY

of

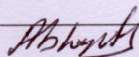**HOMI BHABHA NATIONAL INSTITUTE**

March, 2017

Homi Bhabha National Institute[1]
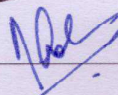
Recommendations of the Viva Voce Committee

As members of the Viva Voce Committee, we certify that we have read the dissertation prepared by Meghraj Sengupta entitled "Studies in Non-neutral Plasmas using Particle-in-Cell Simulations" and recommend that it may be accepted as fulfilling the thesis requirement for the award of Degree of Doctor of Philosophy.

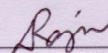|		
Chairman – Prof. A. Sen		Date: 18/08/17
Guide / Convener – Prof. R. Ganesh		Date: 18/8/20
Co-guide - \<Name\> (if any)		Date:
Examiner – Prof. H. S. Ramachandran		Date: 18/8/17
Member 1- Dr. D. Raju		Date: 18/8/17
Member 2- Dr. M. Warrier		Date: 18/08/17
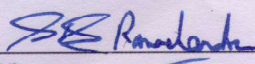
Final approval and acceptance of this thesis is contingent upon the candidate's submission of the final copies of the thesis to HBNI.

I/We hereby certify that I/we have read this thesis prepared under my/our direction and recommend that it may be accepted as fulfilling the thesis requirement.

Date: 18/8/217

Place: Gandhinagar

\<Signature\>

Co-guide (if applicable)

\<Signature\>

Guide

---

[1] This page is to be included only for final submission after successful completion of viva voce.

STATEMENT BY AUTHOR

This dissertation has been submitted in partial fulfillment of requirements for an advanced degree at Homi Bhabha National Institute (HBNI) and is deposited in the Library to be made available to borrowers under rules of the HBNI.

Brief quotations from this dissertation are allowable without special permission, provided that accurate acknowledgement of source is made. Requests for permission for extended quotation from or reproduction of this manuscript in whole or in part may be granted by the Competent Authority of HBNI when in his or her judgment the proposed use of the material is in the interests of scholarship. In all other instances, however, permission must be obtained from the author.

Meghraj Sengupta

DECLARATION

I, hereby declare that the investigation presented in the thesis has been carried out by me. The work is original and has not been submitted earlier as a whole or in part for a degree / diploma at this or any other Institution / University.

Meghraj Sengupta

Meghraj Sengupta

List of Publications arising from the thesis

Journal

1. Destabilization of a cylindrically confined electron cloud by impact ionization of background neutrals : 2D3v PIC simulation with Monte-Carlo-Collisions, M. Sengupta and R. Ganesh, **Physics of Plasmas**, **24**, 032105 (2017)

2. Influence of electron-neutral elastic collisions on the instability of an ion-contaminated cylindrical electron cloud: 2D3V PIC-with-MCC simulations, M. Sengupta and R. Ganesh, **Physics of Plasmas 23**, 102111 (2016)

3. Plasma heating via adiabatic magnetic compression-expansion cylce, K Avinash, M. Sengupta, R. Ganesh, **Physics of Plasmas 23**, 062514 (2016)

4. Linear and nonlinear evolution of the ion resonance instability in cylindrical traps: A numerical study, M. Sengupta and R. Ganesh, **Physics of Plasmas 22**, 072112 (2015)

5. Incrtia driven radial breathing and nonlinear relaxation in cylindrically confined pure electron plasma, M. Sengupta and R. Ganesh, **Physics of Plasmas 21**, 022116 (2014)

Peer Reviewed Conference Proceedings

6. Inertial driven radial breathing and nonlinear relaxation in cylindrically confined pure electron plasma, M. Sengupta and R. Ganesh, **AIP Conference Proceedings 1668**, 020005 (2015)

Meghraj Sengupta

DEDICATION

To my parents,

Mr. Mihir Sengupta & Mrs. Molly Sengupta

ACKNOWLEDGEMENTS

First of all, I would like to express my gratitude to my thesis supervisor Prof. Rajaraman Ganesh for introducing me to this wonderful profession of academia. His guidance at an academic, professional, and personal level has motivated and helped me immensely in putting in the work that has culminated in this thesis. From the years of my association with him, I have a strong respect and admiration for his patience in research, his ability to make quick and effective decisions in crunch situations, his unique skill of detecting the tiniest spaces for improving a work, and many more qualities which I have tried to learn and imbibe in my professional life. At a personal level, Ganesh Sir's friendly, enthusiastic, and approachable nature, made working with him very smooth. I would like to thank him for giving me the opportunity to work with him.

My Doctoral Committee members, Prof. Abhijit Sen, Dr. Manoj Warrier, Dr. Daniel Raju, and Prof. Rajaraman Ganesh, have given insightful comments during my yearly presentations and encouraged me to take the work further. I would like to thank all of them for their time and their comments and suggestions which have helped me improve my research work.

I would like to thank my thesis examiners Prof. Hari S. Ramachandran of IIT Chennai and Prof. Hong Qin of PPPL New Jersey, for their encouraging and insightful comments on my thesis, and for taking time out from their busy schedules to examine my thesis.

My research work brought me in contact with some wonderful senior scientists who have been very helpful. I would like to thank Dr. Gursharan Singh for his discussions on PIC simulation techniques during my academic visit to BARC Vizag. The warm hospitality and cooperation extended by Dr. Manoj Warrier and others at the BARC Vizag, during this academic visit, is something that I cherish and thank them for. I would also like to thank Prof. Avinash Khare of Delhi University for the, often

telephonic, discussions on a physics problem, and letting me work on a project with him.

In my first year at IPR, I got the opportunity to attend some enriching physics and PhD training courses taken by our Faculty. The scientific discussions and practice problems in theory and experiments in the classes taken by Prof. Subroto Mukherjee, Prof. Amita Das, Prof. Sudip Sengupta, Dr. Joydeep Ghosh, Dr. Devendra Sharma, Prof. Abhijit Sen, Dr. M. Kundu, Prof. Rajaraman Ganesh, Prof. Prabal K Chattopadhyay, Dr. Shantanu Karkari, Dr. G. Ravi, Dr. Daniel Raju, Prof. R. Srinivasan, and several other scientists form IPR and FCIPT-IPR have helped me a lot in developing an understanding of plasma physics and its research techniques. I would like to thank all of them for giving their time and effort to teach us this vital course.

For someone like me, who relies on computer simulations for his research, the staff of the Computer Centre of IPR has been a backbone of support. I would like convey my thanks to Dr. A. V. Ravi Kumar, Mr. Hemant Joshi, Mr. Arvind Mohan, Mr. Govind Lokhande, Mr. Gaurav Garg, Mr. Prashant Kumar, and other staff members of the Computer Centre for keeping the Clusters and Ethernet up and running, day and night, for our use.

I would like to thank the staff of IPR's Library, Mr. Saroj Das, Mr. S. Shravan Kumar, Ms. Shilpa Khandker, Ms. Smita K. Parmar, and others for their support and cooperation.

I would like to thank the staff of the Administrative Section of IPR for their cooperation.

I would also like to thank the staff of IPR Hostel who have been so helpful, and the maintenance staff of the excellent facilities and environment in IPR.

A special thanks and high-five to my friends in the hostel, my batch mates and their families, Samir and Kamakshi, Rupendra, Neeraj, Chandrasekhar, Bibhu, Harish,

Mangilal and Family, Vara and Family, Akanksha, Deepa, Vidhi, my seniors Jugal, Satya, Sekhar, Ashwin, Kshitish, Ujjwal, Vikram N, Gurudatt, Pravesh, Rameswar, Sushil, Sanat, Sayak, Manjit, Soumen, Aditya, Veda, Rana, Vikram D, my juniors Umesh, Ratan, Sonu, Debraj, Amit, Modhu, Narayan, Arghya, Bhumika, Surabhi, Sagar, Alamgir, Pallavi, Prabhakar, Meenakshi, Atul, Deepak, Sandeep, Jervis, Harshita, Rupak, Shivam, and many others who have made my stay in IPR Hostel so pleasant.

Finally I would like to thank the most precious people in my life, my parents Mr. Mihir Kumar Sengupta and Mrs. Molly Sengupta, my dear wife Anulekha, and my Family, all of whom have been a constant source of support and motivation for me.

Contents

List of Figures

List of Tables

1

Introduction

1.1 Nonneutral Plasmas: A Background

Non-neutral plasmas are, in general, multi-component, or a single-component, collection of charged particles exhibiting collective behaviour with an unbalanced net charge in the system [1]. Because of their gross non-neutrality these plasmas are characterized by large zeroth order self electric fields which adds unique features to their behaviour, setting them apart from quasi-neutral plasmas [1].

Since the pioneering experiments in the first half of the 20th century investigating properties of electron gas in various early experimental configurations (for example [2]), non-neutral plasmas have generated a lot of interest in basic, as well as applied, plasma physics. Basic plasma physics interests in non-neutral plasmas include using low density electron plasmas as a medium for studies on 2D vortex dynamics of incompressible and inviscid Euler fluids [3, 4], studying behaviour of astro-physical non-neutral plasmas in neutron stars [5], studying phase transitions in strongly coupled non-neutral plasmas [6, 7, 8] and more. Non-neutral plasmas find applications in high-intensity accelerators for high-energy and nuclear physics studies [9, 10], development of positron [11] and antiproton [11, 12] ion sources, coherent electromagnetic wave generation by intense electron beams as in free electron lasers (FEL) [13, 14], to mention a few.

Depending on plasma parameters such as temperature and density, non-neutral plasmas can exhibit a variety of behaviour that can be described either by a Guiding-Centre-Drift (GCD) approximated flow, or a cold macroscopic fluid model, or a kinetic Vlasov model, or even as an ensemble of discrete charged particles with interactions (the Klimontovich-type approach) [1]. Again depending on the strength of influence of self magnetic fields generated by equilibrium plasma currents these models may be electrostatic (requiring solving of Poisson Equation) or electromagnetic (requiring solving of Maxwell's Equations). Each of these models have been applied for describing a variety of non-neutral plasma phenomena occurring in a region of the plasma's parameter space suitable for that model. For example, GCD approximated electron plasmas can be used to study vortex dynamics of incompressible, inviscid Euler fluids [3, 4] as well as Kelvin-Helmholtz instabilities in annular electron plasma profiles [1, 15], cold macroscopic fluid model aptly describes the phenomena of ion-resonance

instability in partially neutralized electron clouds [16], kinetic Vlasov model can describe kinetic modes such as Bernstein modes in non-neutral plasmas [1, 17], and discrete particle model is useful for studying phase transitions in strongly coupled non-neutral plasmas [6, 8].

Such interesting dynamical properties of Non-neutral plasmas motivated experiments to exclusively study non-neutral plasmas in different regions of the parametric space. These experiments have been, and still continue to be conducted by magnetically trapping nonneutral charge clouds in cylindrical (Penning-Malmberg) traps [18, 19, 20, 21, 22, 23], or in fully toridal traps[24], or partially toroidal C traps [25, 26]. In the next Section we will take a look at some of these experimental set-ups for studying nonneutral plasmas.

1.2   Magnetic traps for conducting nonneutral plasma experiments

Fig. 1.1 shows the basic set up of the cylindrical and toroidal non-neutral plasma traps. The cylindrical Penning-Malmberg trap consists of a hollow grounded cylinder, which serves as the trap. On the two axial ends of the trap are two more smaller cylinders maintained at a potentials of the same sign as as the charge of the trapped species, such that the charged particles are axially trapped in an axial potential well. For this reason the two biased cylinders at the axial ends of the trap cylinder are known as the electrostatic end-plugs of the trap. To confine the non-neutral plasma radially an axially uniform magnetic field is applied as shown in the cylindrical trap of Fig. 1.1. Later in this discussion we will explain this radial confinement with the applied axial magnetic field in more detail.

Next, let us look at an alternative way of trapping non-neutral plasma. The inset of Fig. 1.1 represents a toroidal nonneutral plasma trap. In these traps the torodicity of the trap's geometry (defined by its toroidal aspect ratio α_T), as well as the fall of the applied magnetic field with toroidal major radius (also dependent on α_T) inside the trap's vacuum, influence the force-balance equilibrium, plasma drift velocities, and also the poloidal modes of the toroidally trapped nonneutral plasma, in distinctive ways, that sets them apart this arrangement form the cylindrical Penning-Malmberg (PM) traps. Toroidal traps come in two configurations, i) complete toroid traps that do not require axial end plugs[24] ii) partial toroid traps or C-traps that require axial end plugs similar to PM traps [25, 26].

Besides the cylindrical and toroidal set-ups depicted in Fig. 1.1, non-neutral plasma experiments have also been conducted in other geometric configurations and magnetic field topologies, such as stellarators [27, 28], and a quadrupole Penning trap [29].

Sourcing the nonneutral plasma in any of these traps involve placing emitters (for example thermionically emitting coils in electron plasma experiments[18, 25]) at a suitable locations outside the trap's vacuum, near one of the end plugs. The outflux of charge from the emitter is first channeled ("attracted") into the trap by oppositely ("attractively") biasing the electrostatic end plug near which the source is placed. After suitable quantity of of charge builds up inside the trap's vacuum the same end-plug's potential is switched back to its regular trapping ("replusive") potential for the rest of the
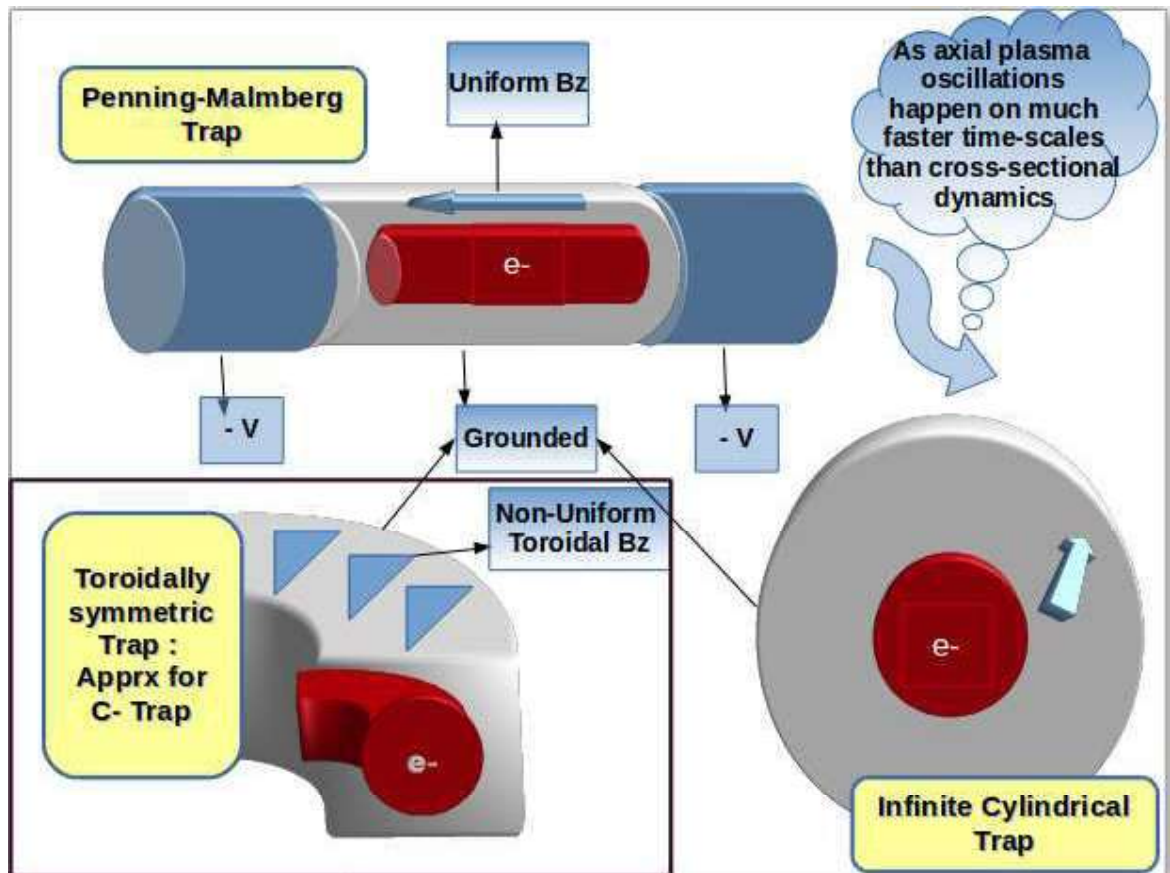
Figure 1.1: Simplified Schematic Cartoon of the Magnetic traps for confining and experimenting with nonneutral plasmas. The figure depicts the basic set-up of a cylindrical Penning-Malmberg trap, and the arrowed call-out demonstrates the 2D approximation of the trap often used in theoretical analysis and numerical simulations. The bottom-left inset is a simplified schematic cartoon of a toroidal trap. Like the cylindrical trap the toroidal trap can also be approximated by its 2D cross-section in theoretical analysis and simulations.

experiment. The source is turned off. Of course all of this is executed electronically[18, 25, 26, 30] in a time-scale faster than the axial dynamics time-scale of the plasma.

1.2.1   2D approximated model of the cylindrical trap

Let us come back to the cylindrical PM trap which is the trap configuration of interest in the work of this thesis. In these traps the trapped charged particles bounce at a high frequency (typically in the orders of $0.1\,MHz$ to $1.0\,MHz$), between the axial electrostatic end plugs. The high frequency axial bouncing is mainly driven by axial electrostatic forces on the particles arising from the combination of the nonneutral plasma's self electric field and the applied end-plug fields. The large axially directed velocities retained by the particles from their initial channelling into the trap also contribute to the high axial bounce frequency of the trapped plasma.

Perpendicular to the magnetic field the motion of the charged particles is guided by the Lorentz force of the axial magnetic field, the cross (perpendicular to the magnetic field) components of the self-electric field of the plasma, and the cross components of the field due to surface charges on the the grounded conducting wall of the trap. The characteristic frequencies associated with the cross-magnetic-field dynamics of the plasma are typically a few orders smaller than the axial bounce frequency.

Now consider the central part of the plasma column far from the axial end plugs in which the bulk of the charge particles are trapped (Fig. 1.1). In this portion any instantaneous axial non-uniformities such as in axial density and velocity distributions may be time-averaged out, in the time-scale of perpendicular dynamics. Hence while investigating cross-magnetic-field dynamics in the bulk of the trapped plasma column, we may approximate the finite length cylindrical trap as being an infinite length cylindrical trap, and the trapped plasma column as being infinitely long with a fixed uniform axial current, that may be offset to zero. With the assumption of total axial uniformity, it is now possible to think of the trap as purely 2D (circular) trap, with an applied uniform magnetic field out of the plane of the trap, that confines the 2D profile of the non-neutral plasma (Fig. 1.1) [1]. The out-of-plane magnetic field, and the planar electric field together guide the dynamics of the 2D plasma profile, in the plane of the trap.

It must be mentioned here that technically such a 2D approximation is also possible for toroidal traps with high axial velocities of the trapped charge particles.

In the past such a 2D approximation of cylindrical PM traps has been successfully used in analytical, and numerical investigation of azimuthal modes (Diocotron modes) [1], rotational Kelvin-Helmholtz instability (Diocotron instability) [1], rotational 2-stream instability (ion resonance instability) [16], vortex merging processes in rotating multiple columns of electron plasma [4], and many more phenomena. However the 2D models fails to explain purely 3D effects in finite length PM traps, such as instabilities arising from differences in the axial profiles of each component of a multi-component non-neutral plasma [20], the effects of axial untrapping of ions from a partially neutralized electron cloud, trapped in PM trap with negatively biased end plugs [31], and other 3D phenomena
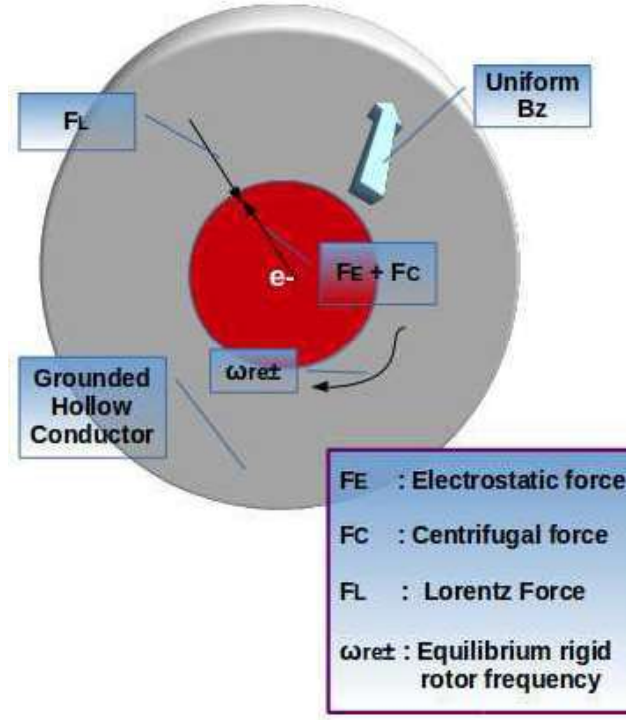
Figure 1.2: Radial force balance on an infinite length *i.e.* 2D approximated, cold, azimuthally symmetric, uniform density trapped electron plasma column

in PM traps. Axial velocities, because of their large magnitudes compared to cross-magnetic field velocities, also play a lead role in the collisional interaction of the nonneutral plasma with background neutrals in a cylindrical trap. Hence while investigating the effects of plasma particle collisions with background neutrals on the cross-magnetic-field dynamics of the plasma [32, 33], the axial velocities can not be neglected.

1.2.2 Radial confinement of nonneutral plasma in cylindrical traps explained with the 2D approximation

Using the 2D approximated model let us examine how a pure electron plasma is radially confined inside a cylindrical trap. Fig. 1.2 shows a 2D approximation of the cylindrical trap with an azimuthally symmetric, uniform density profile of electron plasma trapped inside it. For simplicity let us consider the plasma to be at zero-temperature, and assume that its dynamics in purely electrostatic (*i.e* we are neglecting any self-magnetic field of the plasma).

The radial force balance on the electron plasma profile is maintained by a rigid-rotation of the plasma with it's characterisers equilibrium rigid-rotation frequency, $\omega_{re}^{\pm}$ [1]. As the cold uniform density profile of pure electron plasma rigidly rotates with it's equilibrium angular frequency, it experiences a radially outwards self electric field force plus a centrifugal force due to its rotation. Both these radially

outward forces are balanced at every location in the plasma profile, by the radially inward Lorentz force arising form the rigid rotation of the plasma and the axial magnetic field. Hence the radial force balance is maintained on the plasma profile by the rotation of the plasma at its equilibrium angular frequency. In this respect the role of the equilibrium rotation of a single species plasma column in analogous to the role of the opposite charged species of a quasi-neutral plasma.

1.3 Some open problems in cylindrically confined nonneutral plasmas

As discussed, several fundamental questions related to dissipation-less 2D fluid dynamics have been addressed using low density, or more appropiately low Brillouin ratio, f_b, zero inertia limit of electron plasma equations in 2D (r, θ) plane. However, as f_b is increased, this zero inertia approximation breaks down and several new fundamental questions regarding instabilities in pure electron plasma in this limit emerge.

For example, what happens if a uniform density, cold, circular patch of electrons (or a Rankine vortex in fluid dynamics) is loaded as an initial condition at large f_b? Can one address the linear physics, its nonlinear dynamics, various resonances and the ensuing transport in this system using unapproximated equations of motions? What would be the fate of such a system if a partially neutralizing ion background is pre-loaded, again without approximating the equations of motion? Can the effect of neutral particle collisions be included without actually writing down additional set of equations for neutral particles, say, using a Monte Carlo Collision method for experimentally realistic neutral particle pressures? Is there a way to separate out the effects of ionizing and non-ionzing charge-neutral collisions on the dynamics of the plasma? Finally, can one simulate, a situation where a pre-loaded electron cloud builds naturally a sizeable ion population through ionizing electron-neutral collisions, starting from zero ions, and then make credible predictions of the ensuing dynamics at any desired value of f_b so that comparisons with experiments become a possibility?

Attempts has been made to address several of these questions in this Thesis. The following gives a brief outline of code development and physics problems addressed.

1.4 Nonneutral plasma phenomena investigated in the work of this thesis

This thesis is aimed at investigating dynamics of nonneutral plasmas in cylindrical traps using the numerical technique of Particle-in-Cell (PIC) simulations. We will come back to how the PIC method fits as a simulation tool for non-neutral plasma phenomena in cylindrical traps later in this discussion. Let us first introduce the physics problems targeted in this thesis in bullets.

- Consider the radial force balance of the cold, uniform density electron plasma explained above. A slight perturbation of the plasma from this equilibrium will trigger radial breathing modes

of the plasma. The nonlinear evolution of these radial breathing modes is the first phenomena that is investigated with 2D PIC simulation in this thesis. As will be demonstrated from this set of numerical experiments [34, 35] the radial breathing modes are an inertia driven phenomena, *i.e.* they cease to exist under of GCD approximation of the plasma, that is valid for electron plasmas of very low densities.

- An electron plasma can also exhibit stable and unstable azimuthal modes (Diocotron modes) in the cylindrical trap which has been well investigated in the past [1]. It had also been theorized that elastic collisions of the trapped electron cloud with background neutrals can have a destabilizing effect on the cloud and can excite an unstable fundamental dioctron mode on the cloud [36]. Through numerical experiments performed with a 2D3v PIC code facilitated with 3D Monte-Carlo-Collisions it has now been demonstrated that contrary to existing theory, elastic collisions of electron with background neutrals have no destabilizing influence on the cloud dynamics [32]. A new theory has been put forward in support of this finding.

- PIC simulation has also been used to demonstrate a novel scheme for axial heating of single component plasmas in cylindrical traps without driving the plasma far from thermal equilibrium [37]. Application of this new heating scheme can be possibly extended to magnetic heating of Tokamak plasmas, without driving them far from thermal equilibrium.

- Numerical experiments have also been performed to investigate the phenomenon of ion resonance instability [1] in cylindrically trapped, partially neutralized electron clouds. A linearised, fluid theory of this instability had been put forward by Davidson and Uhm [16] using the 2D approximation of the cylindrical trap. 2D PIC simulations of the ion resonance instability reveal that the instability initially progresses in close adherence to the linear fluid model, but eventually becomes a fully kinetic, nonlinear phenomenon, exhibiting a whole palette of interesting nonlinear dynamics and energetics that have been explained with the help of numerical diagnostics of the simulations.

- In the next set of numerical experiments on the ion resonance the simulations have been taken a notch closer to real experiments by introducing the influence of 3D elastic and excitation collisions of electrons with background neutrals on the progression of the 2D ion resonance instability of a partially neutralized electron cloud [32]. These simulations performed with a 2D3v PIC code facilitated with 3D Monte-Carlo-Collisions reveal that the elastic and excitation collisions can dynamically alter the path of progression of the ongoing ion resonance instability by a feedback of the collisional relaxation of the electron cloud's profile on the instability [32].

- The final numerical experiment of this thesis is a very realistic simulation in which the gradual destabilization of a cylindrically confined pure electron cloud by electron impact ionization of background neutrals in investigated [33]. The ionizing collisions of electrons with background

neutrals release ions, that drive the cloud unstable by means of the ion resonance instability. The electrons also participate in non-ionizing elastic and excitation collisions with background neutrals that influence the dynamics of the ion resonance instability through the feed back of the collisional relaxation of the electron cloud's profile on the instability. The 2D3v PIC code with facility for Monte-Carlo-Collisions has been used to simulate and investigate different aspects of this highly dynamical process.

1.5 Code development part of the thesis work

Another side of the thesis work was the development of simulation tools for carrying out the above listed numerical experiments. The following two subsections discuss how the PIC method fits as a simulation tool for the investigation of nonneutral plasma phenomena, and the suite of PIC codes developed to investigate the above listed phenomena.

1.5.1 The PIC method as a simulation tool for nonneutral plasma devices

Earlier we discussed how nonneutral plasmas behave according to different theoretical models in different regions of its parametric space. A common simulation tool that can bind all these models is the Particle-in-Cell method. PIC simulations, in different regions of plasma's parameter space, can give us a kinetic Vlasov perspective, or a macroscopic fluid perspective, or even a GCD approximated perspective of the dynamics of the plasma without having to make any changes in the internal structure of the simulation code. However the discrete particle perspective of the plasma with microscopic inter-particle interactions is beyond the capability of PIC simulations and specifically require Molecular Dynamics (MD) simulation [8], which has its own limitations making it unsuitable for simulating the macroscopic collective behaviour of the plasma that is the subject of interest of this thesis.

Another advantage of the PIC method it can easily be appended to a Monte-Carlo-Collisions (MCC) code, to create a PIC-with-MCC code that can simulate collisionless dynamics of the plasma in the PIC part of the code, and collisions of the plasma particles with background neutrals in the MCC part of the code.

For these reasons the numerical simulations of the thesis have been performed using a suite Particle-in-Cell codes.

1.5.2 The suite of Particle-in-Cell codes developed for the numerical experiments of the thesis

The suite of PIC codes developed, and the numerical experiments from Section 1.3 that each code is assigned to handle are enlisted below. For simplicity the names assigned to codes are not revealed in this chapter.

- A 2D PIC code: Investigates i) radial breathing phenomena in non-neutral plasma, and ii) the ion resonance instability in partially neutralized electron clouds.

- A 1D PIC code: Used to demonstrate a method for axially heating single species plasmas in PM traps without driving the plasma far from thermal equilibrium

- A 2D3v PIC-with-MCC code: i) Investigates the influence of non-ionizing collisions between electrons and background neutrals on the dynamics of pure electron clouds, and partially neutralized electron clouds. ii) Investigates the process of destabilization of a pure electron cloud by impact ionization of background neutrals.

1.6 Thesis structure

A brief outline of the remaining chapters of the thesis is explained in the following bullets.

- **Chapter 2:** Takes us through the development of the suite of PIC and PIC-with-MCC codes used in the numerical experiments of this thesis. The numerical set up, the applied numerical techniques, and the numerical diagnostics of the codes are all explained in detail. A set of Benchmarks of the codes are also demonstrated.

- **Chapter 3:** Presents the set of numerical experiments performed with pure electron plasmas which include, i) investigation of radial breathing modes, ii) studying the influence of elastic and excitation collisions of electrons with background neutrals on the dynamics of pure electron plasmas, and iii) demonstrating a novel method for axial heating of single species plasmas without driving them far form thermal equilibrium.

- **Chapter 4:** Presents the set of numerical experiments performed with partially neutralized electron clouds which include i) Investigating the linear and nonlinear dynamics of the ion resonance instability ii) Investigating how non-ionizing collisions of electrons with background neutrals influence the dynamics of the ion resonance instability.

- **Chapter 5:** Presents a numerical experiment the investigates the destabilization of a cylindrically trapped pure electron cloud by the process of impact ionization of background neutrals.

- **Chapter 6:** Conclusions, discussions, and scope for future work make up this concluding Chapter of the thesis.

2

Developing the suite of PIC codes

In a 2014 paper [34] an OPEN-MP parallelized 2D Electrostatic Particle-in-cell code that simulates 2D collisionless dynamics of plasmas in cross-sections of magnetic traps with grounded (or equipotent) boundary was introduced. The 2D PIC code is very flexible, and can simulate unapproximated 2D dynamics (right down to Larmor motion) of multi-component plasmas of varying neutrality in traps of arbitrary shapes and sizes, and any toroidal aspect ratio that is > 5.0. A 2D Cartesian PIC grid spans over the cross-section of the simulated trap with grounded wall. The collisionless 2D dynamics of the plasma are simulated on this grid. This 2D PIC code has been now named as PEC2PIC which is short for "Parallelized Electrostatic Cartesian 2d Particle-In-Cell code".

In the initial papers in 2014 [34], and 2015 [38] the development of the 2D PIC code and the numerical techniques involved were reported. Multiple benchmarks of the code were also demonstrated in these two papers [34, 38]. Numerical experiments performed using PEC2PIC yielded interesting new results for radial breathing modes (Bernstenin modes) of cylindrically confined pure electron plasmas in 2014 [34, 35], and ion-resonance instabilities of ion contaminated cylindrical electron clouds in 2015 [38].

In a 2016 work [32] an upgradation of the 2D PIC code to a 2D3v PIC-with-MCC version was reported. This upgraded code was used to investigate the role of elastic and excitation collisions between electrons and background Argon neutrals on the stable dynamics of cylindrically confined pure electron clouds, and unstable dynamics of ion-contaminated cylindrical electron clouds [32]. In the same paper [32] different technical aspects of the newly introduced Monte-Carlo-Collisions (MCC) that simulated elastic and excitation collisions between electrons and Ar neutrals, were explained. In a later Section of the 2016 paper [32] the statistical and mechanical correctness of the $e^- - Ar$ elastic and excitation collision executions were validated.

In a very recent work [33] a further upgradation the 2D3v PIC-with-MCC code to include ionizing collisions between electrons and background Argon neutrals, as well as elastic and charge exchange collisions between Ar^+ ions and background Ar neutrals was reported. Hence the new upgraded 2D3v PIC-with-MCC code can now simulate elastic, first level excitation, and single ionization collisions between plasma-electrons and background Ar atoms, as well as elastic and charge-exchange collisions
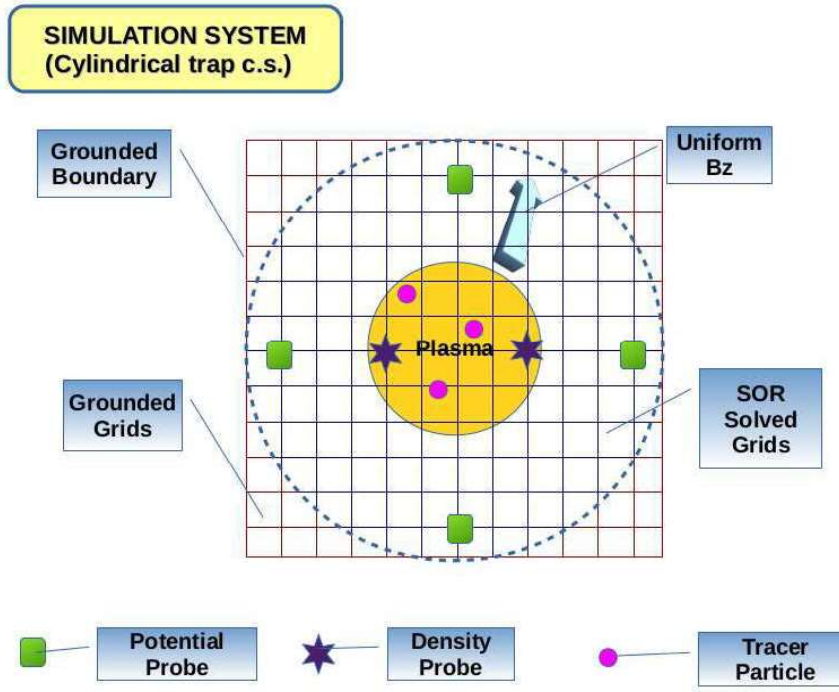
Figure 2.1: Cartoon of the particle-in-cell simulation system

between plasma-Ar^+ and background Ar gas. This 2D3v PIC-with-MCC code has been named as PEC2PIC-3MCC which is short for "Parallelized Electrostatic Cartesian 2d Particle-In-Cell code with 3d Monte-Carlo-Collisions". A validation of the mechanical and stastical correctness of the execution of each of the 5 types of collision by the MCC scheme of the code, was also reported in the recent paper [33]. Using PEC2PIC-3MCC the complex process of destabilization of cylindrically confined pure electron clouds by the electron impact ionization of background Ar atoms was investigated [33].

The 2D PIC code PEC2PIC also has a 1D version PEC1PIC which was used to demonstrate a novel scheme of heating plasmas in a thermodynamic cycle without driving the plasma far away from equilibrium [37]. The unique structure of 1D code to suite the intended purpose, and results of the numerical experiments performed with it were reported in a paper [37].

In the following three sections the numerical details of the three codes are elaborated.

2.1 The 2D Particle-in-cell code PEC2PIC

A 2D Electrostatic Particle-In-Cell code has been developed in FORTRAN-90 using Cartesian co-ordinates, and parallelized with OPEN-MP [34, 35]. It is called PEC2PIC. The code can simulate cross sections of multi-component plasmas of varying neutrality, confined within any perfectly conducting closed boundary curve. The size, shape, and toroidal aspect ratio (limited to > 5.0) of the boundary can be manoeuvred as per requirements, hence easily extendible to large aspect ratio toroidal traps

as well. To load an initial density profile or velocity distribution of the pseudo particles, the code employs a cumulative distribution function inversion method [39] with Halton's sequence of quasi random numbers [40], for smooth distribution of particles under the distribution curves. First order Cloud-in-cell scheme [39] is used to spread the discrete charges of the pseudo particles over the cell as a continuous charge density function. Poisson equation is solved at the cell-nodes to obtain the electrostatic fields on these nodes, with parallelized red-black Successive-Order-Relaxation (SOR) method [41, 42]. To estimate the field at a particle's location, the Cartesian components of the field is first calculated at the nodes of the particle's occupancy cell by centrally differentiating the SOR solved potential at the nodes. These components are then individually area-weighted to the particle's location. The code utilizes the full mass-included equations of motion of all plasma components, to push the particles. Chin's exponential splitting scheme [43, 44] is applied for this purpose. The code employs several numerical diagnostics to investigate the dynamics of the simulated plasma.

The simulation system of the code is schematically represented in Fig. 2.1. Every numerical aspect of PEC2PIC is discussed in detail the following subsections.

2.1.1 Loading the initial conditions of the plasma

As the PIC simulation is essentially an initial value problem, the initial spatial density function and the velocity distribution function of the plasma must be given in some analytical or numerical form, or they may be estimated from other parameters of the plasma such as temperature. To load the initial velocity distribution and spatial density function the method of cumulative distribution function inversion [39] is used with Halton's sequence of quasi random numbers [40] for obtaining smooth distributions.

2.1.2 Charge to mesh assignment by first order Cloud-in-Cell scheme

An important aspect of the particle-in-cell method of simulation than can influence its stability and performance, is the numerical scheme used for switching from the discrete-super-particles-picture to the charge-distributed-over-mesh picture in every time step of the siumalation. For most simulation systems, a very efficient and highly popular scheme that gives good performance of the code is the first order Cloud-In-Cell (CIC) scheme. To explain the first order CIC scheme we will start with the simplest zeroeth order interpolation scheme known as the Near grid point (NGP) scheme for charge to mesh assgignment [39].

Initially the charge density on all inner mesh points is zero. Consider a super particle located inside a mesh cell of area $\Delta x \Delta y$. In the NGP scheme we first identify the nearest gird point of the super particle. Say the net charge of the super particle is q. Then we can assume that this super particle is a uniformly charged cloud of dimensions equal to the PIC cell dimension. Hence the charge density of the cloud is $q/\Delta x \Delta y$. In the NGP scheme we simply approximate that the geometric centre of the charge cloud is at the nearest grid point. This amounts to adding the charge density $q/\Delta x \Delta y$
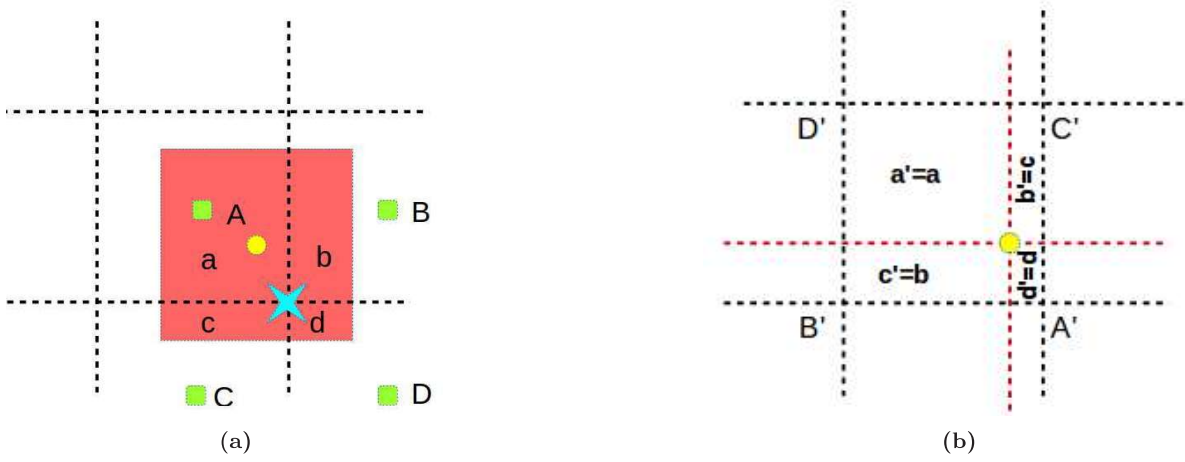
Figure 2.2: Cartoon of the Cloud-in-Cell (CIC) scheme for distribution of charge on the numerical mesh

to the existing charge density of the nearest grid point. Repeating this charge to mesh assignment process for every super particle additively builds up the charge density on all inner mesh points.

A superior method of charge to mesh assignment is a first order interpolation scheme known as the CIC scheme. In this scheme the super particle is again considered as a uniformly charged cloud of dimensions same as that of a PIC cell and uniform charge density, $\rho = q/\Delta x \Delta y$ (see Fig. 2.2a). Now the CIC scheme has two equivalent models (Fig. 2.2a and 2.2b) that, upon implementation, effectively give the same result. In the first model (Fig. 2.2a) we begin with an assumption of zero charge density at the centres of all PIC cells of the mesh. Consider a pseudo particle to be located at an arbitray point in a PIC cell, marked in Fig. 2.2a with yellow filled circle. Now if the location of the particle does not coincide with the geometric centre of its occupancy cell, then the corresponding charge cloud, by virtue of its given dimension, will have one and only one grid point of the occupancy cell located within it. The encompassed grid point is marked by a blue 'X' mark in Fig. 2.2a. Now the intersecting mesh lines at 'X' divide the cloud into areas a, b, c, and d. There are also 4 centres of PIC cells, A, B, C,, and D that constitute the 4 nearest centre-of-cell neighbours of the intersection point 'X'. In the CIC scheme an area weighted first order interpolation is applied to divide the cloud charge density ρ between the 4 centre of cells A, B, C,, and D. For example the interpolated charge density at A is $\rho\, a/(a+b+c+d) = \rho\, a/(\Delta x \Delta y)$. Similarly ρ can be interpolated to the three remaining centre-of-cells. The charge densities interpolated to A, B, C, and D from the super particles location is added to the existing value of charge densities at these centres-of-cells. If the particle's position happens to exactly coincide with the centre of the occupancy cell (point A in Fig. 2.2a) then the the entire charge density ρ is added to the existing charge density of only the occupancy cell's centre. Repeating this interpolation process for all super particles in the mesh will additively build up the charge density distribution over all cell-centres of the mesh.

In the second model of the CIC scheme we begin with an assumption of zero charge density at

all grid points. For a super particle that is located at any arbitrary point inside a PIC cell, the interpolation of its CIC charge density $\rho = q/\Delta x \Delta y$ is made to the four corners of its occupancy cell, A', B', C', and D' (Fig. 2.2b). The constructed vertical and horizontal line that intersect at the particle's location divide the occupancy cell into 4 areas a', b', c', and d'. It can be worked out the these area segments match with the segments a, b, c, and d of Fig. 2.2a as $a' = a$, $b' = c$, $c' = b$, and $d' = d$. The cloud charge ρ is now divided between A', B', C', and D' by an area weighted first order interpolation scheme. The area weight of a cell corner is taken as the fractional area of the area segment that is not bounded by either of the two grid lines that intersect at the cell corner under consideration. For example the charge density interpolated to the grid point A' is $\rho\, a/(a + b + c + d) = \rho\, a/(\Delta x \Delta y)$. Similar the charge density can be interpolated to the other three corners. The interpolated charge at a grid point is added to the existing charge density at that grid point. If the super particle happens to be located exactly at a grid point then its entire charge density ρ is added to the existing charge density of only that grid point. Repeating this interpolation process for all super particles in the mesh will additively build up the charge density distribution over of all grid points.

We see that the first model of the CIC scheme results in charge density distribution at the cell centres of the mesh, whereas in the second model the charge density is distributed on the grid points. A comparison between Fig. 2.2a and Fig. 2.2b shows that the fraction of the clouds charge density distributed to the cell centres A (maximum occupancy cell of the cloud),B (second most occupied cell),C (third in occupancy),and,D (minimum occupancy cell) is equal to the charge density distributed to A' (nearest gird point),C' (second nearest grid point),B' (third nearest gird point),and,D' (farthest grid point) respectively. While working with the first CIC model, the distribution of charge density at the cell centres is followed solving the Poisson Equation for the electrostatic potential at the cell centres. Next the central difference formula is used to find the field component at the cell centres. The field components from the 4 cell centres covered by the charge cloud are then interpolated to the particles location for the trajectory progress of the particle. When using the second CIC model, first the potential function, and then field components are determined at the gird points by the exact same procedures as with the first CIC model. The field components from the occupancy cell's corners are then interpolated to the particle's location to move the particle. An analysis of the two mumerical procedures reveals that they are effectively same, and result in the exact same trajectories of the super particles. While the first model (Fig. 2.2a) serves as a more effective way of understanding the CIC schem, it is the sendond model (Fig. 2.2b) that is more convenient and less expensive to implement in a PIC code. In our PIC code we have also worked with the second model for the CIC scheme.

An OPEN-MP parallelization of the charge-to-mesh distribution by the CIC scheme has been implemented in the PIC code by parallelizing the process over super particles, and then using an OPEN-MP reduction to add up the charge density distribution on the mesh obtained from the chunk of particles in each OPEN-MP thread.

Continuing with second model of the CIC scheme, next we need to work out a procedure to prevent charge density from getting distributed to boundary points or points with pre-fixed potential values, and at the same time conserve the net trapped charge in the system. To explain the numerical procedure of dealing with charge density getting distributed to grid points with maintained potentials, we will consider numerical methods that work for our simulation system. In our system we have a numerical circular boundary of the trap carved out inside the Cartesian mesh (Fig. 2.1). Grid points lying outside this circular boundary are numerically grounded, and particles that happen to touch or cross the circular boundary in course of the simulation, are considered as lost from the system and cease to contribute any further to plasma dynamics. However it may happen that even a trapped particle contributes charge density to a grounded grid, if it happens to lie in a cell that is split into two segments by a section of the circular boundary (see Fig. 2.3a). In such a scenario, the split cell should have at least one point in the trap region of the mesh and at most three points in the grounded region of the mesh and the trapped particle should be located in the segment of the cell that is in the trap region.

The objective now is to re-allocate the charge density that got distributed on the grounded grid points by CIC interpolation to grid points in the trap region. The most technically accurate and elaborate procedure for this charge-density re-assignment is represented in Fig. 2.3a. In this method, we examine the charge density interpolated from each trapped particle on the corners of its occupancy cell. First, we check if any (at most three) corner of the occupancy cell lies in the grounded region. If al teast one corner of the cell is detected to be in the grounded region, we proceed to identify that corner of the occupancy cell which has the lowest value of grid indices. Say, the indices of this corner are identified as (i_l, j_l). The indices of the remaining three corners are then obviously (i_l+1, j_l), (i_l, j_l+1), and $(i_l + 1, j_l + 1)$. We check the relative position of the grounded corner with respect to the lowest indices of cell *i.e.* we identify which indices out of (i_l, j_l), $(i_l + 1, j_l)$, $(i_l, j_l + 1)$, and $(i_l + 1, j_l + 1)$ belongs to the grounded corner. Now for each of these 4 possibilities we know the exact translation required to reach the other three corners of the occupancy cell from the grounded corner. For example if the grounded corner happens to have the indices $(i_l, j_l + 1)$ then we know that the remaining 3 corners can be reached by lowering the y index by 1, raising the x idex by 1, and by raising both indices by 1. Re-allocation of the super particle's CIC interpolated charge density from the grounded grid point is implemented by making the following translations in order of priority:- 1) Re-allocate the particle's interpolated charge density from the grounded corner of the occupancy cell, to that corner of the occupancy cell which is the x-neighbbour (neighbouring grid point along the x axis) of the grounded grid point. For example the particle's interpolated charge density should be transferred from the grounded corner with indices $(i_l, j_l + 1)$ to the x-neighbour in the occupancy cell that has the indices $(i_l + 1, j_l + 1)$. However it may so happen that the x-neighbour itself is also another grounded grid point. In that case we take the second option viz, 2) we re-allocate the particle's iterpolated charge density from the grounded corner of the occupancy cell, to that corner of the occupancy cell which is the y-neighbbour of the grounded grid point. For example the particle's interpolated charge

(a)

(b)

(c)

(d)
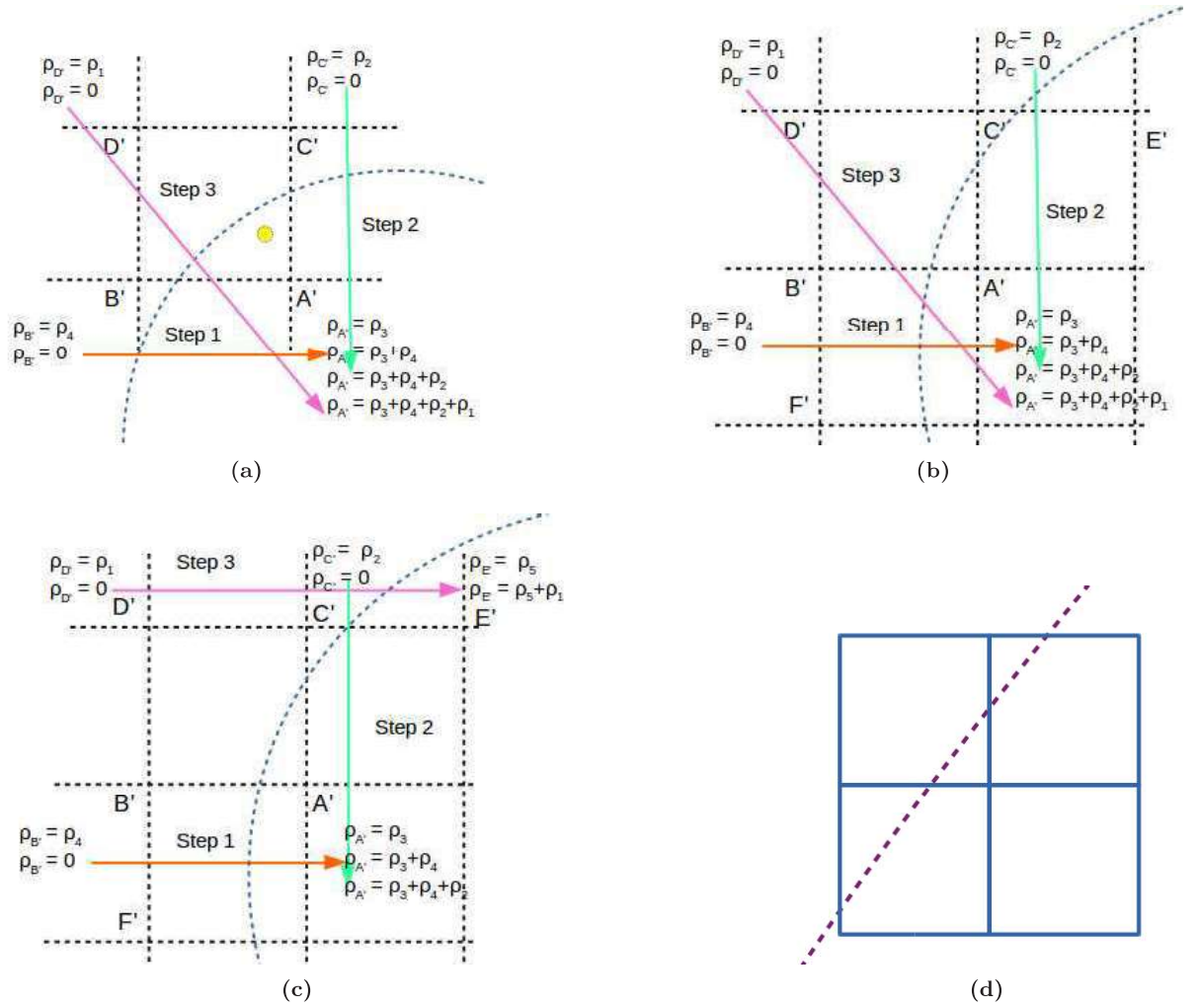
Figure 2.3: Handling curved boundaries with a cartesian grid: A schematic cartoon demonstrating how charge density is re-allocated from grounded grid points in the simulation.

density should be transferred from the grounded corner with indices $(i_l, j_l + 1)$ to the y-neighbour in the occupancy cell that has the indices (i_l, j_l). If the y-neighbour itself is also a grounded point we take the third option viz, 3) re-allocate the particle's charge density from the grounded corner of the occupancy cell, to its diagonally opposite corner in the occupancy cell. For example the particle's interpolated charge density should be transferred from the grounded point with indices $(i_l, j_l + 1)$ to the diagonally opposite corner with indices $(i_l + 1, j_l)$. In this way we re-allocate charge density from every grounded corner of the occupancy cell to another corner of the cell that is not grounded. As an example, in Fig. 2.3a we have schematically shown the charge density re-allocation process in an occupancy cell that has three of its corners in the grounded region of the mess.

It is evident that the above procedure involves checking the corners of the occupancy cell of every super particle and upon encountering any grounded corner of the cell, reallocating the particle's inter-polated charge desnity to another non-grounded grid of the same cell following the algorithm described above. Such a procedure may be parallely implemented by appending it to the CIC distributor in the code under the same parallelized loop over particles. The method is also technically the most accurate as the charge density interpolated from a super particle occupying a cell with grounded corner(s) gets re-distributed only among the non-grounded corner(s) of that very occupancy cell. However the method does involve checking each of the four corners of the occupancy cell of every super particle at every time step and carrying out any required re-allocation of interpolated charge density for individual particles. In the trap cross-section that we are simulating (Fig. 2.1) the bulk plasma remains well confined within the numerical circular boundary and there is no other plasma dynamics taking place at a proximity of one cell length from the circular wall, besides the eventual loss of the particles that got transported so close to the wall. Hence for our system the above described procedure for charge re-allocation is computationally expensive, over-exact, and too elaborate. However this charge density re-allocation recipe should be useful for systems in which major plasma dynamics take place at very close proximity to the wall.

We will now try to find a more practical, and computationally less expensive solution for the charge density re-allocation from grounded grid points. Now suppose the inner circular boundary was absent and the rectangular boundary of the mesh was the only conducting boundary of the system. In that case an equally accurate charge re-allocation as above can be achieved by a simpler process, as follows - 1) Let all particles distribute charge density to the corners of their respective occupancy cells and build up the charge density distribution over the entire mesh including the grounded rectangular boundaries 2) Now re-allocate the charge density from the grounded grid points on the first and last column of the mesh to the corresponding neighbouring grid points on the second column and second-last column of the mesh respectively. 3) Next, the charge density on the grounded gird points on the first row and last row should be re-allocated to corresponding neighbouring grid points on the second row and second last row respectively. Note in this scheme the charge re-allocation becomes a one time procedure carried out on the rectangular boundaries after all particles have distributed charge density on the mesh and hence is computationally much less expensive.

Now when the circular boundary is present within the rectangular mesh it is not possible to work out a post-CIC-distribution scheme for charge density re-allocation from grounded points that matches exactly with the particle-wise re-allocation procedure. Let us explain with an example. Consider the grounded point C' in Fig. 2.3b. Let us say we carry out a post-distribution re-allocation that transfers the total charge density at C' to neighbouring non grounded point E'. If there is a particle in the cell $D'C'A'B'$ which had contributed to the initial charge density at C', then its contribution will also get translated to the point E' which does not belong to its occupancy cell. Hence the loss of information about a) the occupancy cells of particles contributing to the charge density a particular grounded gird point and b) the fraction of charge density contributed by each of them, makes a post-distribution inequivalent and only an approximate substitute to to the particle-wise charge density re-allocation scheme. However as explained earlier, for our simulation system a post-distribution re-allocation procedure is more practical despite its inherent approximations, and also computationally much less expensive. We will now discuss two such post-distribution re-allocation procedures that is suitable for our system.

The first post-distribution scheme is schematically represented in Fig. 2.3b. In this scheme we initially scan all the grounded grid points for non-zero charge density after the CIC distribution. Grounded grid points that got non-zero charge density allocated to them in the CIC distribution, are obviously also corners of a cell that is divided by a segment of the circular boundary. In the remaining procedure we only have to re-allocate charge from these selected grounded points with non-zero charge densities. Hence our computational work is significantly reduced. The re-allocation can be implemented by a simple set of rules as follows - 1) We check if the left or the right neighbour of the grounded point lies in the trap region. If so then we re-allocate the charge to the neighbour that is non-grounded (for our system only one of these two neighbours of a grounded point has the possibility of being non-grounded). For example in Fig. 2.3a charge density from B' is re-allocated to A'. Now it may so happen that both the left and right neighbour are also grounded, as we see for the point C' in Fig. 2.3a. In that case we take the next option ,$i.e.$ 2) We check if the top or the bottom neighbour of the grounded point lies in the trap region. If so then we re-allocate the charge to the neighbour that is non-grounded (for our system only one of these two neighbours of a grounded point has the possibility of being non-grounded). For example in Fig. 2.3a charge density from C' is re-allocated to A'. Again if both these two two neighbours are also grounded points, as is the case for point D' in Fig. 2.3b then we take the next option, viz, 3) We check the four diagonally opposite points to the grounded point to see which of these four points is non-grounded (if we have reached option 3 then not more than one diagonally opposite point will be non-grounded). Once the non-grounded diagonally opposite point is identified then we re-allocate the grounded points charge density to this point. For example in Fig. 2.3a charge density from D' is re-allocated to A'.

The second post-distribution re-allocation scheme, schematically represented in Fig. 2.3c works on the same principle as the first post-distribution re-allocation scheme. Infact all the steps of this scheme is exactly the same as the former except for the last option 3. In this scheme , as a third option, we

check the next to next left and right neighbours and the next to next top and bottom neighbours of the grounded point to see which out of these four next-to-next neighbours is non-grounded (if we have reached option 3 then not more than one next-to-next neighbour will be non-grounded, as is the case with point D' in Fig. 2.3c). Once the non-grounded next-to-next neighbour is identified we re-allocate the charge density of the grounded point to this point. For example in Fig. 2.3c charge density from D' is re-allocated to E'. There is an interesting little proof which makes this scheme work. If the cell dimensions are very small compared to the radius of the circular boundary, then the circular segment divding the cell can obviously be approximated as a straight line. The schematic drawing of Fig. 2.3c is not in scale. We have constructed Fig. 2.3d with the actual dimensions of the our PIC grid and the circular boundary for a correct visual perspective. The apparent dashed straight line in Fig. 2.3c is acctually the segment of the circular boundary while the four squares in soilid lines are PIC cells. Going back to Fig. 2.3c with the straight line approximation of the intersecting circular boundary, we can work out that it is not possible for the boundary (approximate straight line) to cut both $A'C'$ and $A'B'$ at points other than A' at not cut either of $C'E'$ or $B'F'$. This implies we do not have to scan in the x and y directions beyond the next-to-next neighbours of a grounded corner of a cell cut by the circular boundary, to reach another non-grounded point.

In the PIC code we have implemented the second post-distribution re-allocation scheme of Fig. 2.3a.

2.1.3 The SOR Poisson Solver

Consider solving a generalized form of the 2D Poisson equation with Dirichlet Boundary Conditions by Sucessive-Over-Relaxation method. Given below is the 2D Poisson Equation in which $f(x,y)$ is a known function and $U(x,y)$ is the function to be solved within the given boundaries in x and y.

$$U_{xx} + U_{yy} = f, \qquad \text{where } 0 \leq x \leq a, \text{ and } 0 \leq y \leq b \tag{2.1}$$

The Dirichlet's Boundary conditions in x and y for the problem can be expressed by the following set of equations.

$$U(0,y) = g_1(y), \quad U(a,y) = g_2(y), \quad U(x,0) = h_1(x), \quad U(x,b) = h_2(x) \tag{2.2}$$

Here $g_1(y)$, $g_2(y)$, $h_1(x)$, $h_2(x)$ are known functions.

Now the first step of any numerical solution of the Poisson Equation is discretization of the solvable space into a grid system with equispaced points along each axis (Fig. 2.1), and expression of the differentials in the equation by finite differences. For generalization let us suppose that the space between $x=0$ and $x=a$ is now divided into $m+1$ equal divisions of length Δx (i.e. $\Delta x = a/(m+1)$) by $m+2$ number of points marked as x_i where $i = 0, 1, ...m, m+1$. Similarly the space between $y=0$ and $y=b$ is now divided into $n+1$ equal divisions of length Δy (i.e. $\Delta y = b/(n+1)$) by $n+2$ number of points marked as y_j where $j = 0, 1, ...n, n+1$. At each grid point the co-ordinates can be expressed as x_i, y_j while functions like $U(x,y)$ and $f(x,y)$ can be expressed as U_{ij} and f_{ij} respectively. Similarly the boundary functions at the boundary axes points may be expressed as $g_{1j}, g_{2j}, h_{1i}, h_{2i}$.

Now in order to express U_{xx} and U_{yy} as finite differences we need to employ Taylor series expansions. Let us expand $U_{i+1,j}$ in Taylor series about the point $U_{i,j}$

$$U_{i+1,j} = U_{i,j} + \Delta x (U_x)_{i,j} + \frac{\Delta x^2}{2}(U_{xx})_{i,j} + \frac{\Delta x^3}{6}(U_{xxx})_{i,j} + O(\Delta x^4) \tag{2.3}$$

$$U_{i-1,j} = U_{i,j} - \Delta x (U_x)_{i,j} + \frac{\Delta x^2}{2}(U_{xx})_{i,j} - \frac{\Delta x^3}{6}(U_{xxx})_{i,j} + O(\Delta x^4) \tag{2.4}$$

Performing (2.3) - (2.4) and neglecting $O(\Delta x^2)$ terms yields

$$(U_x)_{i,j} = \frac{U_{i+1,j} - U_{i-1,j}}{2\,\Delta x} \qquad \text{the central difference formula for} U_x \tag{2.5}$$

Again performing (2.4)+(2.3)-2$U_{i,j}$ and neglecting $O(\Delta x^2)$ terms gives the central difference formula for U_{xx} as follows

$$(U_{xx})_{i,j} = \frac{U_{i+1,j} - 2U_{i,j} + U_{i-1,j}}{\Delta x^2} \tag{2.6}$$

Applying similar Taylor series expansions of $U_{i,j+1}$ and $U_{i,j-1}$ about $U_{i,j}$ we can arrive at

$$(U_y)_{i,j} = \frac{U_{i,j+1} - U_{i,j-1}}{2\Delta y} \qquad \text{the central difference formula for} U_y \tag{2.7}$$

and

$$(U_{yy})_{i,j} = \frac{U_{i,j+1} - 2U_{i,j} + U_{i,j-1}}{\Delta y^2} \qquad \text{the central difference formula for} U_{yy} \tag{2.8}$$

Using (2.6) and (2.8) we can now express the Poisson Equation (2.1) at the interior mesh point as a set of $m \times n$ equations as follows

$$\frac{U_{i+1,j} - 2U_{i,j} + U_{i-1,j}}{\Delta x^2} + \frac{U_{i,j+1} - 2U_{i,j} + U_{i,j-1}}{\Delta y^2} = f_{i,j} \quad for \ i = 1,2,....m \ \ \& \ j = 1,2,...n \tag{2.9}$$

For solution by an iterative method we can re-write (2.9) as

$$U_{i,j} = \frac{1}{4}\left[\Delta_x{}^2\left(U_{i,j+1} + U_{i,j-1}\right) + \Delta_y{}^2\left(U_{i+1,j} + U_{i-1,j}\right)\right] - \frac{1}{4}\Delta_x{}^2\Delta_y{}^2 f_{i,j} \tag{2.10}$$

The next step is to identify boundary points with given values of $U_{i,j}$ that may be encountered on the RHS of (2.10). For example while solving for $U_{2,1}$ one will encounter the boundary point $U_{2,0}$ (in $U_{i,j-1}$) on the RHS of (2.10). On encountering such boundary points, the RHS of (2.10) will have to be reshuffled as demonstrated below.

First let us introduce flag functions $q_{i,j}$ and $q_{i,j}^*$ such that $q_{i,j} = 0$ and $q_{i,j}^* = 1$ on a boundary point and $q_{i,j} = 1$ and $q_{i,j}^* = 0$ on an interior mesh point. In that case we can re-shuffle the RHS of (2.10) as

$$U_{i,j} = \left[\frac{1}{4}\left\{\Delta_x{}^2\left(q_{i,j+1}U_{i,j+1} + q_{i,j-1}U_{i,j-1}\right) + \Delta_y{}^2\left(q_{i+1,j}U_{i+1,j} + q_{i-1,j}U_{i-1,j}\right)\right\}\right]$$
$$-\left[\frac{1}{4}\left\{\Delta_x{}^2\Delta_y{}^2 f_{i,j} - \Delta_x{}^2\left(q_{i,j+1}^*U_{i,j+1} + q_{i,j-1}^*U_{i,j-1}\right) - \Delta_y{}^2\left(q_{i+1,j}^*U_{i+1,j} + q_{i-1,j}^*U_{i-1,j}\right)\right\}\right] \tag{2.11}$$

The re-arrangement of the RHS in (2.11) helps in expressing the equation set (2.11) in the form of a numerically solvable matrix equation. Notice that now the term inside the first square bracket on the RHS contains values of $U_{i,j}$ on interior mesh points only, *i.e.* $U_{i,j}$ values that need to be solved. The term inside the second square bracket on the RHS all have fixed values for all $U_{i,j}$ on the LHS. Now if we write down the set of $m \times n$ equations of (2.11) arranging the $U_{i,j}$ on the LHS in a ascending order of $j = 1, 2, ...n$ nested within an ascending order of of $i = 1, 2, ...m$, and let $N = m \times n$, then (2.11) can be packed into a matrix equation of the form

$$\mathbf{U} = \mathbf{A}\,\mathbf{U} + \mathbf{F}$$

or in general linear equations matrix form $\quad (\mathbf{I_N} - \mathbf{A})\,\mathbf{U} = \mathbf{F}$

$$(2.12)$$

In (2.12) $\mathbf{U}$ and $\mathbf{F}$ are $N \times 1$ column matrices, $\mathbf{I_N}$ is an Nth order Identity matrix, while $\mathbf{A}$ is $N \times N$ square matrix. Let us make an index transformation here. Let $k = 1, 2, ...N$ be the row index of $\mathbf{U}$ such that $k = (i-1)\,n + j$. A comparison of (2.11) and (2.12) reveals that $\mathbf{U}$ represents the LHS of the equation set (2.11) containing unsolved U_k (*i.e.* $U_{i,j}$) values on the interior mesh points. The product $\mathbf{AU}$ represents in the terms in the first square bracket of (2.11). Specifically $\mathbf{A}$ contains the calculated coefficients of U_k (*i.e.* $U_{i,j}$) in the term of the first square bracket of (2.11). From (2.11) it can be seen that $\mathbf{A}$ is a sparse co-efficient matrix ideal for iterative solutions. $\mathbf{F}$ contains the calculated values of the fixed terms within the second square bracket of (2.11).

The matrix equation (2.12) can also be expressed as a set of equations of its elements as follows.

$$U_k = \sum_{k'=1}^{N} A_{k,k'} U_{k'} + F_k \qquad where \; k = 1, 2, ..., N \tag{2.13}$$

Note that determining the matrix elements of $\mathbf{A}$ and $\mathbf{F}$ is a one time process. Next let us begin solving for U_k iteratively. The iterative process begins with a guessed solution for every U_k. The standard procedure is to initiate the iterative solution process with a guessed common value of $U_k = 0$ for $k = 1, 2, ..., N$. Let us introduce the iteration index l in the superscript of U_k. Hence beginning the iteration with $U_k^0 = 0$ we can express an iterative solution with l as the iteration index, as follows.

$$U_k^{l+1} = \sum_{k'=1}^{N} A_{k,k'} U_{k'}^{l} + F_k \qquad where \; k = 1, 2, ..., N \tag{2.14}$$

$$and \; l = 0, 1, 2.....(upto \; total \; number \; of \; necessary \; iterations)$$

The above equation is the formula for an iterative solution by the Jacobian method. Every successive set of values of U_k^l brings the function numerically closer to actual solution. The iterations can be stopped when the whole set of values of U_k have converged sufficiently towards the solution or, more practically, when in the error in successive sets of solution is sufficiently small, *i.e.*

$$\left| \frac{U_k^l - U_k^{l-1}}{U_k^l} \right| \leq \; error \; tolerance \; (e.g \; 10^{-6}) \; for \; k = 1, 2, ...N \tag{2.15}$$

Now the convergence of (2.14) may be accelerated by using available iterative updates of values of U_k from the same iteration step, instead of updating the whole set of values of U_k together at the end of the iteration step. This implies a tweaking of the formula of (2.14) as follows.

$$U_1^{l+1} = \sum_{k'=1}^{N} A_{1,k'} U_{k'}^l + F_1 \qquad (k = 1)$$

$$U_k^{l+1} = \sum_{k'=1}^{k-1} A_{k,k'} U_{k'}^{l+1} + \sum_{k'=k}^{N} A_{k,k'} U_{k'}^l + F_k \qquad (k = 2, 3, ..., N-1) \qquad (2.16)$$

$$U_N^{l+1} = \sum_{k'=1}^{N-1} A_{N,k'} U_{k'}^{l+1} + F_N \qquad (k = N)$$

$$where \; l = 0, 1, 2.....(upto \; total \; number \; of \; necessary \; iterations)$$

Solving for U_k using (2.16) amounts to using the Gauss-Siedel Method for solution. This method is not only more efficient than the Jacobian method (2.14) as it converges faster than the former, but is also computationally less expensive as only last updated U_k values are retained in the memory in every iteration step.

Now an inspection of (2.10) from which (2.16) was derived reveals that in (2.16) the term $A_{k,k} = 0$ for all values of k. Hence we can remove terms with $A_{k,k}$ from (2.16) as follows.

$$U_1^{l+1} = \sum_{k'=2}^{N} A_{1,k'} U_{k'}^l + F_1 \qquad (k = 1)$$

$$U_k^{l+1} = \sum_{k'=1}^{k-1} A_{k,k'} U_{k'}^{l+1} + \sum_{k'=k+1}^{N} A_{k,k'} U_{k'}^l + F_k \qquad (k = 2, 3, ..., N-1) \qquad (2.17)$$

$$U_N^{l+1} = \sum_{k'=1}^{N-1} A_{N,k'} U_{k'}^{l+1} + F_N \qquad (k = N)$$

$$where \; l = 0, 1, 2.....(upto \; total \; number \; of \; necessary \; iterations)$$

The Subtraction (2.17)-U_k^l yields the expression for $\Delta_{l+1} U_k = U_k^{l+1} - U_k^l$, the change in the value of solution brought about by the $(l+1)^{th}$ Gauss-Seidel iteration as follows.

$$\Delta_{l+1} U_1 = \sum_{k'=2}^{N} A_{1,k'} U_{k'}^l + F_1 - U_1^l \qquad (k = 1)$$

$$\Delta_{l+1} U_k = \sum_{k'=1}^{k-1} A_{k,k'} U_{k'}^{l+1} + \sum_{k'=k+1}^{N} A_{k,k'} U_{k'}^l + F_k - U_k^l \qquad (k = 2, 3, ..., N-1) \qquad (2.18)$$

$$\Delta_{l+1} U_N = \sum_{k'=1}^{N-1} A_{N,k'} U_{k'}^{l+1} + F_N - U_N^l \qquad (k = N)$$

$$where \; l = 0, 1, 2.....(upto \; total \; number \; of \; necessary \; iterations)$$

An iterative solution procedure in which the $\Delta_{l+1} U_k$ of the Gauss-Seidel iteration step (RHS of 2.18) is mathematically manipulated by scaling it by a factor α is the Successive Relaxation method

for solution. The purpose of scaling the change $\Delta_{l+1}U_k$ by α is ofcourse a faster convergence than the Gauss-Seidel Method. The Successive Relaxation Method solution can be expressed as follows.

$$U_1^{l+1} = U_1^l + \alpha \left[\sum_{k'=2}^{N} A_{1,k'} U_{k'}^l + F_1 - U_1^l \right] \qquad (k = 1)$$

$$U_k^{l+1} = U_k^l + \alpha \left[\sum_{k'=1}^{k-1} A_{k,k'} U_{k'}^{l+1} + \sum_{k'=k+1}^{N} A_{k,k'} U_{k'}^l + F_k - U_k^l \right] \qquad (k = 2, 3, ..., N-1) \qquad (2.19)$$

$$U_N^{l+1} = U_N^l + \alpha \left[\sum_{k'=1}^{N-1} A_{N,k'} U_{k'}^{l+1} + F_N - U_N^l \right] \qquad (k = N)$$

$$where \; l = 0, 1, 2.....(upto \; total \; number \; of \; necessary \; iterations)$$

Equation (2.19) can also be expressed as

$$U_1^{l+1} = (1 - \alpha) U_1^l + \alpha \left[\sum_{k'=2}^{N} A_{1,k'} U_{k'}^l + F_1 \right] \qquad (k = 1)$$

$$U_k^{l+1} = (1 - \alpha) U_k^l + \alpha \left[\sum_{k'=1}^{k-1} A_{k,k'} U_{k'}^{l+1} + \sum_{k'=k+1}^{N} A_{k,k'} U_{k'}^l + F_k \right] \qquad (k = 2, 3, ..., N-1) \qquad (2.20)$$

$$U_N^{l+1} = (1 - \alpha) U_N^l + \alpha \left[\sum_{k'=1}^{N-1} A_{N,k'} U_{k'}^{l+1} + F_N \right] \qquad (k = N)$$

$$where \; l = 0, 1, 2.....(upto \; total \; number \; of \; necessary \; iterations)$$

The quantity α in the successive relaxation formula (2.19) and (2.20) is called the accelerating factor. It can be shown that the iterative solution (2.20) converges only for $0 < \alpha < 2$ [45]. The sucessive relaxation method is further classified according to the chosen value of α for the iterative solution.

- $\alpha = 0 \;\Rightarrow\; Stationary \; Solution$

- $0 < \alpha < 1 \;\Rightarrow\; Successive \; Under - Relaxation$

- $\alpha = 1 \;\Rightarrow\; Gauss - Siedel$

- $1 < \alpha < 2 \;\Rightarrow\; Successive \; Over - Relaxation$

For solving Poissons Equation Sucessive Over-Relaxation (or SOR) usually has the fastest convergence among the iterative methods described, and it is the method that we have implemented in our PIC code as the Poisson Solver. Assuming that the Gauss-Seidel iterations converge towards a solution, the SOR accelerates this convergence by stretching the progress of the solution, $\Delta_{l+1}U_k$, in each step to α (where $1 < \alpha < 2$) times the its value in the Guass-Siedel iteration step.

There exists an optimum value of α, $1 < \alpha_{op} < 2$, for which the SOR solution converges fastest. For a general system of linear equations matrix of the form $\mathbf{Px} = \mathbf{q}$ there is no explicit formula

to determine α_{op} for the SOR solution of the system in terms of properties of the system matrix A [45]. However the special structure of the system matrix $(\mathbf{I_N} - \mathbf{A})$ in (2.12) resulting form the finite difference discretization of the Poisson Equation, makes it possible to determine α_{op} for the system [45]. For the above problem it can shown that the optimum accelerating factor for the SOR solution can be determined by the by the following formula [45].

$$\alpha_{op} = \frac{2}{1 + \sqrt{1 - \beta^2}} \tag{2.21}$$

$$where \ \beta = 1 - \sin^2 \frac{\pi}{2(n+1)} - \sin^2 \frac{\pi}{2(m+1)} \tag{2.22}$$

In (2.22) β represents the value of the Spectral Radius of the Jacobian Iteration Matrix of the given system (for definition and significance of Iteration matrices and their spectral radii for different Iterative solution methods refer [45])

Often while simulating experimental systems as Fig. 2.1 one encounters inner mesh points where the potential function is given and should not be solved for. For instance,

- While numerically carving out an artificial boundary shape within the natural rectangular boundaries of the cartesian system, one will also have to include mesh points lying outside the artificial boundary (red grid points in Fig. 2.1) as being points having fixed values of $U_{i,j}$.

- Experimental application of potentials at any region within the solved space (blue region of the mesh in Fig. 2.1 is achieved by fixing potentials of the grid points in that region. In that case such grid points are also to be considered as points with fixed values of $U_{i,j}$.

When we encounter such inner mesh points with given potentials we supply the known value of the potential function of that point as the initial guess for potential value at that particular point and make sure that this value is not updated in the iterative solver. Hence taking these special inner grid points into consideration the SOR solution can be expressed as follows

$$U_1^{l+1} = (1 - \alpha) U_1^l + \alpha \left[\sum_{k'=2}^{N} A_{1,k'} U_{k'}^l + F_1 \right] \qquad (k = 1)$$

$$U_k^{l+1} = (1 - \alpha) U_k^l + \alpha \left[\sum_{k'=1}^{k-1} A_{k,k'} U_{k'}^{l+1} + \sum_{k'=k+1}^{N} A_{k,k'} U_{k'}^l + F_k \right] \qquad (k = 2, 3, ..., N - 1)$$

$$\tag{2.23}$$

$$U_N^{l+1} = (1 - \alpha) U_N^l + \alpha \left[\sum_{k'=1}^{N-1} A_{N,k'} U_{k'}^{l+1} + F_N \right] \qquad (k = N)$$

$$Where \ l = 0, 1, 2..... (upto \ total \ number \ of \ necessary \ iterations)$$

$$And \ where \ \alpha = 0 \ for \ pre \ determined \ U_k \ and \ \alpha = \alpha_{op} \ for \ all \ other \ U_k$$

Once all U_k are solved with adequate number of Iterations they can be mapped back onto the grid as $U_{i,j}$ making use of $k = n(i - 1) + j$.

Now let us see if it possible to computationally parallelize the iterative process of (2.23) to save computation time. For parallelization first we need divide (2.23) into mutually independent processes that may be carried out parally at the same time. Going back to the Gauss-Seidel Scheme of (2.11) from which (2.23) is derived, we see that $U_{i,j}$ is updated using the most recently updated values of the potential at the nearest neighbouring grid points viz $U_{i,j-1}$, $U_{i,j+1}$, $U_{i-1,j}$, and $U_{i+1,j}$. Now if $(i+j)$ of the grid point under consideration is an even number then the four nearest grid points whose potentials are required for the updation of $U_{i,j}$ will all have odd values of $(i+j)$. This implies that for updating $U_{i,j}$ at any grid point with an even value of $(i+j)$, no other $U_{i,j}$ with even value of $(i+j)$ is required. Using the same logic we can deduce that that for updating $U_{i,j}$ at any grid point with an odd value of $(i+j)$, no other $U_{i,j}$ with odd value of $(i+j)$ is required. Herein lies the opportunity to parallelize the iterative process of (2.23). An implication of the above deduction in terms of $k = n(i-1) + j$ index can be simply put as updation of every U_k with odd values of k are mutually independent, and so is updation of every U_k with even values of K. Hence one iteration step can be divided into two parallelized halves as follows. First updation of U_k by (2.23) for every odd value of k is executed parally using latest available values of U_k for even k. We begin with odd k as $k = 1$ is odd. Next we parally update all U_k with even values of k by (2.23) using latest available values of U_k with odd k.

The above described parallelization scheme is known as the red-black parallelization for SOR/ Gauss-Seidel. It is so named because grid points with even and odd values of $(i+j)$ are visually differentiated with red and black colour to explain how the parallelization scheme works. In our code this parallelization of the SOR Poisson Solver (2.23) has been implemented using OPEN-MP parallelization.

2.1.4   Interpolating electric field components from the mesh to the particle-positions

In PIC simulation a procedure for field interpolation to particle position that ensures stability of the simulation, is to use the same scheme that was used to distribute charge density from the particle on to the mesh, only this time in reverse direction *i.e.* from the gird points to the particle's position. In our code we have used the second model of the first order CIC scheme of Fig. 2.2b for charge density distribution on mesh . The corresponding field interpolation procedure would can be implemented as follows.

First we need to determine the x and y components of the electric field on the mesh points by spatially differentiating the SOR solved potential on the mesh using finite differences. To solve for the

x component, E_x on a grid point we use,

$$(E_x)_{i,j} = -\frac{U_{i+1,j} - U_{i-1,j}}{2\,\Delta x} \qquad (for\ 0 \neq i \neq m) \qquad \Rightarrow \quad \text{central difference for inner } i \text{ indices}$$

$$(E_x)_{0,j} = -\frac{U_{i+1,j} - U_{i,j}}{\Delta x} \qquad \Rightarrow \text{ forward difference for } i = 0$$

$$(E_x)_{m,j} = -\frac{U_{i,j} - U_{i-1,j}}{\Delta x} \qquad \Rightarrow \text{ backward difference for } i = m$$

$$(2.24)$$

Similarly to solve for the y component, E_y on a grid point we use,

$$(E_y)_{i,j} = -\frac{U_{i,j+1} - U_{i,j-1}}{2\,\Delta y} \qquad (for\ 0 \neq j \neq n) \qquad \Rightarrow \quad \text{central difference for inner } j \text{ indices}$$

$$(E_y)_{i,0} = -\frac{U_{i,j+1} - U_{i,j}}{\Delta y} \qquad \Rightarrow \text{ forward difference for } j = 0 \quad (2.25)$$

$$(E_y)_{i,m} = -\frac{U_{i,j} - U_{i,j-1}}{\Delta y} \qquad \Rightarrow \text{ backward difference for } j = n$$

Once E_x and E_y are determined on all mesh points, we can interpolate the field components to particle positions, to determine the electrostatic field acting on each particle in its current position. To explain the field component interpolation procedure we will again use Fig. 2.2b. Now suppose the solved values of E_x on the points $D'\,C'\,A'$ and B' are $E_{x(D')}$, $E_{x(C')}$, $E_{x(A')}$, and $E_{x(B')}$ respectively. Then using the CIC scheme principle in the reverse direction, the interpolated value of E_x at the particle's postion, $E_x^{(int)}$ is given by,

$$E_x^{(int)} = \frac{d'\,E_{x(D')} + c'\,E_{x(C')} + b'\,E_{x(B')} + a'\,E_{x(A')}}{\Delta x\,\Delta y} \tag{2.26}$$

Similarly the the interpolated value of E_y at the particle's position, $E_y^{(int)}$ is given by,

$$E_y^{(int)} = \frac{d'\,E_{y(D')} + c'\,E_{y(C')} + b'\,E_{y(B')} + a'\,E_{y(A')}}{\Delta x\,\Delta y} \tag{2.27}$$

2.1.5 Progressing the trajectories of particles in one time step

Once E_x and E_y are interpolated to the position of the charge particle we know the electric field **E**, and the magneitc field, **B** (uniform axial for the cylindrical trap) at the particle's location. Hence the equations of motion of the particle may be expressed as

$$m\frac{d}{dt}\mathbf{v} = q\,[\mathbf{E} + \mathbf{v} \times \mathbf{B}]$$

$$\mathbf{v} = m\frac{d}{dt}\mathbf{r} \tag{2.28}$$

In the above equation m and q are the mass and the charge of the particle respectively. **r** and **v** are the position vector and the velocity vector of the particle. Now, there exist several numerical schemes to evolve the trajectory of the particle from the initial position and velocity, $(\mathbf{r_0}, \mathbf{v_0})$ to the new

position and velocity, $(\mathbf{r_1}, \mathbf{v_1})$ in the time step Δt, approximately (with time-discretization) following (2.28). We will now discuss some of these schemes and their properties from a general standpoint (not pertaining to (2.28)) to finally arrive at the scheme that we have chosen in our simulation. The discussion is intended to justify our choice of particle-pushing scheme.

Consider a n-dimesional Classical system governed by a known Hamiltonian function, H. The generalized form of H for the n-dimensional system is given below.

$$H \equiv H(p_1,\, p_2\,,..,\, p_n,\, x_1,\, x_2,\, ..,x_n,\, t) \tag{2.29}$$

Here p_i and x_i, with $i = 1,\, 2,\, ...,\, n$, represent the generalized momentum and position co-ordinates of the system. The Hamilton's equations of motion of the system are,

$$\frac{d}{dt}\mathbf{x} = \boldsymbol{\nabla}_p H$$
$$\frac{d}{dt}\mathbf{p} = -\boldsymbol{\nabla}_x H \tag{2.30}$$

Here $\mathbf{x}$ and $\mathbf{p}$ are the n-component position and velocity vector of the system. A unique feature of the equations of motion (2.30) is that these equations evolve with symplecticity. A symplectic evolution implies, among other things, that if we have an ensemble of identical non-interacting systems, each defined by the same Hamiltonian function, and each initiated at different points in the 2n dimensional phase space, then the ensemble of systems will evolve in such a manner that the 2n-dimensional volume delimited by the ensemble in phase space will be conserved through the evolution of the ensemble. This is just one way of stating Liouville's Theorem which applies for Hamiltonian systems that evolve symlectically. Another way of stating Liouville's theorem is by considering a very small volume element (analogous to a fluid element in real space) at any arbitrary initial position in the phase space of the system. All constituent system points (analogous to point-particles in a fluid element) within the volume element will evolve in time, changing the shape of the volume element. Liouville's theorem states that the $2n$ dimensional volume of the volume-element will remain conserved through the evolution. The theorem holds irrespective of whether H is an explicit function of time or not.

Now that we have some understanding of how the Hamiltonian equations of motion (2.30) evolve , we will proceed to give a functional form to the Hamiltonian and try to solve (2.30) numerically. Let us suppose the Hamiltonian of the system is defined as,

$$H = A(p_1,\, p_2,\, ..,\, p_n) + V(x_1,\, x_2,\, ..,\, x_n) \tag{2.31}$$

For simplicity we have considered here, a Hamiltonian that does not have explicit time dependence. If we now numerically solve the trajectory of the system in time Δt, from its initial phase-space co-ordinates $(\mathbf{x_0},\, \mathbf{p_0})$ to the final co-ordinates $(\mathbf{x_1},\, \mathbf{p_1})$ by an explicit Euler scheme, then the trajectory

of the numerical solution will evolve in Δt as follows.

$$
\begin{aligned}
\mathbf{x_1} &= \mathbf{x_0} + \Delta t \left(\boldsymbol{\nabla}_p H \right)_{\mathbf{x_0},\mathbf{p_0}} \;\Rightarrow\; x_{1i} = x_{0i} + \Delta t \frac{\partial A}{\partial p_i}\bigg|_{\mathbf{p}=\mathbf{p_0}} \\
\mathbf{p_1} &= \mathbf{p_0} - \Delta t \left(\boldsymbol{\nabla}_x H \right)_{\mathbf{x_0},\mathbf{p_0}} \;\Rightarrow\; p_{1i} = p_{0i} - \Delta t \frac{\partial V}{\partial x_i}\bigg|_{\mathbf{x}=\mathbf{x_0}}
\end{aligned}
\tag{2.32}
$$

Now let us express (2.32) in a more compact and elegant matrix operator notation. Let the phase space vectors $\boldsymbol{\eta}_0$ and $\boldsymbol{\eta}_1$ represent $(x_{10}, x_{20}, .., x_{n0}, p_{10}, p_{20}, .., p_{n0})$ and $(x_{11}, x_{21}, .., x_{n1}, p_{11}, p_{21}, .., p_{n1})$ respectively. Then using (2.32) $\boldsymbol{\eta}_0$ and $\boldsymbol{\eta}_1$ can be connected via a map of the following form.

$$
\boldsymbol{\eta}_1 = \boldsymbol{\eta}_1^{EU}(\boldsymbol{\eta}_0)
\tag{2.33}
$$

The superscript EU in the mapping function of (2.33) stands for Euler scheme. Another way of representing this mapping by Euler scheme is using the Jacobian Matrix Operator $\mathbf{M}^{EU}$ to connect the time derivatives $\dot{\boldsymbol{\eta}}_1$ and $\dot{\boldsymbol{\eta}}_0$ as follows.

$$
\dot{\boldsymbol{\eta}}_1 = \mathbf{M}^{EU} \, \dot{\boldsymbol{\eta}}_0
\tag{2.34}
$$

The operator elements $M_{ij}^{EU} = \frac{\partial \eta_{1i}}{\partial \eta_{0j}}$ can be easily worked out from the component-wise representation of (2.32).

Similarly an infinitesimal displacement of the actual Hamiltonian system (2.31), or for that matter any generalized Hamiltonian system of the form (2.29), in time dt, following the Hamilton equations of motion (2.30) may also be represented in Matrix notation via a mapping function and also using the Jacobian for infinitesimal transformation, $\mathbf{M}$ as follows.

$$
\boldsymbol{\eta}_{(t+dt)} = \boldsymbol{\eta}_{(t+dt)}(\boldsymbol{\eta}_{(t)})
\tag{2.35}
$$

$$
\dot{\boldsymbol{\eta}}_{(t+dt)} = \mathbf{M} \, \dot{\boldsymbol{\eta}}_{(t)}
\tag{2.36}
$$

Using $\boldsymbol{\eta}_{(t+dt)} - \boldsymbol{\eta}_{(t)} = \delta \boldsymbol{\eta}_{(t)}$, the Jacobain $\mathbf{M}$ can be expressed as

$$
\mathbf{M} = \frac{\partial \boldsymbol{\eta}_{(t+dt)}}{\partial \boldsymbol{\eta}_{(t)}} = \mathbf{1} + \frac{\partial \, \delta \boldsymbol{\eta}_{(t)}}{\partial \boldsymbol{\eta}_{(t)}} \;\Rightarrow\; M_{i,j} = 1 + \frac{\partial \, \delta \eta_{(t)i}}{\partial \eta_{(t)j}}
\tag{2.37}
$$

As the Hamiltonian equations (2.30) evolve sympletically, the infinitesimal transformation represented in (2.35) and (2.36) is a Canonical Transformation, and the Jacobian, $\mathbf{M}$, of the Infinitesimal Canonical Transformation (ICT), obeys the symplectic condition for a Cannonical transformation Matrix, viz,

$$
\widetilde{\mathbf{M}}\mathbf{J}\mathbf{M} = \mathbf{J}
\tag{2.38}
$$

where, $\mathbf{J} = \begin{pmatrix} \mathbf{0} & \mathbf{I}_n \\ -\mathbf{I}_n & \mathbf{0} \end{pmatrix}$ is $2n \times 2n$ matrix and $\mathbf{I}_n$ is the identity matrix of order n. Note that the symplectic condition (2.38) holds not just for the ICT (which is basically the evolution of phase

space co-ordinates of the system in an infinitesimal length of time), but is also equally true for any canonical transformation of co-ordinates, both restricted (where transformation mapping does not involve time), as well as unrestricted (where transformation mapping involves time). The sympletic property of canonical transformation will be used later in deriving sympletic integrators. From (2.38) we can also derive that $||\mathbf{M}|| = 1$, where $||\mathbf{M}||$ represents the absolute value of the determinant of $\mathbf{M}$. Coming back to the ICT we can show from (2.36) and (2.37) that the phase space volume elements of the two sets of co-ordinates are related by $d\eta^{vol}_{(t+dt)} = ||\mathbf{M}|| \, d\eta^{vol}_{(t)}$. Since we have $||\mathbf{M}|| = 1$ we get back the statement of Liouville's theorem that the sympletic evolution of Hamiltonian system preserves the volume of the phase space volume-element.

In comparison to the Jacobian, $\mathbf{M}$ of ICT, the Jacobian of Δt transformation by the Euler scheme, $\mathbf{M}_{EU}$ does not obey the symplectic condition, (2.38). So if we use (2.32) to numerically evolve a set of identical non-interacting Hamiltonian systems defined by (2.31), from different starting points in the phase space, then we will see that the volume delimited by the ensemble of systems in phase space is not conserved in the numerical evolution of the ensemble.

Equation (2.32) actually belongs to a class of numerical solvers called non-sympletic integrators. While (2.32) is a first order non symplectic integrator, there are also higher order non-symplectic integrators like the 4th order Runge-Kutta scheme. The non-sympleticity in the transformation of co-ordinates in each time-step of these numerical schemes, causes the error in the total energy of the system to grow in an unbounded manner through the simulation. The growing errors may manifest in the form of numerical artefacts such as artificial damping or excitation after certain number of time steps. To overcome these drawbacks of non-sympletic integrators another class of integrators known as sysmpletic integrators can be used to evolve systems numerically. Let us now derive a sysmplectic integrator for the Hamiltonian system (2.31).

The procedure for obtaining symplectic integration scheme is as follows [46]. Suppose the known coordinates + Hamiltonaian of the given system, $(\mathbf{x}, \mathbf{p}, t, H)$ undergo a restricted canonical transformation to a new set of co-ordinates + Hamiltonian $(\mathbf{x}', \mathbf{p}', t, H')$ describing the same system. Now in time t $(\mathbf{x}, \mathbf{p})$ will evolve from its initial values $(\mathbf{x}_0, \mathbf{p}_0)$ following (2.30) with H as their Hamiltonian to $\mathbf{x}(t), \mathbf{p}(t)$. Let us specify that the initial values of co-ordinates in the transformed co-ordinate system, $(\mathbf{x}', \mathbf{p}')$ are same as the initial values in the $(\mathbf{x}, \mathbf{p})$ co-ordinate system. In that case $\mathbf{x}', \mathbf{p}'$ will evolve in time t from its initial values $\mathbf{x}_0, \mathbf{p}_0$ following (2.30) with H' as their Hamiltonian to $(\mathbf{x}'(t), \mathbf{p}'(t))$. If the Hamiltonian of the transformed coordinates, H' is a explicit function of t of the order of k and higher *i.e.* $H' = \mathcal{O}(t^k)$, then it simple to show from (2.30) that $\mathbf{x}'(t) = \mathbf{x_0} + \mathcal{O}(t^{k+1})$ and $\mathbf{p}'(t) = \mathbf{p_0} + \mathcal{O}(t^{k+1})$. Now if the time of evolution, t is very small, then the $\mathcal{O}(t^{k+1})$ terms may be neglected and we can approximate that $\mathbf{x}'(t) \approx \mathbf{x_0}$ and $\mathbf{p}'(t) \approx \mathbf{p_0}$. This implies that for a small enough t , the $(\mathbf{x}'.\mathbf{p}')$ co-ordinate system has evolved negligibly from its initial values. Now a restricted canonical transformation at time t from $(\mathbf{x}'(t).\mathbf{p}'(t))$ to $(\mathbf{x}(t).\mathbf{p}(t))$, will have a Jacobian of transformation, that obeys the symplecticity condition (2.38), by virtue of the co-ordinate transformation being cannonical. Now for suffienty small t the transformation can also be approximated as a symplectic

map from $(\mathbf{x_0}.\mathbf{p_0})$ to $(\mathbf{x}(t).\mathbf{p}(t))$. Hence we have arrived at a symplectic map for the evolution of the $(\mathbf{x}, \mathbf{p})$ in a small time $t \equiv \Delta t$ of the numerical integrator.

Now that we understand the principle of symplectic integrators, the next job to find a technique for obtaining a $H' = \mathcal{O}(t^k)$ and thereby obtaining the symplectic map from $(\mathbf{x}, \mathbf{p})$ to $(\mathbf{x}', \mathbf{p}')$ and vice versa. We use the method of Generating functions for this purpose. The generating function employed is [46]

$$F = F_3(\mathbf{x}', \mathbf{p}, t) + \mathbf{x} \cdot \mathbf{p} \tag{2.39}$$

where,

$$F_3(\mathbf{x}', \mathbf{p}, t) = -\mathbf{x}' \cdot \mathbf{p} - G(\mathbf{x}', \mathbf{p}, t) \tag{2.40}$$

and the transformation equations are,

$$
\begin{aligned}
\mathbf{x} &= -\boldsymbol{\nabla}_p F_3 = \mathbf{x}' - \boldsymbol{\nabla}_p G(\mathbf{x}', \mathbf{p}, t) \\
\mathbf{p}' &= -\boldsymbol{\nabla}_{x'} F_3 = \mathbf{p} - \boldsymbol{\nabla}_{x'} G(\mathbf{x}', \mathbf{p}, t) \\
H' &= H + \frac{\partial F_3}{\partial t} = H + \frac{\partial G}{\partial t}
\end{aligned}
\tag{2.41}
$$

Suppose we want to have a $H' = \mathcal{O}(t)$ so that a restricted canonical transformation from $(\mathbf{x}', \mathbf{p}')$ to $(\mathbf{x}, \mathbf{p})$ at time t, can be approximated as a symplectic map from the initial values $(\mathbf{x_0}, \mathbf{p_0})$ to $(\mathbf{x}, \mathbf{p})$ correct to the order of t. In that case a suitable form of G is

$$G = -t\, H(\mathbf{p}, \mathbf{x}') = -t\, (A(\mathbf{p}) + V(\mathbf{x}')) \tag{2.42}$$

From (2.41) and (2.42) we get the transformation equations,

$$
\begin{aligned}
\mathbf{p}' &= \mathbf{p} + t\, \boldsymbol{\nabla}_{x'} V(\mathbf{x}') \\
\mathbf{x} &= \mathbf{x}' + t\, \boldsymbol{\nabla}_p A(\mathbf{p})
\end{aligned}
\tag{2.43}
$$

Substituting from (2.43) into the H' in (2.41) we can get the transformed Hamiltonian of the order of 1 in t as follows

$$
\begin{aligned}
H' &= A(\mathbf{p}) + V(\mathbf{x}) - A(\mathbf{p}) - V(\mathbf{x}') \\
&= V(\mathbf{x}) - V(\mathbf{x}') \\
&\text{substituting } \mathbf{x} \text{ from (2.43)} \\
&= V(\mathbf{x}' + t\, \boldsymbol{\nabla}_p A(\mathbf{p})) - V(\mathbf{x}') \\
&\text{substituting } \mathbf{p} \text{ from (2.43)} \\
&= V(\mathbf{x}' + t\, \boldsymbol{\nabla}_p A(\mathbf{p}' - t\, \boldsymbol{\nabla}_{x'} V(\mathbf{x}'))) - V(\mathbf{x}') \\
&\text{Taylor expanding the first term about } \mathbf{x}' \\
&= t\, \boldsymbol{\nabla}_{x'} V(\mathbf{x}') \cdot \boldsymbol{\nabla}_p A(\mathbf{p}') + \mathcal{O}(t^2)
\end{aligned}
\tag{2.44}
$$

Hence with the knowledge of the form of function $G(\mathbf{x}', \mathbf{p}, t)$, we can get any $H' = \mathcal{O}(t^k)$ as in (2.44) and also derive the transformation equations as in (2.43). The next step to substitute $\mathbf{x}' = \mathbf{x_0} + \mathcal{O}(t^2)$ and $\mathbf{p}' = \mathbf{p_0} + \mathcal{O}(t^2)$ in (2.43) as follows

$$
\begin{aligned}
\mathbf{p'(t)} &= \mathbf{p(t)} + t \left(\boldsymbol{\nabla}_{x'} V(\mathbf{x'}) \right)_{\mathbf{x'=x'(t)}} \\
\text{or} \quad \mathbf{p_0} &= \mathbf{p(t)} + t \left(\boldsymbol{\nabla}_{x'} V(\mathbf{x'}) \right)_{\mathbf{x'=x_0}} + \mathcal{O}(t^2) \\
\text{or} \quad \mathbf{p_0} &= \mathbf{p(t)} + t \left(\boldsymbol{\nabla}_{x} V(\mathbf{x}) \right)_{\mathbf{x=x_0}} + \mathcal{O}(t^2) \\
&\qquad\qquad\text{and} \\
\mathbf{x(t)} &= \mathbf{x'(t)} + t \left(\boldsymbol{\nabla}_{p} A(\mathbf{p}) \right)_{\mathbf{p=p(t)}} \\
\text{or} \quad \mathbf{x(t)} &= \mathbf{x_0} + t \left(\boldsymbol{\nabla}_{p} A(\mathbf{p}) \right)_{\mathbf{p=p(t)}} + \mathcal{O}(t^2)
\end{aligned}
\tag{2.45}
$$

Expressing (2.45) in the language of numerical integrators we have neglecting $\mathcal{O}(\Delta t^2)$ terms we have

$$
\begin{aligned}
\mathbf{p_1} &= \mathbf{p_0} - \Delta t \left(\boldsymbol{\nabla}_{x} V(\mathbf{x}) \right)_{\mathbf{x=x_0}} \\
\mathbf{x_1} &= \mathbf{x_0} + \Delta t \left(\boldsymbol{\nabla}_{p} A(\mathbf{p}) \right)_{\mathbf{p=p_1}}
\end{aligned}
\tag{2.46}
$$

For a direct comparison with (2.32) we can express (2.46) as

$$
\begin{aligned}
\mathbf{p_1} &= \mathbf{p_0} - \Delta t \left(\boldsymbol{\nabla}_{x} H \right)_{\mathbf{x_0,p_0}} \Rightarrow p_{1i} = p_{0i} - \Delta t \frac{\partial V}{\partial x_i}\bigg|_{\mathbf{x=x_0}} \\
\mathbf{x_1} &= \mathbf{x_0} + \Delta t \left(\boldsymbol{\nabla}_{p} H \right)_{\mathbf{x_1,p_1}} \Rightarrow x_{1i} = x_{0i} + \Delta t \frac{\partial A}{\partial p_i}\bigg|_{\mathbf{p=p_1}}
\end{aligned}
\tag{2.47}
$$

In the matrix form the symplectic map (2.47) can be expressed as

$$
\boldsymbol{\eta}_1 = \boldsymbol{\eta}_1^{SEU}(\boldsymbol{\eta}_0)
\tag{2.48}
$$

Equations (2.47) and (2.48) are the expressions for the numerical integrator known as Symplectic Euler Scheme (hence the superscript SEU in (2.48)).

Now, in deriving (2.45) we began with a pre-defined correct form of knowledge of $G(\mathbf{x}', \mathbf{p}, t)$ such that the expression (2.45) is correct up to first order in t. However, in general, the correct form of $G(\mathbf{x}', \mathbf{p}, t)$ that will give us a symplectic map correct to k^{th} order in t has to solved, and only then can be find the kth order symplectic map similar to (2.45). We will make use of the fact that terms of the order t^{k-1} and lower should not present in H'.

Taking a cue from (2.45) the general expression for a kth order symplectic map for the given Hamiltonian is given by

$$
\begin{aligned}
\mathbf{p_{j+1}} &= \mathbf{p_j} - c_j\, t \left(\boldsymbol{\nabla}_{x} V(\mathbf{x}) \right)_{\mathbf{x=x_j}} \\
\mathbf{x_{j+1}} &= \mathbf{x_j} + d_j\, t \left(\boldsymbol{\nabla}_{p} A(\mathbf{p}) \right)_{\mathbf{p=p_{j+1}}} \\
&\text{where } j = 0, 1, .., (k-1)
\end{aligned}
\tag{2.49}
$$

It must be noted that in (2.49) the symplectic map is from $(\mathbf{x_0}, \mathbf{p_0})$ to $(\mathbf{x_k}, \mathbf{p_k})$. Any intermediate $(\mathbf{x_j}, \mathbf{p_j})$ are only for mathematical convenience and do not have any physical significance as coordinates.

Let us now try to get back (2.46) from this general approach without a predefined form of the function G. With $k = 1$ in (2.49) we get

$$\mathbf{p_1} = \mathbf{p_0} - c_0\, t\, (\boldsymbol{\nabla}_x\, V(\mathbf{x}))_{\mathbf{x}=\mathbf{x_0}}$$

form (2.46) (with $\Delta t = t$) and (2.45) we can return back to

$$\text{or} \quad \mathbf{p'(t)} = \mathbf{p(t)} + t\, (\boldsymbol{\nabla}_{x'}\, V(\mathbf{x'}))_{\mathbf{x'}=\mathbf{x'(t)}}$$

$$\text{and} \tag{2.50}$$

$$\mathbf{x_1} = \mathbf{x_0} + d_0\, t\, (\boldsymbol{\nabla}_p\, A(\mathbf{p}))_{\mathbf{p}=\mathbf{p_1}}$$

form (2.46) (with $\Delta t = t$) and (2.45) we can return back to

$$\text{or} \quad \mathbf{x(t)} = \mathbf{x'(t)} + t\, (\boldsymbol{\nabla}_p\, A(\mathbf{p}))_{\mathbf{p}=\mathbf{p(t)}}$$

A comparison of (2.50) with the co-ordinate transformation equations in (2.41), shows that $G(\mathbf{x'}, \mathbf{p}, t)$ should have the form

$$G(\mathbf{x'}, \mathbf{p}, t) = -t\, (c_0 V(\mathbf{x'}) + d_0 A(\mathbf{p})) \tag{2.51}$$

Using (2.51) and (2.41) we get

$$H' = V(\mathbf{x}) + A(\mathbf{p}) - c_0 V(\mathbf{x'}) - d_0 A(\mathbf{p})$$

$$\text{Substituting } \mathbf{x} \text{ from (2.50)}$$

$$= V(\mathbf{x'} + d_0\, t\, \boldsymbol{\nabla}_p\, A(\mathbf{p})) - c_0 V(\mathbf{x'}) - d_0 A(\mathbf{p})$$

$$\text{Taylor expanding first term about } \mathbf{x'}$$

$$= V(\mathbf{x'}) + d_0\, t\, \boldsymbol{\nabla}_p\, A(\mathbf{p}) \cdot \boldsymbol{\nabla}_{x'}\, V(\mathbf{x'}) + A(\mathbf{p}) - c_0 V(\mathbf{x'}) - d_0 A(\mathbf{p}) \tag{2.52}$$

$$= (1 - c_0) V(\mathbf{x'}) + (1 - d_0) A(\mathbf{p}) + d_0\, t\, \boldsymbol{\nabla}_p\, A(\mathbf{p}) \cdot \boldsymbol{\nabla}_{x'}\, V(\mathbf{x'}) + \mathcal{O}(t^2)$$

$$\text{as } H' = \mathcal{O}(t) \text{ we get } c_0 = 1 \text{ and } d_0 = 1$$

$$\text{Substituting the values of } c_0 \text{ and } d_0$$

$$= t\, \boldsymbol{\nabla}_p\, A(\mathbf{p}) \cdot \boldsymbol{\nabla}_{x'}\, V(\mathbf{x'}) + \mathcal{O}(t^2)$$

$$\text{Hence we got back (2.44)}$$

Now substituting the values of c_0 and d_0 in (2.49) we get

$$\mathbf{p_1} = \mathbf{p_0} - t\, (\boldsymbol{\nabla}_x\, V(\mathbf{x}))_{\mathbf{x}=\mathbf{x_0}}$$
$$\mathbf{x_1} = \mathbf{x_0} + t\, (\boldsymbol{\nabla}_p\, A(\mathbf{p}))_{\mathbf{p}=\mathbf{p_1}} \tag{2.53}$$

(2.53) is again same as (2.46) as $\Delta t = t$.

Now by the same procedure let us obtain a second order symplectic map. With $k = 2$ in (2.49) we get

$$
\begin{aligned}
\mathbf{p_2} &= \mathbf{p_1} - c_1 \, t \, (\boldsymbol{\nabla}_x \, V(\mathbf{x}))_{\mathbf{x}=\mathbf{x_1}} \\
\mathbf{x_2} &= \mathbf{x_1} + d_1 \, t \, (\boldsymbol{\nabla}_p \, A(\mathbf{p}))_{\mathbf{p}=\mathbf{p_2}} \\
&\qquad\qquad\text{and} \\
\mathbf{p_1} &= \mathbf{p_0} - c_0 \, t \, (\boldsymbol{\nabla}_x \, V(\mathbf{x}))_{\mathbf{x}=\mathbf{x_0}} \\
\mathbf{x_1} &= \mathbf{x_0} + d_0 \, t \, (\boldsymbol{\nabla}_p \, A(\mathbf{p}))_{\mathbf{p}=\mathbf{p_1}}
\end{aligned}
\tag{2.54}
$$

This second order symplectic map is from $(\mathbf{x_0}, \mathbf{p_0})$ to $(\mathbf{x_2}, \mathbf{p_2})$. Hence to obtain the functional form of G we need to find a map from $(\mathbf{x_0}, \mathbf{p_0})$ to $(\mathbf{x_2}, \mathbf{p_2})$ similar to the co-ordinate transformation equations of (2.41). We will use the shorthand representations $(\boldsymbol{\nabla}_x \, V(\mathbf{x}))_{\mathbf{x}=\mathbf{x_j}} \simeq (\boldsymbol{\nabla}_x \, V(\mathbf{x_j}))$ and $(\boldsymbol{\nabla}_p \, A(\mathbf{p}))_{\mathbf{p}=\mathbf{p_j}} \simeq (\boldsymbol{\nabla}_p \, A(\mathbf{p_j}))$ for deriving this map function. From (2.54) we have

$$
\begin{aligned}
\mathbf{x_2} &= \mathbf{x_1} + d_1 \, t \, \boldsymbol{\nabla}_p \, A(\mathbf{p_2}) \\
&= \mathbf{x_0} + d_0 \, t \, \boldsymbol{\nabla}_p \, A(\mathbf{p_1}) + d_1 \, t \, \boldsymbol{\nabla}_p \, A(\mathbf{p_2}) \\
&= \mathbf{x_0} + d_0 \, t \, \boldsymbol{\nabla}_p \, A(\mathbf{p_2} + c_1 \, t \, \boldsymbol{\nabla}_x \, V(\mathbf{x_1})) + d_1 \, t \, \boldsymbol{\nabla}_p \, A(\mathbf{p_2}) \\
&= \mathbf{x_0} + d_0 \, t \, \boldsymbol{\nabla}_p \, A(\mathbf{p_2} + c_1 \, t \, \boldsymbol{\nabla}_x \, \{V(\mathbf{x_0}) + \mathcal{O}(t)\}) + d_1 \, t \, \boldsymbol{\nabla}_p \, A(\mathbf{p_2}) \\
&= \mathbf{x_0} + d_0 \, t \, \boldsymbol{\nabla}_p \, \{A(\mathbf{p_2}) + c_1 \, t \, \boldsymbol{\nabla}_p \, A(\mathbf{p_2}) \cdot \boldsymbol{\nabla}_x \, V(\mathbf{x_0})\} + d_1 \, t \, \boldsymbol{\nabla}_p \, A(\mathbf{p_2}) + \mathcal{O}(t^3) \\
&= \mathbf{x_0} + (d_0 + d_1) \, t \, \boldsymbol{\nabla}_p \, A(\mathbf{p_2}) + d_0 \, c_1 \, t^2 \, \boldsymbol{\nabla}_p^2 \, A(\mathbf{p_2}) \cdot \boldsymbol{\nabla}_x \, V(\mathbf{x_0}) + \mathcal{O}(t^3) \\
&\qquad\qquad\text{and} \\
\mathbf{p_2} &= \mathbf{p_1} - c_1 \, t \, \boldsymbol{\nabla}_x \, V(\mathbf{x_1}) \\
&= \mathbf{p_0} - c_0 \, t \, \boldsymbol{\nabla}_x \, V(\mathbf{x_0}) - c_1 \, t \, \boldsymbol{\nabla}_x \, V(\mathbf{x_1}) \\
&= \mathbf{p_0} - c_0 \, t \, \boldsymbol{\nabla}_x \, V(\mathbf{x_0}) - c_1 \, t \, \boldsymbol{\nabla}_x \, V(\mathbf{x_0} + d_0 \, t \, \boldsymbol{\nabla}_p \, A(\mathbf{p_1})) \\
&= \mathbf{p_0} - c_0 \, t \, \boldsymbol{\nabla}_x \, V(\mathbf{x_0}) - c_1 \, t \, \boldsymbol{\nabla}_x \, V(\mathbf{x_0} + d_0 \, t \, \boldsymbol{\nabla}_p \, \{A(\mathbf{p_2}) + \mathcal{O}(t)\}) \\
&= \mathbf{p_0} - c_0 \, t \, \boldsymbol{\nabla}_x \, V(\mathbf{x_0}) - c_1 \, t \, \boldsymbol{\nabla}_x \, V(\mathbf{x_0} + d_0 \, t \, \boldsymbol{\nabla}_p \, A(\mathbf{p_2})) + \mathcal{O}(t^3) \\
&= \mathbf{p_0} - c_0 \, t \, \boldsymbol{\nabla}_x \, V(\mathbf{x_0}) - c_1 \, t \, \boldsymbol{\nabla}_x \, \{V(\mathbf{x_0}) + d_0 \, t \, \boldsymbol{\nabla}_x \, V(\mathbf{x_0}) \cdot \boldsymbol{\nabla}_p \, A(\mathbf{p_2})\} + \mathcal{O}(t^3) \\
&= \mathbf{p_0} - (c_0 + c_1) \, t \, \boldsymbol{\nabla}_x \, V(\mathbf{x_0}) - c_1 \, d_0 \, t^2 \, \boldsymbol{\nabla}_x^2 \, V(\mathbf{x_0}) \cdot \boldsymbol{\nabla}_p \, A(\mathbf{p_2}) + \mathcal{O}(t^3)
\end{aligned}
\tag{2.55}
$$

A comparison of (2.55) with the co-ordinate transformation equations in (2.41), with $(\mathbf{x_0}, \mathbf{p_0}) \approx (\mathbf{x'}, \mathbf{p'})$ and knowing that $(\mathbf{x_2}, \mathbf{p_2})$ in (2.55) is actually same as the $(\mathbf{x}, \mathbf{p})$ in (2.41), reveal the form of $G(\mathbf{x'}, \mathbf{p}, t)$ as

$$
G(\mathbf{x'}, \mathbf{p}, t) = -t \, (c_0 + c_1) V(\mathbf{x'}) - t \, (d_0 + d_1) A(\mathbf{p}) - c_1 \, d_0 \, t^2 \, \boldsymbol{\nabla}_p \, A(\mathbf{p}) \cdot \boldsymbol{\nabla}_{x'} \, V(\mathbf{x'}) + \mathcal{O}(t^3) \tag{2.56}
$$

Hence from the expression for H', (2.41) we have

$$
\begin{aligned}
H' &= A(\mathbf{p}) + V(\mathbf{x}) - (c_0 + c_1)V(\mathbf{x}') - (d_0 + d_1)A(\mathbf{p}) - 2\,c_1 d_0 t \boldsymbol{\nabla}_p A(\mathbf{p}) \cdot \boldsymbol{\nabla}_{x'} V(\mathbf{x}') + \mathcal{O}(t^2) \\
&= A(\mathbf{p}) + V(\mathbf{x_1} + d_1 t \boldsymbol{\nabla}_p A(\mathbf{p})) - (c_0 + c_1)V(\mathbf{x}') - (d_0 + d_1)A(\mathbf{p}) \\
&\qquad -2\,c_1 d_0 t \boldsymbol{\nabla}_p A(\mathbf{p}) \cdot \boldsymbol{\nabla}_{x'} V(\mathbf{x}') + \mathcal{O}(t^2) \\
&= A(\mathbf{p}) + V(\mathbf{x_1}) + d_1 t \boldsymbol{\nabla}_p A(\mathbf{p}) \cdot \boldsymbol{\nabla}_x V(\mathbf{x_1}) - (c_0 + c_1)V(\mathbf{x}') - (d_0 + d_1)A(\mathbf{p}) \\
&\qquad -2\,c_1 d_0 t \boldsymbol{\nabla}_p A(\mathbf{p}) \cdot \boldsymbol{\nabla}_{x'} V(\mathbf{x}') + \mathcal{O}(t^2) \\
&= A(\mathbf{p}) + V(\mathbf{x_1}) + d_1 t \boldsymbol{\nabla}_p A(\mathbf{p}) \cdot \boldsymbol{\nabla}_x V(\mathbf{x_0}) - (c_0 + c_1)V(\mathbf{x}') - (d_0 + d_1)A(\mathbf{p}) \\
&\qquad -2\,c_1 d_0 t \boldsymbol{\nabla}_p A(\mathbf{p}) \cdot \boldsymbol{\nabla}_{x'} V(\mathbf{x}') + \mathcal{O}(t^2) \\
&= A(\mathbf{p}) + V(\mathbf{x_1}) + d_1 t \boldsymbol{\nabla}_p A(\mathbf{p}) \cdot \boldsymbol{\nabla}_{x'} V(\mathbf{x}') - (c_0 + c_1)V(\mathbf{x}') - (d_0 + d_1)A(\mathbf{p}) \\
&\qquad -2\,c_1 d_0 t \boldsymbol{\nabla}_p A(\mathbf{p}) \cdot \boldsymbol{\nabla}_{x'} V(\mathbf{x}') + \mathcal{O}(t^2) \\
&= A(\mathbf{p}) + V(\mathbf{x_0} + d_0\, t\, \boldsymbol{\nabla}_p A(\mathbf{p_1})) + d_1 t \boldsymbol{\nabla}_p A(\mathbf{p}) \cdot \boldsymbol{\nabla}_{x'} V(\mathbf{x}') \qquad (2.57) \\
&\quad -(c_0 + c_1)V(\mathbf{x}') - (d_0 + d_1)A(\mathbf{p}) - 2\,c_1 d_0 t \boldsymbol{\nabla}_p A(\mathbf{p}) \cdot \boldsymbol{\nabla}_{x'} V(\mathbf{x}') + \mathcal{O}(t^2) \\
&= A(\mathbf{p}) + V(\mathbf{x_0}) + d_0\, t\, \boldsymbol{\nabla}_p A(\mathbf{p_1}) \cdot \boldsymbol{\nabla}_x V(\mathbf{x_0}) + d_1 t \boldsymbol{\nabla}_p A(\mathbf{p}) \cdot \boldsymbol{\nabla}_{x'} V(\mathbf{x}') \\
&\quad -(c_0 + c_1)V(\mathbf{x}') - (d_0 + d_1)A(\mathbf{p}) - 2\,c_1 d_0 t \boldsymbol{\nabla}_p A(\mathbf{p}) \cdot \boldsymbol{\nabla}_{x'} V(\mathbf{x}') + \mathcal{O}(t^2) \\
&= A(\mathbf{p}) + V(\mathbf{x}') + d_0\, t\, \boldsymbol{\nabla}_p A(\mathbf{p_1}) \cdot \boldsymbol{\nabla}_{x'} V(\mathbf{x}') + d_1 t \boldsymbol{\nabla}_p A(\mathbf{p}) \cdot \boldsymbol{\nabla}_{x'} V(\mathbf{x}') \\
&\quad -(c_0 + c_1)V(\mathbf{x}') - (d_0 + d_1)A(\mathbf{p}) - 2\,c_1 d_0 t \boldsymbol{\nabla}_p A(\mathbf{p}) \cdot \boldsymbol{\nabla}_{x'} V(\mathbf{x}') + \mathcal{O}(t^2) \\
&= A(\mathbf{p}) + V(\mathbf{x}') + d_0\, t\, \boldsymbol{\nabla}_p A(\mathbf{p}) \cdot \boldsymbol{\nabla}_{x'} V(\mathbf{x}') + d_1 t \boldsymbol{\nabla}_p A(\mathbf{p}) \cdot \boldsymbol{\nabla}_{x'} V(\mathbf{x}') \\
&\quad -(c_0 + c_1)V(\mathbf{x}') - (d_0 + d_1)A(\mathbf{p}) - 2\,c_1 d_0 t \boldsymbol{\nabla}_p A(\mathbf{p}) \cdot \boldsymbol{\nabla}_{x'} V(\mathbf{x}') + \mathcal{O}(t^2) \\
&= (1 - c_0 - c_1)V(\mathbf{x}') + (1 - d_0 - d_1)A(\mathbf{p}) \\
&\quad + (d_0 + d_1 - 2\,c_1 d_0)t \boldsymbol{\nabla}_p A(\mathbf{p}) \cdot \boldsymbol{\nabla}_{x'} V(\mathbf{x}') + \mathcal{O}(t^2)
\end{aligned}
$$

As $H = \mathcal{O}(t^2)$ the coefficients of all terms with orders less than 2 in t must be zero (2.57). Equating these coefficients to zero we get

$$
\begin{aligned}
1 - c_0 - c_1 &= 0 \\
1 - d_0 - d_1 &= 0 \qquad\qquad (2.58) \\
d_0 + d_1 - 2\,c_1 d_0 &= 0
\end{aligned}
$$

The solutions to the set of equations (2.58) are $c_0 = 0$, $c_1 = 1$, $d_0 = \frac{1}{2}$, and $d_1 = \frac{1}{2}$. Substituing

the values of these coefficients in (2.54) we have

$$\mathbf{p_2} = \mathbf{p_1} - t \left(\boldsymbol{\nabla}_x V(\mathbf{x}) \right)_{\mathbf{x}=\mathbf{x_1}}$$

$$\mathbf{x_2} = \mathbf{x_1} + \frac{1}{2} t \left(\boldsymbol{\nabla}_p A(\mathbf{p}) \right)_{\mathbf{p}=\mathbf{p_2}}$$

and $\qquad$ (2.59)

$$\mathbf{p_1} = \mathbf{p_0}$$

$$\mathbf{x_1} = \mathbf{x_0} + \frac{1}{2} t \left(\boldsymbol{\nabla}_p A(\mathbf{p}) \right)_{\mathbf{p}=\mathbf{p_1}}$$

We can express (2.59) in the numerical integrator form with $t = \Delta t$ as

$$\mathbf{p_1} = \mathbf{p_0} \;\Rightarrow\; p_{1i} = p_{0i}$$

$$\mathbf{x_1} = \mathbf{x_0} + \frac{1}{2} \Delta t \left(\boldsymbol{\nabla}_p H \right)_{\mathbf{x_1},\mathbf{p_1}} \;\Rightarrow\; x_{1i} = x_{0i} + \frac{1}{2} \Delta t \frac{\partial A}{\partial p_i} \bigg|_{\mathbf{p}=\mathbf{p_1}}$$

(2.60)

$$\mathbf{p_2} = \mathbf{p_1} - \Delta t \left(\boldsymbol{\nabla}_x H \right)_{\mathbf{x_1},\mathbf{p_1}} \;\Rightarrow\; p_{2i} = p_{1i} - \Delta t \frac{\partial V}{\partial x_i} \bigg|_{\mathbf{x}=\mathbf{x_1}}$$

$$\mathbf{x_2} = \mathbf{x_1} + \frac{1}{2} \Delta t \left(\boldsymbol{\nabla}_p H \right)_{\mathbf{x_2},\mathbf{p_2}} \;\Rightarrow\; x_{2i} = x_{1i} + \frac{1}{2} \Delta t \frac{\partial A}{\partial p_i} \bigg|_{\mathbf{p}=\mathbf{p_2}}$$

The above second symeplectic numerical integrator is known as the Leap-frog scheme. The symplectic map can also be expressed in matrix form as shown below

$$\boldsymbol{\eta}_2 = \boldsymbol{\eta}_2^{LF}(\boldsymbol{\eta}_0) \qquad (2.61)$$

In (2.61) the phase space vectors $\boldsymbol{\eta}_0$ and $\boldsymbol{\eta}_2$ represent $(x_{10}, x_{20}, .., x_{n0}, p_{10}, p_{20}, .., p_{n0})$ and $(x_{12}, x_{22}, .., x_{n2}, p_{12}, p_{22}, .., p_{n2})$ from the component-wise representations in (2.60). The superscript LF represents Leap-Frog scheme.

By following a similar procedure higher order symplectic numerical integrators can also be derived. Of course it is evident form the above examples that as the order of the symplectic integrator becomes higher, the equations involved in the derivation become more complex and numerous.

There is an alternate procedure for deriving symlectic numerical integrators without the use of generating functions, for systems with separable Hamiltonaians as (2.31). This procedure is known as exponential splitting [44, 47]. As we will show later exponential splitting can also be applied to derive numerical integrators for systems with non-separable Hamiltonians like (2.28). In the latter case the exponential splitting yields integrators that are non-symplectic but can have desired properties that makes them accurate and efficient numerical integrators. First we will derive symplectic integrators for a separable Hamiltonian using exponential splitting.

In matrix notation, where $\boldsymbol{\eta} = (x_1, x_2, .., x_n, p_1, p_2, .., p_n)$ the Hamilton's equations of motion (2.30) can be expressed in a compact form using the Poisson Bracket notation as follows

$$\dot{\boldsymbol{\eta}} = \{\boldsymbol{\eta}, H(\boldsymbol{\eta})\} \;\Rightarrow\; \dot{\eta}_i = \sum_{j=1}^{n} \left(\frac{\partial \eta_i}{\partial x_j} \frac{\partial H}{\partial p_j} - \frac{\partial \eta_i}{\partial p_j} \frac{\partial H}{\partial x_j} \right) \tag{2.62}$$

Infact, using the Hamilton's equations of motion (2.30) the time evolution of any function of $\boldsymbol{\eta}$ that is not an explicit function time may be expressed as

$$\dot{W}(\boldsymbol{\eta}) = \{W(\boldsymbol{\eta}), H(\boldsymbol{\eta})\} = \sum_{j=1}^{n} \left(\frac{\partial W(\boldsymbol{\eta})}{\partial x_j} \frac{\partial H}{\partial p_j} - \frac{\partial W(\boldsymbol{\eta})}{\partial p_j} \frac{\partial H}{\partial x_j} \right) \tag{2.63}$$

Expressing (2.62) in operator form we have

$$\dot{\boldsymbol{\eta}} = \left[\sum_{j=1}^{n} \left(\frac{\partial H}{\partial p_j} \frac{\partial}{\partial x_j} - \frac{\partial H}{\partial x_j} \frac{\partial}{\partial p_j} \right) \right] \boldsymbol{\eta}$$

$$\text{or } \dot{\boldsymbol{\eta}} = \left[\sum_{j=1}^{n} \left(\frac{\partial A(\mathbf{p})}{\partial p_j} \frac{\partial}{\partial x_j} - \frac{\partial V(\mathbf{x})}{\partial x_j} \frac{\partial}{\partial p_j} \right) \right] \boldsymbol{\eta} \tag{2.64}$$

$$\text{or} \quad \dot{\boldsymbol{\eta}} = (\mathcal{A} + \mathcal{B}) \, \boldsymbol{\eta}$$

$$\text{where operators } \mathcal{A} = \sum_{j=1}^{n} \frac{\partial A(\mathbf{p})}{\partial p_j} \frac{\partial}{\partial x_j}, \text{ and } \mathcal{B} = - \sum_{j=1}^{n} \frac{\partial V(\mathbf{x})}{\partial x_j} \frac{\partial}{\partial p_j}$$

Expressing (2.64) in its solution form we have

$$\boldsymbol{\eta}(t) = \mathrm{e}^{t(\mathcal{A}+\mathcal{B})} \, \boldsymbol{\eta}(0) \tag{2.65}$$

(2.63) can also be expressed in its solution form as

$$W(\boldsymbol{\eta}(t)) = \mathrm{e}^{t(\mathcal{A}+\mathcal{B})} \, W(\boldsymbol{\eta}(0)) \tag{2.66}$$

From (2.65) and (2.66) it is clear that $\mathrm{e}^{t(\mathcal{A}+\mathcal{B})}$ is the evolution operator of the system. $\mathrm{e}^{t\mathcal{A}}$ and $\mathrm{e}^{t\mathcal{B}}$ are components of the evolution operator. Now, as the Hamiltonian of the system is separable and $\mathbf{x}$ and $\mathbf{p}$ are classical independent, it is possible to evaluate the operations of components of the evolution operator in closed form as follows.

Expressing $\boldsymbol{\eta}(0) = \left(\begin{smallmatrix} \mathbf{x_0} \\ \mathbf{p_0} \end{smallmatrix} \right)$ we can derive

$$\mathrm{e}^{t\mathcal{A}} \, \boldsymbol{\eta}(0) = \mathrm{e}^{t\mathcal{A}} \begin{pmatrix} \mathbf{x_0} \\ \mathbf{p_0} \end{pmatrix} = \begin{pmatrix} \mathbf{x_0} + t \, (\boldsymbol{\nabla}_p \, A(\mathbf{p}))_{\mathbf{p}=\mathbf{p_0}} \\ \mathbf{p_0} \end{pmatrix}$$

$$\text{and} \tag{2.67}$$

$$\mathrm{e}^{t\mathcal{B}} \, \boldsymbol{\eta}(0) = \mathrm{e}^{t\mathcal{B}} \begin{pmatrix} \mathbf{x_0} \\ \mathbf{p_0} \end{pmatrix} = \begin{pmatrix} \mathbf{x_0} \\ \mathbf{p_0} - t \, (\boldsymbol{\nabla}_x \, V(\mathbf{x}))_{\mathbf{x}=\mathbf{x_0}} \end{pmatrix}$$

Similarly expressing the function $W(\boldsymbol{\eta}(0))$ as $W(\mathbf{x_0}, \mathbf{p_0})$ we can derive

$$
\mathrm{e}^{t\mathcal{A}}\, W(\boldsymbol{\eta}(0)) = \mathrm{e}^{t\mathcal{A}}\, W(\mathbf{x_0}, \mathbf{p_0}) = W\left(\mathbf{x_0} + t\left(\boldsymbol{\nabla}_p\, A(\mathbf{p})\right)_{\mathbf{p}=\mathbf{p_0}}\,,\ \mathbf{p_0}\right)
$$

$$\text{and} \tag{2.68}$$

$$
\mathrm{e}^{t\mathcal{B}}\, W(\boldsymbol{\eta}(0)) = \mathrm{e}^{t\mathcal{B}}\, W(\mathbf{x_0}, \mathbf{p_0}) = W\left(\mathbf{x_0}\,,\ \mathbf{p_0} - t\left(\boldsymbol{\nabla}_x\, V(\mathbf{x})\right)_{\mathbf{x}=\mathbf{x_0}}\right)
$$

Let us demonstrate a proof of (2.68) for a 2 dimensional system. We will prove only the first equation of (2.68). let us start from $\mathrm{e}^{t\mathcal{A}}\{W(x_1, x_2, p_1, p_2)\}$

$$
\begin{aligned}
&\mathrm{e}^{t\mathcal{A}}\{W(x_1, x_2, p_1, p_2)\} \\
&= \left[1 + t\mathcal{A} + \frac{1}{2}t^2\mathcal{A}^2 + \mathcal{O}(t^3)\right] W \\
&= \left[1 + t\left(\frac{\partial A(\mathbf{p})}{\partial p_1}\frac{\partial}{\partial x_1} + \frac{\partial A(\mathbf{p})}{\partial p_2}\frac{\partial}{\partial x_2}\right) + \frac{1}{2}t^2\left(\frac{\partial A(\mathbf{p})}{\partial p_1}\frac{\partial}{\partial x_1} + \frac{\partial A(\mathbf{p})}{\partial p_2}\frac{\partial}{\partial x_2}\right)^2 + \mathcal{O}(t^3)\right] W \\
&= W + t\left(\frac{\partial A(\mathbf{p})}{\partial p_1}\frac{\partial W}{\partial x_1} + \frac{\partial A(\mathbf{p})}{\partial p_2}\frac{\partial W}{\partial x_2}\right) + \\
&\quad \frac{1}{2}t^2\left(\left(\frac{\partial A(\mathbf{p})}{\partial p_1}\right)^2\frac{\partial^2 W}{\partial x_1{}^2} + \left(\frac{\partial A(\mathbf{p})}{\partial p_2}\right)^2\frac{\partial^2 W}{\partial x_2{}^2} + 2\frac{\partial A(\mathbf{p})}{\partial p_1}\frac{\partial A(\mathbf{p})}{\partial p_2}\frac{\partial^2 W}{\partial x_1 \partial x_2}\right) + \mathcal{O}(t^3)
\end{aligned} \tag{2.69}
$$

Now

$$
\begin{aligned}
&W\left(x_1 + t\frac{\partial A(\mathbf{p})}{\partial p_1}, x_2, p_1, p_2\right) \\
&= W + t\frac{\partial A(\mathbf{p})}{\partial p_1}\frac{\partial W}{\partial x_1} + t^2\left(\frac{\partial A(\mathbf{p})}{\partial p_1}\right)^2\frac{\partial^2 W}{\partial x_1{}^2} + \mathcal{O}(t^3) \\
&= W' \text{ say}
\end{aligned} \tag{2.70}
$$

Hence

$$
\begin{aligned}
&W\left(x_1 + t\frac{\partial A(\mathbf{p})}{\partial p_1}, x_2 + t\frac{\partial A(\mathbf{p})}{\partial p_2}, p_1, p_2\right) \\
&= W' + t\frac{\partial A(\mathbf{p})}{\partial p_2}\frac{\partial W'}{\partial x_2} + t^2\left(\frac{\partial A(\mathbf{p})}{\partial p_2}\right)^2\frac{\partial^2 W'}{\partial x_2{}^2} + \mathcal{O}(t^3) \\
&\qquad \text{substituting } W' \text{ from (2.70) we will arrive at} \\
&= W + t\left(\frac{\partial A(\mathbf{p})}{\partial p_1}\frac{\partial W}{\partial x_1} + \frac{\partial A(\mathbf{p})}{\partial p_2}\frac{\partial W}{\partial x_2}\right) + \\
&\quad \frac{1}{2}t^2\left(\left(\frac{\partial A(\mathbf{p})}{\partial p_1}\right)^2\frac{\partial^2 W}{\partial x_1{}^2} + \left(\frac{\partial A(\mathbf{p})}{\partial p_2}\right)^2\frac{\partial^2 W}{\partial x_2{}^2} + 2\frac{\partial A(\mathbf{p})}{\partial p_1}\frac{\partial A(\mathbf{p})}{\partial p_2}\frac{\partial^2 W}{\partial x_1 \partial x_2}\right) + \mathcal{O}(t^3)
\end{aligned} \tag{2.71}
$$

Comparing (2.69) and (2.71) we see that coefficients of t and t^2 are identical in the two expressions. In fact we evaluate further it can be shown that coefficients of all higher order terms in t are also

identical in the two expressions. Thus for the 2 dimensional system we arrive at the closed form

$$
e^{t\mathcal{A}}\left\{W(x_1, x_2, p_1, p_2)\right\} = W\left(x_1 + t\frac{\partial A(\mathbf{p})}{\partial p_1}, x_2 + t\frac{\partial A(\mathbf{p})}{\partial p_2}, p_1, p_2\right)
$$

$$
\text{or } e^{t\mathcal{A}}\left\{W(x_1, x_2, p_1, p_2)\right\}_{(x_{10}, x_{20}, p_{10}, p_{20})} = \tag{2.72}
$$
$$
W\left(x_{10} + t\left(\frac{\partial A(\mathbf{p})}{\partial p_1}\right)_{\mathbf{p}=\mathbf{p_0}}, x_{20} + t\left(\frac{\partial A(\mathbf{p})}{\partial p_2}\right)_{\mathbf{p}=\mathbf{p_0}}, p_{10}, p_{20}\right)
$$

Extending the proof (2.72) to an n dimensional system, we can arrive at the closed form for the operation of the evolution operator component $e^{t\mathcal{A}}$ in (2.68). Similarly the closed form for the operation of $e^{t\mathcal{B}}$ can also be proven. From (2.68) it is simple to arrive at (2.67). From (2.68) and (2.67) we see that the components of the evolution operator operate as simple translation operators for the position vector and the momentum vector of the system. This is only possible because the Hamiltonian of the system is separable. Had the Hamiltonian been inseparable then $\nabla_p A(\mathbf{p})_{\mathbf{p}=\mathbf{p_0}}$ and $\nabla_x V(\mathbf{x})_{\mathbf{x}=\mathbf{x_0}}$ in (2.67) would have to replaced by $\nabla_p H(\mathbf{p}, \mathbf{x})_{\mathbf{x_0}, \mathbf{p_0}}$ and $\nabla_x H(\mathbf{p}, \mathbf{x})_{\mathbf{x_0}, \mathbf{p_0}}$ respectively in which case the resultant transformations of $\boldsymbol{\eta}$ would not be simple translations. More importantly it would also not be possible to derive the closed form of (2.68), which classifies these operators are translation operators.

The fact that the components of the evolution operator operate as translation operators helps in deriving numerical integrators of any order for the system. It also turns out that a numerical integrators of any order derived from exponential splitting of the evolution operator the system with separable Hamiltonian is a symplectic integrators. We will now demonstrate how the numerical integrators are derived by the exponential splitting technique.

All that is required is to approximate the evolution operator by multiple operations of the component operators as followa

$$
e^{t(\mathcal{A}+\mathcal{B})} = \prod_{k=0}^{m} e^{td_k(\mathcal{A})} e^{tc_k(\mathcal{B})} + \mathcal{O}(t^{m+2}) \tag{2.73}
$$

Equation (2.73) is the exponential splitting scheme for an $(m+1)^{th}$ order symplectic integrator. The equation means that the product of the evolution component operators on the RHS is equal to the evolution operator on the LHS correct upto order of t^{m+1}. The set of d_k and c_k are the coefficients to determined by expanding the LHS and RHS in exponential series and matching the coefficients on both sides of powers of t upto t^{m+1}. Once we evaluate the values of all d_k and c_k we can express the

$(m + 1)^{th}$ order numerical integrator as

$$\mathbf{p_{k+1}} = \mathbf{p_k} - c_k \, \Delta t \, (\boldsymbol{\nabla}_x V(\mathbf{x}))_{\mathbf{x=x_k}} \; \Rightarrow \; p_{(k+1)\,i} = p_{ki} - c_k \, \Delta t \frac{\partial V}{\partial x_i}\Big|_{\mathbf{x=x_k}}$$

$$\mathbf{x_{k+1}} = \mathbf{x_k} + d_k \, \Delta t \, (\boldsymbol{\nabla}_p A(\mathbf{p}))_{\mathbf{p=p_k}} \; \Rightarrow \; x_{(k+1)\,i} = x_{ki} + d_k \, \Delta t \frac{\partial A}{\partial p_i}\Big|_{\mathbf{p=p_k}}$$

$$\text{where } k = 0, 1, 2, .., m$$

(2.74)

It can be shown that if we evaluate the co-efficients d_k and c_k by the exponential series expansion of (2.73) for a 1st $((m+1) = 1)$ and 2nd $((m+1) = 2)$ order numerical integrator then (2.74) matches with (2.47) and (2.60) respectively. Hence with (2.74) we have arrived at general algorithm for generating symplecitc numerical integrator of any order for an system with a separable Hamiltonaian, without deriving Generating functions of the form shown in (2.39) or carrying out co-ordinate and Hamiltonian transformations. The exponential splitting of the evolution operator of the system yields the required symplectic numerical integrators.

It must be noted however that evaluating the set of c_k and d_k from (2.73) directly as discussed above, still invloves solving a set of nonlinear algebraic equations in c_k and d_k which can get just as complex and numerous for higher values of m as in the earlier method. However the exponential splitting scheme has the added advantage that using the Baker-Campbell-Hausdorff (BCH) formula it is possible to generate higher even order symplectic integrators more easily from the second order symplectic integrator. The time reverislibility of even order symplecitc integrators is a key factor that is taken advantage of, in this even order symplectic integrator generating scheme. We will not discuss this method here. Intersted readers may refer [47]

So far all our derivations of symplectic integrators have been restricted to Hamiltonians that are separable. Now consider a charge particle of charge q, mass m, in a magnetic field $\mathbf{B}(\mathbf{x})$. The Hamiltonian of the system is

$$H = \frac{1}{2m} \left[\mathbf{p} - q\mathbf{A}(\mathbf{x})\right]^2$$

where $\mathbf{A}(\mathbf{x})$ is the magnetic vector potential

(2.75)

The motion of the particle is governed by the Lorentz force law given below

$$m\frac{d\mathbf{v}}{dt} = q\mathbf{v} \times \mathbf{B}(\mathbf{x})$$

(2.76)

We may also express the Hamiltons equation of motion of the system from (2.75) as

$$\dot{\mathbf{x}} = \frac{1}{m} \left[\mathbf{p} - q\mathbf{A}(\mathbf{x})\right]$$

and

$$\dot{\mathbf{p}} = \frac{q}{m} \sum_{i=1}^{3} \left[\{p_i - qA_i(\mathbf{x})\} \, \boldsymbol{\nabla}_x \, A_i(\mathbf{x}) \right]$$

(2.77)

Although it is possible to obtain a symplectic integrator for a non-separable Hamiltonian such as (2.75), the procedure is mathematically complex. Alternatively the desired result of a stable and accurate itegrator may be obtained from the exponential splitting of the evolution operator. The result is an Exact energy Conserving (EEC) integrator that shows greater stability and are much less susceptible to phase errors than symplectic integrators for such systems.

From (2.76) we get the equations of motion of the system as -

$$\dot{\mathbf{v}} = -\frac{qB(\mathbf{x})}{m}\,\hat{\mathbf{B}}(\mathbf{x}) \times \mathbf{v}$$

and

$$\dot{\mathbf{x}} = \mathbf{v}$$

where $\hat{\mathbf{B}}(\mathbf{x}) = \dfrac{\mathbf{B}(\mathbf{x})}{B(\mathbf{x})}$

(2.78)

Hence the time evolution of a function $W(\mathbf{x}, \mathbf{v})$ that is not an explicit function of time, will be given by

$$\frac{dW}{dt} = \boldsymbol{\nabla}_x W \cdot \dot{\mathbf{x}} + \boldsymbol{\nabla}_v W \cdot \dot{\mathbf{v}}$$

substituting the time derivatives from (2.78)

$$= \left[\mathbf{v} \cdot \boldsymbol{\nabla}_x - \frac{qB(\mathbf{x})}{m}\,\hat{\mathbf{B}}(\mathbf{x}) \times \mathbf{v} \cdot \boldsymbol{\nabla}_v\right] W$$

(2.79)

The operator solution of (2.79) can be expressed as

$$W(t) = \mathrm{e}^{t(\mathcal{T}+\mathcal{V})}\, W(0)$$

where operators $\mathcal{T} = \mathbf{v} \cdot \boldsymbol{\nabla}_x$ and $\mathcal{V} = -\dfrac{qB(\mathbf{x})}{m}\,\hat{\mathbf{B}}(\mathbf{x}) \times \mathbf{v} \cdot \boldsymbol{\nabla}_v$

(2.80)

Similarly the evolution of the co-ordinates from (2.78) may be expressed as

$$\begin{pmatrix} \mathbf{x}(t) \\ \mathbf{v}(t) \end{pmatrix} = \mathrm{e}^{t(\mathcal{T}+\mathcal{V})} \begin{pmatrix} \mathbf{x}(0) \\ \mathbf{v}(0) \end{pmatrix}$$

(2.81)

Here $\mathrm{e}^{\mathcal{T}}$ and $\mathrm{e}^{\mathcal{V}}$ are the component operators of the evolution operator. Note that $\mathcal{T}$ and $\mathcal{V}$ do not have an unmixed form as the operators $\mathcal{A}$ and $\mathcal{B}$ derived from a separable Hamiltonian in (2.64). Let us now check if the operation of the component operators on the position and velocity co-ordinates can be evaluated in a closed form.

The first component operator, $\mathrm{e}^{\mathcal{T}}$ is similar in form to $\mathrm{e}^{\mathcal{A}}$ and hence can be shown to be a translation operator as follows

$$\mathrm{e}^{t\,\mathcal{T}} \begin{pmatrix} \mathbf{x} \\ \mathbf{v} \end{pmatrix} = \begin{pmatrix} \mathbf{x} + t\mathbf{v} \\ \mathbf{v} \end{pmatrix}$$

(2.82)

The second component operator $\mathrm{e}^{\mathcal{V}}$, which has a mixed form, operates on the velocity co-ordinates. Let us check how it operates on a velocity co-ordinate, say v_1

$$\mathrm{e}^{t\mathcal{V}}\,v_1 = \left[1 + t\mathcal{V} + t^2\frac{\mathcal{V}^2}{2!} + t^3\frac{\mathcal{V}^3}{3!} + t^4\frac{\mathcal{V}^4}{4!} + \ldots\right] v_1$$

(2.83)

Now

$$\mathcal{V} v_1 = -\frac{qB}{m} \left[(\hat{B}_2 v_3 - \hat{B}_3 v_2)\frac{\partial}{\partial v_1} + (\hat{B}_3 v_1 - \hat{B}_1 v_3)\frac{\partial}{\partial v_2} + (\hat{B}_1 v_2 - \hat{B}_2 v_1)\frac{\partial}{\partial v_3} \right] v_1$$

$$= -\frac{qB}{m} (\hat{B}_2 v_3 - \hat{B}_3 v_2) = -\frac{qB}{m} (\hat{\mathbf{B}} \times \mathbf{v})_1$$

Next

$$\mathcal{V}^2 v_1 = \mathcal{V} \{\mathcal{V} v_1\}$$

substituting $\mathcal{V} v_1$

$$= \left(\frac{qB}{m}\right)^2 \left[(\hat{B}_2 v_3 - \hat{B}_3 v_2)\frac{\partial}{\partial v_1} + (\hat{B}_3 v_1 - \hat{B}_1 v_3)\frac{\partial}{\partial v_2} + (\hat{B}_1 v_2 - \hat{B}_2 v_1)\frac{\partial}{\partial v_3} \right] (\hat{B}_2 v_3 - \hat{B}_3 v_2)$$

$$= \left(\frac{qB}{m}\right)^2 \left[(\hat{B}_3 v_1 - \hat{B}_1 v_3)(-\hat{B}_3) + (\hat{B}_1 v_2 - \hat{B}_2 v_1)(\hat{B}_2) \right]$$

$$= \left(\frac{qB}{m}\right)^2 \left[\hat{B}_2(\hat{\mathbf{B}} \times \mathbf{v})_3 - \hat{B}_3(\hat{\mathbf{B}} \times \mathbf{v})_2 \right]$$

$$= \left(\frac{qB}{m}\right)^2 \left[\hat{\mathbf{B}} \times (\hat{\mathbf{B}} \times \mathbf{v}) \right]_1$$

Next

$$\mathcal{V}^3 v_1 = \mathcal{V} \{\mathcal{V}^2 v_1\}$$

substituting $\mathcal{V}^2 v_1$

$$= -\left(\frac{qB}{m}\right)^3 \left[(\hat{B}_2 v_3 - \hat{B}_3 v_2)\frac{\partial}{\partial v_1} + (\hat{B}_3 v_1 - \hat{B}_1 v_3)\frac{\partial}{\partial v_2} + (\hat{B}_1 v_2 - \hat{B}_2 v_1)\frac{\partial}{\partial v_3} \right]$$

$$\left[(\hat{B}_3 v_1 - \hat{B}_1 v_3)(-\hat{B}_3) + (\hat{B}_1 v_2 - \hat{B}_2 v_1)(\hat{B}_2) \right] \tag{2.84}$$

$$= -\left(\frac{qB}{m}\right)^3 \left[(\hat{B}_2 v_3 - \hat{B}_3 v_2)(-\hat{B}_3^2 - \hat{B}_2^2) + (\hat{B}_3 v_1 - \hat{B}_1 v_3)\hat{B}_1\hat{B}_2 + (\hat{B}_1 v_2 - \hat{B}_2 v_1)\hat{B}_1\hat{B}_3 \right]$$

$$= -\left(\frac{qB}{m}\right)^3 \left[v_3(-\hat{B}_3^2\hat{B}_2 - \hat{B}_1^2\hat{B}_2 - \hat{B}_2^3) + v_2(\hat{B}_1^2\hat{B}_3 + \hat{B}_2^2\hat{B}_3 + \hat{B}_3^3) \right]$$

$$= -\left(\frac{qB}{m}\right)^3 \left[v_3\hat{B}_2(-\hat{B}_3^2 - \hat{B}_1^2 - \hat{B}_2^2) + v_2\hat{B}_3(\hat{B}_1^2 + \hat{B}_2^2 + \hat{B}_3^2) \right]$$

$$= -\left(\frac{qB}{m}\right)^3 \left[v_2\hat{B}_3 - v_3\hat{B}_2 \right]$$

$$= -\left(\frac{qB}{m}\right)^3 \left(-(\hat{\mathbf{B}} \times \mathbf{v})_1 \right)$$

Next

$$\mathcal{V}^4 v_1 = \mathcal{V} \{\mathcal{V}^3 v_1\}$$

substituting $\mathcal{V}^3 v_1$

$$= \left(\frac{qB}{m}\right)^4 \left[(\hat{B}_2 v_3 - \hat{B}_3 v_2)\frac{\partial}{\partial v_1} + (\hat{B}_3 v_1 - \hat{B}_1 v_3)\frac{\partial}{\partial v_2} + (\hat{B}_1 v_2 - \hat{B}_2 v_1)\frac{\partial}{\partial v_3} \right] (-)(\hat{B}_2 v_3 - \hat{B}_3 v_2)$$

substituting form definition of $\mathcal{V}^2 v_1$

$$= \left(\frac{qB}{m}\right)^4 \left(-\left[\hat{\mathbf{B}} \times (\hat{\mathbf{B}} \times \mathbf{v}) \right]_1 \right) \text{ , and so on ..}$$

Let $\theta(\mathbf{x}, t) = -(tqB)/m$. Then from (2.83) and (2.84) we have

$$
\mathrm{e}^{t\mathcal{V}} v_1 = \left[v_1 + \theta(\hat{\mathbf{B}} \times \mathbf{v})_1 + \frac{\theta^2}{2!} \left[\hat{\mathbf{B}} \times (\hat{\mathbf{B}} \times \mathbf{v}) \right]_1 - \frac{\theta^3}{3!}(\hat{\mathbf{B}} \times \mathbf{v})_1 - \frac{\theta^4}{4!} \left[\hat{\mathbf{B}} \times (\hat{\mathbf{B}} \times \mathbf{v}) \right]_1 + ... \right]
$$

$$
\text{expressing as } \sin(\theta) \text{ and } \cos(\theta) \text{ series} \qquad (2.85)
$$

$$
= \left[v_1 + \sin\theta \, (\hat{\mathbf{B}} \times \mathbf{v})_1 + (1 - \cos\theta) \left\{ \hat{\mathbf{B}} \times (\hat{\mathbf{B}} \times \mathbf{v}) \right\}_1 \right]
$$

From (2.85) we can deduce that

$$
\mathrm{e}^{t\mathcal{V}} \mathbf{v} = \left[\mathbf{v} + \sin\theta \, (\hat{\mathbf{B}} \times \mathbf{v}) + (1 - \cos\theta) \left\{ \hat{\mathbf{B}} \times (\hat{\mathbf{B}} \times \mathbf{v}) \right\} \right] \qquad (2.86)
$$

Now the operation of the second component operator on the position and velocity coordinates may be expressed in matrix form as

$$
\mathrm{e}^{t\,\mathcal{V}} \begin{pmatrix} \mathbf{x} \\ \mathbf{v} \end{pmatrix} = \begin{pmatrix} \mathbf{x} \\ \mathbf{v}_B \Big(\mathbf{x}, \mathbf{v}, t\Big) \end{pmatrix}
$$

$$
\text{where}
$$

$$
\mathbf{v}_B \Big(\mathbf{x}, \mathbf{v}, t\Big) = \left[\mathbf{v} + \sin(\theta(\mathbf{x}, t)) \left(\hat{\mathbf{B}}(\mathbf{x}) \times \mathbf{v} \right) \right. \qquad (2.87)
$$

$$
\left. + \Big(1 - \cos(\theta(\mathbf{x}, t)) \Big) \left\{ \hat{\mathbf{B}}(\mathbf{x}) \times \Big(\hat{\mathbf{B}}(\mathbf{x}) \times \mathbf{v} \Big) \right\} \right]
$$

Hence we obtain the operation of both components of the evolution operator in a closed form. However we have not yet physically defined the operation of $\mathrm{e}^{t\,\mathcal{V}}$. Let us proceed to do so. From (2.80) $\mathcal{V}$ may also be expressed as

$$
\mathcal{V} = -\frac{qB}{m} \hat{\mathbf{B}} \cdot (\mathbf{v} \times \boldsymbol{\nabla}_v) = -\mathrm{i}\frac{qB}{m} \hat{\mathbf{B}} \cdot \mathbf{J} \qquad (2.88)
$$

$$
\text{where } \mathbf{J} = -\mathrm{i}\mathbf{v} \times \boldsymbol{\nabla}_v \text{ is the "angular momentum" operator in velocity space}
$$

Hence

$$
\exp(t\,\mathcal{V}) = \exp(\mathrm{i}\,\theta\,\mathbf{B}\cdot\mathbf{J}) \qquad (2.89)
$$

From (2.89) we can recognize $\mathrm{e}^{t\,\mathcal{V}}$ as being the rotation operator that rotates the velocity $\mathbf{v}$ about the axis $\hat{\mathbf{B}}$ by an angle θ. The resultant velocity is then $\mathbf{v}_B(\mathbf{x}, \mathbf{v}, t)$.

Now that we have obtained a closed form of the operations of both components of the evolution operator, we can use the exponential splitting of the evolution operator to obtain algorithms of different orders of numerical integrators for the system. The formula to be used is again

$$
\mathrm{e}^{t(\mathcal{T}+\mathcal{V})} = \prod_{k=0}^{m} \mathrm{e}^{td_k(\mathcal{T})} \, \mathrm{e}^{tc_k(\mathcal{V})} + \mathcal{O}(t^{m+2}) \qquad (2.90)
$$

Of course the solutions for d_k and c_k in (2.89) for any given order of numerical integrator will be the same as in (2.73). With the solutions d_k and c_k numerical integrators of any order may be constructed for the particle in magnetic field. For example a first order solution with $d_0 = c_0 = 1$ can be expressed as

$$\mathbf{v_1} = \mathbf{v}_B(\mathbf{x_0}, \mathbf{v_0}, \Delta t) \;\Rightarrow\; v_{1\,i} = v_{Bi}(\mathbf{x_0}, \mathbf{v_0}, \Delta t)$$

$$\mathbf{x_1} = \mathbf{x_0} + \Delta t\, \mathbf{v_1} \Rightarrow\; x_{1\,i} = x_{0i} + \Delta t\, v_{1i} \tag{2.91}$$

$$\text{where } i = 1, 2, 3$$

Let us now classify this type of numerical integrator. It can be easily proved that

$$\mathrm{e}^{t\,\mathcal{V}}\, v^2 = v^2$$

$$\text{and } \mathrm{e}^{t\,\mathcal{T}}\, v^2 = v^2$$

$$\text{hence } \prod_{k=0}^{m} \mathrm{e}^{td_k(\mathcal{T})}\, \mathrm{e}^{tc_k(\mathcal{V})}\, v^2 = v^2 \tag{2.92}$$

Hence numerical integrators obtained from the above procedure of energy splitting are all Exact Energy Conserving (EEC) integrators for the charged particle in a magnetic field. When the magnetic field $\mathbf{B}$ is a constant, one can go a step further and obtain the operation of the full evolution operator $\mathrm{e}^{t(\mathcal{T}+\mathcal{V})}$ on the position and velocity algorithm in a closed form. Then the integrator becomes an Exact integrator for the system. We will not derive the exact integrator here.

This exponential splitting scheme may also be extended for a charged particle in an electric field $\mathbf{E}(\mathbf{x})$ plus a magnetic field $\mathbf{B}(\mathbf{x})$. The force equation for this system is

$$m\frac{d\mathbf{v}}{dt} = q\left[\mathbf{v} \times \mathbf{B}(\mathbf{x}) + \mathbf{E}(\mathbf{x})\right] \tag{2.93}$$

From (2.93) we can obtain the evolution operator of this system as $\mathrm{e}^{t(\mathcal{T}+\mathcal{V}_{BF})}$, where

$$\mathcal{T} = \mathbf{v}\cdot \boldsymbol{\nabla}_x \text{ and } \mathcal{V}_{BF} = \left[-\frac{qB(\mathbf{x})}{m}\,\hat{\mathbf{B}}(\mathbf{x}) \times \mathbf{v} + \frac{q}{m}\mathbf{E}(\mathbf{x})\right]\cdot\boldsymbol{\nabla}_v \tag{2.94}$$

Now the first component of the evolution operator $\mathrm{e}^{t\mathcal{T}}$ is the translation operator. Let us check how the second component $\mathrm{e}^{t\mathcal{V}_{BF}}$ operates. We have

$$\mathrm{e}^{t\mathcal{V}_{BF}}\, v_1 = \left[1 + t\mathcal{V}_{BF} + t^2\frac{\mathcal{V}_{BF}^2}{2!} + t^3\frac{\mathcal{V}_{BF}^3}{3!} + t^4\frac{\mathcal{V}_{BF}^4}{4!} + ...\right] v_1 \tag{2.95}$$

Let $a_1 = E_1/B$. Then,

$$\mathcal{V}_{BF}\, v_1 = -\frac{qB}{m}\left[(\hat{B}_2 v_3 - \hat{B}_3 v_2 - a_1)\frac{\partial}{\partial v_1} + (\hat{B}_3 v_1 - \hat{B}_1 v_3 - a_3)\frac{\partial}{\partial v_2} + (\hat{B}_1 v_2 - \hat{B}_2 v_1 - a_2)\frac{\partial}{\partial v_3}\right] v_1$$

$$= -\frac{qB}{m}(\hat{B}_2 v_3 - \hat{B}_3 v_2 - a_1) = -\frac{qB}{m}(\hat{\mathbf{B}} \times \mathbf{v})_1 + \frac{q}{m}E_1$$

Next

$$\mathcal{V}^2_{BF}\, v_1 = \mathcal{V}_{BF}\left\{\mathcal{V}_{BF}\, v_1\right\}$$

substituting $\mathcal{V}_{BF}\, v_1$

$$= \left(\frac{qB}{m}\right)^2\left[(\hat{B}_2 v_3 - \hat{B}_3 v_2 - a_1)\frac{\partial}{\partial v_1} + (\hat{B}_3 v_1 - \hat{B}_1 v_3 - a_2)\frac{\partial}{\partial v_2} + (\hat{B}_1 v_2 - \hat{B}_2 v_1 - a_3)\frac{\partial}{\partial v_3}\right](\hat{B}_2 v_3 - \hat{B}_3 v_2 - a_1)$$

$$= \left(\frac{qB}{m}\right)^2\left[(\hat{B}_2 v_3 - \hat{B}_3 v_2 - a_1)\frac{\partial}{\partial v_1} + (\hat{B}_3 v_1 - \hat{B}_1 v_3 - a_2)\frac{\partial}{\partial v_2} + (\hat{B}_1 v_2 - \hat{B}_2 v_1 - a_3)\frac{\partial}{\partial v_3}\right](\hat{B}_2 v_3 - \hat{B}_3 v_2)$$

$$= \left(\frac{qB}{m}\right)^2\left[(\hat{B}_3 v_1 - \hat{B}_1 v_3)(-\hat{B}_3) + (\hat{B}_1 v_2 - \hat{B}_2 v_1)(\hat{B}_2)\right] + \left(\frac{qB}{m}\right)^2(a_2\hat{B}_3 - a_3\hat{B}_2)$$

$$= \left(\frac{qB}{m}\right)^2\left[\hat{\mathbf{B}} \times (\hat{\mathbf{B}} \times \mathbf{v})\right]_1 - \left(\frac{qB}{m}\right)\left(\hat{\mathbf{B}} \times \frac{q}{m}\mathbf{E}\right)_1$$

Next

$$\mathcal{V}^3_{BF}\, v_1 = \mathcal{V}_{BF}\left\{\mathcal{V}^2_{BF}\, v_1\right\}$$

substituting $\mathcal{V}^2_{BF}\, v_1$

$$= -\left(\frac{qB}{m}\right)^3\left[(\hat{B}_2 v_3 - \hat{B}_3 v_2 - a_1)\frac{\partial}{\partial v_1} + (\hat{B}_3 v_1 - \hat{B}_1 v_3 - a_2)\frac{\partial}{\partial v_2} + (\hat{B}_1 v_2 - \hat{B}_2 v_1 - a_3)\frac{\partial}{\partial v_3}\right]$$

$$\left\{\left[(\hat{B}_3 v_1 - \hat{B}_1 v_3)(-\hat{B}_3) + (\hat{B}_1 v_2 - \hat{B}_2 v_1)(\hat{B}_2)\right] + (a_2\hat{B}_3 - a_3\hat{B}_2)\right\}$$

$$= -\left(\frac{qB}{m}\right)^3\left[(\hat{B}_2 v_3 - \hat{B}_3 v_2 - a_1)\frac{\partial}{\partial v_1} + (\hat{B}_3 v_1 - \hat{B}_1 v_3 - a_2)\frac{\partial}{\partial v_2} + (\hat{B}_1 v_2 - \hat{B}_2 v_1 - a_3)\frac{\partial}{\partial v_3}\right]$$

$$\left[(\hat{B}_3 v_1 - \hat{B}_1 v_3)(-\hat{B}_3) + (\hat{B}_1 v_2 - \hat{B}_2 v_1)(\hat{B}_2)\right]$$

$$= -\left(\frac{qB}{m}\right)^3\left[v_3(-\hat{B}_3^2\hat{B}_2 - \hat{B}_1^2\hat{B}_2 - \hat{B}_2^3) + v_2(\hat{B}_1^2\hat{B}_3 + \hat{B}_2^2\hat{B}_3 + \hat{B}_3^3)\right]$$

$$- \left(\frac{qB}{m}\right)^3(a_1\hat{B}_3^2 + a_1\hat{B}_2^2 - a_2\hat{B}_1\hat{B}_2 - a_3\hat{B}_1\hat{B}_3)$$

$$= -\left(\frac{qB}{m}\right)^3\left[v_3\hat{B}_2(-\hat{B}_3^2 - \hat{B}_1^2 - \hat{B}_2^2) + v_2\hat{B}_3(\hat{B}_1^2 + \hat{B}_2^2 + \hat{B}_3^2)\right]$$

$$- \left(\frac{qB}{m}\right)^3\left(-\hat{B}_2(a_2\hat{B}_1 - a_1\hat{B}_2) + \hat{B}_3(+a_1\hat{B}_3 - a_3\hat{B}_1)\right)$$

$$= -\left(\frac{qB}{m}\right)^3\left[v_2\hat{B}_3 - v_3\hat{B}_2\right] - \left(\frac{qB}{m}\right)^3\left(-\hat{B}_2(\hat{\mathbf{B}} \times \mathbf{a})_3 + \hat{B}_3(\hat{\mathbf{B}} \times \mathbf{a})_2\right)$$

$$= -\left(\frac{qB}{m}\right)^3(-(\hat{\mathbf{B}} \times \mathbf{v})_1) + \left(\frac{qB}{m}\right)^2\left(\hat{\mathbf{B}} \times \left(\hat{\mathbf{B}} \times \frac{q}{m}\mathbf{E}\right)\right)_1$$

, and so on ..

(2.96)

Hence

$$
\mathrm{e}^{t\mathcal{V}_{BF}}\, v_1 = \left[v_1 + \theta(\hat{\mathbf{B}} \times \mathbf{v})_1 + t\frac{q}{m}E_1 + \frac{\theta^2}{2!}\left(\hat{\mathbf{B}} \times (\hat{\mathbf{B}} \times \mathbf{v})\right)_1 + \frac{t}{2!}\theta\left(\hat{\mathbf{B}} \times \frac{q}{m}\mathbf{E}\right)_1 - \frac{\theta^3}{3!}(\hat{\mathbf{B}} \times \mathbf{v})_1 \right.
$$

$$
\left. + \frac{t}{3!}\theta^2\left(\hat{\mathbf{B}} \times \left(\hat{\mathbf{B}} \times \frac{q}{m}\mathbf{E}\right)\right)_1 + ... \right]
$$

$$
= \left[v_1 + \theta(\hat{\mathbf{B}} \times \mathbf{v})_1 + \frac{\theta^2}{2!}\left(\hat{\mathbf{B}} \times (\hat{\mathbf{B}} \times \mathbf{v})\right)_1 - \frac{\theta^3}{3!}(\hat{\mathbf{B}} \times \mathbf{v})_1 + ... \right]
$$

$$
+ t\left[\frac{q}{m}E_1 + \frac{1}{2!}\theta\left(\hat{\mathbf{B}} \times \frac{q}{m}\mathbf{E}\right)_1 + \frac{1}{3!}\theta^2\left(\hat{\mathbf{B}} \times \left(\hat{\mathbf{B}} \times \frac{q}{m}\mathbf{E}\right)\right)_1 + ... \right]
$$

$$
= \left[v_1 + \theta(\hat{\mathbf{B}} \times \mathbf{v})_1\left(\theta - \frac{\theta^3}{3!} + ...\right) + \left(\hat{\mathbf{B}} \times (\hat{\mathbf{B}} \times \mathbf{v})\right)_1\left(\frac{\theta^2}{2!} + ...\right) \right] \quad (2.97)
$$

$$
+ \left[t\frac{q}{m}E_1 + \frac{t}{\theta}\left(\hat{\mathbf{B}} \times \frac{q}{m}\mathbf{E}\right)_1\left(\frac{\theta^2}{2!} + ..\right) + t\left(\hat{\mathbf{B}} \times \left(\hat{\mathbf{B}} \times \frac{q}{m}\mathbf{E}\right)\right)_1\left(\frac{1}{3!}\theta^2 + ..\right) \right]
$$

Using $\sin\theta$ and $\cos\theta$ series

$$
= \left[v_1 + \theta(\hat{\mathbf{B}} \times \mathbf{v})_1\,(\sin\theta) + \left(\hat{\mathbf{B}} \times (\hat{\mathbf{B}} \times \mathbf{v})\right)_1(1 - \cos\theta) \right]
$$

$$
+ \left[t\frac{q}{m}E_1 + \frac{t}{\theta}\left(\hat{\mathbf{B}} \times \frac{q}{m}\mathbf{E}\right)_1(1 - \cos\theta) + t\left(\hat{\mathbf{B}} \times \left(\hat{\mathbf{B}} \times \frac{q}{m}\mathbf{E}\right)\right)_1\left(1 - \frac{\sin\theta}{\theta}\right) \right]
$$

From (2.97) it can be deduced that

$$
\mathrm{e}^{t\mathcal{V}_{BF}}\, \mathbf{v} = \left[\mathbf{v} + \theta(\hat{\mathbf{B}} \times \mathbf{v})\,(\sin\theta) + \left(\hat{\mathbf{B}} \times (\hat{\mathbf{B}} \times \mathbf{v})\right)(1 - \cos\theta) \right]
$$

$$
\quad (2.98)
$$

$$
+ \left[t\frac{q}{m}\mathbf{E} + \frac{t}{\theta}\left(\hat{\mathbf{B}} \times \frac{q}{m}\mathbf{E}\right)(1 - \cos\theta) + t\left(\hat{\mathbf{B}} \times \left(\hat{\mathbf{B}} \times \frac{q}{m}\mathbf{E}\right)\right)\left(1 - \frac{\sin\theta}{\theta}\right) \right]
$$

Now the operation of the second component operator on the position and velocity coordinates may

be expressed in matrix form as

$$e^{t\,\mathcal{V}_{BF}} \begin{pmatrix} \mathbf{x} \\ \mathbf{v} \end{pmatrix} = \begin{pmatrix} \mathbf{x} \\ \mathbf{v}_B\Big(\mathbf{x},\mathbf{v},t\Big) + \mathbf{v}_F\Big(\mathbf{x},t\Big) \end{pmatrix}$$

where

$$\mathbf{v}_B\Big(\mathbf{x},\mathbf{v},t\Big) = \bigg[\mathbf{v} + \sin(\theta(\mathbf{x},t))\Big(\hat{\mathbf{B}}(\mathbf{x})\times\mathbf{v}\Big)$$

$$+\Big(1-\cos(\theta(\mathbf{x},t))\Big)\Big\{\hat{\mathbf{B}}(\mathbf{x})\times\Big(\hat{\mathbf{B}}(\mathbf{x})\times\mathbf{v}\Big)\Big\}\bigg] \tag{2.99}$$

$$\text{and } \mathbf{v}_F\Big(\mathbf{x},t\Big) = \bigg[t\frac{q}{m}\mathbf{E}(\mathbf{x}) + \frac{t}{\theta(\mathbf{x},t)}\Big(\hat{\mathbf{B}}(\mathbf{x})\times\frac{q}{m}\mathbf{E}(\mathbf{x})\Big)(1-\cos(\theta(\mathbf{x},t))) +$$

$$t\Big(\hat{\mathbf{B}}(\mathbf{x})\times\Big(\hat{\mathbf{B}}(\mathbf{x})\times\frac{q}{m}\mathbf{E}(\mathbf{x})\Big)\Big)\Big(1-\frac{\sin(\theta(\mathbf{x},t))}{\theta(\mathbf{x},t)}\Big)\bigg]$$

Hence we obtain the operation of both components of the evolution operator, $e^{t\mathcal{T}}$, and $e^{t\mathcal{V}_{BF}}$ in a closed form. However we have not yet physically established the operation of $e^{t\,\mathcal{V}_{BF}}$. Let us proceed to do so. Now we know the operation of $e^{t\,\mathcal{V}_{BF}}$ can be divided into two operations. The first operation is a rotation operation caused by the Lorentz force resulting in the velocity vector $\mathbf{v}_B(\mathbf{x},\mathbf{v},t)$. The second operation yields the velocity vector $\mathbf{v}_F(\mathbf{x},t)$. This velocity can be shown to be the result of the $\mathbf{E}\times\mathbf{B}$ drift in the plane perpendicular the magnetic field, and the translational velocity gained by the particle due to the field $\mathbf{E}$ in the direction parallel to the magnetic field.

Now that we have established the operation of both components of the evolution operator in closed form we can use this exponential splitting to obtain numerical integrators of any order using,

$$e^{t(\mathcal{T}+\mathcal{V}_{BF})} = \prod_{k=0}^{m} e^{td_k(\mathcal{T})}\,e^{tc_k(\mathcal{V}_{BF})} + \mathcal{O}(t^{m+2}) \tag{2.100}$$

The resultant numerical integrators are neither symplectic , nor fully energy conserving, but they do yield qualitatively correct trajectories of charged particles in electric + magnetic and bounded periodic energy errors.

We should mention here that besides (2.100) given by Chin's procedure [44] there have also been other forms of numerical integrators developed for plasma simulation. For example, in 2008 a variational symplectic integrator for guiding center dynamics of charged particles, starting from a guiding center Lagrangian, has also been demonstrated [48].

In the PIC code we have used the first order apporximation $e^{t(\mathcal{T}+\mathcal{V}_{BF})} \approx e^{td_0(\mathcal{T})}\,e^{tc_0(\mathcal{V}_{BF})}$ to get

$d_0 = c_0 = 1$ and the following first order numerical integrator

$$\mathbf{v_1} = \mathbf{v}_B(\mathbf{x_0}, \mathbf{v_0}, \Delta t) + \mathbf{v}_F(\mathbf{x_0}, \mathbf{v_0}, \Delta t) \;\Rightarrow\; v_{1\,i} = v_{Bi}(\mathbf{x_0}, \mathbf{v_0}, \Delta t) + v_{Fi}(\mathbf{x_0}, \mathbf{v_0}, \Delta t)$$

$$\mathbf{x_1} = \mathbf{x_0} + \Delta t\, \mathbf{v_1} \Rightarrow\; x_{1\,i} = x_{0i} + \Delta t\, v_{1i}$$

$$\text{where } i = 1, 2, 3$$

(2.101)

This popular first order scheme is very stable gives very good conservation of conserved quatities over long periods of simulation, as we will later demonstrate in our benchmarks of the PIC code.

Now let $\mathbf{x}$ and $\mathbf{y}$ refer to the co-ordinate axes fo our simulation sytem (Fig. 2.1). In this cross-section of the cylindrical trap we have the electric field $\mathbf{E}(\mathbf{x}, \mathbf{y}) = E_x(\mathbf{x}, \mathbf{y})\,\hat{\mathbf{x}} + E_y(\mathbf{x}, \mathbf{y})\,\hat{\mathbf{y}}$ and the constant magneitc field $\mathbf{B}\,\hat{\mathbf{z}}$. Hence expressing (2.101) for each particle in the simulation system we have

$$v_{x1} = v_{x0} - v_{y0}\sin\theta - v_{x0}\left(1 - \cos\theta\right) + \Delta t\frac{q}{m}E_x - \frac{\Delta t}{\theta}\left(1 - \cos\theta\right)\frac{q}{m}E_y - \Delta t\left(1 - \frac{\sin\theta}{\theta}\right)\frac{q}{m}E_x$$

$$v_{y1} = v_{y0} + v_{x0}\sin\theta - v_{y0}\left(1 - \cos\theta\right) + \Delta t\frac{q}{m}E_y + \frac{\Delta t}{\theta}\left(1 - \cos\theta\right)\frac{q}{m}E_x - \Delta t\left(1 - \frac{\sin\theta}{\theta}\right)\frac{q}{m}E_y$$

and

$$x_1 = x_0 + v_{x1}\Delta t$$

$$y_1 = y_0 + v_{y1}\Delta t$$

(2.102)

In the code we have OPEN-MP parallelized (2.102) over particles.

2.1.6 Diagnostics of the 2D PIC code

To investigate the dynamics of the plasma in the cylindrical trap the 2D PIC code is facilitated with a set of numerical diagnostics that can be called upon as per requirement of the numerical experiment. These diagnostics are described in the following bullets.

- Nonneutral plasmas are characterized by large self electric fields. Any dynamics of the nonneutral cloud will have a signature in a modification of the toplologies of the electric field and the electrostatic potential in the trap's vacuum. Hence in an electrosatic simulation of a non-neutral plasma a very useful diagnostic tool is to record the electrostatic potential at strategic locations i.e selected mesh nodes, in the trap. This numerical diagnostic is qualitatively equivalent to the capacitive probes used in non-neutral plasma experiments [49]. PEC2PIC has 4 such azimuthally equispaced potential probes located at the same radial location just inside the grounded circular boundary of the trap (Fig. 2.1). These probes pick up dynamics of the plasma such as azimuthal modes, radial breathing modes, radial transport of the plasma. By analysing the signals of these potential probes the frequencies and growth rates of modes of the plasma can be determined.

The potential probes have been extensively used to analyze plasma dynamics in all experiments performed with the code.

- In the simulations of radial breathing modes in pure electron clouds, fluctuations of charge density at mesh nodes located within the plasma occupied region of the trap, can give information about the frequency and growth rate of such radial breathing modes. Such density probes (Fig. 2.1) have been utilized in the numerical experiments on radial breathing modes.

- In some numerical experiments performed with PEC2PIC code, trajectories of quasi-randomly selected tracer particles serve as useful diagnostics of the collecitve motion of the plasma. For example if there is a rigid rotation of a uniform density electron cloud, the linear oscillations of the Cartesian, $x(t)$ and $y(t)$ co-ordinates of a pseudo particle can give us information about the angular frequency of the collective rotation of the plasma. Again when there is collective radial breathing motion of the plasma, the radial co-ordinate $r(t)$ of a pseudo particle will oscillate with the frequency of the radial breathing mode.

- A non-neutral plasma under the influence of unstable fundamental Diocotron mode can exhibit gross radial transport of the cloud. And when an unstable fundamental Diocotron mode is excited on a multi-component nonneutral plasma then the radial transport of different plasma component may happen in different time-scales. It is useful in some experiments to trace such radial transport by recording the radial co-ordinate of the centre-of-mass of each component of the plasma. The radial co-ordinate of the centre of the mass of the ith plasma component, r_{CMi} is given by

$$r_{CMi}(t) = \frac{1}{N_i} \sum_{j=i_l}^{i_u} \sqrt{x_j^2(t) + y_j^2(t)} \tag{2.103}$$

where j is the particle index in the particle array while i_l and i_u are the starting index and ending index respectively of the ith species in the array of pseudo particles. $N_i = i_u - i_l + 1$ is the total of pseudo particles representing the ith component of the plasma. $x_j(t)$ and $y_j(t)$ are are the x and y co-ordinates of the jth pseudo particle in time t.

- The potential and kinetic energy of each plasma component and the total energy of the plasma are recorded thorough the entire length of simulations. These records not only serve as important benchmarking tools for the code, demonstrating conservation properties wherever applicable, but also help in understanding energetics associated with instabilities, such as potential energy pumping from one plasma component to another during a 2-stream instability between the components. The formula for calculating potential energy E_Pi and kinetic energy E_Ki of the ith

plasma component and the total energy E_T of the plasma are given below

$$E_{Pi}(t) = q_i \sum_{j=i_l}^{i_u} \phi(x_j(t), y_j(t))$$

$$E_{Ki}(t) = \frac{1}{2} m_i \sum_{j=i_l}^{i_u} (v_{xj}^2(t) + v_{yj}^2(t)) \qquad (2.104)$$

$$E_T(t) = \sum_i (E_{Pi}(t) + E_{Ki}(t))$$

In the above set of formulas, q_i and m_i is the charge and mass respectively of pseudo particles of the ith component of the plasma. v_{xj} and v_{yj} are Cartesian velocity components of the jth pseudo particle at time t.

- The magnetic angular momentum, and the kinetic angular momentum of each component of the plasma as well as the total angular momentum of the plasma are recorded through the simulations. Like the energy, the angular momentum records also serve as benchmarking tools, showing conservation where applicable. They also help in understanding the azimuthal dynamics in multicomponent plasma simulations. The formulas for calculating the magnetic angular momentum of the ith plasma component L_{zi}^{mag}, and the kinetic angular momentum for the ith plasma component, L_{zi}^K, and the total angular momentum of the plasma L_z^T are given below

$$L_{zi}^{mag}(t) = \frac{1}{2} B q_i \sum_{j=i_l}^{i_u} (x_j^2(t) + y_j^2(t))$$

$$L_{zi}^K(t) = m_i \sum_{j=i_l}^{i_u} v_{\theta j}(t) \sqrt{x_j^2(t) + y_j^2(t)} \qquad (2.105)$$

$$L_z^T(t) = \sum_i \left(L_{zi}^{mag}(t) + L_{zi}^K(t) \right)$$

where $v_{\theta j}(t)$ is the azimuthal component of the linear velocity, $\mathbf{v}_j(t)$ of the jth pseudo-particle in time t. As PEC2PIC runs on a Cartesian grid, incorporating a running calculation of $v_{\theta j}(t)$ involves a co-ordinate transformation of the velocity of each particle from a Cartesian to Cylindrical system which can significantly slow down the diagnostic part of the code. Hence calculation of L_{zi}^K and L_z^T are carried out only for those simulations where these quantities might be essential in describing the plasma dynamics.

- The net population of each of plasma componenet in the trap is also recorded as a functions of time

2.1.7 Algorithm of PEC2PIC

The processes of executed within and outside the time loop of PEC2PIC may be summarized by the followign steps

- Load initial conditions of the plasma

- time loop starts

    - Charge to mesh distribution by first order CIC scheme; OPEN-MP parallelized over particles

    - Solving Poisson Equation on mesh nodes by red-black parallelized SOR; OPEN-MP parallelized over mesh nodes

    - Interpolating Electric field components from mesh nodes to particle positions by reverse first order CIC scheme + particle pushing by Chin's exponential splitting scheme; OPEN-MP parallelized over particles

    - Calculating and record diagnostics at regular intervals of say 10 simulation time steps; OPEN-MP parallelized over particles and then assimilated with OPEN-MP Reduction

    - forwarding the time by the simulation time step

- time loop ends

2.1.8 Benchmarking experiments performed with PEC2PIC

The 2D PIC code has been benchmarked by simulating, on the system of Fig. 2.1, initial plasma parameters that have known linear analytical results. The benchmarks have been achieved by extracting linear phase results form these simulations, and matching these results with the available linear analytical results. The conservation properties of the conserved system parameters of these simulations have also been verfied from simulation.

The benchmarking experiments described below are divided into three sets - i) A set of experiments with pure electron plasmas of very low Brillouin Ratios, $f_b < 0.02$ that verify the applicability of the code in the Guiding centre drift approximated limit of pure electron plasmas, ii) A set of experiments with electron plasmas of different Brillouin ratios distributed over the entire confineable range of Brillouin ratio values i.e. $1 < f_b < 0$, which validate the extent of applicability of the code to the limit where inertia of the plasma plays an influential role in its dynamics iii) A set of unstable rotational equilibrium of a two-component nonneutral plasma susceptible to the rotational two-stream (ion-resonance) instability, which demonstrate that the code is capable of handling multi-component plasmas.

The three sets of numerical experiments were carried out for typical parameters found in experiments of cylindrical traps. [18], in particular, a wall radius, $R_w = 0.125m$, and axial magnetic field, $B_z = 0.015T$. The simulation time step, $\delta t = 10^{-11} sec$ is chosen much smaller than the cyclotron time period of electrons, $T_{ce} = 2.38 \times 10^{-9} sec$, such that the code can well resolve the cyclotron motion of electrons and ions. PIC-parameters used in these simulations are 87834 pseudo particles on a 70×70 grid. For the first set of benchmarking experiments with pure electron plasmas of very low Brillouin

Table 2.1: The frequency, ω_s, and growth rate α_s of the Diocotron modes obtained from simulation are compared with their corresponding analytical values, ω_a and α_a respectively.

$mode$	f_b	r_b^-/r_b^+	$\omega_s(rad/sec)$	$\omega_a(rad/sec)$[1]	$\alpha_s(rad/sec)$	$\alpha_a(rad/sec)$[2]
1	0.011	0	1.77688×10^6	1.76997×10^6		
2	0.012	0.35	7.66549×10^6	7.69106×10^6	0.85×10^6	0.7965×10^6
3(and 2)	0.017	0.6	10.7694×10^6	10.6186×10^6	2.25×10^6	2.38×10^6

ratio, 67500 electron pseudo particles were used to represent the electron cloud in the simulations. For the second set of numerical experiments 87834 electron pseudo particles were used to represent the electron plasma, and for the third set of simulations the ion component and the electron component of the non-neutral plasma were each represented by 87834 pseudo particles.

Benchmark at the Guiding-Centre-Drift approximated limit of electron plasma

To benchmark the code in the low density limit of electron plasma we have reproduced several analytical results obtained by R. C. Davidson and others for Diocotron modes in a cylindrically confined, axially symmetric electron plasma column [1, 15]. It must be noted here that the analytical results were obtained in the guiding centre drift approximation valid in the low density limit, while our code employs the full mass-included dynamics. The experiments performed were as follows. i) We generate a stable 1st Diocotron mode in a filled circular plasma cross section of uniform $f_b = 0.011$ and radius, $r_p = 0.5\,R_w$ by loading the centre of the patch slightly shifted from the central axis by $0.05\,R_w$. The frequency of the mode was then calculated by Fourier analysing the potential probes' readings and the stability of the mode was checked by letting the simulation run for $37790\,T_{ce}$. ii) We excite a pure, unstable 2nd Diocotron mode on an annular profile of uniform $f_b = 0.012$, inner radius, $r_b^- = 0.175\,R_w$, and outer radius $r_b^+ = 0.5\,R_w$. In course of the simulation over $37790\,T_{ce}$, initially an exponential growth of the pure 2nd mode was found, and then gradually higher non-linearities came into the evolution. The potential probes' readings were truncated to capture the pure 2nd mode growth. Fourier analysis and exponential envelope fitting on these truncated readings gave the mode frequency and growth rate respectively. iii) To excite an unstable 3rd mode an annular profile of $f_b = 0.017$, $r_b^- = 0.3\,R_w$, $r_b^+ = 0.5\,R_w$ is allowed to evolve for $37790\,T_{ce}$. The growth rate and frequency of the mode is estimated in the same way as (ii). It is not possible to excite a pure 3rd mode on an annular profile [15]. However we have chosen the dimensions of the loaded profile such that there is only a much weaker 2nd mode mixed with the 3rd mode in the initial stages. Hence the growth rate and frequency extracted form potential probes' data are essentially due the 3rd mode.

The results obtained from these benchmarking simulations demonstrate very close agreement with analytical results. These are presented in Table 2.1 and Fig. 2.4-2.6. Table 2.1 compares the experimental frequencies and growth rates with the corresponding analytical values. Fig. 2.4 depicts the evolution of a self-excited 3rd Diocotron mode in an annular profile. Fig. 2.5 show the potential probe reading analysis to determine the frequency and growth rate for the mode. Fig. 2.6 shows the
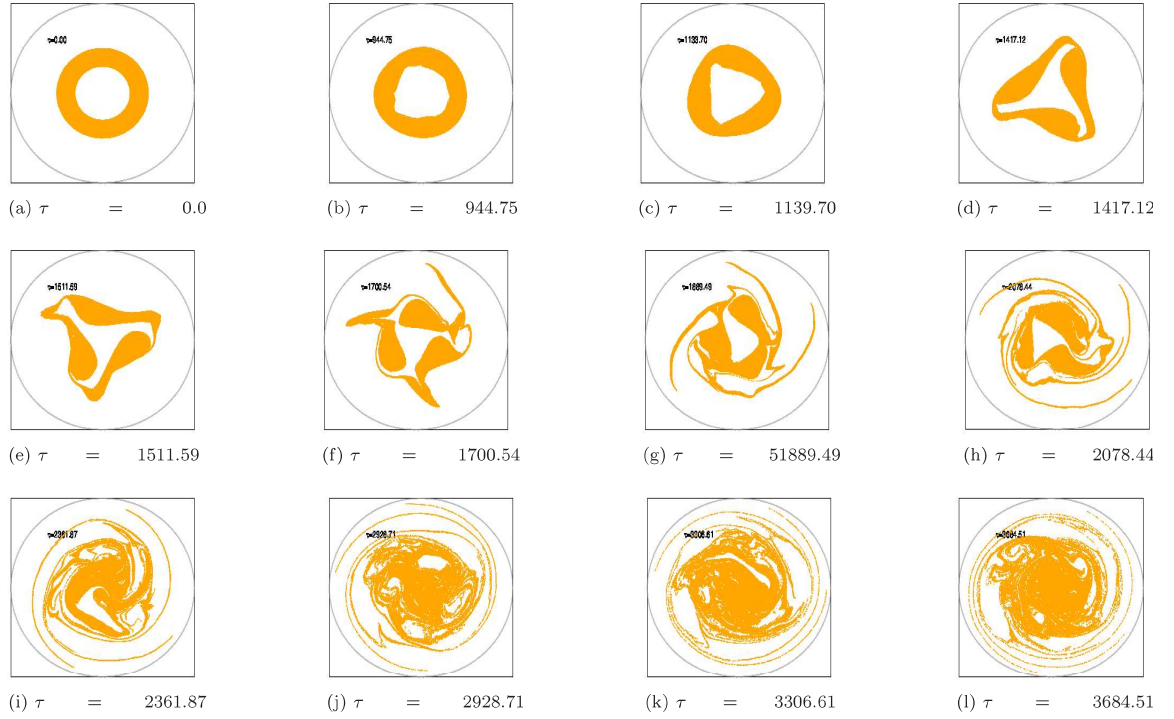
Figure 2.4: Snapshots of pseudo particles in the evolution of the 3rd Diocotron mode. In the snaps $\tau = t/T_{ce}$, represents the number of cyclotron time periods over which the plasma has evolved.

conservation of total energy, and magnetic angular momentum of the system (The magnetic angular momentum $\approx$ total angular momentum, for the low Brillouin ratio of $f_b = 0.017$) during the process.

For these simulations the uniform density profiles should have ideally been loaded with their respective rigid rotor angular velocities of equilibrium. However loading the particles with zero velocities (frozen load) gave exactly the same results because the very low value of f_b makes the dynamics essentially Guiding-centre-drift motion. Being almost devoid of inertia in this limit the plasma instantaneously adjusts to the exact guiding-centre drift velocity required for maintaining balance of radial forces, as soon as the simulation starts irrespective of what rotation velocity it might be loaded with.

Benchmark with pure electron plasmas distributed over the entire confineable Brilllouin ration spectrum

In these numerical experiments step density profiles of electron plasma in both slow mode and fast mode of the cold rigid-rotor equilibrium were simulated. A set of step-densities spanning over the entire range of f_b (i.e. $0 < f_b < 1$) and loaded with only their respective equilibrium angular velocities, ω_{re}^- or ω_{re}^+ were simulated for $3779\,T_{ce}$. The rigid rotor frequencies obtained form simulation were then compared with corresponding analytical values as shown in Fig. 2.7.

Step density profiles of radius, $r_p = 0.3\,R_W$ loaded in the fast mode and slow mode of rigid rotor equilibrium maintain their equilibrium rotation for the entire duration of the simulation ($= 3779\,T_{ce}$). Fourier analysing the $x(t)$ and $y(t)$ co-ordinates of three tracer particles located at radii

(a)

(b)

(c)
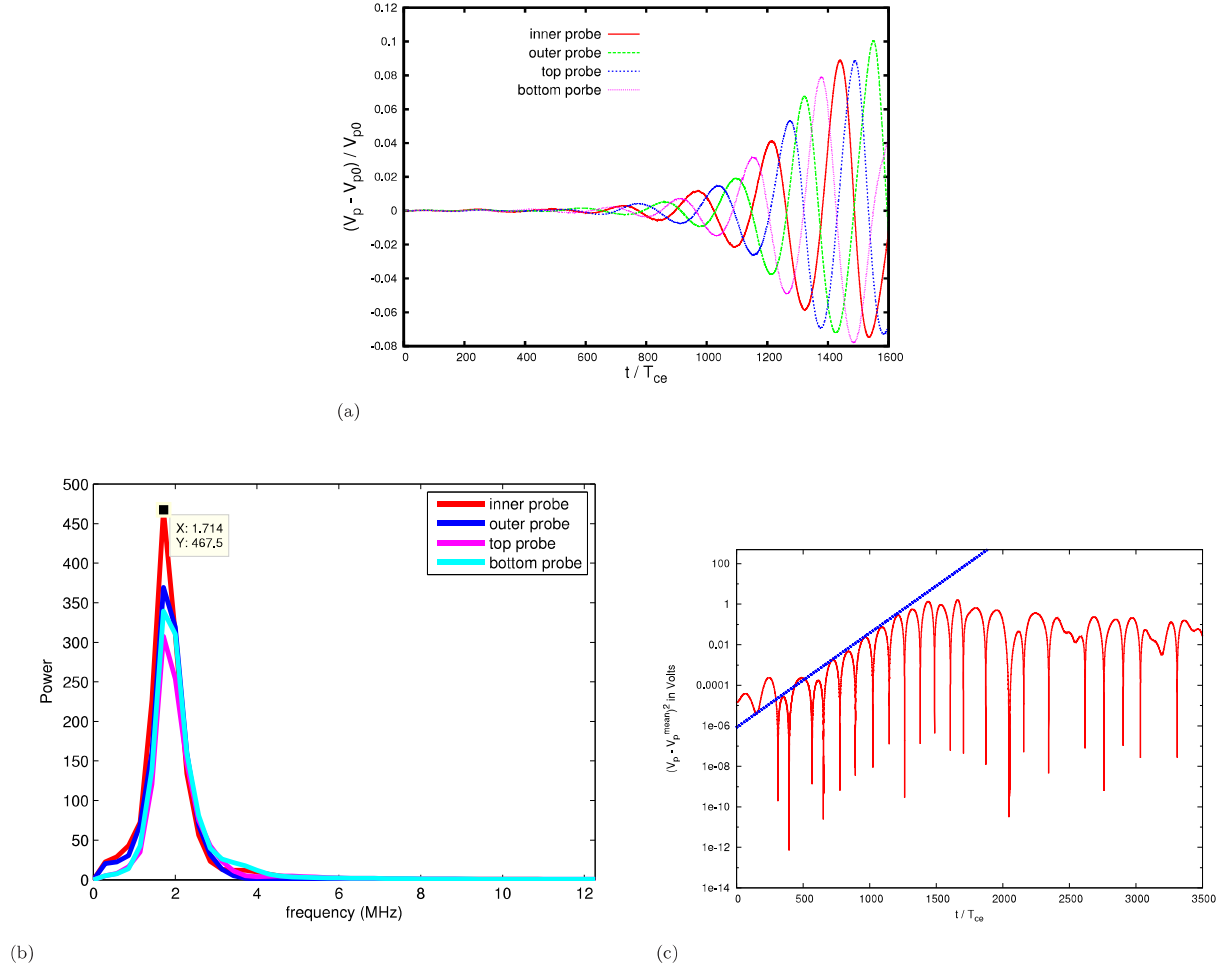
Figure 2.5: Analysis of the Potential probes' reading for the simulation of the $l = 3$ Diocotron mode: (a) Truncated readings of the four potential probes for the 3rd Diocotron mode simulation. (b) Fourier spectrum obtained from the truncated readings of the potential probes for the 3rd Diocotron mode simulation. (c) Logscaled plot of of the function $(V_p - V_p^{mean})^2$ against time, normalised by T_{ce}. An exponential envelope is fitted on the curve to estimate growth rate of the 3rd Diocotron mode.
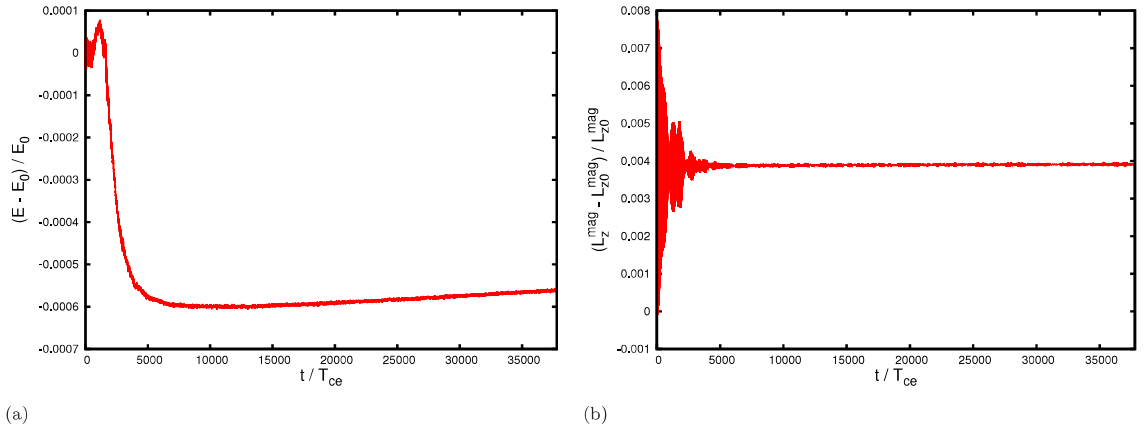
Figure 2.6: Energy and Magnetic component of the angular momentum for the simulation of the $l = 3$ Diocotron mode:(a) E is the total energy, and E_0, it's initial value for the 3rd Diocotron mode simulation. The fractional deviation of E from E_0 is plotted against time which is normalized by T_{ce}. (b) L_z^{mag} is the magnetic angular momentum, and L_{z0}^{mag}, it's initial value for the 3rd Diocotron mode simulation. The fractional deviation of L_z^{mag} from L_{z0}^{mag} is plotted against time which is normalized by T_{ce}

$0.29\,R_w$, $0.25\,R_w$, and $0.18\,R_w$, we obtained the rotation angular frequency, ω_{rot} of the profile. Ideally for this particular experiment, the potential probes are supposed to record only a fixed dc-potential but because of small inherent azimuthal asymmetry in numerical loading of the profile, the potential probes also capture the rotation as a very small ac component which is advantage because the potential probes' signals can also be Fourier analysed to double check the rotation frequency in the simulations. The frequencies obtained from both the above diagnostics agree with each other and with theoretical values (Fig. 2.7).

For these rigid rotations E, L_z, L_z^{mag} are all conserved quantities as seen in Fig. 2.8. As the code was written using cartesian co-ordinate system, incorporating a running calculation of the kinetic part of L_z increases the runtime of simulations by a large margin. For this reason we have avoided calculating the the kinetic angular momentum here.

Benchamrking simulations of the ion resonance instability

Experiments 1 to 4 in Table 2.2 constitute the set of benchmarking experiments on ion resonance (two-stream) instability. In this set the loading parameters f_b, m_i/m_e, and r_p/R_w are fixed at the values of 0.02, 1836, and 0.5 respectively while the fractional neutralization, f takes increasing values in the range 0.05 to 0.4, from Expt. 1 to 7. All experiments in this set are simulated till $\tau \approx 22674$.

A sample set of snapshot of the linear phase of an ion resonance instability is shown in Fig. 2.9 of the ion resonance instability. The linear phase analysis of the ion resonance instability is performed with the help of the potential probes (Fig. 2.10) which can pick up the frequencies of the excited Diocotron modes in the system. A FFT performed on the potential probes' signal in the linear phase gives the individual frequencies, ω_s of the linearly growing Diocotron modes in the system (Column 9 of Table 2.2). A measure of an effective growth rate, α_s^{eff} (Column 11 of Table 1) due to all growing

(a)   (b)
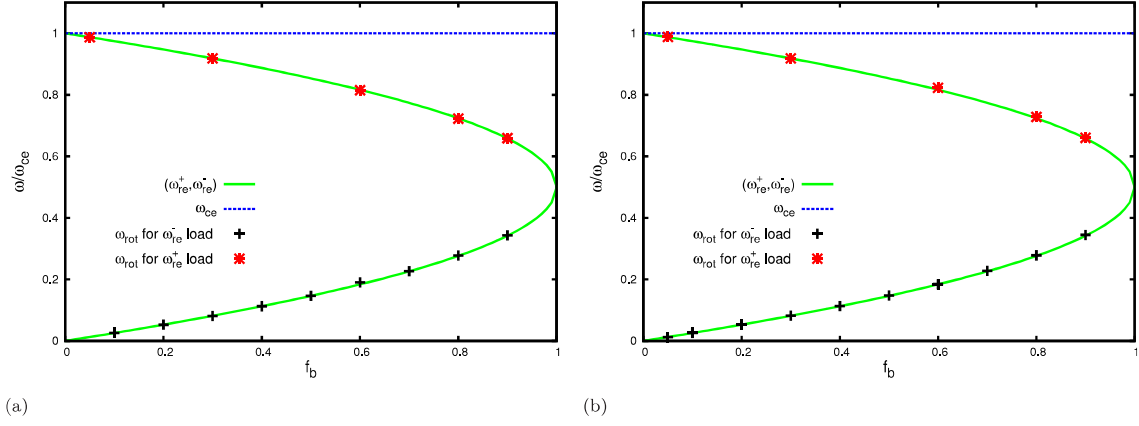
Figure 2.7: Equilibrium rigid rotation frequencies, ω_{rot}, of step density profiles obtained through FFT of (a) the x and y coordinate trace of 3 pseudo particles, and (b) the four potential probes' signals, are plotted as a function of f_b along with the analytical ω_{re}^+, ω_{re}^-, and ω_{ce} values for the f_b. All frequencies have been normalised by ω_{ce}.

(a)   (b)

(c)   (d)
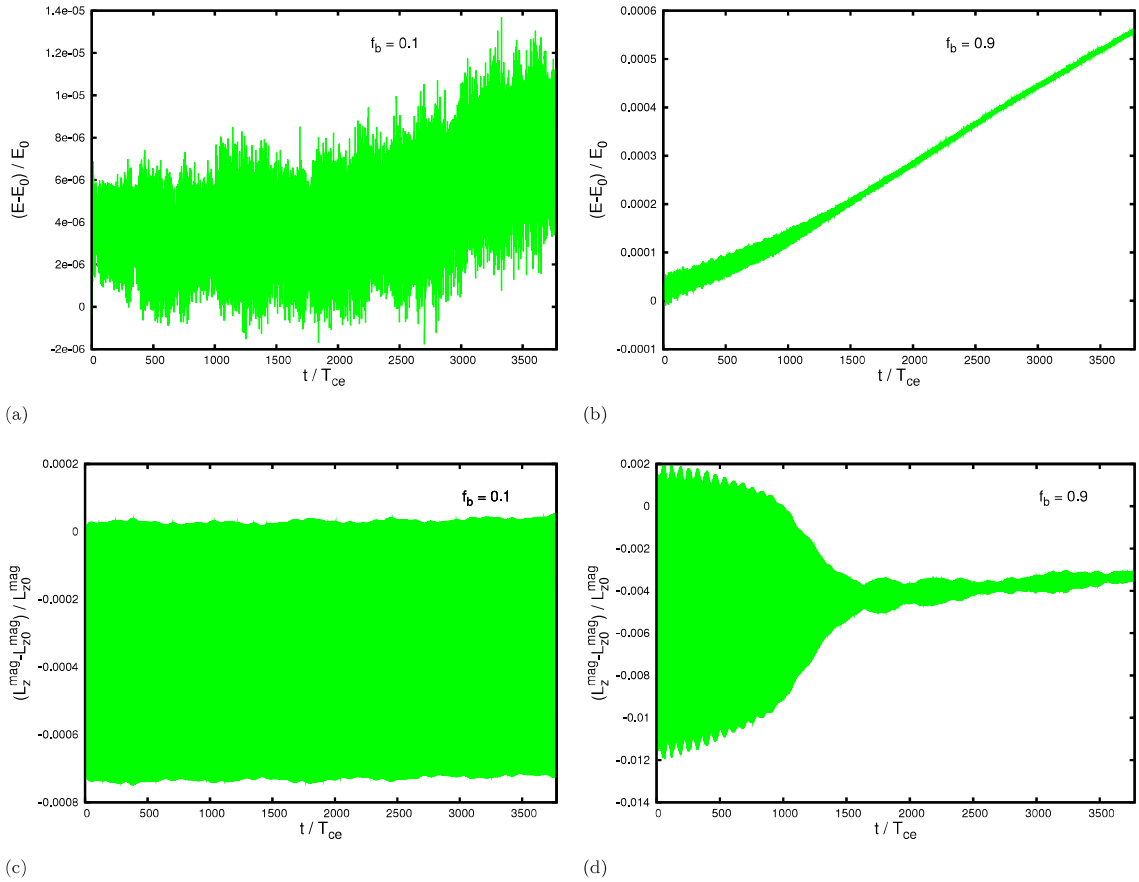
Figure 2.8: Energy conservation for step density profile of (a) $f_b = 0.1$ and (b) $f_b = 0.9$ in slow rigid rotor mode is shown. E is the total energy and, E_0 it's initial value. Magnetic angular momentum conservation for step density profile of (c) $f_b = 0.1$ and (d) $f_b = 0.9$ in slow rigid rotor mode is also shown. L_z^{mag} is the magnetic angular momentum and L_{z0}^{mag} is it's initial value.

Table 2.2: Results from different cases of equilibrium loading: The effective growth rate, α_s^{eff} for the combination of excited Diocotron modes, and the frequencies ω_s of each mode, are obtained from analysis of the potential probes' signal in the linear growth phase. These values are tabulated along with the theoretical growth rates, α_a and frequencies, ω_a of the Diocotron modes. Here l_a represents the theoretically predicted mode number of excited modes. The equilibrium loading parameters for each experiment of column 1 are tabulated in columns 2 to 6.

Expt.	f	F	(m_i/m_e)	r_p/R_w	ω_{re},ω_{ri}	l_a	$\omega_a(rad/sec)^a$	$\omega_s(rad/sec)$	$\alpha_a(rad/sec)^b$	$\alpha_s^{eff}(rad/sec)$
1	0.05	0.019	1836.0	0.5	$\omega_{re}^-,\omega_{ri}^-$	1	3.505×10^6	3.491×10^6	0.746×10^6	0.700×10^6
2	0.15	0.017	1836.0	0.5	$\omega_{re}^-,\omega_{ri}^-$	1	2.827×10^6	2.792×10^6	0.947×10^6	0.96×10^6
3	0.3	0.014	1836.0	0.5	$\omega_{re}^-,\omega_{ri}^-$	1	1.894×10^6	imperceptible	1.308×10^6	
						2	6.597×10^6	6.283×10^6	2.540×10^6	2.100×10^6
4	0.4	0.012	1836.0	0.5	$\omega_{re}^-,\omega_{ri}^-$	1	1.705×10^6	imperceptible	1.231×10^6	
						2	5.680×10^6	5.026×10^6	2.924×10^6	
						3	10.053×10^6	10.050×10^6	2.924×10^6	2.215×10^6

[a]Estimated from Fig. 8b and 9b of Ref. 3
[b]Estimated from Fig. 8a and 9a of Ref. 3

(a) $\tau = 0.0$ **(b)** $\tau = 1133.696$ **(c)** $\tau = 1228.170$ **(d)** $\tau = 1322.645$

Figure 2.9: Snapshots of the initial linear phase of an initial unstable equilibrium that excites a dominant second Diocotron mode in the profile (3rd experiment in Table 2.2). Ions in green are plotted on top of the electrons in red. snapshots of the entire simulation, extending into the nonlinear phase will be shown in a later chapter. Below each snap, the time elapsed is mentioned in normalised units of electron cyclotron time, *i.e.* $\tau = t/T_{ce}$.

modes in the linear phase is obtained by fitting an exponential envelope on the linear growth phase of one probe's signal (Fig. 2.10). Wherever analytical values of excited mode frequencies and their growth rates are available, these values (columns 7,8, and 10 of Table 2.2) have been compared with the corresponding values obtained from simulation. It should be noted however that the analytical values of the growth rates are for individual modes whereas the growth rate obtained from the probe signal is an effective value for all growing modes in the system. It is interesting that for cases where there are multiple modes excited the value of the effective growth rate comes out to be close to the average value of individual analytical growth rates of the excited modes (as in Expt. 3 and 4 of Table 2.2). For experiments 3 and 4 of Table 2.2 the frequencies of the slowest growing modes in the system are not picked up by the probe in the short linear phase. The match of the linear phases frequencies, and growth rates with corresponding linear analytical values in Table 2.2 serve as the third benchmark of the code.

Convergence tests by changinng simulation parameters Scaling studies were also performed by repeating selected experiments from the above three sets with i) doubled pseudo particle representation on the same grid and ii) doubled pseudo-particle representation on a finer 130×130 grid. The results of all scaling study simulations, matched well with the corresponding benchmarking experiment, thus demonstrating that the PIC parameters chosen for our simulations give accurate results, devoid of numerical artefacts.

2.2 The 2D3v PIC-with-MCC code PEC2PIC-3MCC

In non-neutral plasma experiments charged partciles in the trapped plasma can undergo collisions with residual neutrals in the trap at its operating pressure [20], or with externally injected neutrals within the trap vacuum [50]. Such charge-neutral collisions can, in turn, influence the dynamics of the trapped plasma in different ways. For example a trapped electron plasma can ionize the background neutrals in the trap, and thereby get destabilized through the process of ion resonance instability [20, 50]. In order to investigate the role of charge-neutral collisions on the dynamics of

(a)

(b)

(c)

(d)
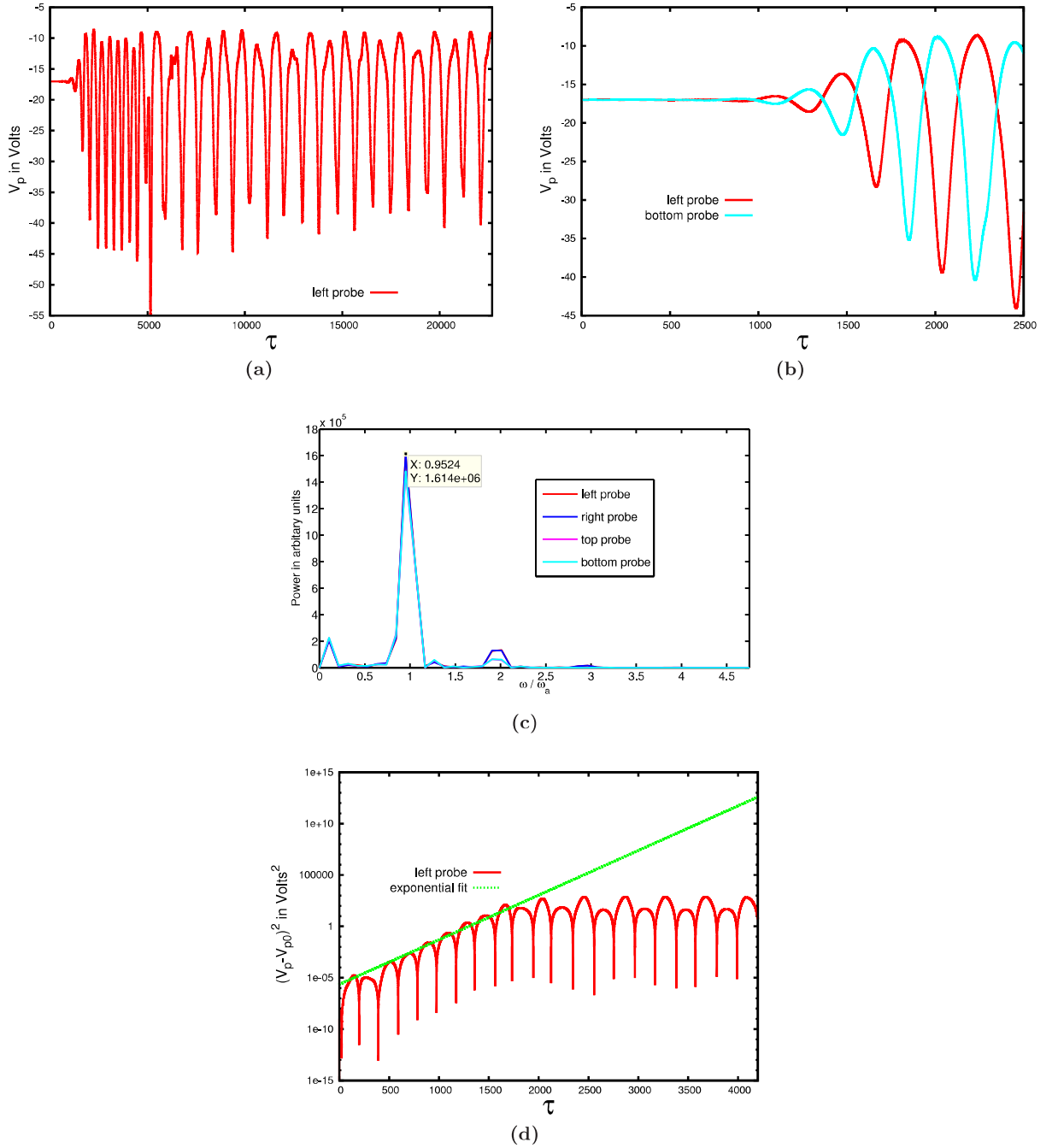
Figure 2.10: Potential-probe signal analysis for Expt. 3: (a) V_p is electrostatic potential recorded by innermost probe. Normalized time, τ is in units of electron cyclotron time, *i.e.* $\tau = t/T_{ce}$. (b) is a zoomed in plot of the signals of all the four probes in the initial linear growth stage. This linear growth stage is analysed to measure the Diocotron frequency ω_s and the effective growth rate α_{eff} shown in Table I. (c) is a FFT plot of the readings of (b) used to determine ω_s. Here the x-axis is the frequency in MHz and the y-axis is the power factor in arbitrary units. (d) is an exponential fit on the linear growth phase readings of the inner probe used to measure α_{eff}. V_{p0} is the initial probe reading. The y-axis is in log scale while time is in linear scale.

the plasma through simulation, the 2D PIC code, PEC2PIC was upgraded to a 2D3v PIC code with Monte-Carlo-Collisions (MCC), named PEC2PIC-3MCC, which is short for (Open-mp Parallelized Electrostatic Cartesian 2d Particle-In-Cell code with 3d Monte-Carlo-Collisions). PEC2PIC-3MCC retains all features of PEC2PIC, and its additional feautrea are introduced explained below. For convenience of describing the new numerical features of the upgraded code, the computational particles of simulation will be explicitly referred to as pseudo-electrons/ions in the rest of this Section instead of the usual practice of loosely calling them electrons/ions.

2.2.1 Giving the pseudo-electrons an axial velocity component perpendicular to the 2D PIC plane

In addition to the 2D Cartesian components of velocity the pseudo-electrons now have a 3rd velocity component representing their axial velocities. A common fixed magnitude of this component is initially given to all pseudo-electrons. The axially up or down direction for this component is selected randomly using a pseudo random number generator. The axial velocity does not get modified by the 2D PIC dynamics of the pseudo-electron. It can get modified only when the pseudo-electron is scattered by a collisional event. Thus the extra axial component, with a suitable choice of magnitude, will have an effect on the collisional dynamics of the pseudo-electrons in simulation, very similar to that of the axial bouncing of electrons between electrostatic end plugs [18] in cylindrical trap experiments.

2.2.2 The MCC procedure

The MCC is a technique of making computational particles undergoing guided motion in a simulation collide at suitable intervals (collision time step) with background neutrals (Neutral Argon in PEC2PIC-3MCC) that is not represented in any form in the simulation [51]. The method is useful when we are interested only in the effect (through collisions) of the latter on the former and not vice versa. To set up the MCC within the framework of a PIC code, the computational particles (pseudo electrons/ pseudo ions) of the simulation have to be treated as real particles (electrons/ions) inside the MCC algorithm [52]. This implies that mass of a pseudo particle entering the MCC routine gets divided by its representation number. MCC can be implemented using a pseudo random number generator if the collision cross-section of the charge-neutral collisions is available in analytical or numerical form as a function of the real particle's kinetic energy [53]. Taking the average kinetic energy of a particle (particle here being a pseudo-electron/ion represented as an electron/ion by scaling down its mass) in the collision time step, its collision probability in that interval is determined from the available analytical/numerical collision cross-section. Then the pseudo random number generator churns out a pseudo random number that decides whether the particle undergoes a collision or not based on its collision probability (the Monte-Carlo method). If there are more than one kind of collision possible between the particle and the background then the generated random number can also decide between different possible types of collision and the possibility of no collision for the particle [54]. Of course the probability of each type of collision in the collision time step should be available [53].

If the fate of the particle is found to be no collision then its velocity components are left untouched else the code proceeds to the next step of the MCC which is to execute the selected collision type for the particle. In its present version PEC2PIC-3MCC is capable of simulating 3 types of $e^- - Ar$ collisions viz, i) elastic, ii) first level excitation (most probable among different levels of $e^- - Ar$ excitation collisions), iii) and single ionization (most probable among different degrees of $e^- - Ar$ ionization collisions). It can also simulate 2 types of $Ar^+ - Ar$ collisions viz, iv) elastic, v) and charge exchange. The process of execution of each of these 5 types of charge-neutral collisions will be discussed later in this section. Presently the MCC routine in PEC2PIC-3MCC runs serially at every collision time interval, Δt_c.

2.2.3 The collision time interval

The interval of time representing the collision step is a critical parameter which determines how closely and how efficiently the MCC simulates the collisional interaction of particles with the background. The first criterion the collision time step should satisfy is that its value should be so small that possibility of simulation particles colliding more than once with the background matter in this interval is practically removed all through the simulation [51]. Otherwise the MCC routine will overlook possible collisions leading to divergence of the simulation from a real experiment. Now for a charged particle the net probability of one collisions is the sum of the probabilities of each type of collisions it can participate in with the background. Given a representative sample velocity distribution of pseudo electrons/ions for the simulation time period, it is possible to determine a maximum probability of single collision of the electron/ion from within this representative sample velocity distribution. If this maximum probability of single collision for the electrons/ions remains below the value 0.095 for the chosen value of Δt_c, then the first criterion for Δt_c is satisfied [51].

At the same time one should avoid diminishing the size of the collision time step beyond the point at which average (over particles) probability of collision in the interval becomes less than $1/N$, where N is the size of the colliding pseudo-particle population. This is because such a choice will result in too many executions of the MCC routine in the simulation period with zero or very few pseudo particles actually colliding in each execution. Hence it will bring down the speed of execution of the PIC-with-MCC code. However improving efficiency of the MCC by increasing size of the collision time step should only be attempted as long as the primary criterion (related to accuracy of simulation) is satisfied for all pseudo particles.

In our simulations the pseudo electrons are loaded in rigid rotor equilibrium with a fixed angular velocity and a common fixed magnitude of the axial velocity component. Hence a pseudo electron lying at the half-radius of the cylindrical, uniform density electron cloud will have the mean speed and the average collision cross section for electrons in the cloud. Hence in order to ensure that the first criterion is satisfied for our chosen collision time step we checked that the collision probability of the pseudo electrons at half-radius of the cloud is well below the 0.095 limit [51]. This automatically also satisfies the first criterion of the collision time step for $Ar^+ - Ar$ collisions as probability of an

$Ar^+ - Ar$ collision in the collision time step is smaller than the probability of an $e^- - Ar$ collision. The Ar^+ ions are themselves generated in course of the simulation from $e^- - Ar$ ionization collisions. Keeping the first criterion satisfied, the size of the collision time step is extended so that on a average a fraction of ≈ 0.001 from the total pseudo electron population of 87834 collides in every collision step, thus satisfying the second criterion for $e^- - Ar$ collisions.

2.2.4 Simulated collision types

Electron-Argon Collisions

- **Elastic Collision:** If the fate of the pseduo electron happens to be an elastic collision, then using a set of numerical formulas relying on pseudo random numbers the scattered speed and direction of the particle from the collision is determined [55, 56]. These formulas are fed with the incident kinetic energy of the colliding particle and also the fixed temperature and pressure of the background gas to produce the required outputs. In the MCC routine of PEC2PIC-3MCC, the set of formulas for elastic collision execution are very realistic. They implement the change in kinetic energy of the particle as a result of the elastic collision as well as the natural anisotropy of the scattering with respect to the incident direction of the particle. The scattering angle is determined from a very accurate formula for differential scattering cross section introduced in the year 2002 [56]. This formula is actually a correction on the differential scattering cross section formula that had been in use earlier [51, 55].

- **First level excitation collision:** If on the other hand, the collision happens to be a first excitation of the background (Ar atom), then the MCC follows a two step algorithm to simulate the collision. First the kinetic energy of the particle (pseudo electron with mass scaled down to electron mass) is reduced by an amount equal to the first excitation energy (= 11.55 eV for Ar atom) [51]. Next the particle with reduced velocity goes through an elastic scattering procedure as explained above. In effect the first elevel excitation collision is the same as elastic collision. Both produce elastic relaxation of the electron cloud. Note that in MCC, the effect on the neutral is not of interest, unless it gets ionized and becomes part of the plasma.

- **single ionization collision:** If an electron with kinetic energy greater than the first ionization energy of $15.76eV$, happens to get selected for an ionization collision with a neutral, the implementation of the collision event is carried out in the following steps.

  First we deal with the colliding electron and secondary electron that is generated by the collision. $15.76eV$ of single ionization energy is subtracted form the kinetic energy of the colliding electron, and a random number based formula divides the remaining kinetic energy between the primary and secondary electron [51]. The redistributed kinetic energies between the primary, and secondary electron serve as incident kinetic energies for their elastic scattering by the colliding neutral. Hence the new kinetic energies of the two electrons are independently fed as inputs into

the elastic scattering (by neutral atom) algorithm [32]. For the elastic scattering the incident direction of the secondary electron assumed to be same as that of the primary electron. The elastic collision algorithm operating independently upon the parent, and the progeny electron, scatters them and also reduces their incident kinetic energies (inputs in the elastic collision algorithm) by very small fractions (for example see kinetic energy of elastically colliding electrons before and after collision in Table II). The two electrons are then updated with their scattered velocities, at the collision point *i.e.* at last updated location of the colliding electron pseudo particle on the PIC grid, before it entered the MCC routine.

Next, with the help of random numbers the velocity of the collision generated ion has to be numerically extracted from the 3D velocity distribution function of the background Ar atoms [57]. In the simulations of Sec III the Ar^+ pseudo particles have a representation number that is 0.25 times the representation number of the e^- pseudo particles. This helps in adequate representation of the less dense ions in the PIC simulations. Now each e^- pseudo particle has a 4 times greater representation value than each Ar^+ pseudo particles, and each e^- pseudo particle is also scaled down to a real electron for an $e^- - Ar$ ionization collision inside the MCC. Hence an Ar^+ pseudo particle will have to scaled down to $(1/4)^{th}$ of a real Ar^+ ion for the same $e^- - Ar$ ionization collision. This implies that 4 such $(1/4)^{th}$ Ar^+ ion (Ar^+ pseudo particles scaled down to $(1/4)^{th}$ Ar^+ ion) are to be generated in every $e^- - Ar$ ionization collision to represent generation of 1 Ar^+ ion. This is done simply by generating 4 velocities by numerical extraction from the 3D velocity distribution of the Ar atoms [57], and assigning these velocities to the 4 new $(1/4)^{th}$ Ar^+ ions created at the collision point.

As noted earlier there were very small fractions of kinetic energy lost by the parent, and progeny electron, supposedly to the kinetic energy of the neutral, in their respective elastic scattering event with the latter. This extremely small amount of kinetic energy transfer is however, neglected while generating the initial kinetic energy of the ionized neutral, *i.e.* the four $(1/4)^{th}$ Argon ions in the collision event. In the very next simulation time step the generated Ar^+ pseudo particles will participate in PIC dynamics and gain much larger velocities from electrostatic forces, even more so because of the large self electric field of the non-neutral plasma. Hence we find that it is not necessary to be overtly cautious while assigning the initial thermal velocities of the ions.

After the MCC procedure is complete the masses of the computational particles are again scaled up to their original values for the regular PIC part of the code.

Argon ion (Ar^+) Argon collisions

The $Ar^+ - Ar$ collision types simulated by the MCC scheme are elastic, and charge exchange collisions. The technique used is that given by Vahedi and Surendra [51]. For $Ar^+ - Ar$ collisions each Ar^+ pseudo particle is scaled down in mass and charge to a real Argon ion. A formula based

on random number, and the most recently updated velocity of the Ar^+ ion is used to determine if it undergoes a collision and if so, which type of collision it is [32].

- **elastic collision:** Now if the Ar^+ ion is selected for an elastic collision with an Ar atom, then first of all the velocity of the colliding neutral Ar atom is extracted from the 3D velocity distribution of Ar atoms using random numbers [57]. Isotropic and uniform scattering is assumed for $Ar^+ - Ar$ elastic collisions [51]. The velocity of the Ar^+ ion is then transferred to the frame in which the the Ar atom is at rest. A set of random number based formulas determine the scattered kinetic energy and direction of the Ar^+ ion in this modified frame of reference. From there it is a matter of simple geometric consideration to determine the scattered velocity of the Ar^+ ion in the modified reference frame. The scattered velocity of the Ar^+ ion is then transferred back to the laboratory frame.

- **charge exchange collision:** If the Ar^+ happens to undergo a charge-exchange collisions with an Ar atom, the collision is implemented in the MCC scheme as follows. The velocity of the colliding Ar atom is first extracted from the 3D velocity distribution of Ar atoms using random numbers. Then the velocity of the Ar^+ ion is updated with the extracted velocity of the colliding Ar atom. This actually implies, replacing the Ar^+ ion losing it's charge in the charge exchange collision, with the newly ionized Ar atom, in the computational array for ions within the simulation code.

After passing out of the MCC routine the mass and charge of the Ar^+ ion is again scaled up by it's representation number so that it can participate as an Ar^+ pseudo particle in the PIC part of the code.

2.2.5   The MCC algorithm in short

The MCC routine in PEC2PIC-3MCC may be summarized by the following algorithm.

- Scale down the mass of the pseudo electron/ion to that of an electron/ion

- Now calculate the electron's/ion's kinetic energy

- Calculate the probability each type of collision and probability of no collision for that kinetic energy of the electron/ion

- Generate a pseudo random number to decide the fate of the particle

- For each type of collisions execute by the given procedures. For no collision leave the velocity components of the particle untouched

- Scale up the mass and charge of the particle and the any new particle/s generated by the collision to that pseudo particles for the regular PIC part of the code.

2.2.6 Validation of the correctness of the MCC routine of 2D3v PIC-with-MCC code

Set-up of the MCC Validation experiment:

To validate the stastical and mechanical correctness of the execution of 3 types of $e^- - Ar$ collisions and 5 types of $Ar^+ - Ar$ collisions, a numerical experiment has been set up as follows. Typical parameters found in experiments of cylindrical traps [20, 58] have been chosen, in particular, a wall radius, $R_w = 0.125\,m$, and axial magnetic field, $B_z = 0.03\,T$. A cylindrical (circular in 2D) pure electron cloud with a uniformly low Brillouin ratio, $f_b = 0.2076$, and a radial extent $r_p = 0.5 \times R_w$ is loaded symmetrically about the axis of the trap. The background Ar gas is maintained at a pressure, $P_{bg} = 2 \times 10^{-7}\,Torr$ [20, 58], and temperature, $T_{bg} = 300\,K$. The pure electron plasma is initially in its slow mode of the rigid rotor equilibrium [1, 34] in the trap, rotating with an angular frequency ω_{re}^-. In the axial direction the electrons are loaded with randomly up or down directed velocities with a common magnitude, $v_z = 1.02727 \times 10^7\,m/s$, which maintained the average collision cross section of the electrons at moderate values of $\sigma_e = 2.207 \times 10^{-20}\,m^2$, $\sigma_x = 2.741 \times 10^{-21}\,m^2$, $\sigma_i = 1.402 \times 10^{-20}\,m^2$, and $\sigma_t = 3.883 \times 10^{-20}\,m^2$, where σ_e, σ_x, and σ_i, are the elastic, first level excitation, and single ionization collision cross section for $e^- - Ar$ collision (see Fig. 3 of Vahedi and Surendra, 1994 [51]), and $\sigma_t = \sigma_e + \sigma_x + \sigma_i$, is the total collision cross section for $e^- - Ar$ collision.

The PIC simulation time step, $\delta t = 10^{-11}\,s$ is chosen much smaller than the cyclotron time period of electron, $T_{ce} = 1.191 \times 10^{-9}\,sec$, such that the code can well resolve the cyclotron motion of both the electrons, and the collision generated Argon ions. A common collision time step, $\Delta t_c = 6 \times 10^{-7}\,s$ is maintained for both $e^- - Ar$ and $Ar^+ - Ar$ collisions in the simulation. This value of Δt_c satisfies the required criteria for collision time step [32] for the numerical experiment.

PIC-parameters used in the simulations are 87834 pseudo particles initially representing the loaded electron cloud, on a 70×70 grid. $e^- - Ar$ collisions create an additional 35713 e^- pseudo particles and $35713 \times 4 = 142852$ Ar^+ pseudo particles in course of simulation. The mass of Ar atom and Ar^+ ion is taken as 72820.77 times the mass of an electron. The simulation is carried out till time, $t = 2.88 \times 10^{-4}\,s$ which is roughly $2.42 \times 10^5\,T_{ce}$.

MCC Validation results: Table 2.3 is a validation of the collision statistics for each of the 5 simulated types of collision in the experiment. As shown in Table I, this validation has been accomplished by matching the final collision count for the 5 types of collision at the end of the simulation, with corresponding theoretical expected values in the time-length of the simulation. To obtain the simulation record of the number of occurrences of each type of charge-neutral collision (column 3 of Table 2.3), we scaled up the raw counts of the 5 types of Monte-Carlo-Collision events at the end of the simulation, by a factor equal to the representation value of the charged species (pseudo electron/ion) involved in each type of collision [32]. This was done so that the collision statistics from the simulation (column 3 of Table 2.3) represent values for collisions between real electrons/ions and

Table 2.3: Collision statistics of Expt 1: The number of possible occurrences of each of the 5 types of charge-neutral collisions in course of the simulation have been theoretically estimated. These estimated values are compared here with corresponding collision counts obtained from the simulation. The 5 types of collisions simulated are **EL**astic, **EX**citation, and **IO**nization between electron-Argon atom ($e^- - Ar$) and **EL**astic and **C**harge **E**xchange between Argon ion and Argon atom ($Ar^+ - Ar$).

Collision type	Theoretical No. Occurrence	Recorded No. Occurrence
$e^- - Ar$ EL	7.422×10^{12}	7.742×10^{12}
$e^- - Ar$ EX	9.222×10^{11}	8.690×10^{11}
$e^- - Ar$ IO	4.716×10^{12}	4.532×10^{12}
$Ar^+ - Ar$ EL	9.872×10^{10}	7.740×10^{10}
$Ar^+ - Ar$ CE	7.966×10^{10}	6.675×10^{10}

neutrals, and hence are directly comparable to the theoretically expected number of occurrences of the 5 collision types in column 2 of Table 2.3 [32].

The recorded number of occurrences of the three types of $e^- - Ar$ collision simulated in the simulation, are in excellent agreement with corresponding theoretical estimates in Table 2.3. The theoretical estimates for the number of occurrences of each type of $e^- - Ar$ collision in the duration of the numerical experiment, are calculated using average collision cross sections for each of the 3 types of $e^- - Ar$ collisions, and a time-averaged trapped electron population from the simulation. The procedure for estimating average collisions cross-sections for $e^- - Ar$ collisions in the simulation is explained in detail in Sec V of [32]. To put it briefly, the average collision cross sections are calculated using a representative value for the 3D speed of electrons in the simulation. It is to be noted that the velocity component that contributes most to the magnitude of electron velocities in the simulation, are the large axial speeds of the electrons that initially have a common value. The axial speeds are not modified by the 2D PIC dynamics of the electron cloud, and are only updated when the pseudo electron collides with the background gas. So the larger contribution of the axial speed to the speed of electrons, and slower change of these axial electron speeds from their initial common value, in course of the simulation, make the initial average speed of electrons an ideal representative value for electron speeds throughout the simulation. The average collision cross-sections of the 3 types of $e^- - Ar$ collisions are now calculated from this representative speed of electrons [32]. Now, as will be seen later when this experiment is re-examined in detail in Chapter 6, the population of trapped electrons varies by a maximum of about 0.3 times it's initial value in the time-length of this simulation from ionization collisions and radial loss of electrons. This implies that the changing electron population should not bring about very drastic changes in collision-counts of the 3 types of $e^- - Ar$ collisions in progressive collisions time-steps. Hence the median value of electron population in the simulation time period can be used a good representative value for trapped electron population in the entire length of simulation. The theoretical collision counts for the three types of $e^- - Ar$ collisions are then calculated using

their respective average collision cross sections and the representative electron population. The slow change in the 3D speeds, and the population of trapped electrons in course of the simulation, are both contributory factors for the high accuracy in estimation of the theoretical $e^- - Ar$ collision counts.

As compared to $e^- - Ar$ collisions, the theoretical collision counts for the two types of $Ar^+ - Ar$ collisions, have greater degree of unavoidable error in their estimation. For instance there is obviously a large percentage change in the collision generated ion population in course of the simulation, because of its initial null value. Maximum ion population recorded in course of the simulation also 0.3 times the initial electron population. Moreover in contrast with the electrons, the ions do not have any one particular velocity component that contributes largely to their velocity magnitudes, and at the same time, also changes slowly from a common initial value. In fact the three components of ion velocities are initiated randomly from 3D $e^- - Ar$ ionization collisions. The velocity components in the PIC plane get updated at simulation time steps and collision time steps, while the axial velocity component gets updated only at collision time steps. To estimate the theoretical collision count for the two types of $Ar^+ - Ar$ collision we have used the median ion population in the simulation as the representative trapped ion population for the duration of the simulation. The median value of total kinetic energy of ions in the simulation was divided by the median value of the ion population in the simulation to estimate a representative kinetic energy of the ions, and thereby their representative speed, in the time-length of the simulation. Using the representative values for the ion speed and ion population in the experiment, the theoretical collision counts for the $Ar^+ - Ar$ collisions were estimates using the same technique as applied for the $e^- - Ar$ collisions [32]. Considering the error factors involved in estimating the theoretical collision counts for $Ar^+ - Ar$ collisions by this method, there is still reasonable agreement of the theoretical estimates with corresponding experimental $Ar^+ - Ar$ collision statistics.

Next, in Table 2.4 we have verified the correct implementation of collision mechanics for each of the 5 types of charge-neutral collisions simulated by the MCC scheme, in the MCC validation experiment. Table 2.4 basically demonstrates a random check of the pre-collision and post-collision velocities and kinetic energies of colliding pseudo particles. It can be seen from this table that for elastic collisions between electrons and Argon atoms a tiny fraction of the incident kinetic energy of the electron is lost to the Argon atom, and there is also a scattering of the electron. For first level excitation collisions between electrons and Argon atoms an excitation energy of $11.55\,eV$ is first deducted from the kinetic energy of the colliding electron, and then the electron undergoes a regular elastic collision process in the MCC scheme. The correct execution of the excitation collision mechanics can also be verified from Table 2.4. In the single ionization collisions between electrons and Argon atoms, an ionization energy of $15.76\,eV$ is first deducted from the kinetic energy of the colliding electron. Then the remaining kinetic energy is divided by a random number based formula between the parent and progeny electron, followed by independent elastic collisions of the parent and progeny electron. The correct execution of the single ionization collision procedure can also be worked out from the details of the ionization collision events, tabulated in Table 2.4. There are also 4 pseudo-ions generated with thermal velocities

Table 2.4: Collision dynamics of Expt 1: Cartesian velocity components and kinetic energies of random electrons and ions just before and just after their collision with a neutral atom are tabulated. The electrons/ions represented here are basically pseudo electrons/ions which have been scaled down in mass to that of an electron/ion inside the MCC routine. v_{x0}, v_{y0}, and v_{z0} are the three velocity components of the colliding electron/ion just before the collision, with v_{z0} being the axial velocity outside the PIC plane. v_{r1}, v_{y1}, and v_{z1} are the same velocity components just after the collision. ϵ_{k0} and ϵ_{k1} represent the kinetic energy of the electron/ion just before and just after the collision. The time of the collision, t_{col} and the collision type, CT are also tabulated. The simulated collision types are **EL**astic or **EX**citation or **IO**nization between electron-neutral ($e^- - Ar$) and **EL**astic or **C**harge **E**xchange between ion-neutral ($Ar^+ - Ar$).

$v_{x0}(m/s)$	$v_{y0}(m/s)$	$v_{z0}(m/s)$	$\epsilon_{k0}(eV)$	$t_{col}(\mu s)$	CT	$v_{x1}(m/s)$	$v_{y1}(m/s)$	$v_{z1}(m/s)$	$\epsilon_{k1}(eV)$
$e^- - Ar$									
−4235467.64925396	21135900.8099545	8495139.13664410	1526.11593103726	36.6	EL	−2906190.35215793	21038176.2849105	9261859.53146072	1526.11583873508
−4637681.88859874	6678316.25119301	−10272700.0000000	487.930236683854	108.6	EL	−6788463.28086423	5807139.51985400	−9582806.63167438	487.930007888424
20205480.9989267	4203619.54235750	−10272700.0000000	1510.84253489131	36.6	EX	20413956.1677387	3659081.93360819	−9863058.56220294	1499.29549779000
232936.068304277	−5464943.34633788	−10272700.0000000	385.054102409687	108.6	EX	−472408.285572328	−4524890.63129702	−10520827.7003468	373.504858606777
−4690966.20980994	−9183481.09289777	10272700.0000000	602.306552022837	36.6	IO^b	−6380732.71430728	−10320915.2940663	7638654.29947009	584.437271676916
						813231.577272733	98755.3815314820	−266914.287396589	2.11033857106242
−16711760.5695191	25964.1849942025	−10272700.0000000	1093.94882119745	108.6	IO^b	−15381436.2239788	−1255280.30993793	−11798182.2387060	1072.76824441914
						−78601.1211769516	1350743.35187685	276774.162029079	5.42206946944836
$Ar^+ - Ar$									
−3347.43062092832	−3505.81988283191	12.6287559118807	4.86409216254737	36.6	EL	−3520.39461181783	−2927.12229928271	956.645220357786	4.52876137153578
−10395.2970239912	−83512.6572417450	−11526.9700766424	1493.68127898971	108.6	EL	17794.9480617796	−61456.4187597471	23721.2669233844	963.917830846369
−75829.6443868395	69637.1105974454	506.918203640084	2194.31045496851	36.6	CE^c	−224.626564122239	−146.413981386944	119.943936796727	0.01786147630003
52994.5442052929	−75380.2259407936	−39.0835075897046	1757.68960531197	108.6	CE^c	200.796749119599	257.822408738941	−43.7309213239008	0.02250348239004

^{b} The additional row of v_{x1}, v_{y1}, v_{z1}, and ϵ_{k1} belong to the secondary electron pseudo particle (scaled down to an electron in the MCC procedure) released by the ionization process. Also (not shown in the table) 4 new ion-pseudo particles are created by the ionization.

^{c} The v_{x1}, v_{y1}, v_{z1}, and ϵ_{k1} actually belong to the neutral that got ionized by the charge exchange process. This implies that in the PIC code the charge exchange resulted in a new ion pseudo particle (scaled down to an ion within the MCC procedure) that replaced the colliding ion pseudo particle.

in the ionization collision event which are not tabulated in Table 2.4. A general point to be noted about the tabulated $e^- - Ar$ collisions is that, some of the electrons in the table share a common magnitude of $1.02727 \times 10^7 \, m/s$ in their pre collisional axial velocities, v_{z0}. This common magnitude is actually the initial common axial speeds of electrons, indicating that these particular electrons are undergoing their first collision in the tabulated collision event.

In elastic collisions between the equally heavy Argon ions and Argon atoms there can be a significant percentage of the ion kinetic energy transferred to the thermally moving atom. There is also a scattering of the colliding Argon ion. The charge exchange collision between Argon ions and Argon atoms is implemented by replacing the velocity and kinetic energy of the ion that loses it's charge by the thermal velocity and kinetic energy of the neutral that is ionized. All these aspects of the elastic and charge exchange $Ar^+ - Ar$ collisions can be verified from their respective examples from the MCC Validation Experiment that are tabulated in Table 2.4.

2.3 The 1D PIC code, PEC1PIC

As this code is desgined to simulate compression-expansion cylces in quasi-neutral plasma [37], the set up of the code has two mechanical perfectly reflecting walls at $x = 0$ and at $x = L(t)$, where $L(t)$ is the length of the 1D plasma. The wall at $x = 0$ is fixed and the other wall at $x = L(t)$ is movable to produce the effects of compression and expansion. The instantaneous length L(t) of the bound plasma is divided into 100 cells for the Particle-in-cell motion in that time step. The time step chosen is $\Delta t = 10^{-14} \, s$. In the simulations performed with the PEC1PIC the 1D quasineutral plasma is mechanically compressed by means of the moving wall from initial length $L = 0.2 \, m$ to $L = 0.017 \, m$. The minimum cell length encountered by the particle in the course of simulation is $\Delta x = 0.017/100 = 1.7 \times 10^{-4} \, m$. The velocity required by the particle to cover Δx in one time step is $2 \times 10^8 \, m/s$. In this simulation the velocity of all particles remain well below this magnitude ensuring thereby that at no stage of the simulation does a particle cover distance $\geq \Delta x$ in one time step . Thus the basic requirement of the PIC simulation is met. The boundary condition on the electrostatic potential is that it goes to zero away from quasi neutral plasma. In the code this condition is met by having a set of 100 extra cells on the outer sides of the two walls. These vacant cells have the same length as the bounded cells in that time step. The first and last node of the full set of 300 cells (100 bounded and 200 vacant) are grounded and serve as the actual electrostatic boundaries for the potential solver of our code. The simulation is carried out with 5×10^5 electrons and 5×10^5 ions (pseudo particles) while the number of pseudo particles per cells is 5000 which is more than adequate for the accuracy of our PIC simulation.

This code was bench marked with numerical simulation results of Schmit et al [59] for the evolution of 1D bump in tail instability in a similar reflecting wall system. In the benchmarking experiment the evolution of a bump in tail instability was simulated for the parameters of Schmit et al [59]. The evolution of the instability in the benchmarking experiment, wherein electron hole pairs form and

merge resulting in a final state with just one BGK mode, is in very good agreement to the results of Schmit et al [59].

3

Pure Electron Plasma Numerical EXperiments (PEPNEX)

Most cylindrical trap experiments on pure electron plasma are performed at a low ratio of the mean electron number density, n_e to the applied axial magnetic field, B_z, or for values of Brillouin fraction, $f_b \leq 0.1$ where [1] $f_b = (2m_e n_e)/(\epsilon_0 B_z{}^2)$, m_e is mass of an electron, and ϵ_0 is permittivity of free space. In this low f_b limit, the relative magnitudes of terms in the equations of motion of the electron fluid become such that, terms containing the mass of electron can be neglected, resulting in a set of equations that make the fluid massless and hence devoid of inertia and cyclotron motion [1]. Under this approximation known as the Guiding Centre Drift (GCD) approximation, the set of equations of motion resemble that of an inviscid, incompressible, 2D Euler fluid, and an exact one-to-one mapping can be done between corresponding terms in the two sets of equations. In the past, this morphological similarity between (3.5) and (3.6) has been extensively exploited in large number of studies that are equally applicable to both low density electron plasma as well as inviscid, incompressible, Euler fluids under different terminologies. For example, theories on Diocotron modes [1, 15], Continuum and quasi-discrete Diocotron modes [60], and studies on electron plasma vortex merging and vortex crystals [3, 4] all reflect this dual application.

At the high end of the Brillouin ratio spectrum, where inertia becomes important, there has been comparatively less work. In 1995, the stability of resonant azimuthal modes for step-like and smooth density profiles at high f_b was addressed analytically by Bhattacharyya [61]. In 1997 Goswami et al have analytically shown the existence of a stationary (in the laboratory frame) and infinitely degenerate azimuthal mode in a non-neutral plasma column using the mass-included model for arbitrary Brillouin ratio [62]. There have also been some experiments performed in the high density limit. These include studies on the modes of a spheroidal ion plasma confined in a quadrupole Penning trap [29], and Penning Fusion experiment (PFX) [63, 64] in which electron plasma of densities beyond the Brillouin density limit (*i.e* the maximum cylindrically confineable, Brillouin ratio, $f_b = 1.0$ [1]) is successfully confined in spherical potential well. Also, irrespective of the f_b value, the effect of mass becomes naturally important in describing the thermodynamics of real collisional systems [1], and the transport

caused by the thermal properties [19, 65]. In 2013, there was a numerical experiment using mass-included dynamics to describe axisymmetric, and fully kinetic, Bernstein modes of an infinite length non-neutral plasma of arbitrary f_b [17]. The initial radial density profiles of the electron plasma used in these simulations were thermally equilibrated profiles at a given temperature and simulation code was a 1D PIC code [17].

PEPNEX1 (Pure Electron Plasma Numerical EXperiments 1) are a set of simulations performed with PEC2PIC that investigate the radial breathing modes exhibited by intially cold (through this thesis the term "cold" will mean "zero temperature") step density profiles of pure electron plasma, that are not in mechanical equlibrium *i.e.* the balance of the inward and outward radial forces on these profiles are systematically disturbed [34, 35]. The radial breathing modes that follow are an effect driven by inertia of the plasma [34, 35]. As PEPNEX1 simulations are 2D, the plasma is free to exchange momentum and kinetic energy between its radial and azimuthal degrees of freedom unlike in Ref. [17]. The numerical experiments reveal that the radial breathing mode becomes negligibly weak in amplitude, in the limit where the plasma can be described by a guiding-centre-drift approximation *i.e.* for low values of f_b ($f_b < 0.2$). For high f_b values the profile relaxation mediated by the radial breathing modes exhibits interesting nonlinear dynamics such as spontaneous hollow density structure formation, excitation of poloidal modes, etc., leading finally to a monotonically falling density profile in equilibrium [34, 35]. So PEPNEX1 venture beyond GCD approximated low f_b electron plasmas, into the realm of inertia influenced dynamics at high f_b.

In PEPNEX2 (Pure Electron Plasma Numerical EXperiments 2) electron clouds in stable $l = 1$ (l being the Diocotron mode number) mode orbits of very small radius we inititated, and PEC2PIC-3MCC with ionziation collisions turned off was utilzed to simulate non-ionizing elastic and excitation collisions of these electrons with a neutral background in course of the simulations [32]. The objective of this set of numerical experiments was to test if such non-ionizing collisions can destabilize the stable motion of the pure electron clouds. It had been theorized by Davidson and Chao [36] that elastic collisions between electrons and background neutrals will not only cause relaxation of the electron cloud's profile but can also destabilize any small-amplitude, stable $l = 1$ mode azimuthal asymmetry present in the cloud into a growing $l = 1$ mode by virtue of their capability of extracting potential energy from the cloud. Contrary to these theoretical predictions, our simulations [32] show that such non-ionizing collisions between electrons and background neutrals can not by themselves destabilize a stable configuration of the cloud. From PEPNEX2 it is now understood that this has got to do with the manner in which potentially energy of the cloud gets reduced by such collisions. A descriptive comparison of the potential energy extraction process between non-ionizing collisions and a resistive wall instability [66, 67] that is known to be capable of destabilizing the cloud, will be made to make this point clear.

PEPNEX3 (Pure Electron Plasma Numerical EXperiments 3) technically are not simulations performed with pure electron plasma. These are 1D simulations of quasi-neutral plasma performed with PEC1PIC [37]. The reason for classifying these 1D numerical experiments as pure electron plasma

experiments is that the results of these numerical experiments, among other quasi-neutral plasma devices, also potentially find direct application in single species plasma experiments. Hence in keeping with the nonneutral plasma topic of thesis thesis, these experiments have aptly grouped with the other PEPNEX.

In PEPNEX3 a new way of achieving significant heating of plasmas without driving them far away from thermodynamic equilibrium was demonstrated[37]. The proposed adiabatic heating scheme works by taking the plasma through a closed thermodynamic cycle comprising of a quasi-static compression, followed by constrained non-quasi-static expansion of the plasma back to it's initial dimensions [37]. While this kind of heating scheme is primarily targeted for fusion-grade plasmas in Tokamaks where the compression-expansion cycle can be achieved by varying the external magnetic field of the Tokamak, the scheme can also be extended to cylindrical non-neutral plasma traps (which is the subject of interest of the thesis), where it can yield axial heating of trapped single species by means of controlled variation of the electrostatic potential of the axial end-plugs of the trap. The return of the plasma to a thermodynamic equilibrium state at a higher temperature is the motivation for applying the scheme to such experiments.

To prove that this plasma heating scheme is viable, PEC1PIC was used to perform 1D PIC simulations of quasineutral plasma, in which the propsed cycle was executed mechanically (as opposed to magnetically in Tokamaks, and electrostatically in nonneutral plasma traps) with rigid reflecting walls [37].

3.1 PEPNEX1: Inertia driven radial breathing and nonlinear relaxation in cylindrically confined pure electron plasma

A concise theoretical background for numerical experiments, the numerical experimental setup, results of the simulations with coherent figures, and convergence tests with changed PIC parameters, are discussed in the subsections below.

3.1.1 Theoretical Background

Radial force balance equation of a fluid element, in a cold, collisionless electron plasma, magnetized in a cylindrical trap of infinite length, is given under the 2D, electrostatic approximation is given as [1]

$$\frac{m_e v_{e\theta}^2(r)}{r} - eE_r(r) - ev_{e\theta}(r)B_z = 0, \tag{3.1}$$

where the first term is the centrifugal force, the second term is the dispersing Electric field force, and the third term is the confining Lorentz force which balances the first two terms to achieve equilibrium. Here m_e and $-e$ are the electron mass and electron charge respectively, r and $v_{e\theta}$ are the radial location and azimuthal velocity of the fluid element, E_r is the radial electric field acting on the element, B_z is the applied uniform axial magnetic field. The quadratic equation (3.7), directly derived form equations

(3.2) by a change of co-ordinates, can be easily solved to obtain the equilibrium angular velocity of the fluid element, $\omega_{re}(r) = v_{e\theta}(r)/r$ as [1]

$$\omega_{re}(r) = \frac{1}{2}\omega_{ce}\left[1 \pm \left(1 - \frac{2\omega_{pe}^2(r)}{\omega_{ce}^2}\right)^{\frac{1}{2}}\right]. \tag{3.2}$$

Here $\omega_{pe}(r) = e^2 n_e(r)/\epsilon_0 m_e$ and $\omega_{ce} = eB_z/m_e$ are the electron plasma frequency, and cyclotron frequency respectively, n_e is the number density of the plasma, and ϵ_0 is the permittivity of free space. The quantity in the parenthesis, $2\omega_{pe}^2/\omega_{ce}^2 = f_b = (2m_e n_e)/(\epsilon_0 B_z{}^2)$, [1] measures the relative strength of the dispersing space charge force and the focusing magnetic force. Now, if the radial density profile is a step function of the form $n_e(r) = n_e$ for $r < r_p$ and and $n_e(r) = 0$ for $r > r_p$ (where $r_p < R_w$) then the r-dependencies in the solution are removed and it reduces to two rigid-rotor frequencies given by [1]

$$\omega_{re}^{\pm} = \frac{1}{2}\omega_{ce}\left[1 \pm \left(1 - \frac{2\omega_{pe}^2}{\omega_{ce}^2}\right)^{\frac{1}{2}}\right]. \tag{3.3}$$

The solutions ω_{re}^+ and ω_{re}^- can be termed as the fast rotor mode and slow rotor mode respectively.

In PEPNEX1 step density profiles of different f_b distributed over the entire confineable range, were initialized away form equilibrium by cold-loading them with the off-equibrium rigid rotation frequencies, i) zero (frozen load) and ii) ω_{ce} (cyclotron frequency load), and the evolution of the plasma towards a new equilibrium was studied with the help of several diagnostics. From Fig. 2.7 it can be seen that that the separation between the $\omega = \omega_{ce}$ line and the $\omega = \omega_{re}^+$ curve is the same as that between the the $\omega = 0$ axis and the $\omega = \omega_{re}^-$ curve. Hence it is intuitively clear that the frozen load and cyclotron frequency load for a given value f_b are equally removed the slow rigid rotor equilibrium and fast rigid rotor equilibrium, and so the comparisons can be made between the two loads.

3.1.2 Numerical Setup

PEPNEX1 were carried out for typical parameters found in experiments of cylindrical traps. [18], in particular, a wall radius, $R_w = 0.125 m$, and axial magneitc field, $B_z = 0.015 T$. The simulation time step, $\delta t = 10^{-11} sec$ is chosen much smaller than the cyclotron time period, $T_{ce} = 2.38 \times 10^{-9} sec$, such that the code can well resolve the cyclotron motion. PIC-parameters used in the simulations of sections IV and V are 87834 pseudo particles on a 70×70 grid. Convergence of simulation results have also been tested systematically by varying the grid size and total number of pseudo particles .

3.1.3 Off-equilibrium loading of the step density profiles

When the step density profiles are loaded with the non-equilibrium angular frequencies ω_{ce} and zero, and allowed to evolve till $t = 3779 T_{ce}$, the plasma profile is seen to evolve to a new equilibrium through three phases. In the first phase there is steady radial expansion and contraction, or radial breathing
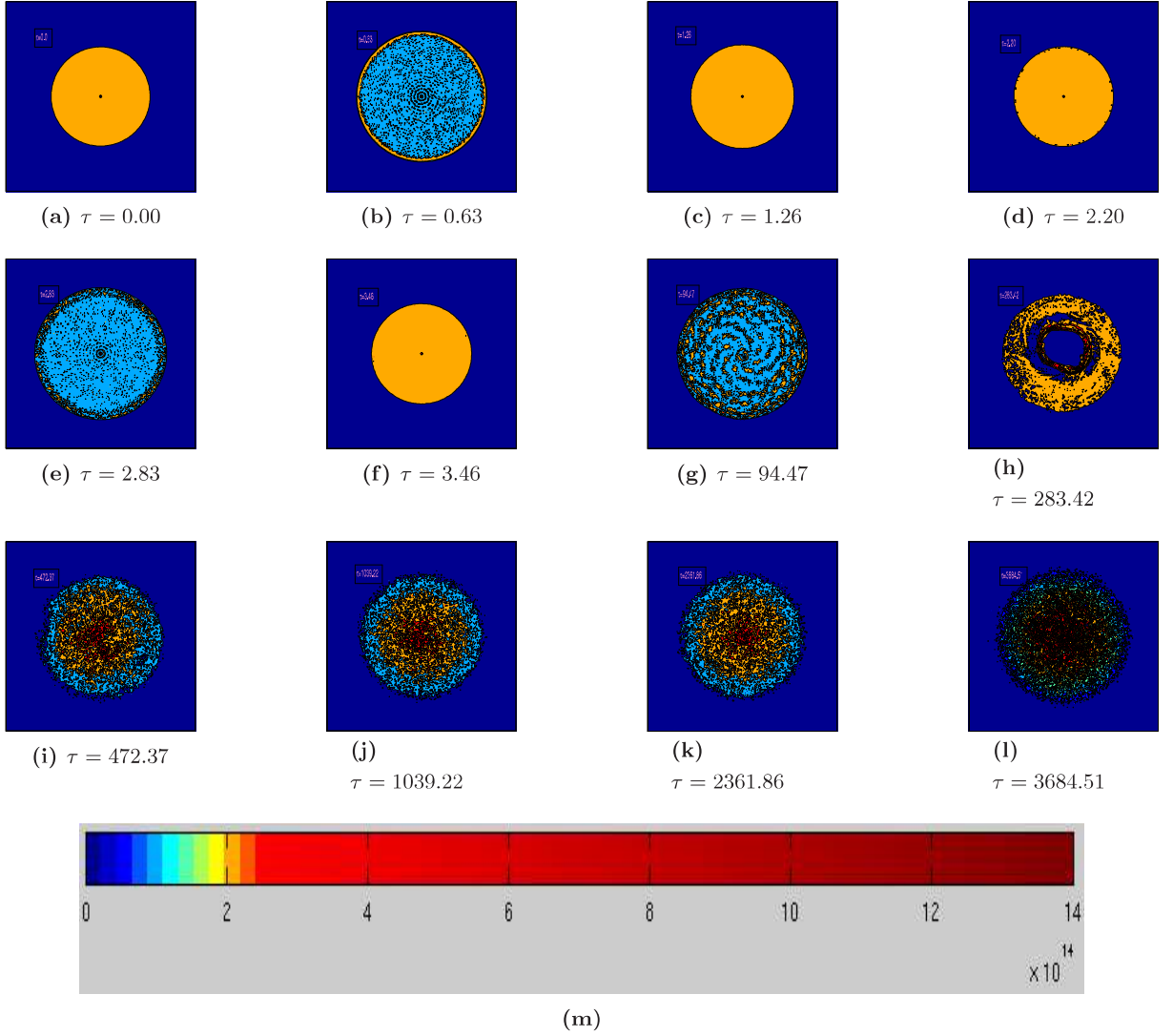
Figure 3.1: 2D density contour of n_e (in m^{-3}) showing evolution for the frozen load of $f_b = 0.6$. (a-f), (g-i), (j-l) roughly represent the 1st, 2nd, and 3rd phase respectively. m is density the colour code in uits of m^{-3}. $\tau = t/T_{ce}$. For clarity radius only up to $0.57\,R_w$ is depicted in these density plots, while the wall at radius R_w is grounded.

of the plasma profile (Fig. 3.1a-f). We call this the Steady Breathing Phase. The second phase is called the Growth Phase because in this phase, the plasma is seen to gradually expand and contract by larger radial distances beyond the loaded radius (Fig.3.1g-i). Finally in the third phase the radial oscillations decay and saturate as the plasma settles down to a equilibrium state with a monotonically falling density profile having a larger radius than it's initial. (4th row of Fig.3.1j-l).

All the three phases of the profile evolution were observed to vary with change in f_b of the loaded step density function. For the lowest density loads ($0 < f_b < 0.1$) the entire radial breathing phenomenon remains negligibly subdued and the profile continues to rotate nearly rigidly. Around $f_b = 0.1$ observable radial breathing sets in, and with further increase in f_b the radial breathing of the first two phases increase in amplitude. Growth and saturation of the breathing motion also set in faster with increase in f_b. During the 2nd phase of profiles loaded with $f_b \geq 0.6$, the growing radial oscillations lead to spontaneous formation of a density-void structure at the centre of the profile, which then excites unstable azimuthal modes [1, 15]. Weaker flute modes are also observed during the growth phase of $0.2 \leq f_b \leq 0.5$. These too are excited by the formation of a density maximum, at some intermediate radius within the profile's radial extent [68].

The radial breathing phenomenon is driven by the inertia of the electrons. If we neglect the mass term in Eq. (3.1) then the radial forces would always balance, with the $v_{e\theta}$ adjusting instantaneously (no inertia) to the exact $\mathbf{E} \times \mathbf{B}$ drift velocity required for radial force balance. That is why the lowest f_b systems, remain very close to a rigid rotor state even for the off-equilibrium loads. As we move towards larger f_b, inertia gains importance and the radial breathing phenomenon becomes more pronounced. Another important parameter influencing the motion is, how far removed from equilibrium the system was loaded. In our experiment, the chosen off-equilibrium angular frequencies are such that, with increase in f_b of the loaded step density profile the initial shift from equilibrium also increases. This factor further enhances the contrast in the magnitude of the radial breathing phenomenon as we move from the lowest to the highest f_b.

The onset of breathing motion happens with the radial inward and outward forces in the L.H.S. of Eq. (3.1) not balancing because of the choice of $v_{e\theta}$ loaded. This causes a collective motion of the plasma in the direction of the resultant radial force, and a new density profile $n_e(r, \theta, t)$ takes shape, which in turn changes the radial electric field function, $E_r(r, \theta, t)$. The modified $E_r(r, \theta, t)$ now changes the $\mathbf{E} \times \mathbf{B}$ drift velocity. The resulting $v_{e\theta}(r, \theta, t)$ along with the present $E_r(r, \theta, t)$ set up new radial forces. Depending on the direction of the resultant force the plasma again moves radially outward or inward. The dynamics work out in such a way that the resultant radial force switches direction after exactly equal time intervals, thus sustaining linear breathing oscillation of the first phase. It should be emphasized that the model put forward here is very simplistic. In reality the above quantities are not modified sequentially as described but evolve dynamically in unison, maintaining the collective breathing motion.

In the limit of low amplitude as seen for smaller f_b, the steady breathing oscillations of the first phase are the collective Bernstein modes of a zero temperature electron plasma [1, 17], all of which have

the same frequency, $\omega_{uh} = \sqrt{\omega_{ce}^2 - \omega_{pe}^2}$, known as the coriolis-shifted upper hybrid frequency [17] (see Fig. 3.2c-d). In this respect the radial breathing phenomenon in higher f_b can be alternatively described as the full nonlinear dynamics of high amplitude Bernstein modes in cold electron plasma, set up by the significantly off-equilibrium loading of the high f_b profiles.

We analysed the evolution of the non-equilibrium loads with three types of diagnostic probes, namely, the potential probes, a density probe located at a radius of $0.75 r_p = 0.225 R_w$, and the $x(t)$, $y(t)$, and $r(t)$ co-ordinate traces of the three particles located at radii $0.29\,R_w$, $0.25\,R_w$, and $0.18\,R_w$. For step-densities of $f_b > 0.1$ the readings of all the probes could be separated into an initial steady oscillation region, followed by an algebraically growing oscillation region, followed by a decay and saturation of the oscillation. The radial breathing motion was detected by the potential probes, the density probe, and the $r(t)$ co-ordinate traces. The rotational motion of the plasma was detected by the $x(t)$ and $y(t)$ co-ordinate traces and also by the potential probes (because of small inherent azimuthal asymmetry in numerical loading of the profile as explained earlier in Subsection 2.1.8).

Through Fourier analysis of the full simulation time-range as well as only the initial steady oscillation time-window of different probe data we extracted exact values of radial oscillation frequency, ω_{rad} and rotation frequency ω_{rot} of the plasma profile in the steady breathing phase. All probes corresponding to either frequencies yielded perfectly matching frequency values indicating that in the steady phase there is a fixed rotation frequency and a fixed radial oscillation frequency of the plasma profile. The obtained frequencies have been plotted as a function of f_b of the loaded step density profile in Fig. 3.2c-d and Fig. 3.2c . From these plots it is observed that for frozen loads the radial oscillation frequency curve skirts the ω_{re}^+ curve from above remaining below ω_{ce} line for all f_b values, while the rotation frequency curve skirts the ω_{re}^- curve from below remaining above the zero frequency line for all f_b values. For the cyclotron frequency loads the rotational motion and radial breathing of the plasma profile happen at the same frequency which skirts the ω_{re}^+ line with nearly the same values as the radial breathing frequency for the frozen loads. For both the loads the breathing frequency is almost equal to the coriolis-shifted upper hybrid frequency ω_{uh} for $f_b < 0.4$ and deviates above and away form the ω_{uh} curve for higher values of f_b (Fig. 3.2c-d). The percentage fluctuations in density in the initial phase (Fig. 3.3b), for the high f_b values, indicates that in the high density limit radial breathing takes place at a high amplitude from the onset of the relaxation process. Thus terms containing higher powers of these quantities, cannot be neglected in an analytical study of these oscillations. So the first order perturbation recipe used in the Diocotron mode analysis [1, 15], is not applicable here.

To obtain an average measure of the algebraic growth in the next phase, we fitted a straight line envelope on the growing oscillations of one potential probe's reading (Fig. 3.2a), and measured it's slope as the rate of growth (Fig. 3.2e). Comparison of FFT analysis of potential probe date in the growing phase time window, steady breathing phase time-window, and the full simulation time-range indicates that there is frequency chirping in radial oscillation and rotational motion occuring in the growing phase followed by gradual transition of the collective motion to a nonlinear phase. The breaking of

(a)

(b)

(c)

(d)

(e)
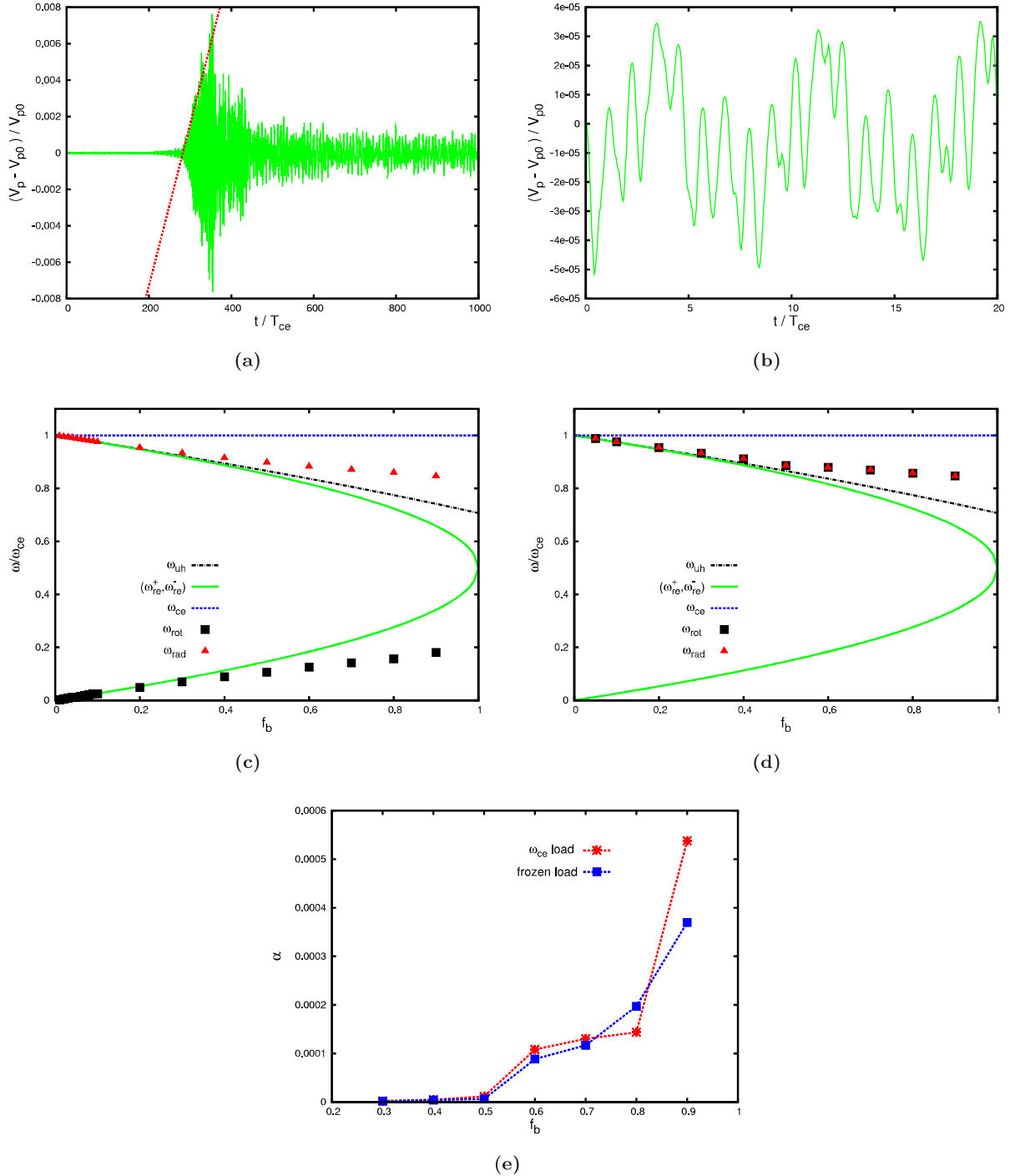
Figure 3.2: Potential probe data analysis for the off-equilibrium loads: (a) is a single Potential probe's reading for frozen load of $f_b = 0.6$ shown here till $t = 1000\,T_{ce}$ for clarity. V_p is the probe reading and V_{p0}, it's initial value. The time axis is normalized by T_{ce}. A straight line envelope is fitted on the growing part to estimate the steady growth rate. (b) is a zoomed-in plot of the initial readings of (a) showing that in the steady breathing phase the potential probe captures two frequencies; one for the slower rotation, and the other for the faster radial breathing. (c) is a plot of the rotation frequency, ω_{rot}, and radial breathing frequency, ω_{rad} of the steady phase as a function of f_b, for the frozen loads. (d) is the same as (c), except that it is for the cyclotron frequency loads. In (e) the steady growth rate, α obtained as the slope of the normalized readings in (a) is plotted as a function of f_b for both the off-equilibrium loads.

(a)

(b)

(c)
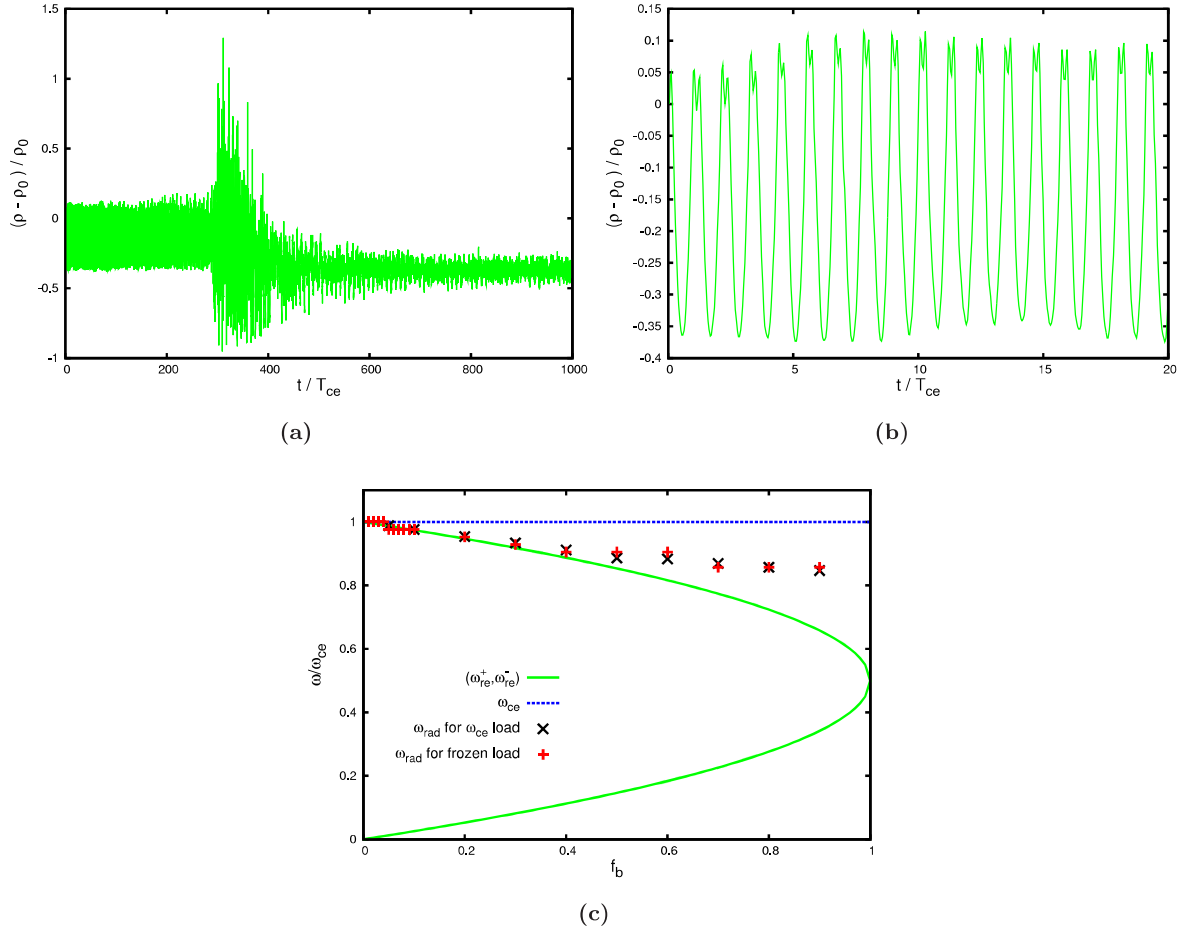
Figure 3.3: Density probe data analysis for the off-equilibrium loads: (a) is the Density probe readings for frozen load of $f_b = 0.6$ shown here till $t = 1000\,T_{ce}$ for clarity. ρ is the probe reading, and ρ_0, it's initial value. (b) is a zoomed-in plot of the most initial readings of (a) showing that in the steady phase the density probe captures only the frequency of radial oscillations, ω_{rad}. (c) is a plot of the obtained ω_{rad}, as a function of f_b, for the two off-equilibrium loads.
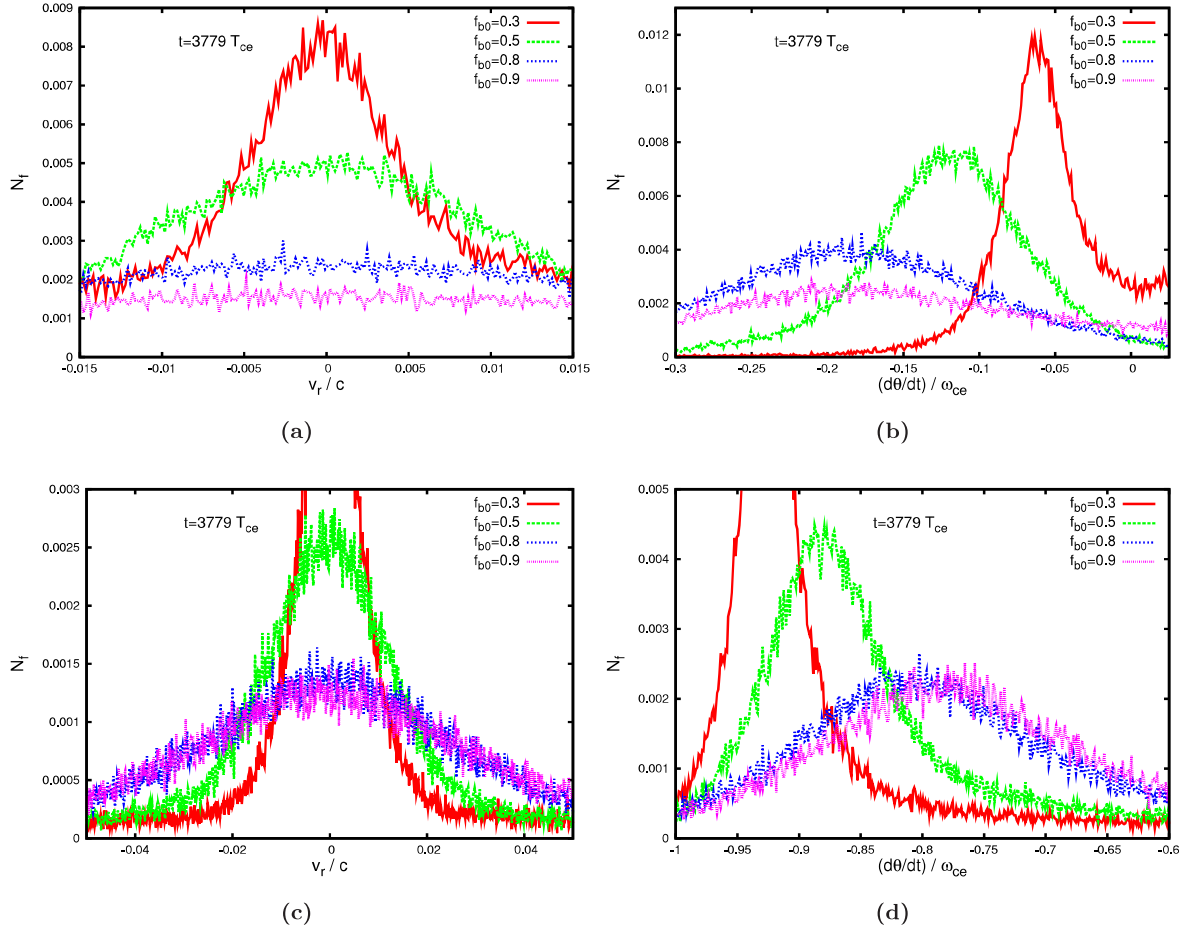
Figure 3.4: Velocity distributions at the end of simulation at $t = 3779T_{ce}$: Radial velocity and angular velocity distributions for the frozen loads are in (a) and (b) respectively. (c) and (d) are radial velocity and angular velocity distributions for cyclotron frequency loads. Here N_f is the fraction of total number of pseudo particles present at the velocity value. c is the velocity of light in free space.
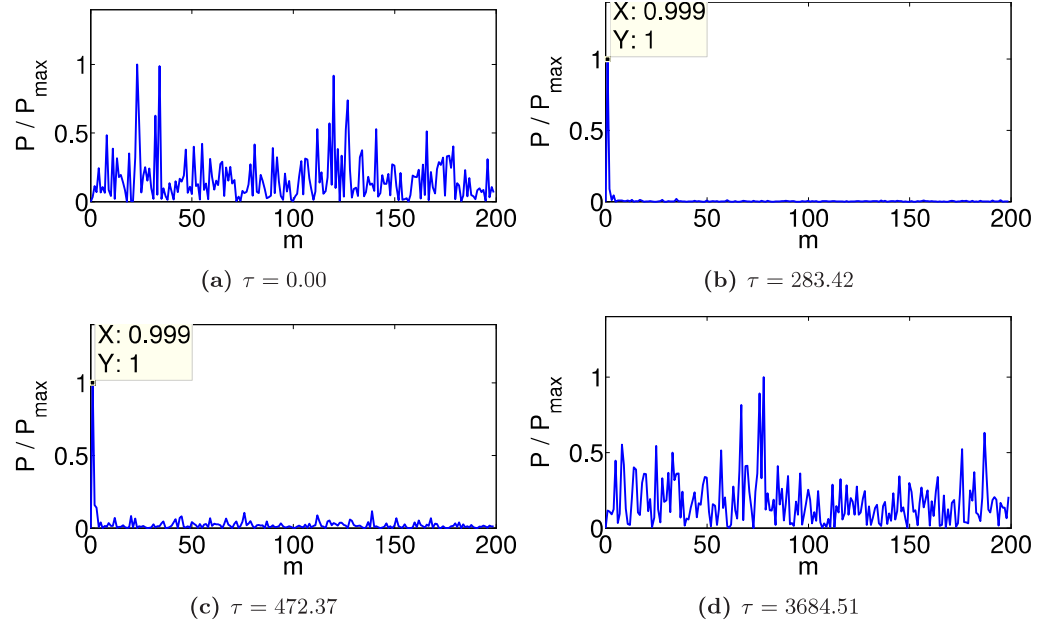
Figure 3.5: Fourier transform of $< n_e(r, \theta, t) >_r$ over θ-space at different times: m is azimuthal mode number. P is the power-value for the mode. The power-values have been normalized by their maximum value P_{max} in the plot. $\tau = t/T_{ce}$. Here (a) belongs to 1st phase, (b) and (c) are in the 2nd phase, while (d) is in the 3rd phase.

θ-symmetry of the $f_b = 0.6$ profile due to excitation of a transient, small amplitude fundamental dioctron mode, during the growth phase, is studied by Fourier transforming the r-averaged number density function $< n_e(r, \theta, t) >_r$ over the θ-space (Fig. 3.5). The Fourier spectra obtained from the density profile of Fig. 3.1a in the steady breathing phase (Fig. 3.5a), and the density profile of Fig. 3.1l in the saturation phase (Fig. 3.5d) have no exceptionally large peaks. This confirms that the motion is azimuthally symmetric at these times. The spectra corresponding to the profiles of Fig. 3.1h-i (Fig.3.5b-c), in the growth phase however show a sharp peak at mode number, $m = 1$, indicating the θ-symmetry has been broken here by the combination of the azimuthal instabilities and radial breathing. In the plots of Fig. 3.5 we have deliberately not chosen the same normalization constant for the power-values, P in each of the plots as quantitative comparison between the spectra is not possible because large scale variation in the overall averaged density $< n_e(r, \theta, t) >_{r,\theta}$ due to radial breathing scales the power-values differently in each spectrum.

The simulations of the off-equilibrium loads also showed good energy conservation with maximum fluctuation from initial value being 0.12% for frozen load of $f_b = 0.6$. However here unlike the rigid rotor equilibrium, the total angular momentum and its magnetic component are not conserved quantities because of momentum exchange between the two degrees of freedom of the system, radial and azimuthal. The maximum fluctuation in L_z and L_z^{mag} from their initial values went up as far as 45% and 80% for frozen load of $f_b = 0.6$. This non-conservation is also in contrast with the Diocotron mode simulations in the low density limit, (Sec II) where $L_z = L_z^{mag}$ is a conserved quantity.

The spread in the distribution of radial velocities, v_r, and angular velocities, $d\theta/dt$ of the pseudo particles (Fig. 3.4), at the end of the simulation (at $t = 3779T_{ce}$) give a measure of the remoteness of the eventual plasma profile from the rigid rotor state that the it was initially loaded in. A collisionless rigid rotor should have no spread in radial and angular, velocities of constituent particles, but a collisional electron plasma profile in rigid rotor equilibrium can acquire a spread in these velocity distributions through microscopic Coulomb collisions. A profile loaded off-equilibrium can gain an even larger velocity spread through macroscopic phenomena like radial breathing, azimuthal modes, and their associated non-linearities along with the microscopic collisions. The PIC code we have used does not have an additional collision term or random walk incorporated in the pseudo particles' motion to simulate microscopic collisions. However it does reproduce the collisionless velocity spreading caused by macroscopic phenomenon and also to some extent, large scale Coulomb interactions, at ranges greater than grid size. So these distribution curves can only be used qualitatively, to compare the gain in entropy between different f_b values, as a result of macroscopic phenomena.

For the comparative distribution curves of Fig. 3.4a-d only $f_b > 0.2$ have been used, as these high density profiles are well into their 3rd phase of evolution at $t = 3779T_{ce}$. Having undergone all the macroscopic collisionless processes mentioned above, these profiles have reached a state of equilibrium. It is observed in Fig. 3.4a-d that with increase in f_b of the loaded step-density profile, the spread in the final v_r and $d\theta/dt$ distributions also increase. This can be understood on the grounds that the non-linear radial breathing phenomenon, causing this entropy gain, also acquires greater amplitude and growth rate with increase in f_b. The peaks of angular velocity distributions have a gradual shift with increase in Brillouin ratio. For the frozen loads higher f_b have larger magnitudes of peak angular velocity (Fig. 3.4b) similar to the ω_{re}^- versus f_b curve (see also Fig. 3.2d). In contrast peak angular velocities for cyclotron frequency loads are shifted towards lower magnitudes of $d\theta/dt$ for higher f_b (Fig. 3.4d), similar to the ω_{re}^+ versus f_b curve (see also Fig. 3.2c). The negative sign of $d\theta/dt$ values indicating clockwise $\mathbf{E} \times \mathbf{B}$ rotation, is a result of the axial magnetic field acting into the plane of the paper.

It must be emphasized again, that the the velocity distribution curves obtained here are only useful for studying trends of how the magnitude of the breathing phenomenon and the degree of disorder brought in by them vary, with change in f_b of the loaded step density profile. It cannot be determined whether any of the profiles have attained thermal equilibrium (at $t = 3779T_{ce}$), though profiles with $f_b > 0.2$ are all well into their saturation phase. Also because of reasons mentioned earlier, neither can these distribution curves be used quantitatively to measure the temperature of the plasma. The peak angular velocity values are a measure of the mean rotation frequency of the plasma profile at $t = 3779T_{ce}$, and their gradual shift with increase in f_b indicates how the mean rotation frequency of the plasma profiles vary with increase in Brillouin ratio at this stage.
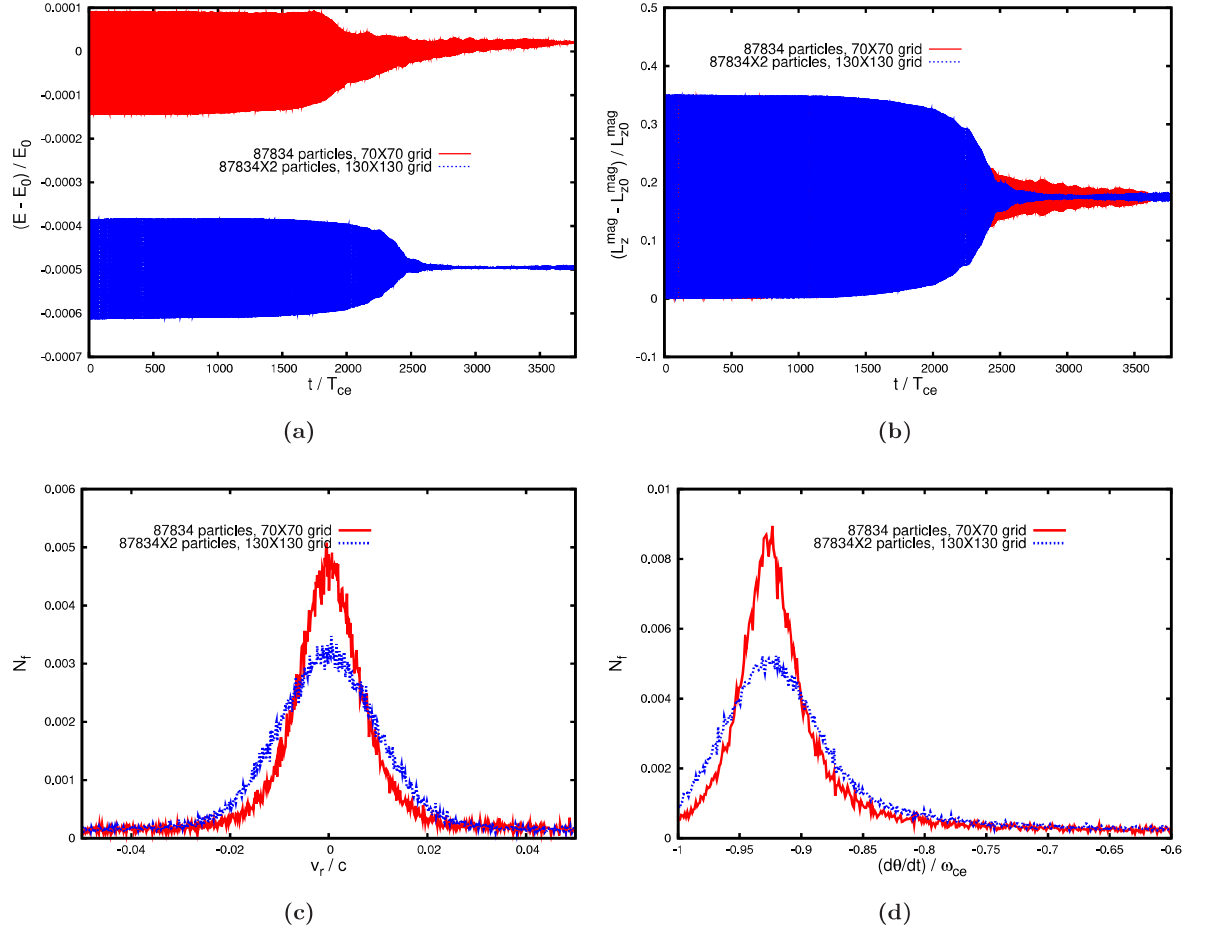
Figure 3.6: Results of convergence tests between the two PIC parameters for the cyclotron frequency load of $f_b = 0.3$. In (a)-(b) Energy, E, and Magnetic Angular Momentum, L_z^{mag} are compared between the two PIC parameters. E_0, L_{z0}^{mag}, are the initial values of energy and magnetic angular momentum, for the < 87834 particles - 70×70 grid$>$ simulation. (c) compares the radial velocity distributions at $t = 3779 T_{ce}$, between the two PIC parameters, and (d) does the same for the angular velocity distribution. Again c is the velocity of light in free space.

3.2   Convergence test with changed simulation parameters

As a further check for the accuracy of the above simulations, we repeated some of the simulations from PEPNEXI on a 130×130 grid with $87834 \times 2 = 175668$ particles and compared the corresponding diagnostic readings between the two PIC parameters. The results of the convergence test is shown here for the cyclotron frequency load of $f_b = 0.3$ (Fig. 3.6). Energy and magnetic angular momentum diagnostic data are in very close agreement (Fig. 3.6a-b). The convergence test also shows about 10% variation in the growth rate with the change in the PIC parameters. The difference in the spread of the velocity distributions at $t = 3779\,T_{ce}$ obtained from the two simulation parameters (Fig. 3.6c-d), indicates the sensitivity of this diagnostic to grid size and pseudo particle number, and exemplifies why we have studied these curves only qualitatively.

3.3   PEPNEX2: Dynamics of $l = 1$ perturbed pure electron clouds in presence of collisional background

The set-up of the numerical experiment, its results are discussed below.

3.3.1   The numerical setup

The PEPNEX2 simulations were performed with the 2D3v PIC-with-MCC code PEC2PIC-3MCC **with ionization collisions turned off** for typical parameters found in experiments of cylindrical traps [18, 69], in particular, a wall radius, $R_w = 0.125m$, and axial magnetic field, $B_z = 0.015T$, and radial extent of the uniform density plasma, $r_p = 0.5 \times R_w$. The simulation time step, $\delta t = 10^{-11}sec$ is chosen much smaller than the cyclotron time period, $T_{ce} = 2.38 \times 10^{-9}sec$ of electrons, such that the code can well resolve the cyclotron motion of both ions and electrons. The collision time step Δt_c is adjusted according to the chosen pressure and temperature of the background gas. The magnitude of axial velocity with which the electrons are loaded (to mimic their bouncing motion in an experimental cylindrical trap) is $1.02727 \times 10^7 ms^{-1}$ which implies that for a typical cylindrical plasma column of length of $60cm$ [58] the bounce frequency of electrons is roughly 8.5 MHz. This value of the axial bounce frequency is higher than the typical experimental bounce frequency (< 0.2 MHz [58]) of a $60cm$ long cylindrical plasma column. By loading the electrons with high axial speeds we have made the electrons more energetic and thereby maintain the average total non-ionizing (elastic + excitation) collision cross section between the moderate orders of $10^{-21}\,m^2$ and $10^{-20}\,m^2$ (see Fig. 3 of Reference 30 [51]) in PEPNEX2. It must be re-emphasized here that the loaded value of the axial velocity of electrons in the simulations serves only to adjust the collisional probabilities and does not partake in any of the regular PIC dynamics of the plasma.

PIC-parameters used in PEPNEX2 are 87834 pseudo electrons on a 70×70 grid. The background atom (Ar atom) is taken as 72820.77 times heavier than an electron.
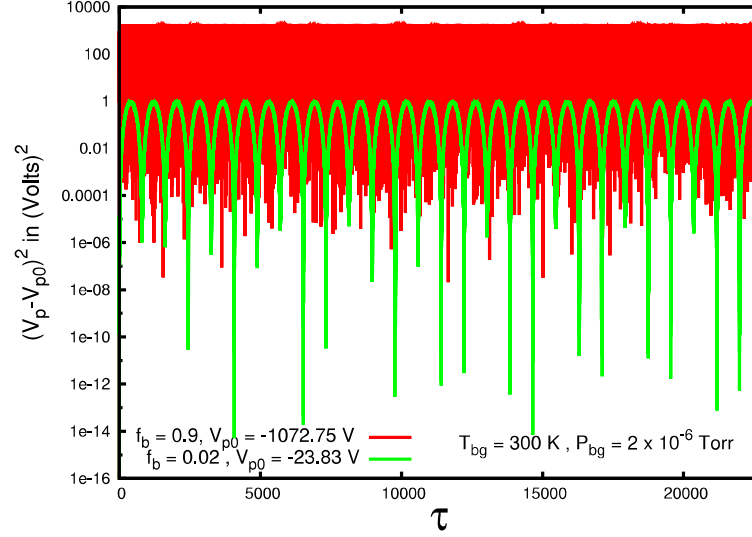
Figure 3.7: Potential probe data for the perturbed load (off-axis by $0.1 \times R_W$) of the $f_b = 0.02$ and the $f_b = 0.9$ pure electron clouds at a common background pressure, $P_{bg} = 2 \times 10^{-6} Torr$: V_p is the reading of the left potential probe and V_{p0} represents its corresponding initial value in the two simulations. The y axis is plotted in logscale for clarity. $T_{bg} = 300K$ is the temperature of the background gas in this set of runs. Normalized time, τ is in units of electron cyclotron time, *i.e.* $\tau = t/T_{ce}$. Hence it is clear from the potential probe's data that there is no growth of the initially implanted $l = 1$ mode in the simulation. The other three potential probes also gave similar results for this set of simulations.

3.3.2   Results

Two uniform density cylindrical pure electron profiles were loaded with a very small $l = 1$ perturbation seeded from the outset *i.e.* the profiles' central axis were shifted from the trap's central axis by a very small distance of $0.1 \times R_W$. The Brillouin ratios of the profiles chosen were $f_b = 0.9$ and $f_b = 0.02$. It is well understood that in the absence of any other influence these profiles will continue to make stable $l = 1$ orbits at their preset orbital radius with their characteristic $l = 1$ mode frequency [1, 34]. In PEPNEX2 we loaded these profiles at background pressure $P_{bg} = 2 \times 10^{-6} Torr$ of the Ar neutrals. Most present day electron plasma traps operate at background pressures below $10^{-8} Torr$ wherein H_2^+ is the predominant background gas [20]. The purpose of choosing a higher background pressure than experiments In PEPNEX2 was to ensure greater exposure of the profiles to elastic and excitation collisions and their effects. However both simulations revealed no destabilization of the stable orbital motion caused by the collisions for both the high and the low Brillouin ratios. Fig. 3.7 shows the squared and logscaled plot of the reading of the left potential probe for these two simulations. The signals have been plotted in such a manner for accurate exponential fitting of any observable growth of the signals (see also Fig. 3d) and also for the purpose of depicting on the same graph the two signals with vast difference in their mean values as well as their amplitudes. Fig. 3.7 shows that both the signals remain perfectly stable throughout the simulations.

The PEPNEX2 simulation results also contradict a theoretical model by Davidson and Chao [36]

for the effects of electron-neutral elastic collisions on the dynamics of the cloud. This model predicts that the non-ionzing collisions should destabilize the initially stable $l = 1$ orbital motion in the above two simulations into a growing $l = 1$ mode with growth rate, $\gamma = 2\pi\nu_{en}\omega_0/\omega_{ce}$ [36], where ν_{en}, ω_{ce}, and ω_0 are the non-ionizing collision frequency in s^{-1}, cyclotron frequency in rad/s and characteristic frequency of the $l = 1$ mode [1] in the loaded electron cloud expressed in rad/s.

The actual theory considered only electron-neutral elastic collisions contributing to the collision frequency ν_{en}. Excitation collisions between electrons and neutrals are also in effect elastic collisions, as these collisions also elastically scatter the electrons. Only the kinetic energy lost by the colliding electrons is greater in excitation collisions than in elastic elastic collisions. So in principle excitation collisions behave very much like elastic collisions with respect to their influence on cloud dynamics. As we already have $e^- - Ar$ first level excitation collisions taking place in PEPNEX2, it is only logical to modify ν_{en} by the addition of the first level excitation collision frequency to it. The resultant theoretical growth rate γ may then be directly compared to any growth rate obtained from the simulations of PEPNEX2.

It must be noted that the theoretical model [36] considers a low f_b electron plasma for which the massless fluid approximation is valid. PEPNEX2 on the other hand simulates both low and high f_b profiles, which are, $f_b - 0.02$ and $f_b = 0.9$. As the ojective of PEPNEX2 is to test the influence of non-ionizing collisions at all f_b, as opposed to modelling its effects only in the limit of low f_b [36], it is only logical to calculate a theoretical γ even at $f_b = 0.9$ from Davidson and Chao's model as a reference, to compare with any growth rate obtained form the simulation at $f_b = 0.9$. Evidently if the non-ionizing collisions can destabilize the cloud, the inclusion of mass in modelling its effects should only alter the value of the growth rate from the value obtained neglecting mass effects.

The model also assumed a constant temperature of the plasma profile maintained by electron-electron collisions in the derivation of the above expression for the growth rate, γ due to electron-neutral collisions. There are no electron-electron collisions happening in PEPNEX2. But the plasma is loaded at zero temperature and does not undergo any collsionless heating process, although there is some amount of heating by the non ionizing electron-neutral collisions. So applying the above expression for γ to the numerical experiments will include the approximation of a constant temperature of the plasma profile.

The procedure for obtaining the growth rates from Davidson and Chao's [36] model when applied to PEPNEX2 is as follows: From the initial cold loads of the plasma profiles it is simple to find an average velocity magnitude of electrons which would approximate as the average velocity magnitude of all electrons through the simulation. The total non-ionizing (elastic + excitation) collision cross-section can then be estimated using this average velocity magnitude, which leads to a value for the collision frequency ν_{en}. This value comes out to be 2.3985×10^4 per sec for the $f_b = 0.02$ load and 1.7548×10^4 per sec for the $f_b = 0.9$ load. Plugging in the other fixed frequencies in the above expression for the growth rate, γ, the growth rate from Davidson and Chao's model can be estimated to be 1.8838×10^2 rad/sec for the $f_b = 0.02$ load and 6.2021×10^3 rad/sec for the $f_b = 0.9$ load.

These growth rates imply that at the end of the simulations period of 5.4×10^{-5} seconds, the $l = 1$ orbital radius should have increased by 1.02% for the $f_b = 0.02$ load and by 39.78% for the $f_b = 0.9$ load according to the model of Davidson and Chao [36]. Even if we neglect the theoretical small increase in orbital radius for the $f_b = 0.02$ load, the theoretically predicted increase in orbital radius is substantial for the $f_b = 0.9$ load and should be detected by the simulation diagnostics. However as we discussed earlier using the potential probe diagnostic (Fig 6) the stability and initial amplitude of the $l = 1$ mode remains completely unaltered in both the simulations, $f_b = 0.02$ and $f_b = 0.9$.

It must be **emphasized** here that the results of the PEPNEX2 **stand independently, irrespective** of whether the approximations and assumptions of Davidson and Chao's theoretical model[36] are fully or partially satisfied by the simulations. We have obtained from the 2D electrostatic simulations with 3D collisions (using PEC2PIC-3MCC) that the stability of electron plasma profiles of both low and high Brillouin ratio is not affected in an way by the ongoing non-ionizing collisions between the plasma and the background. A new theoretical explanation in support of this finding of PEPNEX2 results is provided below.

The electron plasma in Diocotron motion, *e.g.* a stable $l = 1$ orbit, can be thought of as having its electrostatic potential energy in two parts. The first part is the electrostatic energy of the profile without the surface wave/ Diocotron mode and the other part which is a negative quantity is the electrostatic energy associated with the Diocotron mode. Any process that further draws out energy from the mode *i.e.* makes the mode's electrostatic energy even more negative and thereby also reduces the total potential energy of the profile, will bring about growth of the mode. A process that only reduces the first part of the potential energy *i.e.* the profile's electrostatic energy by virtue of its internal configuration without any surface wave, can not cause growth of the Diocotron mode. Through our simulations we found that the elastic and excitation collisions can only reduce this first part of the potential energy by means of profile relaxation. However these collisions can not directly influence the energy associated with Diocotron mode. On the other hand a process like a resistive wall instability can directly takes away energy from the Diocotron mode by changing surfaces charge configuration on the grounded wall (or alternatively the virtual image charge configuration) that interacts with the Diocotron mode of the plasma. So while a resistive wall may cause growth of negative energy Diocotron modes on the electron plasma the elastic and excitation collisions can not directly influence Diocotron motion by virtue of their potential energy reduction capability. Hence contrary to the theory by Davidson and Chao [36] which predicts that elastic collisions can reduce both parts of the potential energy of an electron cloud and destabilize them, our simulations show that elastic (and excitation) collisions can only cause reduction in the first part of the potential energy through relaxation of the profile.

3.4 PEPNEX3: Significant Heating of electron/quasi-neutral plasma without driving the plasma far away form equilibrium

Averaging the equilibrium density function of a cylindrically trapped electron plasma over r and θ leaves an axial density profile distributed between the electrostatic end plugs of the trap. It is possible to further heat up this r and θ averaged axial profile in equilibrium by additional quasi-static electrostatic compression from the end plugs. Of course, once the compression is released quasi-statically, the profile relaxes back to its initial thermal equilibrium. PEPNEX3 are a set up numerical experiments that demonstrate a new way of compressional heating of plasmas, in which the plasma retains most of heat it gained during compression even after the compression is relaxed, and the same time quickly attains a new thermal equilibrium after the compression is relaxed. To numerically demonstrate this heating in a PM trap would require full 3D simulation of the trap. Alternately one can demonstrate the working principle of the heating scheme using movable 1D reflecting walls that can compress a 1D quasineutral plasma confined within them. This is basically what has been done in PEPNEX3. However as PEPNEX3 only demonstrate a principle, care should taken while applying the principle for electrostatic heating of single species plasmas in PM traps, or magnetic heating of quasi-neutral plasmas in toroidal traps.

The following subsections discuss the theoretical background, numerical set-up, and results of PEPNEX3.

3.4.1 Theoretical Background based on Thermodynamic Principles

In PEPNEX3 the 1D PIC code PEC1PIC is used to perform two simulations- (i) the proposed thermodynamic cycle involving quasi static compression of a quasi-neutral plasma followed by a non quasi static expansion back to its initial dimension, and (ii) a control experiment in which a fully quasi static compression-expansion cycle was simulated as reference for the proposed cycle for net temperature gain. The movable rigid wall of PEC1PIC at $x = L(t)$, $L(t)$ being the instantaneous confinement length of the plasma, is used to carry out the compression and expansion of the plasma. In PEPNEX3 the non-quasi-static expansion part of (i), the proposed cycle, was executed as a free expansion of the plamsa, i.e., where plasma is initially in equilibrium with $P = P_{ext}$ and then P_{ext} is suddenly (i.e., in a span of time that is much smaller than the plasma timescales) reduced to zero. This is achieved by moving the rigid wall back to its original position in a time-scale much faster than the plasma's response time-scale. As the free expansion is a zero work process at $P_{ext} = 0$, the internal energy and temperature of the plasma remain conserved at their respective values attained at the end of the compression, thus ensuring the free expansion will retain all the heat gained in the compression phase of the cycle. In contrast, in a constrained non-quasi-static expansion (equivalent to relaxing the magnetic field in Tokamak plasmas, and relaxing end plug electric field in electron plasmas), the plasma will lose some of the energy gained in the compression phase to the expanding wall. A freely expanding plasma should also undergo maximum deviation from equilibrium during relaxation as compared to any form

of constrained or controlled expansion. The nonlinear dynamics of the plasma associated with an electrostatic free expansion of the plasma in the simulation (very similar to diffusive free expansion of gases) should also be far more turbulent that in a constrained non-quasi-static expansion. Hence, if we can show through simulation of the free expansion that the plasma attains a final Maxwellian equilibrium after the turbulent processes have completely damped, it will ensure that attainment of a final equilibrium Maxwellian is guaranteed for any form of controlled expansion as well.

3.4.2 Numerical Set-up

For simulations of the temperature gaining cycle as well as the reference experiment of the fully quasi static cycle, we consider a hot plasma with number densities $n_e = n_i = 3142 \times 10^{18} \, m^{-3}$, plasma frequencies, $\omega_{pe} = \omega_{pi} = 10^{11} \, rad/s$ (i.e $\tau_{pe} = \tau_{pi} = 6.28 \times 10^{11} \, s$), and temperatures $T_e = T_i = T = 2.198 \, keV$. The PEPNEX3 simulations have been carried out for different values of the ion to electron mass ratio m_i/m_e, the selected values being 1, 10, and 100. The details of the PIC simulations parameters are as follows. The quasi neutral electron-ion plasma is bounded by two perfectly reflecting walls with which electrons and ion undergo elastic collisions. The wall at $x = 0$ is fixed and the other wall at $x = L(t)$ is movable to produce the effects of compression and expansion. The instantaneous confinement length $L(t)$ of the bound plasma is divided into 100 cells for the Particle-in-cell motion in that time step. The time step chosen is $\delta t = 10^{-14} \, s$. The simulation is carried out with 5.0×10^5 pseudo electrons and 5.0×10^5 pseudo ions which implies a more than adequate 5000 particles per cell for each component of the plasma throughout the simulation.

3.4.3 Results

For the simulation of the quasi static compressionfree expansion cycle, we consider the plasma in an initial equilibrium state A where the electron and ion velocity distribution functions (f_e, f_i) are Maxwellian (with common temperature $T_A = 2.198 \, keV$) and the plasma length is $L_A = 0.02 \, m$. The first part of the cycle consists of quasi static adiabatic compression of the plasma from state A to B where $L_B = 0.017 \, m$. This part was simulated by moving the wall inwards with a very slow velocity $V_W = 1.510^5 \, m/s$ which is two orders smaller than the thermal speeds of electrons and also much smaller than the ion thermal speeds (for all the three values of ion mass used in simulation) throughout the compression. Hence, the distribution function (f_e, f_i) remained very close to Maxwellian at all times and the temperature increased according to the quasi static adiabatic law $TL^{\gamma 1} = $ constant, where T and L are the instantaneous temperature and length of the plasma and $\gamma = 3$ for 1D plasma (see Fig. 3.8), thus $T_B = T_A(L_A/L_B)^2 3.042 \, keV$. Adherence of the plasma compression to the above law and final temperature to the theoretical prediction is verified from simulation (Fig. 3.8). After the quasi static compression, the wall is kept static for short time lasting $5 \times 10^5 \, \delta t$ to make sure that the plasma returns to equilibrium. The cycle is then closed by free expansion of plasma from $L_B = 0.017 \, m$ to $L_A = 0.02 \, m$. The free expansion of plasma was initiated by moving the wall at $x = 0.017 \, m$ to the final location at $x = 0.02 \, m$ in just 3000 δt (i.e., with a velocity $V_w = 10^8 \, m/s$).

(a)
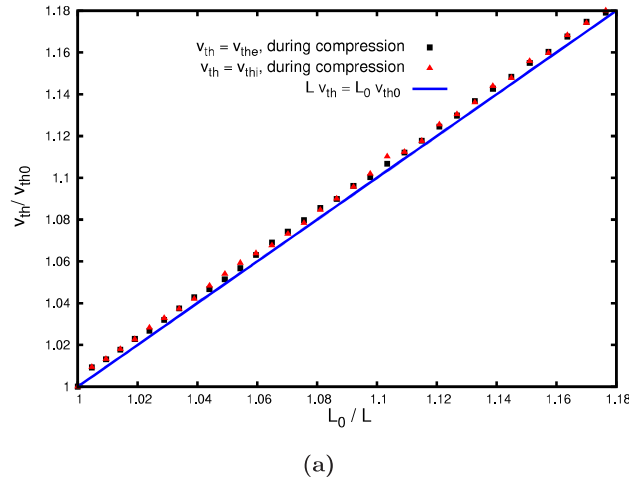
Figure 3.8: Taking $m_i = m_e$ the instantaneous thermal velocities of electrons v_{the} and ions v_{the} during the quasi-static compression is plotted a function of the length $L(t)$ of the plasma column. Here L_0 is the initial lenght of the plasma column and v_{th0} is initial common thermal velocity of electrons and ions. The instantaneous thermal velocities are obviously proportional to the square root of the instantaneous temperatures, $T_e = T_i$. Hence the linear variation of the thermal velocities vs $L(t)$ verifies the adiabatic quasi-static law.

This expansion of the reflecting wall system is instantaneous in comparison the time scales of electron and ion motion. Once the wall is moved to $0.02\,m$, it is kept static for another $2.497 \times 10^6\, \delta t$ during which the plasma expands freely and quickly relaxes to a new Maxwellian. However, during the relaxation, the simulations show that plasma becomes turbulent and distribution functions (f_e, f_i) deviate considerably from Maxwellian.

We find that in the simulations with different ion masses, the dynamics of the plasma is typically similar. At the end of the expansion phase of the cycle, the plasma attains equilibrium by turbulent relaxation which is dominated by two stream and bump-in-tail instabilities. Fig.3.9 shows some snapshots of the plasma in phase space for the simulation with equal electron and ion masses, the case which relaxes the quickest. From Fig.3.9c we see that immediately after the removal of the wall to $x = 0.02\,m$, there is a flux of electrons and ions from $x = 0.017\,m$ towards the shifted wall by the process of free expansion. As the particles in the freely expanding front no longer encounter a rigid wall to reflect them back into negative velocity space, a vacant region is created in the negative velocity space to the left of $x = 0.017\,m$ while the flux particles fill up a new region in the positive velocity space to the right of $x = 0.017\,m$ (Fig. 3.9(c)). This process of removal of particles from the negative velocity space to the left of the $x = 0.017\,m$ and the accumulation of other particles in the positive velocity space to the right of $x = 0.017\,m$ continues till the expanding front hits the wall at $x = 0.02\,m$ (Fig.3.9(d)). These particles then get reflected by the wall at $x = 0.02\,m$ and form a beam that partially fills up the vacuum that had been created in the negative velocity space (Fig.3.9(e)). The beam then undergoes a second reflection at the wall at $x = 0.0\,m$ only to form a positively directed beam on top of the main distribution in phase space (Fig.3.9(f)). Formation of striations in the phase
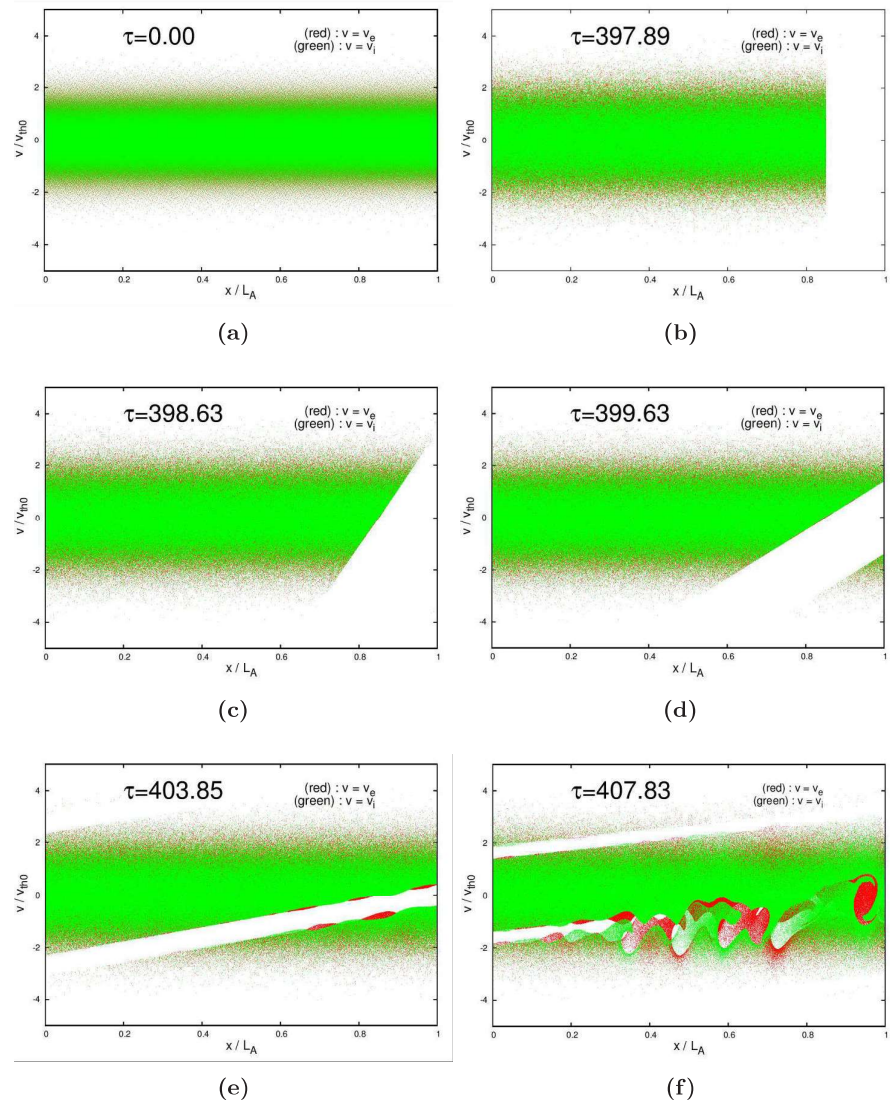
Figure 3.9: Snapshots of the ions (green) and electrons (red and underneath the ions) at different stages of the quasi static compressionfree expansion cycle for the $m_i = m_e$ case. The spatial axis, x, is normalized by $L_A = 0.02\,m$ while the velocity axis, v, is normalized by the common initial thermal velocity of electrons and ions, v_{th0}. $\tau = t/\tau_p$ represents the normalized time corresponding to the snapshot. (a) Initial state with Maxwellian distribution of electrons and ions, (b) at the end of quasi static compression and rest, (c) rearrangement of the phase space distribution due to free expansion, (d) expanding front hitting the wall at $x = 0.02\,m$, (e) formation of reflected beam and triggering of anomalous processes, (f) formation of holes and BGK modes, (g) phase mixing and coalescence of structures, (h) final relaxed state with almost Maxwellian electrons and ion.
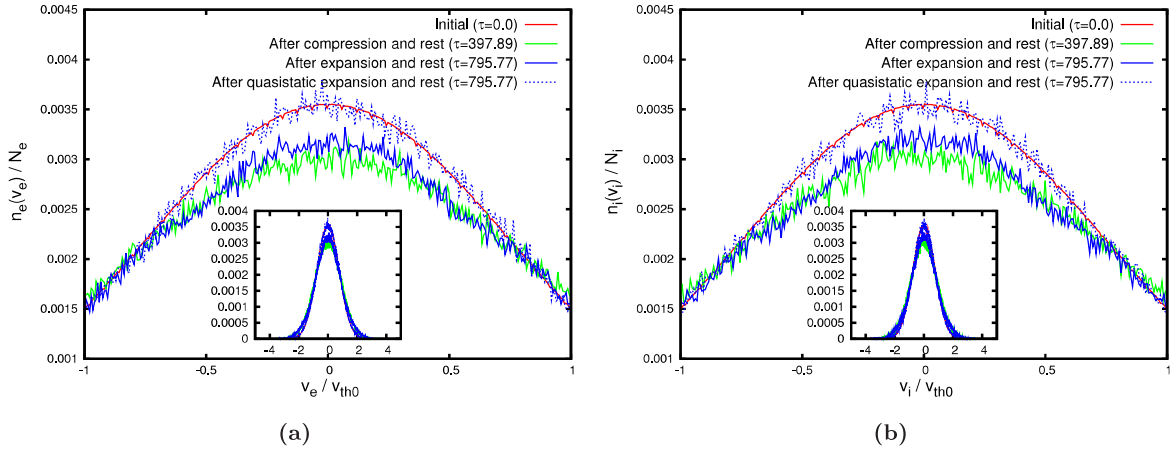
Figure 3.10: Velocity distributions of (a) electrons and (b) ions for quasi static compression free expansion and quasi static compression quasi static expansion cycles with $m_i = m_e$. There is net heating in the former and no heating in the later cycle as evident from the respective final velocity distributions of electrons and ions in the two cycles. The electron and ion velocities are normalized by the common initial thermal speed of the two species. The quantity on y axis represents the distribution functions of electrons and ions. $\tau = t/\tau_p$ is the normalised time.

space distribution leads to excitation of anomalous processes such as bump-in-tail instabilities and two stream instabilities in the plasma (Fig.3.9(e)). The excitation of the instabilities is accompanied by electric field generation in the plasma. The ensuing turbulence manifests itself in the form of large number of electron and ion phase space holes and BGK modes (Fig.3.9(f)). Subsequently, the BGK modes and the phase space holes coalesce typically on time scale of $300\,\tau_p$ to $400\,\tau_p$ accompanied by simultaneous decay of the electric field (Fig.3.9(g)). Eventually, the plasma relaxes to a quiescent equilibrium with electron and ion distribution functions returning to Maxwellian and the electric field decaying to zero (Fig.3.9(h)). Phase mixing and Landau damping are the important dissipating mechanisms here. It is seen that at the end of free expansion and relaxation, the temperature T_{Aj} of plasma remains same as what it was at maximum compression, i.e., $T_{Aj} \approx T_B = 3.042\,keV$. This implies a gain of 1.384 ($= T_{Aj}/T_A$) in temperature in the cycle.

To verify that the gain is indeed a result of the non quasi static nature of the expansion phase, the expansion to $x = 0.02\,m$ was also carried out in quasi static manner in the control simulation. For this simulation, we get T_{Aj}/T_A, implying that plasma loses all the energy it gained in the compression phase. Fig.3.10 shows the electron and ion distribution functions corresponding to T_A, T_{Aj}, and T_B for the quasi static compression-free expansion and quasi static compression-quasi static expansion cycles.

Fig.3.11, shows a comparison of the turbulent relaxation processes in one and two step free expansion simulations. E_Q, which is the total electrostatic potential energy in the cycle, remains small in the quasi static phase but increases rapidly in the non quasi static phase immediately following removal of the wall. It should be noted that the peaks of E_Q in the two step free expansion are significantly
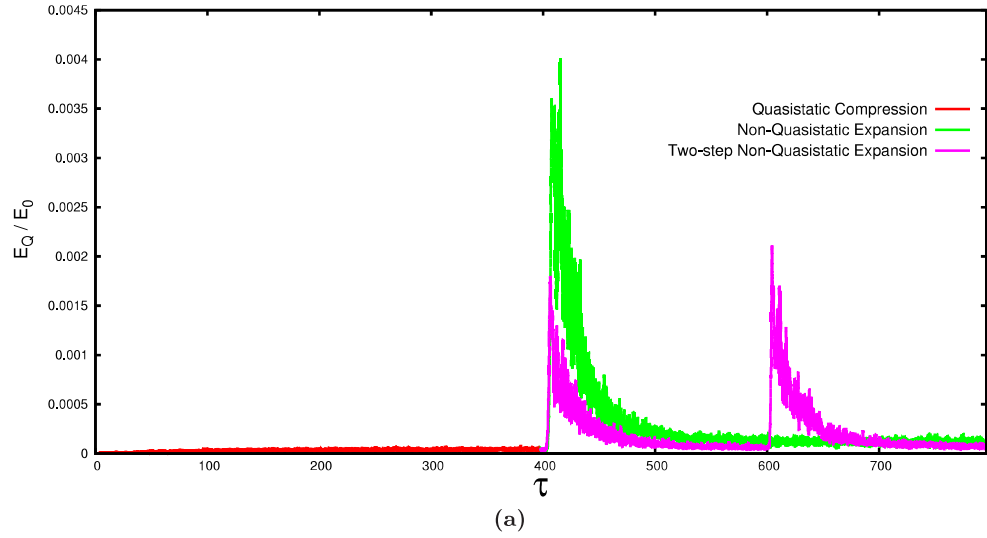
Figure 3.11: Comparison of relaxation processes in one and two step free expansion for the $m_i = m_e$ case. The total electrostatic energy E_Q is normalized by its initial value E_0 while the time axis is normalized by τ_p. In two step expansion, the peaks in E_Q/E_0 are smaller indicating that anomalous processes in this case are weaker.

smaller, nearly half of that in single step free expansion indicating that anomalous processes in two step expansion are weaker as compared to those in one step expansion. The simulation results in Figs. 3.10(a), 3.10(b), and 3.11 thus establish two important points: (a) the anomalous processes excited in non quasi static expansion can indeed lead to turbulent relaxation of plasma to equilibrium and (b) anomalous processes are weaker in multi step expansion as compared to one step expansion. We have shown that the plasma relaxes to equilibrium in the most turbulent case of free expansion; hence, relaxation is most likely for the proposed constrained expansion where turbulent relaxation processes are relatively weaker. Multiple applications of such quasi-static compression : non-quasi-static expansion cycles can raise the temperature of the plasma significantly.

3.5 Conclusions and discussions on PEPNEX

In PEPNEX1 we investigated using the 2D PIC code PEC2PIC, the inertia driven electrostatic relaxation process of a pure electron plasma from a state of non-equilibrium. A step density profile of high Brillouin ratio loaded off-equilibrium with unbalanced radial forces relaxes to a stable equilibrium state, through a radial breathing process comprising of three phases, namely an azimuthally symmetric steady breathing phase, an algebraic growth phase with non linearly triggered azimuthal modes, and finally a decay and saturation phase leading to steady equilibrium state. Unlike Diocotron modes in low density electron plasma, the radial breathing phenomenon is driven by inertia of the plasma, and hence can be considered more of a high Brillouin ratio phenomenon. For low Brillouin fractions ($f_b < 0.1$) growing Diocotron modes in their initial stages have been successfully described

by a first order perturbation analysis [1, 15]. A similar analytical treatment may not be possible for the breathing oscillations because even in the steady phase of the evolution, density fluctuations within the plasma have been observed to be as much as 50% for the higher f_b values (Fig. 3.3a-b). It is interesting that in spite of particles oscillating radially with large amplitudes about their mean positions the collective oscillatory motion remains totally coherent with a sharp frequency peak, in the initial steady breathing phase of the motion. These breathing oscillations are basically collective Bernstein modes of a cold electron plasma excited by the off-equilibrium loading of the profiles. Their frequencies match well the Bernstein mode frequency of a zero-temperature electron plasma predicted by linearized theory in the limit of small amplitude as seen for low f_b values, and deviate away form the theoretical curve for higher amplitudes.

It is clear that the amplitude of the breathing oscillations in the first phase depends on the inertia i.e. f_b of the plasma and also on the strength of the applied perturbation from equilibrium i.e. the magnitude of difference between the equilibrium rigid rotor frequency and the loading angular frequency. Hence it would be an interesting numerical experiment to tune the loading frequencies in such a way that only one of these two parameters varies and see how the breathing oscillations respond in terms of frequency and amplitude. A comparison of the deviation of the breathing frequency from the coriolis-shifted upper hybrid frequency, ω_{uh} produced as a result of these two controlled parameter variation would also be relevant and informative about the nature of these oscillations. Also studies on the effect of loading the plasma at varying temperatures on the dynamics of radial breathing would be in line with the kinetic model of Bernstein modes [17]. It could also be interesting to study the influence of elastic collisions of the electrons with background neutrals, on the dynamics of radial breathing modes, using the 2D3v PIC-with-MCC code PEC2PIC-3MCC.

In PEPNEX2 it is demonstrated that contrary to an existing theory [36] on influence of elastic collisions between electrons and background neutrals, the collisions themselves can not destabilize an otherwise stable electron cloud. This has been explained to be caused by the nature of extraction of potential energy from the cloud by the collisions. However the fact that the $e^- - Ar$ elastic and elastic-like excitation collision can not be the source of destabilization of the cloud does not imply that they can not influence other ongoing instabilities of the cloud. In fact in the very next chapter it will shown how non-ionizing collisions of electrons with background neutrals influence the dynamics of an ongoing ion resonance (two-stream) instability, through a feedback mechanism. It would also bee an interesting pure electron plasma numerical experiment to study the influence of electron-background non-ionizing collisions on the dynamics of the Kelvin-Helmholtz instability in an annular cylindrical electron cloud.

From the 2D cross-sectional dynamics of trapped pure electron plasmas in PEPNEX 1 and 2 we shifted focus to the axial dynamics of electron plasmas in finite length traps in PEPNEX3. PEPNEX3 demonstrates a scheme for controlled heating of a plasmas without driving the plasma far away from thermal equilibrium. The proposed scheme may be applied for axial heating of electron plasmas or other single species plasma in cylindrical traps by controlled variation of the end-plug potentials of

the trap. When the plasma is composed of two species with significant mass difference the scheme may be tweaked so that the cycle is quasi-static compression : non-quasi-static expansion for heavier species, and quasi-static compression : quasi-static expansion for the lighter species. In that case the heating scheme gives preferential heating of one species over the other. It may be interesting to carry out a 1D simulation of such a differential heating scheme with PEC1PIC.

So far we have discussed the numerical experiments performed with pure electron plasmas. In the next chapter the focus will be on numerical experiments performed with partially neutralized electron clouds, *i.e* 2-component nonneutral plasmas.

4

Partially Neutralized Electron Plasma Numerical EXperiments (PNEPNEX)

In the 2D numerical experiments of the previous Chapter, collisionless processes in pure electron plasma were investigated together with the influence of non-ionizing electron-background collisions on some of these processes. Purely 2D collisionless processes were simulated with the 2D PIC code PEC2PIC, and the 2D dynamics influenced by 3D non-ionizing electron-neutral collisions were simulated with the 2D3v PIC-with-MCC code PEC2PIC-3MCC. In this Chapter we propose to carry out simulations of collisionless dynamics, with, and without the influence of non-ionIzing electron-neutral collisions for a cylindrically trapped, partially neutralized electron cloud. The instability of interest in this set of simulations is the ion resonance instability.

The ion resonance instability is one of the fundamental instabilities of partially neutralized electron plasmas in cylindrical and toroidal magnetic traps. The first analytical model for this instability was developed by Levy *et al* in 1969 [70]. They showed that, under certain conditions, a stable equilibrium of a cylindrically confined electron cloud can be driven unstable by the addition of a certain fraction of ions resulting in excitation of an exponentially growing $l = 1$ Diocotron mode, where l is mode number. However this model is only applicable for equilibria in which a cylindrically trapped electron cloud of low Brillouin ratio is weakly neutralized by ions. A more generalized linear model for the ion resonance instability in cylindrical traps, was developed by Davidson and Uhm [1, 16] who described it as a rotating two-stream instability, in which the differential rotation between the electrons and ions in equilibrium, drove the instability; the rotation itself being a result of the radial self-electric field of the nonneutral plasma. This linearised model of the instability works for any cold equilibrium of the two component plasma in cylindrical confinement. The model shows that depending on the equilibrium parameters, one or more exponentially growing Diocotron modes may be excited on the plasma profile with the equilibrium condition determining the fastest growing Diocotron mode in the system. In the limit of low Brillouin ratio of electrons and weak neutralization by ions, the model produces results consistent with the resonance model by Levy *et al* [70], with the $l = 1$ Diocotron being the fastest growing mode. The model can also be extended to two stream instabilities between two cylindrically

confined plasma components having the same sign of charge [1]. Davidson and Uhm [71] further generalised this linear model, to include the effects of finite ion Larmor radius on the ion resonance instability. In this, more generalised version, the cold fluid model for the two components was replaced by a hybrid Vlasov-fluid model where the ions, at a certain temperature, are described by the Vlasov equation and the electrons are described as a cold fluid. Another analytical model for the instability induced by untrapped ions on a trapped electron cloud was introduced by Fajans [31]. This model describes the instability of an electron cloud in a Penning-Malmberg trap, caused by the presence of axially drifting ions that are produced by ionization of the background gas by the hot electrons; the drift of ions being towards the negatively charged electrostatic end-plugs. The model shows that in these conditions the instability of the electron cloud, grows algebraically rather than exponentially. The cold fluid, two-stream instability model [1, 16] was later numerically investigated by Chen [72] for a wide range of equilibria, which helped in comprehending the dependencies of the instability, in its linear phase, on the equilibrium parameters. The ion resonance instability in a modified Betatron accelerator, has also been modelled by Uhm and Davidson within the framework of Vlasov-Maxwell equations [73].

There have been extensive experimental investigation of the ion resonance instability in different configurations of electron plasma traps. In all these experiments, the ions were formed through ionization of the background gas by the heated electrons. In 1980, evidence of the instability in an electron cloud trapped in a magnetic mirror, was reported by Eckhouse *et al* [74]. Peurrung *et al* [75], Bettega *et al* [76], and Kabantsev and Driscoll [20] studied the instability in Penning-Malmberg trap experiments with electron plasmas. An experimental technique to control the growth of the ion-resonance instability in cylindrical traps, and thereby improve confinement of the electrons, has also been proposed by Bettega *et al* [77]. The proposed method involves application of axisymmetric ion removing fields, by methodically biasing separated, inner longitudinal sections of the cylindrical trap. Ion resonance instability has been observed and investigated in a nonneutral stellarator by Marksteiner *et al* [27]. It has also been studied in a partial toroid configuration of the electron trap by Stoneking *et al* [78] and Lachvani *et al* [25]. The latter have proposed ways to improve vacuum in the trap, in order to reduce creation of destabilizing ions by electron impact ionization of the background gas, and thereby enhance confinement of the electron plasma in the partial torus [25].

PNEPNEX1 (Partially Neutralized Electron Plasma Numerical EXperiments 1) aims to investigate the ion resonance instability in its nonlinear phase, with the help of numerical experiments using the 2D PIC code PEC2PIC [38]. A cylindrically confined nonnenutral cloud, composed of electrons partially neutralized by an ion species of single ionization and realistic mass, is simulated from different initial conditions in these numerical experiments. The initial conditions are a set of parametrically different unstable equilibria of the cloud, that excite different Diocotron modes in the evolution of the ion resonance instability. As all the initial equilibria are cold, the linear phase (or pure exponential growth phase) results of these simulations demonstrate an excellent agreement with the linearised cold

fluid, two stream instability model [1, 16](see Table I). The results obtained from the nonlinear phase of these simulations will constitute the main subject of PNEPNEX1 [38].

These ion resonance instability simulations of the PNEPNEX1 [38] were performed in an ideal scenario with a perfect vacuum as a background. In PNEPNEX2 [32] (Partially Neutralized Electron Plasma Numerical EXperiments 2) we have taken these simulations a notch closer to a usual experimental scenario by including the effect of elastic and excitation collisions of the electrons with background neutrals that could be present at experimental low pressures inside the trap. PNEP-NEX2 are 2D3v PIC-with-MCC simulations, performed with PEC2PIC-3MCC, that investigate how collisional relaxation of the electron cloud's profile can influence dynamics of the ion resonance instability happening due to the ion contamination of the cloud [32]. It must be mentioned here that the collisionless dynamics of the ion resonance (two-stream) instability simulated in PNEPNEX1 and PNEPNEX2, is adopted from Davidson and Uhm's model [16] described above, wherein the source of the two-stream instability, *i.e.* the differential rotation between the components, is a direct consequence of the mutual equilibrium of the two components in the 2D cross-section of the cylindrical trap. In electron-trap experiments there may be other mechanisms producing differential rotation between electrons and ions and thereby driving the two-stream instability. For instance in cylindrical traps the electrons and the ions can have different axial profiles which can result in differential rotation between the two components [75], while in toroidal traps the curvature drift can cause differential rotation between electrons and ions [78]. However irrespective of the source of the two-stream instability, the elastic and excitation collisions between electrons and background neutrals will influence it's dynamics through collisional relaxation of the electron cloud's profile.

4.1 PNEPNEX1: Linear and nonlinear evolution of the ion resonance instability in cylindrical traps

The theoretical background, numerical set-up, and results of the PNEPNEX1 are presented in the following subsections.

4.1.1 Background Formulation

The equilibrium of a cold (implying zero-temperature), collisionless, multispecies plasma magnetized in a cylindrical trap of infinite length is considered as the starting point of the analysis. Assuming the equilibrium properties to be axially uniform and azimuthally symmetric and approximating that the plasma evolves only electrostatically, the equilibrium can be described by the radial force balance on each component of the plasma. In general the force balance equation can be written for the jth component fluid element as, [1]

$$\frac{m_j v_{j\theta}^2(r)}{r} + e_j E_r(r) + e_j v_{j\theta}(r) B_z = 0, \tag{4.1}$$

4. PARTIALLY NEUTRALIZED ELECTRON PLASMA NUMERICAL EXPERIMENTS (PNEPNEX)

where the first term is the centrifugal force, the second term is the electric field force, and the third term is the Lorentz force. Here m_j and e_j are respectively the mass and the charge of the jth species, r is the radial co-ordinate, $v_{j\theta}$ is the azimuthal velocity of the fluid element, E_r is the radial electric field acting on the element, and B_z is the applied uniform axial magnetic field. The given quadratic equation can be solved for the equilibrium angular velocity of the jth component fluid element, $\omega_{rj}(r) = v_{j\theta}(r)/r$ as, [1]

$$\omega_j(r) = -\frac{\omega_{cj}\epsilon_j}{2}\left[1 \pm \left(1 - \frac{4}{\epsilon_0 r^2}\sum_k \frac{e_j e_k}{m_j \omega_{cj}{}^2}\int_0^r n_k(r')r'dr'\right)^{\frac{1}{2}}\right] \qquad (4.2)$$

Here the indices j and k denote plasma component, ϵ_j is the sign of e_j, $\omega_{cj} = |e_j|B_z/m_j$ is the cyclotron frequency of the jth component, n_k is the number density of kth component, and ϵ_0 is the permittivity of free space. Now, if the radial density profile of every component is a step function to the same radial extent having the form, $n_j(r) = n_j$ for $r < r_p$ and and $n_j(r) = 0$ for $r > r_p$ (where $r_p < R_w$), then the r-dependencies in the solution are removed and it reduces to two rigid-rotor frequencies given by [1]

$$\omega_{rj}^{\pm} = -\frac{\omega_{cj}\epsilon_j}{2}\left[1 \pm \left(1 - \frac{2}{\epsilon_0}\sum_k \frac{e_j e_k n_k}{m_j \omega_{cj}{}^2}\right)^{\frac{1}{2}}\right]. \qquad (4.3)$$

The solutions ω_{rj}^+ and ω_{rj}^- can be termed as the fast rotor mode and slow rotor mode respectively.

In the present study a two-component nonneutral plasma having this kind of a step density profiles is considered. The plasma is made up of a major component of electrons of density, n_e, and a minor component of ions of single ionization having a density, $n_i = fn_e$, where f is a constant fraction measuring the fractional charge neutralization provided by the ions. For this special case of equilibrium, the rigid rotor frequencies of Eq. (3) reduce to, [1]

$$\omega_{re}^{\pm} = \frac{\omega_{ce}}{2}\left[1 \pm \left(1 - \frac{2\omega_{pe}^2}{\omega_{ce}^2}(1-f)\right)^{\frac{1}{2}}\right], \qquad (4.4)$$

$$\omega_{ri}^{\pm} = -\frac{\omega_{ci}}{2}\left[1 \pm \left(1 + \frac{2\omega_{pi}^2}{\omega_{ci}^2}\frac{(1-f)}{f}\right)^{\frac{1}{2}}\right]. \qquad (4.5)$$

Here the subscript j has been replaced by e and i to denote electron component, and ion component respectively. Given that $0 < f \leq 1$ the quantity $F = 2\omega_{pe}^2(1-f)/\omega_{ce}^2$ has a similar significance as the Brillouin fraction, $f_b = 2\omega_{pe}^2/\omega_{ce}^2$ in pure electron plasma. This can be understood from Eq.(4), which shows that for the range of f-values given by $0 < f \leq 1$, the condition $0 \leq F \leq 1$ should be satisfied for a real solution for $\omega_{re}^{\pm}$. Hence F can be termed as the modified Brillouin fraction for the above equilibrium. An analysis of this pair of solutions shows that for $0 < f \leq 1$ (implying $0 \leq F \leq 1$) and any given ratio of the masses i.e. $0 < (m_i/m_e) < \infty$, the solutions $\omega_{re}^{\pm}$ and ω_{ri}^- have the same sense of rotation with their magnitudes ordered as $\omega_{re}^+ > \omega_{re}^- \geq \omega_{ri}^-$ (with $\omega_{re}^- = \omega_{ri}^-$ only for $f = 1.0$) while ω_{ri}^+

has the opposite sense of rotation and a greater magnitude than ω_{ri}^-. The important conclusion here is that for $0 < f < 1$ (meaning $0 < F \leq 1$), and $0 < (m_i/m_e) < \infty$, the solutions satisfy the inequality $\omega_{ri}^\pm \neq \omega_{re}^\pm$, which implies that such a two-component step density profile of nonneutral plasma should always have a differential rotation between its components in equilibrium. This differential rotation makes the equilibrium susceptible to a rotational form of the two-stream instability known as the ion resonance instability, which under suitable conditions can produce exponentially growing Diocotron mode(s) in the system. A linearised stability analysis of the equilibrium [1, 16] reveals that for a given combination of the equilibrium solutions $(\omega_{re}^\pm, \omega_{ri}^\pm)$ certain equilibrium points in the parametric space of f, F, m_i/m_e, and r_p/R_w (within their respective range of values) can be unstable and excite one or more growing Diocotron modes in the system while other points in the same parametric space can be stable. The growth rates and frequencies of the unstable modes can be determined by applying a first order perturbation analysis at the unstable equilibrium point [1, 16]. The set of numerical experiments described in Section 4.1 are simulations of the evolution of such a two-component step density profile loaded at different equilibrium points in the parametric space. For stable equilibrium loads the plasma components simply continue to rotate rigidly with their respective equilibrium angular velocities, as expected. For unstable equilibrium loads however, the differential rotation excites the same azimuthal mode(s) on both components, but with a phase difference. During the initial exponential growth phase of the mode(s), their frequencies and growth rates are found to be consistent with linearised calculations [1, 16]. In the nonlinear phase the plasma shows some interesting dynamics such as wave breaking on the ion cloud followed by substantial loss of heated ions to the wall through radial transport, and pinching of the peaks of the dominant azimuthal mode on the electron cloud followed by azimuthally symmetric tearing across the pinches into l sections where l is the mode number of the dominant mode. Late nonlinear phase dynamics include an inverse cascade of the torn sections of the electron cloud into a single cloud, and general phase mixing of the modes leading to the formation of a diffused profile from the initial step function. In Subsection 4.1.3 all the linear and nonlinear dynamics of the ion resonance instability are investigated.

4.1.2 Numerical Setup

All simulations of PNEPNEX1 were carried out for typical parameters found in experiments of cylindrical traps. [18], in particular, a wall radius, $R_w = 0.125m$, and axial magnetic field, $B_z = 0.015T$. The simulation time step, $\delta t = 10^{-11} sec$ is chosen much smaller than the cyclotron time period, $T_{ce} = 2.38 \times 10^{-9} sec$ of electrons, such that the code can well resolve the cyclotron motion of both ions and electrons. PIC-parameters used in the simulations are 87834 pseudo particles for each plasma component, on a 70×70 grid. As the actual population of the ions is a fraction, f of the electron population, the number of real ions represented by each ion pseudo-particle has also been scaled down to a fraction, f of the representation value of electron pseudo-particles.

The initial condition of the set of simulations are two-component step density profiles loaded with both the electron and ion component in the slow mode of rigid rotor equilibrium $(\omega_{re}^-, \omega_{ri}^-)$ at nine

different points in the parametric space of f, F, m_i/m_e, and r_p/R_w. The exact values of the loading parameters for each experiment are tabulated in columns 2 to 6 of Table 4.1. Based on these parameters the nine experiments have also been divided into two sets within the table. All experiments in a set have common values of the loading parameters $f_b = F/(1-f)$, m_i/m_e, and r_p/R_w, and are arranged in ascending (descending) order of the parameter f (F) (see Table 4.1). These two sets of simulations will be discussed separately in the following two subsections.

4.1.3   Results from two-component equilibrium loads at low f_b

Experiments 1 to 7 constitute the first set of Table. 4.1. In this set the loading parameters f_b, m_i/m_e, and r_p/R_w are fixed at the values of 0.02, 1836, and 0.5 respectively while the fractional neutralization, f takes increasing values in the range 0.05 to 1.0, from Expt. 1 to 7. All experiments in this set besides Expt. 6, are simulated till $\tau \approx 22674$. The simulation time for Expt. 6 is extended upto $\tau \approx 56685$.

The linear phase analysis of the ion resonance instability is performed with the help of the potential probes (Fig 4.1) which can pick up the frequencies of the excited Diocotron modes in the system. A FFT performed on the potential probes' signal in the linear phase (Fig. 4.1c) gives the individual frequencies, ω_s of the linearly growing Diocotron modes in the system (Column 9 of Table 4.1). A measure of an effective growth rate, $\alpha_s{}^{eff}$ (Column 11 of Table 4.1) due to all growing modes in the linear phase is obtained by fitting an exponential envelope on the linear growth phase of one probe's signal (Fig. 4.1d). Wherever analytical values of excited mode frequencies and their growth rates are available, these values (columns 7,8, and 10 of Table4.1) have been compared with the corresponding values obtained from simulation. It should be noted however that the analytical values of the growth rates are for individual modes whereas the growth rate obtained from the probe signal is an effective value for all growing modes in the system. It is interesting that for cases where there are multiple modes excited the value of the effective growth rate comes out to be close to the average value of individual analytical growth rates of the excited modes (as on Expt. 3 to 5). Precisely for this reason, the period of effective exponential growth of the probe signal due to multiple excited modes is not necessarily the extent of the actual linear phase of the profile evolution. Pure linear dynamics of the profile lasts only up to the time till which the fastest growing mode is linear, whereas the probe signal, growing at averaged growth rate, remains linear for typically longer periods due to the slower growing modes. However the energetics of the profile evolution gives an accurate measurement of the extent of the linear phase. The start of the energy exchange process between the components marks the beginning of the actual nonlinear phase of the system. This can also be verified by comparing the snapshots of the profile just before, and just after this point. Hence for all the experiments the extent of the linear phase is determined from the energetics of the system. For experiments 3 to 5 the frequencies of the slower growing modes in the system are not picked up by the probe in the short linear phase. In Experiment 6 the linear growth phase of the probe signal is too short-lived for an effective FFT to be performed for obtaining frequencies of excited modes. Experiment 7 has been loaded at a stable equilibrium point in the parametric space where there is no differential rotation
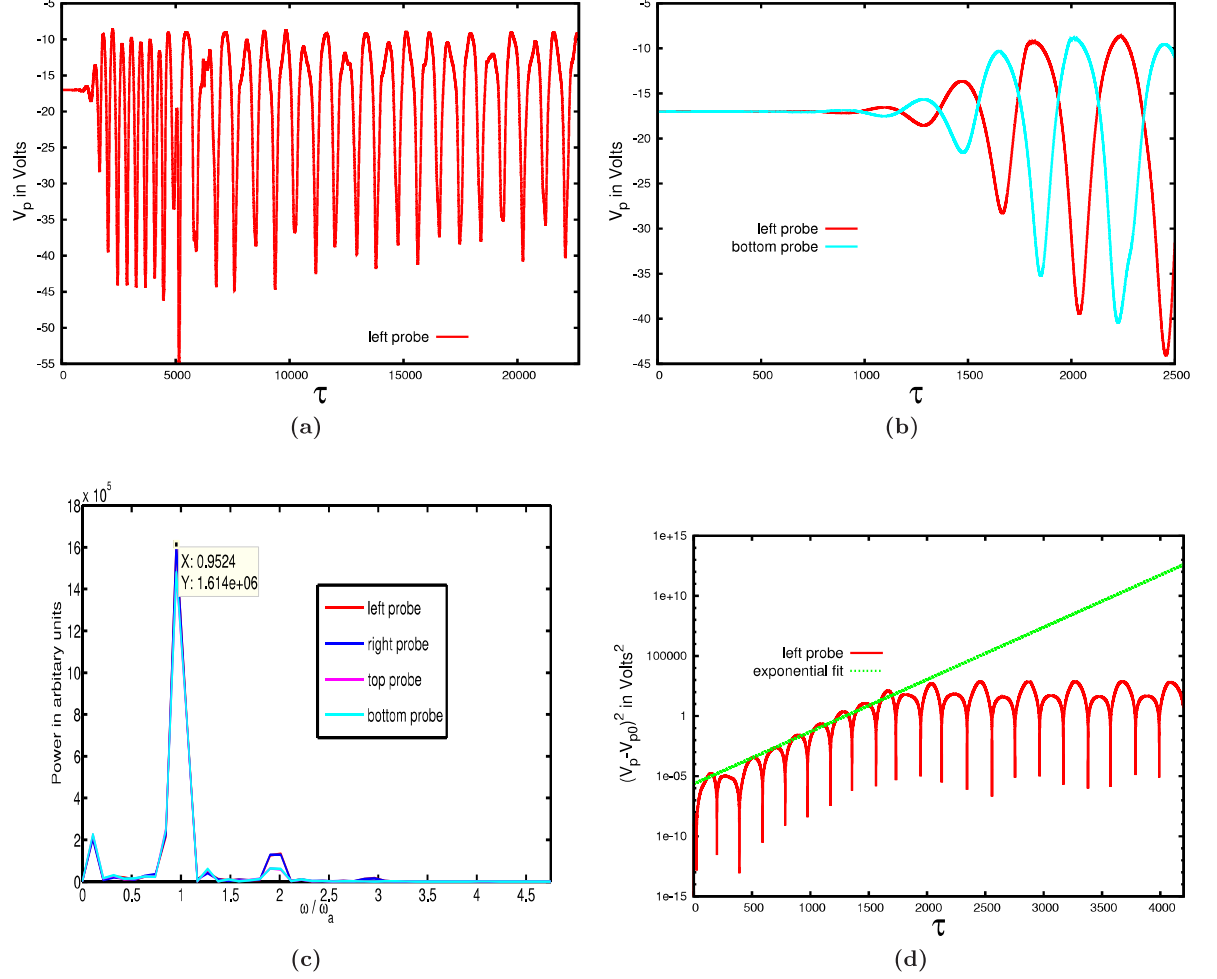
Figure 4.1: Potential-probe signal analysis for Expt. 3: (a) V_p is electrostatic potential recorded by the left probe. Normalized time, τ is in units of electron cyclotron time, *i.e.* $\tau = t/T_{ce}$. (b) is a zoomed in plot of the signals of two probes in the initial linear growth stage. This linear growth stage is analysed to measure the Diocotron frequency ω_s and the effective growth rate α_{eff} shown in Table I. In (c) an FFT is performed on the readings of the four probes in the linear growth stage to determine ω_s. Here the x-axis is angular frequency normalised by the analytical angular frequency of the $l = 2$ mode, $\omega_a = 6.597 \times 10^6$ rad/sec, and the y-axis is the power factor in arbitrary units. It is seen that the FFT plots of all the four probes are quite overlapped and peak at the same frequency. (d) is an exponential fit on the linear growth phase readings of the left probe used to measure α_{eff}. V_{p0} is the initial probe reading. The y-axis is in log scale while time is in linear scale.

Table 4.1: Results from different cases of equilibrium loading: The effective growth rate, α_s^{eff} for the combination of excited Diocotron modes, and the frequencies ω_s of each mode, are obtained from analysis of the potential probes' signal in the linear growth phase. These values are tabulated along with the theoretical growth rates, α_a and frequencies, ω_a of the Diocotron modes. Here l_a represents the theoretically predicted mode number of excited modes. The equilibrium loading parameters for each experiment of column 1 are tabulated in columns 2 to 6. The table is also segmented by a horizontal line into two sets, in each of which all experiments have a common value of the secondary parameter, $f_b = F/(1-f)$.

Expt.	f	F	(m_i/m_e)	r_p/R_w	ω_{re},ω_{ri}	l_a	$\omega_a(rad/sec)$[a]	$\omega_s(rad/sec)$	$\alpha_a(rad/sec)$[b]	$\alpha_s^{eff}(rad/sec)$
1	0.05	0.019	1836.0	0.5	$\omega_{re}^-,\omega_{ri}^-$	1	3.505×10^6	3.491×10^6	0.746×10^6	0.700×10^6
2	0.15	0.017	1836.0	0.5	$\omega_{re}^-,\omega_{ri}^-$	1	2.827×10^6	2.792×10^6	0.947×10^6	0.96×10^6
3	0.3	0.014	1836.0	0.5	$\omega_{re}^-,\omega_{ri}^-$	1	1.894×10^6	imperceptible	1.308×10^6	
						2	6.597×10^6	6.283×10^6	2.540×10^6	2.100×10^6
4	0.4	0.012	1836.0	0.5	$\omega_{re}^-,\omega_{ri}^-$	1	1.705×10^6	imperceptible	1.231×10^6	
						2	5.680×10^6	5.026×10^6	2.924×10^6	
						3	10.053×10^6	10.050×10^6	2.924×10^6	2.215×10^6
5	0.5	0.01	1836.0	0.5	$\omega_{re}^-,\omega_{ri}^-$	1	0.770×10^6	imperceptible	1.077×10^6	
						2	4.233×10^6	imperceptible	2.771×10^6	
						3	8.466×10^6	8.375×10^6	3.386×10^6	2.450×10^6
6	0.85	0.003	1836.0	0.5	$\omega_{re}^-,\omega_{ri}^-$	multiple	values unavailable	too short linear phase	values unavailable	3.500×10^6
7	1.0	0.00	1836.0	0.5	$\omega_{re}^-,\omega_{ri}^-$	no mode	none	none	no growth	no growth
8	0.1	0.9	1836.0	0.5	$\omega_{re}^-,\omega_{ri}^-$	no mode	none	2.713×10^7 $(l=1)$	no growth	0.040×10^7
9	0.15	0.85	1836.0	0.5	$\omega_{re}^-,\omega_{ri}^-$	1	5.387×10^7	5.236×10^7	1.89×10^7	1.80×10^7

[a]Estimated from Fig. 8b and 9b of Ref. 3
[b]Estimated from Fig. 8a and 9a of Ref. 3

between the components ($\omega_{re}^{-} = \omega_{ri}^{-} = 0$), and as such there are no unstable modes excited in this experiment throughout the simulation.

The full linear and nonlinear evolution of the ion resonance instability in this set of simulations will be described in detail for four selected profiles out of the seven, viz. Experiments: 2, 3, 5, and 6, as each of these profiles' evolutions is dominated by a different Diocotron mode. Snapshots of the selected profiles, at different stages in their evolution, will be used as illustrations for the plasma dynamics being described (Figures 4.2, 4.4, 4.8, and 4.10). It is to be noted that in these snapshots both components are represented by the same number of pseudo-particles, but ratio of the number of real particles of each component depends on f. To understand the energetics of the process of instability, the potential and kinetic energies of the two plasma components have been plotted as a function of time for each of these profiles, along with their total energies (Figures 4.3, 4.5, 4.9, and 4.11). Plots showing the population of trapped electrons and ions as a function of time for all simulations in Set 1 (Fig. 4.12 and 4.13) will be useful in comprehending the mechanism of particle loss for the two components and understanding how fractional neutralization parameter, f influences cross-field transport of electrons and ions in these simulations. Experiment 3 will be described with help of some additional diagnostics such as a plot of the magnetic and kinetic, angular momentum of both components as a function of time along with the total angular momentum of the system (Fig. 4.6), and a set of plots showing the variation in the radial and azimuthal velocity distribution functions with time in the early nonlinear stages of the instability (Fig. 4.7). Besides these diagnostics, an example of the potential probe data analysis in linear phase, has also been shown earlier using the probe signal of Expt. 3 (Fig. 4.1).

In Expt. 2 the differential rotation between the two components makes the equilibrium unstable, and leads to the growth of an $l = 1$ mode in the system. Analysis of the energetics (Fig. 4.3) shows that the energy exchange process between the two components begins roughly from $\tau \approx 4000$ which also marks the end of the linear phase of the evolution. Analysis of the potential probe signal in the linear phase shows that the $l = 1$ mode has an angular frequency of 2.792×10^6 rad/sec and a growth rate of 0.96×10^6 rad/sec. Fig. 4.2 shows selected snapshots of the profile at different stages of the simulation. Of these, Fig. 4.2a-b can be considered to be in the linear phase while the rest are in the nonlinear phase of the evolution. Unlike higher modes of the two stream instability that are excited with a phase difference of π between the two components, the $l = 1$ mode is initially excited on both components at the same phase i.e. without any azimuthal separation between the two clouds. However the initial phase synchronization is lost as the two clouds move increasingly out of phase in their $l = 1$ orbits, evident from the increasing azimuthal separation between them (Fig. 4.2b-e). The evolving phase difference between the two components during the linear and early nonlinear stages of the instability, is also a unique feature of the $l = 1$ mode. In the nonlinear phase the ion profile also undergoes a growing surface filamentation at the end farthest from the electron cloud (Fig. 4.2d-i). 100% particle confinement lasts only up to $\tau \approx 4500$ after which the ion concentration is drastically reduced by their thermal transport to the grounded walls (Fig. 4.13), while the electron population remains conserved till the end of the simulation (Fig. 4.12). The loss of ions can be understood from

(a) $\tau = 0.0$

(b) $\tau = 3684.511$

(c) $\tau = 3967.935$

(d) $\tau = 4156.885$

(e) $\tau = 4345.834$

(f) $\tau = 4440.309$

(g) $\tau = 4723.732$

(h) $\tau = 4912.682$

(i) $\tau = 5007.157$

(j) $\tau = 5101.631$

(k) $\tau = 5196.106$

(l) $\tau = 5290.580$

(m) $\tau = 5574.004$

(n) $\tau = 6046.378$

(o) $\tau = 6235.327$

(p) $\tau = 6518.751$

(q) $\tau = 8030.345$

(r) $\tau = 22673.917$
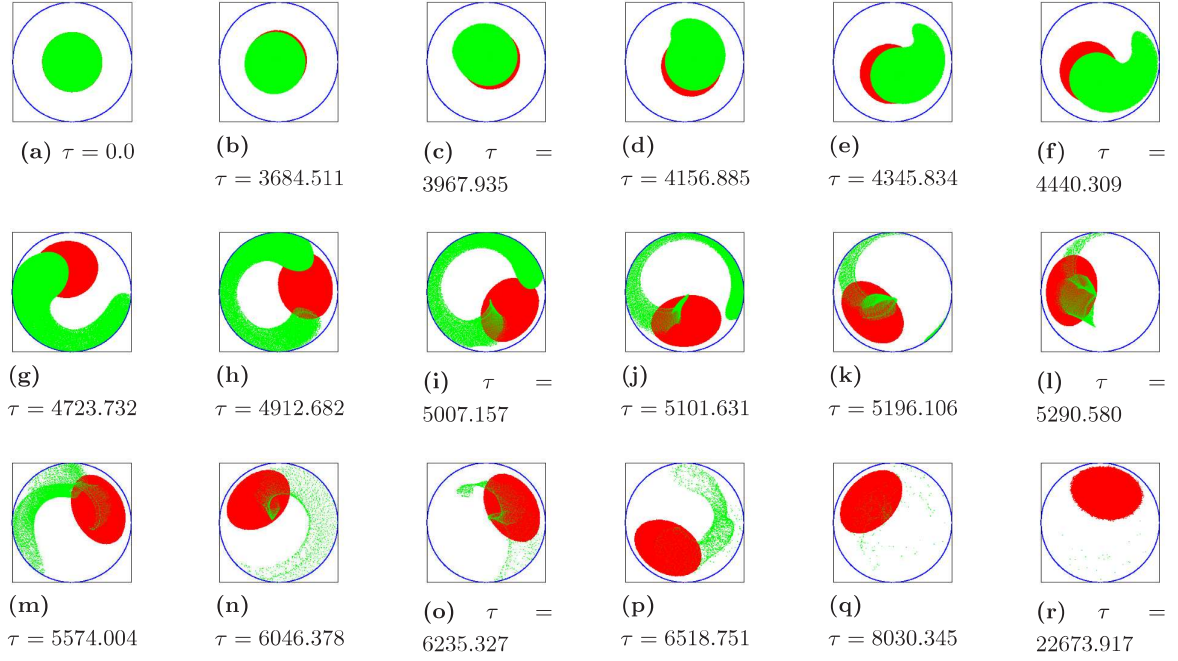
Figure 4.2: Snapshots of pseudo particles (electrons in red and ions in green) for an initial unstable equilibrium that excites a dominant $l = 1$ Diocotron mode in the profile (Expt. 2 of Table 4.1). Below each snap, the time elapsed is mentioned in normalised units of electron cyclotron time, *i.e.* $\tau = t/T_{ce}$.
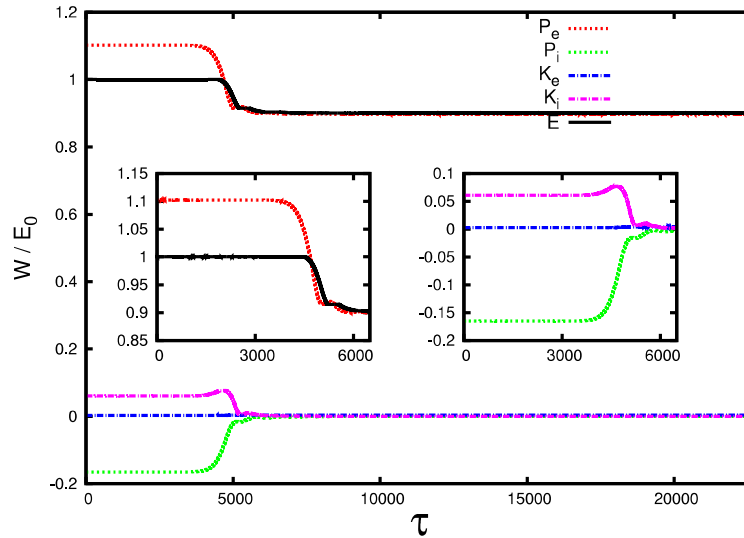
Figure 4.3: Energy curves of Expt. 2 of Table 4.1 : W represents the energy components in the legend, E_0 is the initial total energy, and $\tau = t/T_{ce}$. P_e and P_i are the potential energies of electrons and ions respectively. K_e and K_i are the kinetic energies of electrons and ions respectively. E is the total energy of the system. The energy components are normalised by E_0 and plotted as a function of time. The time axis is normalised by the cyclotron time period of electrons, T_{ce}. *Inset:* Zoomed-in snaps of initial sections of these curves are shown here for clarity.

the energetics of the instability (Fig 2). Between $\tau = 4000$ and $\tau = 4500$ of the nonlinear phase (Fig. 4.2d-f), the initially cold ions not only gain potential energy but also thermal kinetic energy at the expense of potential energy of the electrons. The gain in thermal energy of heavier ions increases their Larmour radii that results in their radial transport and eventual loss to the grounded wall. The transfer of potential energy from the electrons to the ions continues till $\tau \approx 6000$ but after $\tau \approx 4500$ the total kinetic energy of ions drops due to heavy loss of particles between $\tau \approx 4500$ and $\tau \approx 6000$ (Fig. 4.2g-m). At $\tau \approx 6000$ the ion concentration reduces to 3.7% of its initial value (Fig. 4.13). At this point the energy exchange process ceases and the electron cloud now continues to make stable nonlinear $l = 1$ orbits very close to the circular boundary; its profile shape having become elliptical due to close proximity to the grounded wall (Fig 4.2n-r). By the end of the simulation all ions have been lost while electron population remains intact at 100% of its initial value.

In Expt. 3 the initial unstable equilibrium conditions are such that the ion resonance instability is dominated by a $l = 2$ mode in the linear growth phase which lasts up to $\tau \approx 1400$. As with the other experiments, the end of the linear phase is marked by the start of the energy exchange process in the energetics of the simulation (Fig. 4.5). Fig. 4.1 shows the potential probe analysis for this experiment. It can be seen from Fig. 4.1c-d that during the linear growth phase the $l = 2$ mode has an angular frequency of 6.283×10^6 rad/sec and there is a effective growth rate (mainly due the $l = 2$ mode) of 2.1×10^6 rad/sec in the system.

Fig.4.4 shows the evolution of the profile through the simulation. Fig. 4.4a-d are in the linear phase while the remaining snapshots of Fig. 4.4 are in the nonlinear phase of the evolution. The $l = 2$ mode is excited with a phase difference of π between the two components which implies an azimuthal separation, $\Delta\theta = \pi/2$ between the peaks of the mode on the two components (as $l\Delta\theta = \pi$). Hence the two clouds acquire ellipticity in perpendicular direction to each other (Fig. 4.2b-c). The phase difference between the two components is maintained through the linear and early nonlinear stages of the simulation (Fig. 4.4b-e) before the ion profile gets diffused through cross-field transport and phase mixing. In the nonlinear phase the elliptical ion cloud undergoes wave breaking at its radially stretching vertices while the elliptical electron cloud undergoes a gradual pinch from its radially stretching vertices towards the centre, along its major axis (Fig 4.4d-e).

Fig. 4.12 and Fig. 4.13 shows that 100% particle confinement lasts up to $\tau \approx 1650$ after which the ion count plummets because of their radial transport to the walls while the number of electrons remain nearly conserved up to $\tau \approx 5000$. The energetics of the system (Fig. 4.5) show that from the start of the nonlinear phase at $\tau \approx 1400$ up to $\tau \approx 1650$ (Fig. 4.4e) the initially cold ions not only gain potential energy but also thermal kinetic energy at the expense of the potential energy of electrons. The increase in thermal energy of the heavier ions results in their radial transport and eventual loss to the wall as in Expt. 2 (Fig. 4.13). The transfer of potential energy from the electrons to the ions continues till $\tau \approx 6000$ but after $\tau \approx 1650$ the total kinetic energy of ions drops due to heavy loss of ions between $\tau \approx 1650$ and $\tau \approx 6000$ (Fig. 4.4f-w). At $\tau \approx 6000$ the ion concentration reduces to 2.9% of its initial value (Fig 13).

(a) $\tau = 0.0$

(b) $\tau = 1133.696$

(c) $\tau = 1228.170$

(d) $\tau = 1322.645$

(e) $\tau = 1511.594$

(f) $\tau = 1700.544$

(g) $\tau = 1889.493$

(h) $\tau = 2078.442$

(i) $\tau = 2172.917$

(j) $\tau = 2456.341$

(k) $\tau = 2645.290$

(l) $\tau = 2834.240$

(m) $\tau = 3495.562$

(n) $\tau = 4345.834$

(o) $\tau = 4818.207$

(p) $\tau = 5101.631$

(q) $\tau = 5196.106$

(r) $\tau = 5290.581$

(s) $\tau = 5385.055$

(t) $\tau = 5479.530$

(u) $\tau = 5574.004$

(v) $\tau = 5668.479$

(w) $\tau = 5857.428$

(x) $\tau = 6329.802$

(y) $\tau = 6613.226$

(z) $\tau = 22673.917$
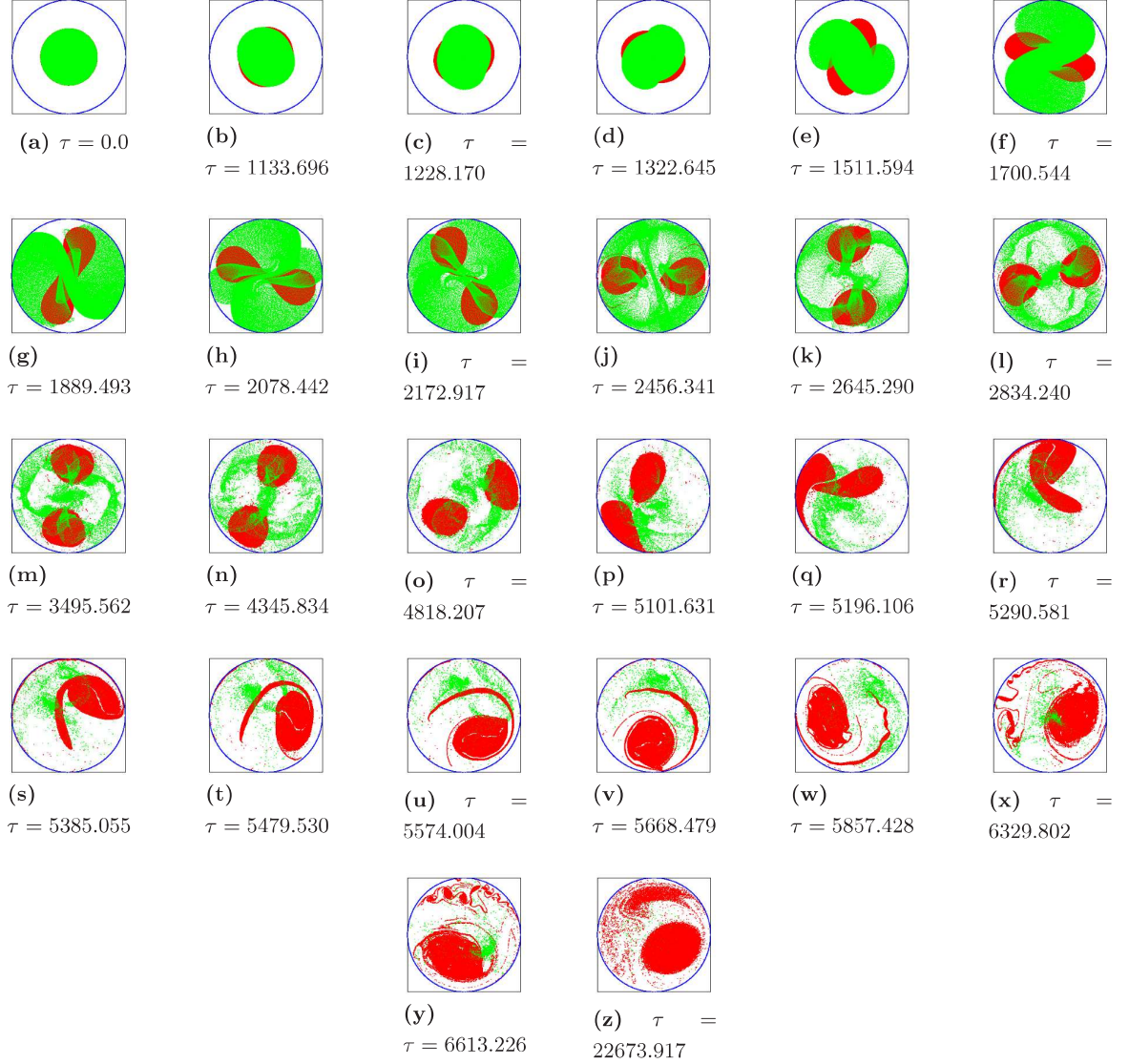
Figure 4.4: Snapshots of pseudo particles (electrons in red and ions in green) for an initial unstable equilibrium that excites a dominant $l = 2$ Diocotron mode in the profile (Expt. 3 of Table 4.1). Below each snap, the time elapsed is mentioned in normalised units of electron cyclotron time, *i.e.* $\tau = t/T_{ce}$.
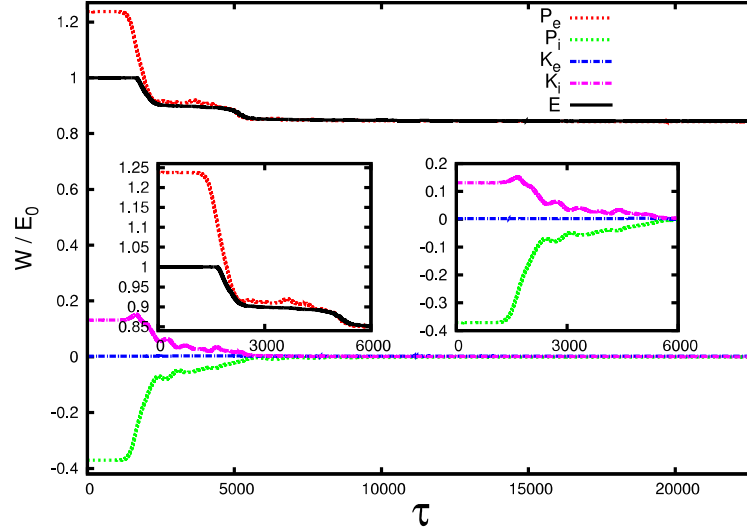
Figure 4.5: Energy curves of Expt. 3: W represents the energy components in the legend, E_0 is the initial total energy, and $\tau = t/T_{ce}$. P_e and P_i are the potential energies of electrons and ions respectively. K_e and K_i are the kinetic energies of electrons and ions respectively. E is the total energy of the system. The energy components are normalised by E_0 and plotted as a function of time. The time axis is normalised by the cyclotron time period of electrons, T_{ce}. *Inset:* Zoomed-in snaps of initial sections of these curves are shown here for clarity.
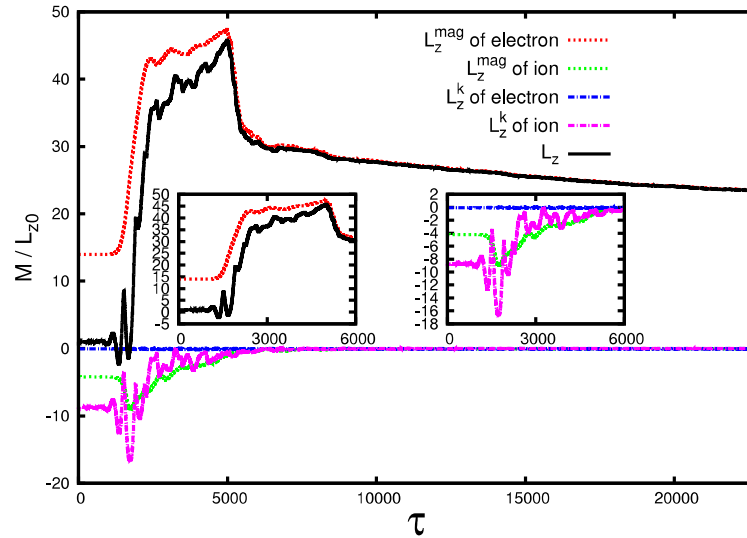
Figure 4.6: Angular Momentum curves of Expt. 3: M represents the angular momentum components in the legend, L_{z0} is the initial total angular momentum, and $\tau = t/T_{ce}$. The magnetic component of the angular momentum $L_z{}^{mag}$ of both species, and the kinetic component of the angular momentum, $L_z{}^k$, of both species, are plotted as a function of time along with the total angular momentum of the plasma, L_z. *Inset:* Zoomed-in snaps of initial sections of these curves are shown here for clarity.
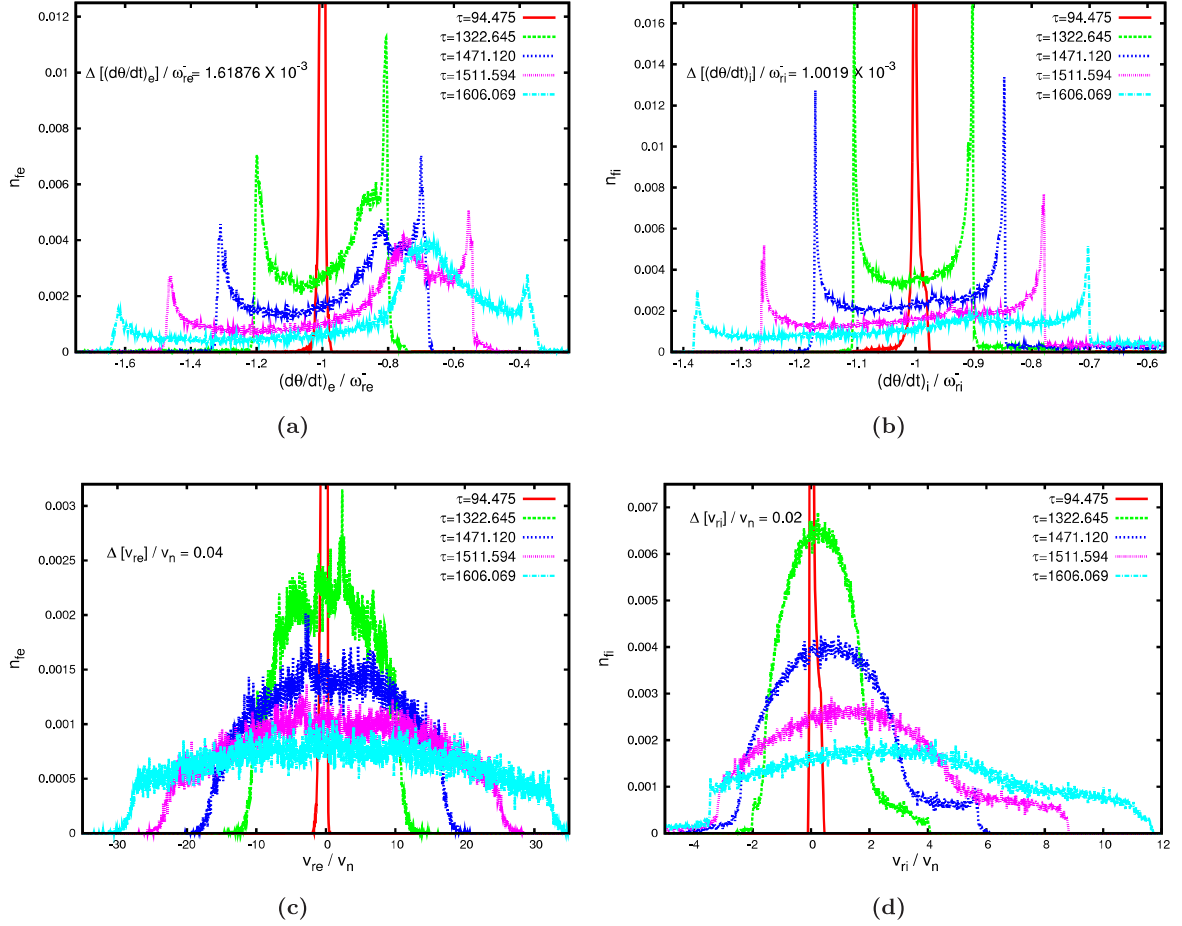
Figure 4.7: Zoomed in plots of the distributions in angular velocity and radial velocity, of electrons and ions, in the early nonlinear stages of Expt. 3, before the loss of ions. (a) and (b) are the angular velocity distributions of electrons and ions respectively. (c) and (d) are the radial velocity distributions of electrons and ions respectively. ω_{re}^{-}, ω_{ri}^{-}, and τ are predefined normalising constants. Normalising velocity, $v_n = 10000$ m/s. n_{fe} and n_{fi} represent fraction of electrons and fraction of ions corresponding to the velocity. The velocity-intervals in which the particles are binned are indicated in the top left corners of each plot.

4.1 PNEPNEX1: Linear and nonlinear evolution of the ion resonance instability in cylindrical traps

Between the start of the nonlinear phase at $\tau \approx 1650$ and the time, $\tau \approx 5000$, up to which the total number of electrons is nearly conserved (Fig. 4.12), there are some interesting dynamics of the electron cloud. During this interval the electron cloud first gradually pinches off into two identical clouds arranged axisymmetrically (Fig. 4.4f-n), and then gradually there is a shift from the axisymmetry in the arrangement of the two electron clouds as they come closer azimuthally (Fig. 4.4o). With this axially asymmetric arrangement the centre of mass of electrons gets displaced from the central axis, indicating that an $l = 1$ mode is now dominant. From $\tau \approx 5000$ to $\tau \approx 6000$ the electron population drops to 83% of its initial value (Fig. 4.12), as the two electron clouds undergo a complex inverse cascading process that results in their recombination to a single cloud configuration (Fig. 4.4p-w). $\tau \approx 6000$ marks the end of the significant loss period of electrons and also the end of the energy exchange processes in the system (Fig 4.5).

Beyond $\tau \approx 6000$ up to the end of the simulation the electron population remains nearly stable (Fig. 4.12) as the recombined electron cloud makes stable nonlinear $l = 1$ orbits close to the wall (Fig. 4.4x-z). The protruding filaments on the surface of the electron cloud that are reminiscent of the merging process that led to its formation also get diffused through Kelvin-Helmholtz instability. At the end of the simulation, electron and ion populations decrease to 75.51% and 0.3% of their respective initial values (Fig. 4.12 and Fig. 4.13).

Fig. 4.6 shows the variation of the different angular momentum components of the system as a function of time. Because the direction of the axial magnetic field, B_z is chosen into the plane of the paper the equilibrium rigid rotations in the slow mode of both components has a clockwise sense. Hence the initial kinetic angular momentum for both components (Eq. 2.105) is a negative quantity in Fig. 4.6 . For the same reason the magnetic angular momentum of electrons is a positive quantity while that of ions is a negative quantity. From the start of the nonlinear phase till the time, $\tau \approx 1650$, up to which there is 100% conservation of both components (Fig. 4.12 and Fig. 4.13), the magnitudes of the magnetic angular momentum of both components increases because the pinching of the electron cloud as well as the combined effect of wave breaking of the ion cloud and ion heating, results in a net radial transport of particles of their respective components. The magnitude of magnetic angular momentum of electrons continues to increase till $\tau \approx 5000$ as the pinching process continues while the magnitude of magnetic angular momentum of ions drops after $\tau \approx 1650$ because of particles loss.

To show that the ion resonance instability causes collisionless heating of the plasma, the distribution of radial and azimuthal velocities of both components has been plotted in the early nonlinear stages of the instability before the loss of ions commences (Fig. 4.7). As both components are initially cold the value of the distribution functions at $\tau = 0$ is a delta function. Again the negative values of the angular velocities in Fig. 4.7a-b is because of the chosen direction of B_z.

Expt. 5 has a dominant $l = 3$ mode excited by its loading parameters. The energetics (Fig. 4.9) and the potential probe analysis reveals that the linear phase lasts till $\tau \approx 1130$ during which the mode has a frequency of 8.375×10^6 rad/sec and the effective growth rate rate of the instability (mainly due to the $l = 3$ mode) is 2.450×10^6 rad/sec. Among the snapshots of Fig. 4.8, Fig. 4.8a-c
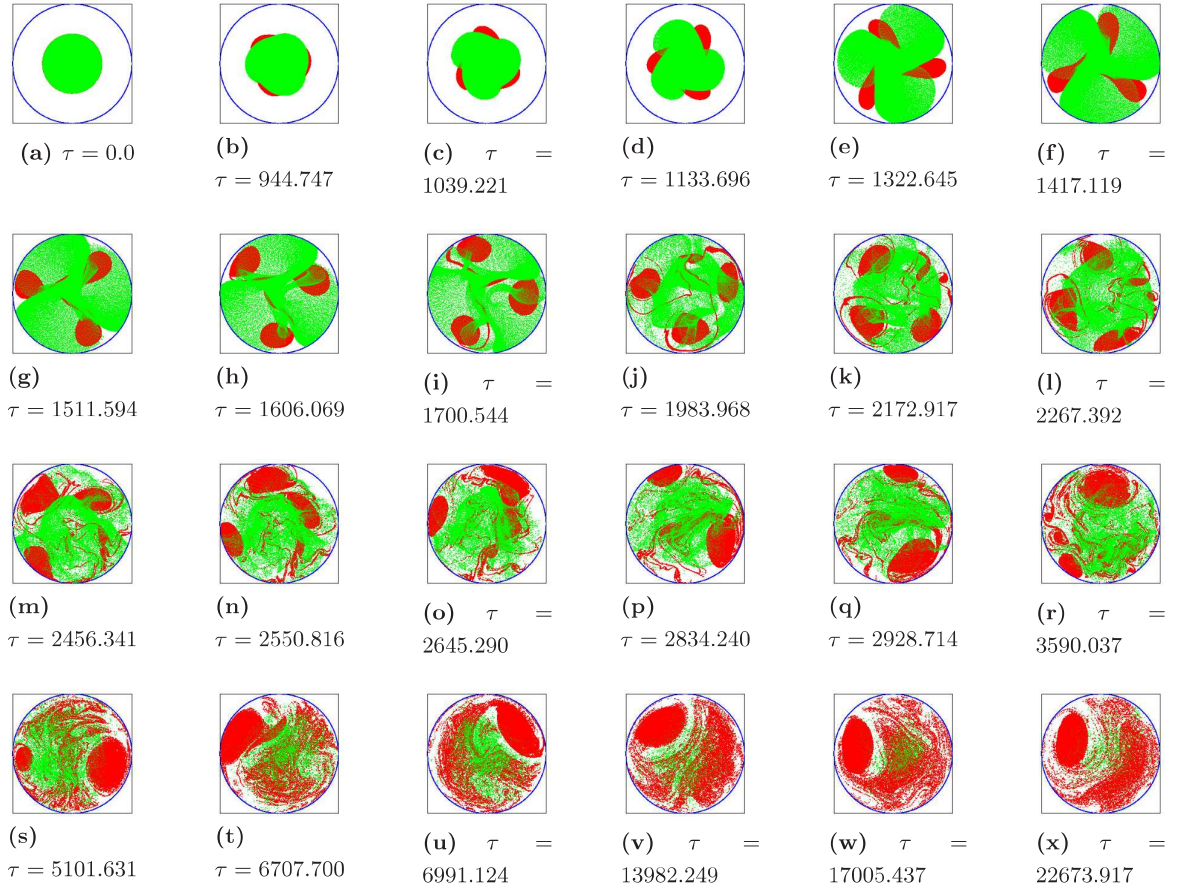
Figure 4.8: Snapshots of pseudo particles (electrons in red and ions in green) for an initial unstable equilibrium that excites a dominant $l = 3$ Diocotron mode in the profile (Expt. 5 of Table 4.1). Below each snap, the time elapsed is mentioned in normalised units of electron cyclotron time, *i.e.* $\tau = t/T_{ce}$.
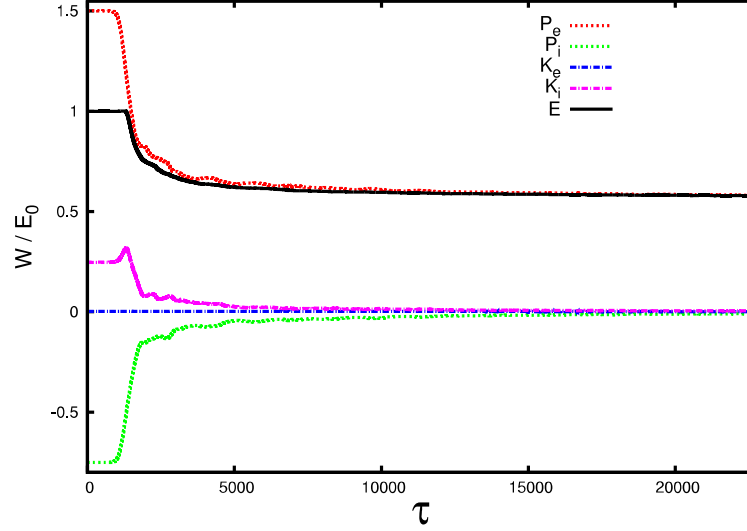
Figure 4.9: Energy curves of Expt. 5: W represents the energy components in the legend, E_0 is the initial total energy, and $\tau = t/T_{ce}$. P_e and P_i are the potential energies of electrons and ions respectively. K_e and K_i are the kinetic energies of electrons and ions respectively. E is the total energy of the system. The energy components are normalised by E_0 and plotted as a function of time. The time axis is normalised by the cyclotron time period of electrons, T_{ce}.

are in the linear phase, while the remaining snapshots are in the nonlinear phase of the instability. In the linear phase there is steady equilateral-triangulation of the two clouds at a phase difference of π which implies an azimuthal separation, $\Delta\theta = \pi/3$ between the peaks of the $l = 3$ mode on the two components (Fig. 4.8b-c). The mode continues to evolve with this phase difference between the components through the early nonlinear stages (Fig. 4.8d-e) before the ion profile gets diffused through cross-field transport and phase mixing. In the nonlinear phase there is also wave breaking at the stretching vertices of the ion cloud, and a gradual pinch from the stretching vertices of the electron cloud towards the centre (Fig. 4.8d-e). 100% particle conservation lasts up to $\tau \approx 1280$ after which there is rapid fall in ion population (Fig. 4.13). Electron population remains conserved up to $\tau \approx 1680$ after which there is loss of electrons right up to the end of the simulation (Fig. 4.12). The energetics of the simulation (Fig. 4.9) shows that from the start of the nonlinear phase up to $\tau \approx 1280$ (Fig. 4.8d) the potential energy of the electrons gets transferred into the potential and kinetic, energy of the ions, through the instability. After $\tau \approx 1280$ the heated ions undergo rapid radial transport and loss to the grounded wall, as explained in Expt. 2. Potential energy from electrons continues to be pumped into the potential energy of ions up to $\tau \approx 5000$, but after $\tau \approx 1280$, the total kinetic energy of ions falls due to rapid loss of ions. At $\tau \approx 5000$ the energy exchange process ceases and all energy components stabilize, with the electron and ion populations at 73.01% and 15.22% of their initial values (Fig. 4.12 and Fig. 4.13). The dynamics of the electron cloud from the start of the nonlinear phase up to $\tau \approx 7000$ (Fig. 4.8d-r) involves pinching off into three identical daughter clouds (Fig. 4.8d-k), after which the three electron clouds merge through an inverse cascading process (Fig. 4.8l-u). After $\tau \approx 7000$ the
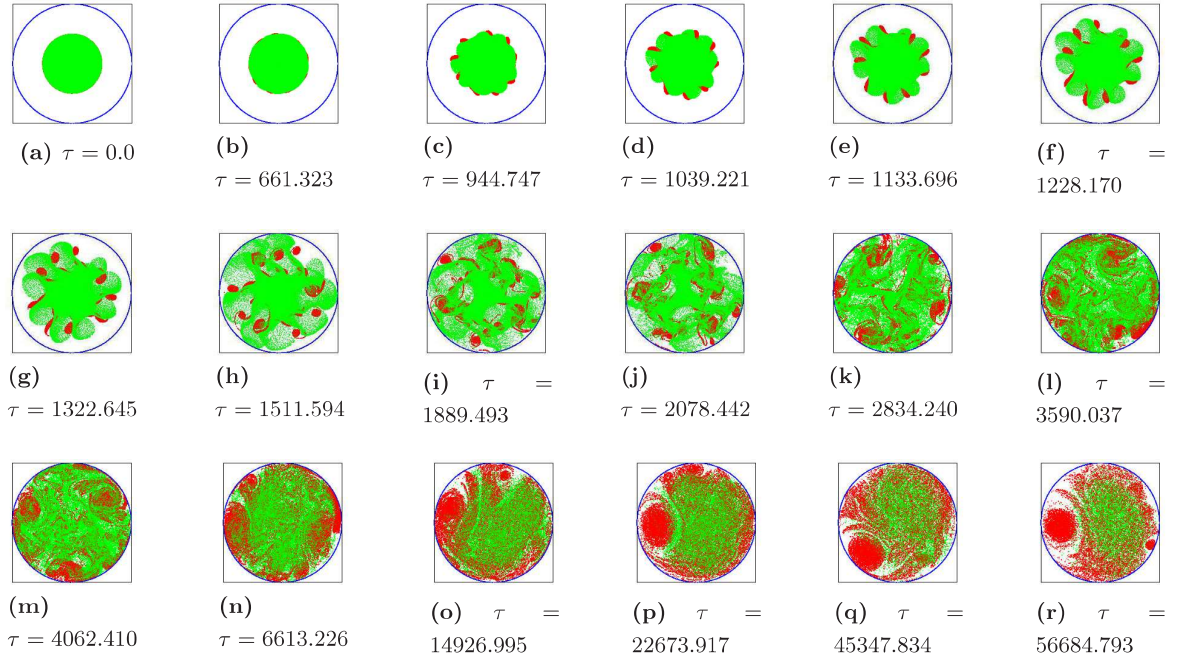
Figure 4.10: Snapshots of pseudo particles (electrons in red and ions in green) for an initial unstable equilibrium that excites a dominant $l = 9$ Diocotron mode in the profile (Expt. 6 of Table 4.1). Below each snap, the time elapsed is mentioned in normalised units of electron cyclotron time, *i.e.* $\tau = t/T_{ce}$.

merged cloud continues to make nonlinear $l = 1$ orbits close to the wall, till the end of the simulation (Fig. 4.8v-x). By the end of the simulation electron population decreases to 55.81% of its initial value (Fig. 4.12), while the ion population is reduced to 2.51% of its initial value (Fig. 4.13).

In Expt. 6, the loading parameters are such that the two-stream instability grows in the system via multiple Diocotron modes. The energetics (Fig. 4.11) and the potential probe analysis shows that the linear growth phase lasts up to $\tau \approx 730$, during which the instability grows in the system at an effective growth rate of 3.5×10^6 rad/sec. The linear phase of the probe signal is too short for determining frequencies of the linear modes. Among the snapshots of Fig. 4.10, Fig. 4.10a-b are in the linear phase while the rest are all in the nonlinear phase of the evolution. In the snapshots of the linear and early nonlinear stages (Fig. 4.10b-g), a growing $l = 9$ mode, excited with a phase difference of π between the two components (i.e. an azimuthal separation of $\pi/9$ between the modal peaks on the two components), is the only mode that can be visibly distinguished. 100% particle conservation lasts up to $\tau \approx 1400$, after which the ions are first to be lost while the electron population continues to be conserved up to $\tau \approx 1870$ (Fig. 4.12 and Fig. 4.13). The energetics of the simulation (Fig. 4.11) shows that from the start of the nonlinear phase up to $\tau \approx 1400$ the potential energy of the electron component is transferred to the ion component in the form of ion potential energy and ion thermal energy. During this interval (Fig. 4.10c-g) the nonlinear growth of the $l = 9$ mode on the ion cloud produces wave breaking at the 9 azimuthal peaks of the cloud, as the peaks continue to attain greater
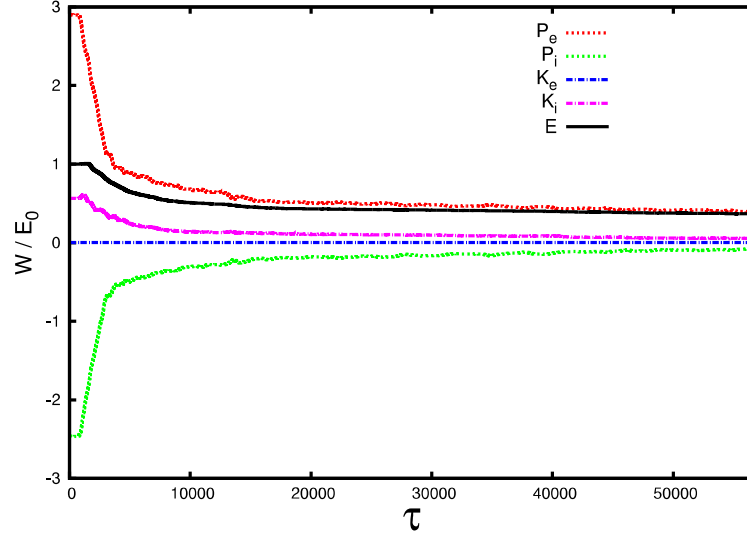
Figure 4.11: Energy curves of Expt. 6: W represents the energy components in the legend, E_0 is the initial total energy, and $\tau = t/T_{ce}$. P_e and P_i are the potential energies of electrons and ions respectively. K_e and K_i are the kinetic energies of electrons and ions respectively. E is the total energy of the system. The energy components are normalised by E_0 and plotted as a function of time. The time axis is normalised by the cyclotron time period of electrons, T_{ce}.

radial amplitude. On the electron component, the nonlinear growth of the same mode, causes a gradual pinch from the 9 radially stretching peaks towards the centre. After $\tau \approx 1400$ there is loss of heated ions to the walls, as in the above experiments. This causes the kinetic energy of ions to fall, but the ion potential energy continues to rise at the expense of the potential energy of electrons up to $\tau \approx 15000$ (Fig. 11). $\tau \approx 15000$ marks the end of the energy exchange process (Fig. 4.11), with the electron and ion populations having reduced to 46.91% and 29.82% of their respective initial values (Fig. 4.12 and Fig. 4.13). The dynamics of the electron cloud between $\tau \approx 1400$ and $\tau \approx 15000$ (Fig. 10h-q) involves fragmentation at the constrictions into 9 smaller clouds followed by inverse cascading of the fragmented clouds into a single cloud. During this interval the remaining confined ions gradually diffuse to form a positively charged background. After $\tau \approx 15000$ the merged electron cloud continues to make stable nonlinear $l = 1$ orbits through the ionic background till the end of the simulation (Fig. 4.10r). At $\tau \approx 22674$, which is the point upto which the other experiments of this set were simulated, electron and ion populations for this experiment reduces to 40.06% and 25.08% of their respective initial values (Fig. 4.12 and Fig. 4.13). On further extending the simulation till $\tau \approx 56685$ it is found that the loss rate for electrons and ions slows down further in this extended period as the nonliner $l = 1$ orbital motion of the fused electron cloud continues within the slowly diminishing background population of ions. At the end of the simulation electron and ion populations go down to 27% and 11% of their initial values (Fig. 4.12 and Fig. 4.13).

The numerical experiments of Set 1 are simulations of the same electron cloud for different percentages of a heavier ion species uniformly mixed with it. Hence it is relevant to make a generalized as
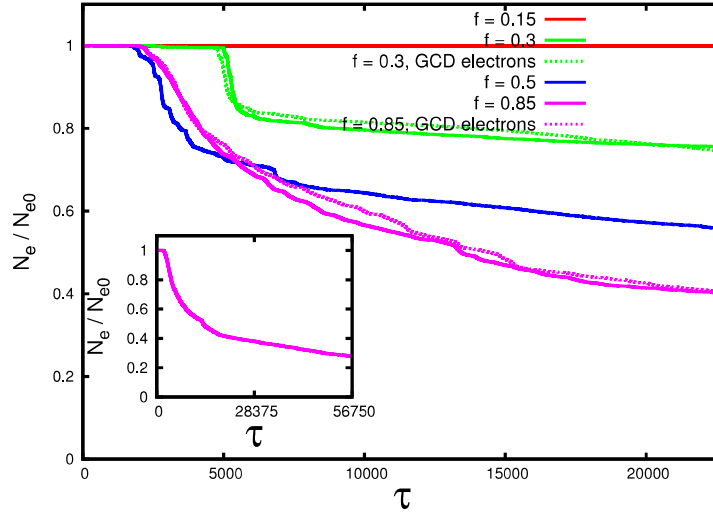
Figure 4.12: Trapped electron population as a function of time for the four selected simulations of Set 1 *i.e.* Expt 2,3,5, and 6 and also for the numerical Expt. 3 and 6 when performed with Guiding Centre Drift (GCD) approximation for the electron component: N_e is the trapped electron population at a given time and N_{e0} is the initial population of trapped electrons. The time axis is normalised by the cyclotron time period of electrons, T_{ce} (Here $\tau = t/T_{ce}$). The corresponding value of of f for each experiment is mentioned in the key. *Inset:* The trapped electron population as function of time for the extended simulation time of Expt. 6.

well as comparative analysis of this set of experiments. For equilibria where the differential rotation between the two components triggers an $l \neq 1$ mode on them, the mode is excited at a phase difference of π between the the two components. This implies that the peaks of the mode on the two components have an azimuthal separation , $\Delta\theta = \pi/l$ between them. This phase difference of the excited $l \neq 1$ mode on the two components, is maintained throughout the linear phase and early nonlinear phase of the instability before the ion profile gets diffused through thermal cross-field transport and phase mixing of the mode. The $l = 1$ mode is however excited without any phase difference between the two components. But as the mode grows on the two clouds they increasingly move out of phase in their orbital motion which is evident form the increasing azimuthal separation between them.

The evolution of all $l \neq 1$ modes also follow a general pattern in the nonlinear phase. There is wave breaking at the modal peaks on the ion cloud and a pinching from the modal peaks of the electron cloud towards its centre followed by symmetric tearing of the electron cloud. At later stages of the nonlinear phase, the fragmented sections of the electron cloud merge to form a single electron cloud which makes nonlinear $l = 1$ orbits very close to the wall up to the end of the simulation.

Fig. 4.12 shows how the total population of trapped electrons varies with time for the four selected equilibrium loads of Set 1, namely Expt. 2, 3, 5, and 6 which have loading f values of 0.15, 0.3, 0.5, and 0.85 respectively. The two dashed electron population curves in Fig. 4.13 are for the equilibrium loads of Expt. 3 and 6 simulated with Guiding Centre Drift (GCD) approximation for the electron component. In Expt. 2 the loaded population of electrons remains confined for the entire length
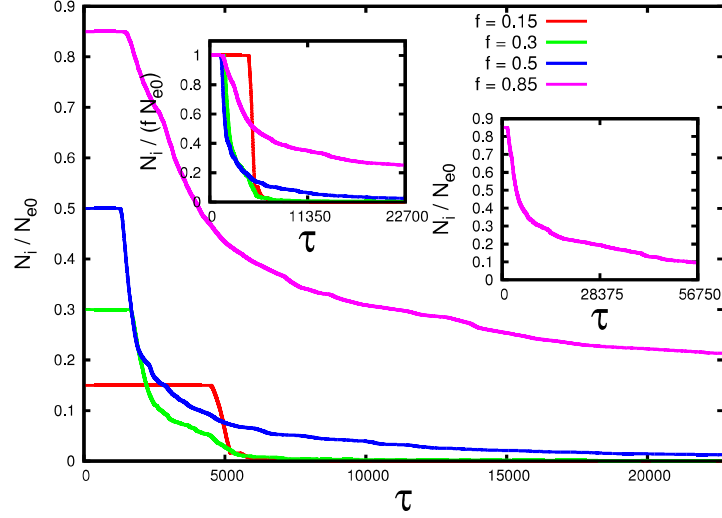
Figure 4.13: Trapped ion population as a function of time for the four selected simulations of Set 1 *i.e.* Expt 2,3,5, and 6: N_i is the trapped ion population at a given time and N_{e0} is the initial population of trapped electrons. The time axis is normalised by the cyclotron time period of electrons, T_{ce} (Here $\tau = t/T_{ce}$). The corresponding value of of f for each experiment is mentioned in the key. *Inset left:* The same plot with the ion population axis normalised for each experiment by the respective value of initial trapped ion population, fN_{e0}. *Inset right:* The trapped ion population as function of time for the extended simulation time of Expt. 6.

of simulation. In Expt. 3, 5, and 6 100% confinement of electrons lasts till $\tau \approx 5000$, $\tau \approx 1680$, and $\tau \approx 1870$ respectively, after which the the three populations follow different loss curves. The snapshot of the plasma profile nearest to the time of commencement of electron loss in Expt 3, 5, and 6 (Figures 4.4p, 4.8i, and 4.10i) shows that the loss process is initiated shortly after the fragmented electron clouds have begun the process of merging (inverse cascade) in these simulations. The fact that the dynamics of Expt 2 (Fig. 4.2) does not involve any fragmentation of the electron cloud is the reason why this simulation is free from electron loss. Coming back to Expt. 3, 5, and 6, snapshots (Figures 4.4q-u, 4.8j-u, and 4.10j-o) between the time of commencement of electron loss and the time of completion of the merging process (at $\tau \approx 5570$, $\tau \approx 7000$, and $\tau \approx 15000$ for Expt 3, 5, and 6 respectively) reveal the actual mechanism of loss of electrons during the merging process. It is seen that when fragmented electron clouds undergo an inverse cascade in the presence of radially transported heavier ions, portions of the surface, and surface filaments of the merging clouds repeatedly come in contact with the conducting boundary all through the merging process. Evidently such contacts lead to untrapping of electrons from these surfaces to the conducting wall. The longer the duration of the merging dynamics, higher is the loss of electrons incurred by the end of this process. Once the electron clouds have completely merged to a single cloud configuration there is much less contacts of the fused cloud surface and its diffused tail with the wall in the nonlinear $l = 1$ orbits (Fig. 4.4v-aa, 4.8v-x, and 4.10p-r). Hence the rate of electron loss reduces significantly after completion of the merging process in the three simulations. The two additional plots with GCD approximation for electrons in Expt. 3
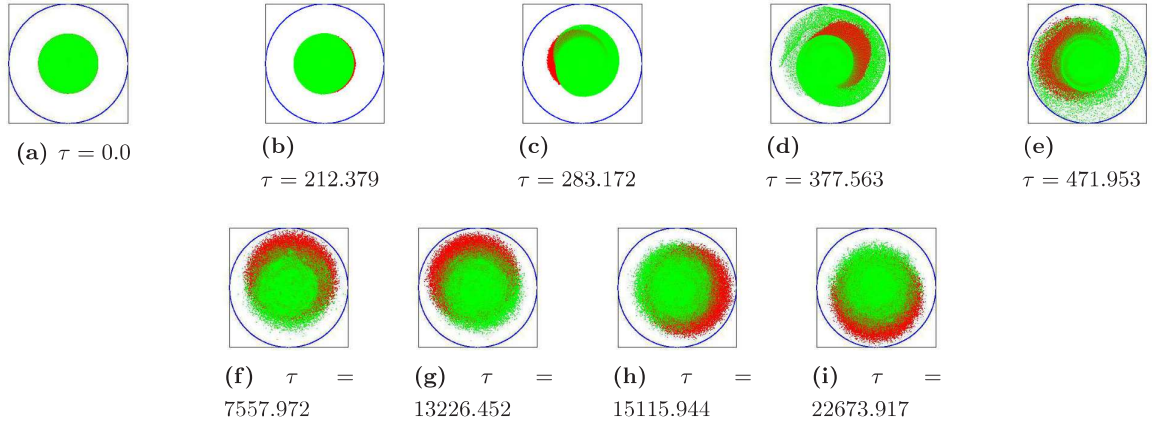
**Figure 4.14:** Snapshots of pseudo particles (electrons in red and ions in green) for an initial unstable equilibrium that excites an $l = 1$ Diocotron mode at $f_b = 1.0$ (Expt. 9 in Table 4.1). Below each snap, the time elapsed is mentioned in normalised units of electron cyclotron time, *i.e.* $\tau = t/T_{ce}$.

and 6 also closely follow the corresponding curves with mass included dynamics for electrons. This indicates that the it is the kinetic effects of the heavier ions still trapped in the system that makes the electron clouds drift on to the wall surface, and that loss of electrons is not simply a case of electrons from a confined cloud hitting the wall because of Finite Larmor Radius (FLR) effect.

Fig. 4.13 shows how the total population of trapped ions varies with time for the same four experiments. 100% confinement of the loaded ion populations lasts till $\tau \approx 4500$, $\tau \approx 1650$, $\tau \approx 1280$, and $\tau \approx 1400$ in Expt. 2, 3, 5, and 6 respectively. In these simulations the snapshot that is closest to the time of commencement of the ion loss process (Figures 4.2f, 4.4f, 4.8e, 4.10g) clearly shows that untrapping of ions begins as soon as the modal peaks of the stretching ion cloud touch the the conducting wall, or in case of Expt. 2, the filamental tail of the orbiting ion cloud touches the wall. In all the four simulations the rate of ion loss is highest at the time of first contact with the wall and reduces gradually after that. The ion loss curves depend on the mode number, l of the excited Diocotron mode. For lower azimuthal modes, a larger fraction of the loaded ion population is radially transported in regions of the cloud that make contact with the wall *i.e.* the wave-breaking peaks of $l \neq 1$ modes and the filamental tail of the cloud in $l = 1$ orbits (compare spatial distribution of ions in Fig. 4.2g, 4.4f, 4.8e, and 4.10h). As a result the simulations with lower azimuthal modes loose ions more rapidly (Fig. 4.13). Quantitatively, in Expt. 6 which has a dominant $l = 9$ mode, the ion population drops to 10% of its initial value at $\tau \approx 56750$, while in Expt. 2, 3, and 5 which excite a dominant $l = 1$, $l = 2$, and $l = 3$ mode respectively, the same percentage reduction in ion population is reached before $\tau \approx 7500$.

4.1.4 Two-Component Equilibrium loads at high f_b

Experiments 8 and 9 constitute the second set of Table 1. In this set the loading parameters f_b, m_i/m_e, and r_p/R_w are fixed at the values of 1.0, 1836, and 0.5 respectively while the fractional neutralization,
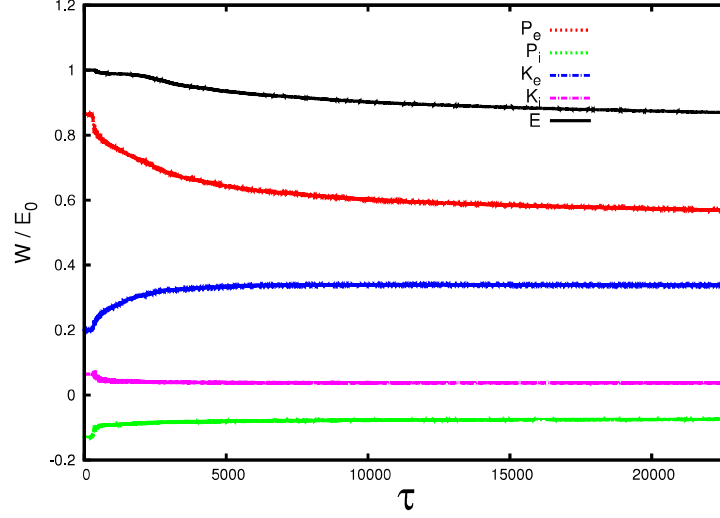
Figure 4.15: Energy curves of Expt. 9: W represents the energy components in the legend, E_0 is the initial total energy, and $\tau = t/T_{ce}$. P_e and P_i are the potential energies of electrons and ions respectively. K_e and K_i are the kinetic energies of electrons and ions respectively. E is the total energy of the system. The energy components are normalised by E_0 and plotted as a function of time. The time axis is normalised by the cyclotron time period of electrons, T_{ce}.
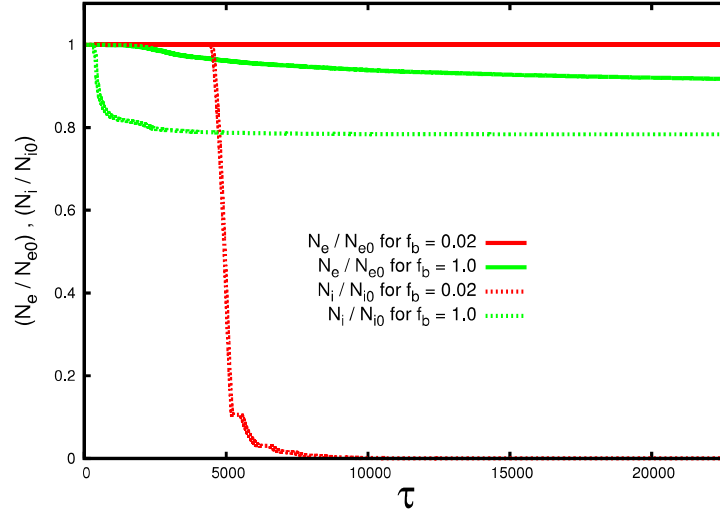
Figure 4.16: Trapped electron (ion) population as a function of time for Expt 2 and 9: N_e (N_i) is the trapped electron (ion) population at a given time and N_{e0} (N_{i0}) is the initial population of trapped electrons (ions) for that simulation. The time axis is normalised by the cyclotron time period of electrons, T_{ce} (Here $\tau = t/T_{ce}$). The corresponding value of of f_b for each experiment is mentioned in the key.

4. PARTIALLY NEUTRALIZED ELECTRON PLASMA NUMERICAL EXPERIMENTS (PNEPNEX)

f has a value 0.1 in Expt. 8 and 0.15 in Expt. 9. These two experiments are simulated till $\tau \approx 22674$. The same diagnostics and data analysis methods that are used in the simulations of Set 1 are also applied here.

The equilibrium loads of both these experiments excite an $l = 1$ mode on the two components. But while the $l = 1$ mode in Expt. 9 has a growth rate (5.236×10^7 rad/sec) and a frequency (1.89×10^7 rad/sec) which match with corresponding analytical values, the excitation of the $l = 1$ mode in Expt. 8 is a discrepancy from analytical results. Linearised theory [1, 16] predicts that the rigid rotor equilibrium of Expt. 8 should be stable. But the simulation reveals that the differential rotation between the two components excites an $l = 1$ mode of frequency 2.713×10^7 rad/sec and a growth rate of 4×10^5 rad/sec. Even though the equilibrium points of Expt. 8 and 9 are located quite close in the parametric space differing only in the value of f, the growth rate of the mode in Expt. 8 has a value that is two orders smaller than that of Expt. 9. This indicates that the discrepancy from linearised theory in Expt. 8 is only a small nonlinear correction to the zero growth rate (no mode) obtained from linearised theory. To rule out the possibility that the discrepancy is a numerical error, Expt. 8 was repeated on the same grid with doubled computational particles (175668 per component) to check whether changing the weight of the pseudo particles modified the growth rate and frequency of the $l = 1$ mode. However even these repeated experiments yielded almost exactly the same results for the excited $l = 1$ mode, showing that it is indeed a physical effect.

The full linear and nonlinear dynamics of the instability will be described in detail for Expt. 9. Fig. 4.14 shows some selected snapshots of this simulation. From the energetics of the simulation (Fig. 4.15) it can be seen that the energy exchange process of the instability begins at $\tau \approx 220$ which also marks the end of the linear phase. Hence among the snapshots, only Fig. 4.14a-b are in the linear phase while the rest are in the nonlinear phase of the instability. It is worth investigating the dynamics of the $l = 1$ mode, and other results such as particle loss (Fig. 4.16) of this experiment comparatively with that of Expt. 2, which has the same loading values of the parameters f, m_i/m_e, and r_p/R_w for a smaller value of f_b (see Table 1). In Expt. 9 the $l = 1$ mode on the two components start off in phase, but acquire an increasing phase difference as the mode grows in the linear and early nonlinear stages of the instability (Fig. 4.14a-d). A similarly evolving phase difference has been described earlier for Expt. 2. But in stark contrast with Expt. 2, the instability of Expt. 9 radially transports electrons more efficiently than ions (Fig. 4.14e-i). This difference is also reflected in the energetics of the two experiments. While Fig. 4.3 of Expt. 2 shows ions gaining thermal kinetic energy from the instability during the energy exchange phase, Fig. 4.15 shows the same process happening for electrons in Expt. 9. In Fig.4.16 the electron and ion, population curves of Expt. 9 are plotted with the corresponding curves of Expt. 2 for comparison. These population curves show that the equilibrium at higher Brillouin ratio $i.e.$ Expt. 9, has better conservation of the initial neutrality level of the plasma. At the end of Expt. 9 (at $\tau \approx 22674$) the electron and ion, populations drop to 92% an 78% of their respective initial values while at the end of Expt. 2 (also at $\tau \approx 22674$) the electron and ion populations, are at 100% and 0% of their respective initial values.

In the next set of numerical experiments PNEPNEX2, we will investigate the influence of non-ionzing collisions between electrons and background neutrals on the dynamics and energetics of the ion resonance instability.

4.2 PNEPNEX2: Ion resonance instability in presence of electron-neutral elastic collisions

The theoretical background, numerical set-up, and results of PNEPNEX2 are presented in the following subsections.

4.2.1 Theoretical Background

Davidson and Uhm's linear analytical theory [16], when applied to Expt. 2 ($f_b = 0.02$, $f = 0.15$) at zero background pressure (absence of neutrals) predicts growth of an unstable $l = 1$ azimuthal mode (l being the mode number) on both components with angular frequency $2.827 \times 10^6 rad/sec$ and growth rate $9.47 \times 10^5 rad/sec$. Our simulation of the same equilibrium sans neutrals, in PNEPNEX1, are in excellent agreement with the linearised theory in the linear phase of the instability. We get an unstable $l = 1$ mode with angular frequency $2.792 \times 10^6 rad/sec$ and growth rate $9.6 \times 10^5 rad/sec$ (see Table 4.1). A linear perturbation analysis of the high f_b Equilibrium, Expt. 8 ($f_b = 1.0$, $f = 0.1$) at zero background pressure predicts that this equilibrium should be stable [16]. However we have seen in PNEPNEX1 that this equilibrium infact destabilizes very slowly in the the form of a nonlinear $l = 1$ mode accompanied by a few higher weaker modes [38]. A linearly fitted growth rate of the impure (mixed with a few higher weaker modes) $l = 1$ mode is obtained as $4.0 \times 10^5 rad/sec$ while its angular frequency comes out to be $2.733 \times 10^7 rad/sec$ [38] (see Table 4.1). The slower nonlinear destabilization of the second equilibrium in absence of neutrals is attributed to nonlinear terms in the perturbed equations of motion that have been neglected in its linear analysis.

We now subjected these two unstable equilibria to three different values of neutral background pressures, P_{bg}. The values of P_{bg} chosen are $2 \times 10^{-8} Torr$, $2 \times 10^{-7} Torr$, and $2 \times 10^{-6} Torr$ at a common fixed background temperature $T_{bg} = 300K$. The collision time step, Δt_c for the lowest background pressure was chosen as $6 \times 10^{-6} sec$ and it was reduced by an order of magnitude and two orders of magnitude for the $2 \times 10^{-7} Torr$ and $2 \times 10^{-6} Torr$ background pressures respectively. This kind of scaling of Δt_c between the three background pressures helped in maintaining uniformity of the MCC routine's collision resolving capacity among the different experimental pressures. Of course all the three values of Δt_c satisfy the two criteria for collision time interval in their corresponding experiments (discussed in Chapter 2). With the help of these PIC-with-MCC simulations we were able to study the effect of electron-neutral elastic (and exciting) collisions on two ion resonance instabilities that are growing via the fundamental $l = 1$ mode at different rates. A point to be noted here is that in these sets of experiments the loaded ions are not of the same species as the background gas while in typical electron plasma traps the destabilizing ions are created from the ionization of the background

atoms by electrons. The background gas with which the electrons make non-ionizing collisions is Argon. As the MCC is constrained to only execute non-ionizing $e^- - Ar$ collisions in PNEPNEX2, the Ar background will only influence the instability through collisional relaxation of the electron cloud's profile. So the experiments of this Section can be described as a qualitative investigation of how such a process of profile relaxation of the electron cloud due to an arbitrary neutral species influences the ion-resonance instability due to an arbitrary ion contaminant mixed in the electron cloud.

4.2.2   Numerical Setup

In PNEPNEX2 Expt. 2 and 8 of Table 4.1 are repeated (with PEC2PIC-3MCC), in the presence of Background Ar neutrals that are constrained to make only non-ionizing elastic, and excitation collisions with the electrons of the two-component (e^- and H^+) non-neutral plasma. Hence the basic numerical set-up and PIC parameters of PNENX2 are the same as in PNEPNEX1. The only additional features are that of the constrained MCC operating on the plasma. The collision time step Δt_c is adjusted according to the chosen pressure and temperature of the background gas. The values of P_{bg} chosen are $2 \times 10^{-8} Torr$, $2 \times 10^{-7} Torr$, and $2 \times 10^{-6} Torr$ at a common fixed background temperature $T_{bg} = 300K$. The magnitude of axial velocity with which the electrons are loaded is $1.02727 \times 10^7 ms^{-1}$ which implies that for a typical cylindrical plasma column of length of $60cm$ [58] the bounce frequency of electrons is roughly 8.5 MHz. This value of the axial bounce frequency is higher than the typical experimental bounce frequency (< 0.2 MHz [58]) of a $60cm$ long cylindrical plasma column. By loading the electrons with high axial speeds we have made the electrons more energetic and thereby maintain the average total non-ionizing (elastic + excitation) collision cross section between the moderate orders of $10^{-21} m^2$ and $10^{-20} m^2$ (see Fig. 3 of Ref [51]) in PNEPNEX2. It must be re-emphasized here that the loaded value of the axial velocity of electrons in the simulations serves only to adjust the collisional probabilities and does not partake in any of the regular PIC dynamics of the plasma.

4.2.3   Results

The unstable two-component ($e^- - H^+$) equilibrium of Expt. 2 in Table 4.1 *i.e* with $f_b = 0.02$, $f = 0.15$, is loaded in the presence of an Ar neutral background at the three experimental background pressures. For the three PIC-with-MCC simulations the electrons are also loaded with an added axial velocity component enabling them for 3D elastic and exciting collisions with background neutrals. What we observe from our diagnostics comprising of potential probes (Fig 1), radius of centre-of-mass of the electron component, and the potential energy of the electron component, is that there is negligible variation in the dynamics of this instability brought about by the electron-neutral non ionizing collisions for the above set of background pressures. The diagnostics record values with progression of the simulation that are identical to the zero pressure experiment for all the three experimental background pressures. More specifically for all the experimental P_{bg} values including $P_{bg} = 0$, the potential probes record a similar exponential growth and saturation of $l = 1$ mode, the potential energy of the electron cloud decreases and saturates similarly with time, and the radial
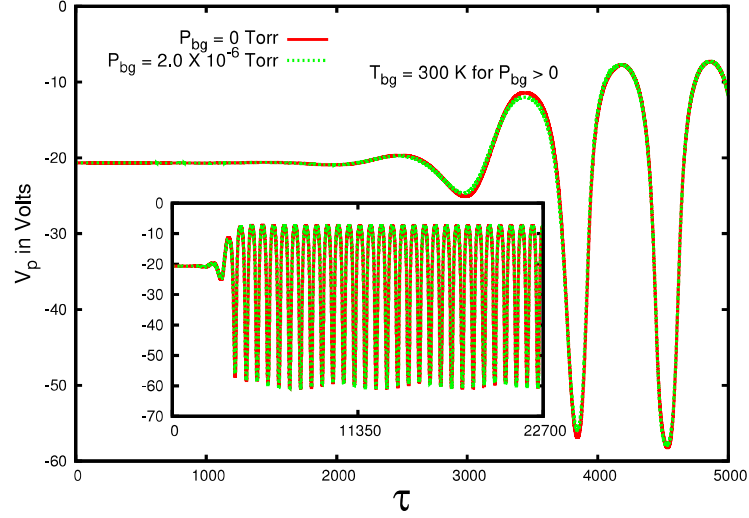
Figure 4.17: Readings of the left potential probe, V_p for the $f_b = 0.02$, $f = 0.15$ equilibrium at background pressure, P_{bg} values of 0 and $2 \times 10^{-6} Torr$. V_p readings of the equilibrium at the other two simulated background pressures of $2 \times 10^{-7} Torr$ and $2 \times 10^{-8} Torr$ (not shown here) also overlap nearly perfectly with the plotted readings in this figure. $T_{bg} = 300K$ is the chosen temperature of the background gas in this set of runs for all $P_{bg} > 0$. Normalized time, τ is in units of electron cyclotron time, *i.e.* $\tau = t/T_{ce}$. Readings up to the growth phase (till $\tau = 5000$) have been zoomed in here for clarity while the inset has the complete readings up to the end of the simulations. The other three potential probes also recorded almost perfectly overlapping readings for all the four values of P_{bg}.

location of the electron cloud also increases and saturates similarly with time. As a illustrative example, we have shown in Fig. 4.17 the left potential probe's reading for the lowest and the highest background pressures ($P_{bg} = 0$ and $P_{bg} = 2 \times 10^{-6} Torr$). It can bee seen that the the two signals lie nearly on top of one another. All these diagnostic results bring us to the conclusion that for this particular equilibrium at the chosen set of background pressures the electron-neutral elastic and exciting collisions can not influence the evolution of the ion resonance instability on the e- H+ cloud. We will get back to reason for this in a later comparison with the results for the second equilibrium.

Next we come to the set of MCC simulations performed on equIlibrium of Expt. 8 in Table 4.1 $f_b = 1.0$, $f = 0.1$. Loading this equilibrium at zero pressure produces a slower growing $l = 1$ mode than the $f_b = 0.02$, $f = 0.15$ equilibrium of Expt. 2 as seen in PNEPNEX1. Now the $f_b = 1.0$, $f = 0.1$ equilibrium is loaded at the three selected background densities of Ar. The electron now have cylindrical trap like axial velocities and are capable of 3D elastic and excitation collisions with the background neutrals. The collisions relax the profile of the electron cloud and the resultant changes in the electron density profile influences the ongoing collisionless ion resonance instability. Specifically collisional relaxation of the electron cloud reduces the average density of the electron cloud and thereby increases the fractional density of the ions mixed in it. The dynamically changing electron density and fractional density of ions feed back on the ongoing ion-resonance (two-stream) instability between the two components of the nonneutral cloud and produce deviations in the paths of progression of

the instability that are uncorrelated at different background gas pressures. As the variations in the path of evolution of the plasma at the experimental background pressures are small in comparison to average evolution over time it is sufficient to identify and discuss these variations only qualitatively without quantifying their magnitudes with direct measurements. We will discuss these variations with the help of the diagnostic results of Fig. 4.18.

First let us look at radial location of the electron component as a function of time which directly shows how the $l = 1$ mode grows in orbital radius and saturates at different background pressures for the electron component (Fig. 4.18a). It can be seen from Fig. 4.18a that the $P_{bg} = 0$ load has the slowest increase in orbital radius of the electron cloud with the growth rate increasing the in the order of $P_{bg} = 2 \times 10^{-7} Torr$, $P_{bg} = 2 \times 10^{-6} Torr$, and $P_{bg} = 2 \times 10^{-8} Torr$. After the growth period the $l = 1$ mode for the lower background pressures of $P_{bg} = 0$ and $P_{bg} = 2 \times 10^{-8} Torr$ saturate at slightly smaller orbital radii as compared to the two higher background pressures of $P_{bg} = 2 \times 10^{-7} Torr$ and $P_{bg} = 2 \times 10^{-6} Torr$ (see inset of Fig. 4.18a). The potential probe readings also mirror the same information about the growth of the mode (Fig. 4.18b).

Next we have also compared the time evolution of two energy components between the different background pressures, viz the potential energy energy of the electron cloud and the potential energy of the ion cloud. We know form our eaRlier experiments PNEPNEX1 that for the $P_{bg} = 0$ load the potential energy of the electron component decreases while that of ion component increases during the growth of the instability. Fig. 4.18c and 5d show the potential energies of the electron component and ion component respectively up to the the growth phase of the instability for the experimental background pressures. It can be seen from Fig. 4.18c-d that the rates of decrease/increase in potential energy of electrons/ions increases with increase in background pressure.

Hence we can conclude that changing the collisionality of the electron cloud by changing the background gas densities has brought about interesting subtle variations in the dynamics of the ion-resonance instability that are unique to each experimental background gas pressure. It is also to be noted that once the growth of the collisionless ion resonance instability saturates there is no further destabilization caused by the continuing collisions (see inset of Fig. 4.18a) which further emphasizes that the collisions are only influencing the dynamics of the cloud through feedback of electron cloud's profile relaxation on the growing ion resonance instability.

We have seen that elastic and excitation collision of electrons with background neutrals influence the dynamics of the ion resonance instability for the $f_b = 1.0$, $f = 0.1$ equilibrium while they have no effect on the instability dynamics for the $f_b = 0.02$, $f = 0.15$ equilibrium. From the nature of the growth of instability in the two equilibria it is evident that this is a due to the different lengths of growth phase in the two equilibria. The excited $l = 1$ mode in the $f_b = 0.02$, $f = 0.15$ equilibrium (Expt 2 in Table 4.1) grows faster and saturates quicker than the $f_b = 1.0$, $f = 0.1$ equilibrium (Expt. 8 in Table 4.1). So at a particular background pressure there will be more elastic and excitation collisions occurring during the growth phase of the instability for the $f_b = 1.0$, $f = 0.1$ equilibrium as compared to the $f_b = 0.02$, $f = 0.15$ equilibrium. Hence there is more feedback on the instability by the collisional
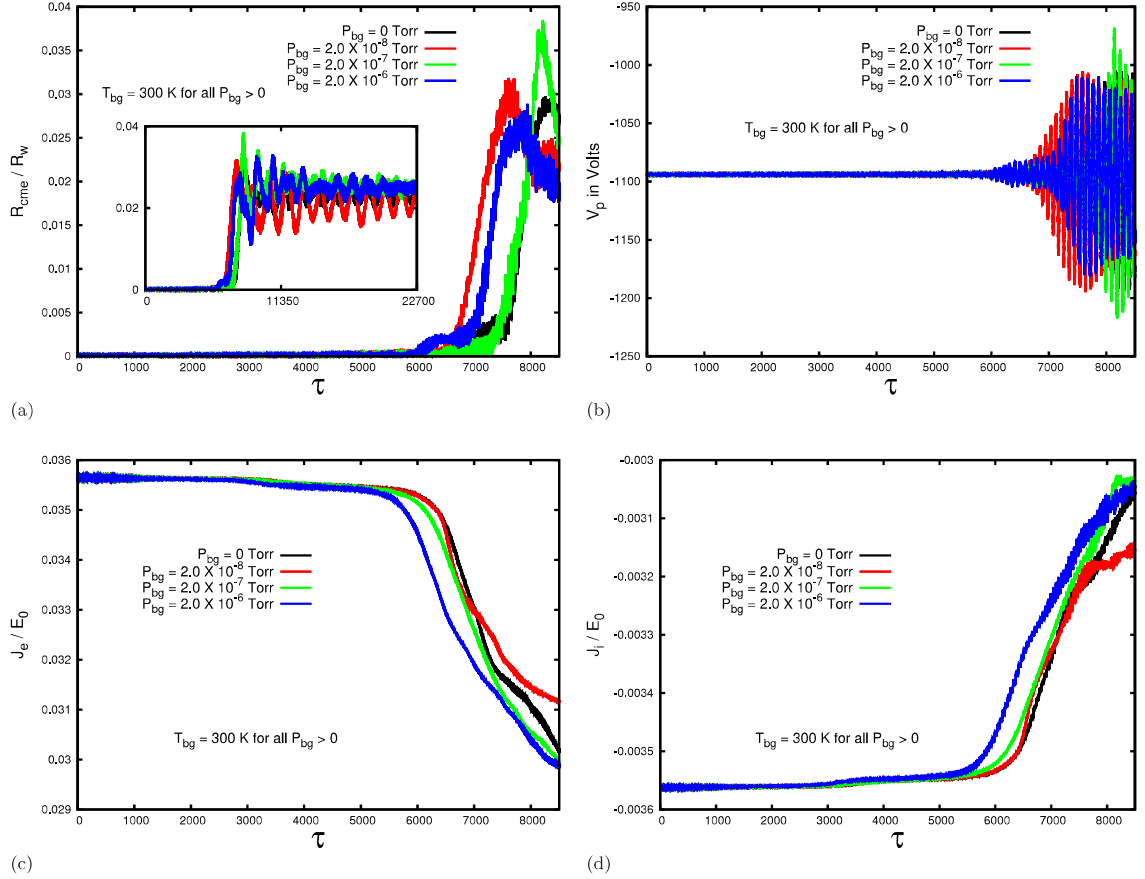
Figure 4.18: Comparison of diagnostic results between different background pressure, P_{bg}, for the $f_b = 1.0$, $f = 0.1$ equilibrium load: With $\tau = t/T_{ce}$ the set of plots are zoomed in showing their respective diagnostic readings upto $\tau = 8500$ for clarity. T_{bg} is the temperature of the background gas for all $P_{bg} > 0$. (a) The radius of the centre-of-mass of the electron component, R_{cme} normalised by the wall radius R_W is plotted as a function of time. *Inset*: The same set of plots is extended upto the end of the simulations at $\tau = 22700$ (b) The left potential probe's reading, V_p as a function of time at different background pressures. (c) The Potential Energy of the electron component, J_e normalised by the initial total energy of the 2-component plasma, E_0 is plotted as a function of time.(d) The Potential Energy of the ion component, J_i normalised by the initial total energy of the 2-component plasma, E_0 is plotted as a function of time.

relaxation of the electron cloud for the $f_b = 1.0$, $f = 0.1$ equilibrium. The feedback process brings about the subtle changes in the evolution of this equilibrium at the experimental background pressures. Furthermore we have already seen that once saturation of the mode is achieved, the ongoing collisions can not further destabilize the cloud. Hence a smaller time window of influence of the electron-neutral collisions for the $f_b = 0.02$, $f = 0.15$ equilibrium is the precise reason why we do not observe any deviation in dynamics at different experimental background pressures for this equilibrium.

4.3 Conclusions and Discussions on PNEPNEX

In PNEPNEX1 the ion resonance instability in cylindrical traps has been investigated with emphasis on the Diocotron frequency, growth rate, and phase difference between the two components in the linear phase, and the nonlinear dynamics, energetics, cross-field transport, and loss of electrons and ions in the nonlinear phase. Several new results have been obtained from all these aspects of the instability. The low Brillouin ratio simulations of (Expt. 1-7 of Table 4.1) have been carried out for a wide range of fractional neutralizations spanning between the values 0.05 and 0.85. All these simulations have cold starts of the plasma. Similar zero temperature loads of higher values of f which are less than 1.0 (specifically $0.9 < f < 1.0$), are numerically difficult to simulate. From the linearised cold fluid model [1, 16] it can be seen that cold starts of the equilibria at $0.9 < f < 1.0$ will trigger very high modes of the plasma (the triggered mode numbers get higher the closer the equilibrium is to $f = 1.0$, falling abruptly to zero modes triggered at $f = 1.0$). Very high modes may cause numerical instability in the simulation because of the finite grid size. In actual experiments however, there is a cut-off for the highest mode that the system can support, because of thermal effects of the plasma. So it would be more meaningful as well as numerically easier to study this range of f values with a warm load of the plasma. In fact carrying out simulations of the ion resonance instability, in general, with warm loading conditions is an interesting avenue to take this work further. In relation to this point, it was reasonable to perform an extra check of the numerical stability of the simulation with the highest value of f in in Experiments 1 to 7, *i.e.* Expt. 6 with $f = 0.85$. A check was performed by the repeating the the numerical experiment on a finer 100×100 grid. This test produced highly convergent results with the original Expt. 6, thus verifying its numerical stability.

In PNEPNEX2 we have addressed how the dynamics of a trapped electron cloud is influenced by elastic collisions with an inert neutral gas that is always present in an experimental trap, usually at very low pressures. Our simulations reveal the true nature of the interaction of the electron-neutral elastic collisions with the dynamics of the cloud. We have investigated how a ongoing collisionless ion-resonance instability due to ion impurities mixed with the cloud is dynamically influenced by the feedback of the electron cloud's collisional profile relaxation on the instability. The effect of feedback is visible in the energetics and growth rate of the instability. As this feedback is a highly dynamical nonlinear process it effects also do not follow any particular trends with increase/decrease of the background gas pressure. We also observed that the feedback can influence a growing ion resonance

instability but can not alter the stable dynamics of the cloud once the instability has saturated. So if the period of growth of the instability is very short, then there may not be sufficient number of collisions in the short growth phase to influence the dynamics of the instability. Such a case of a quickly saturating ion resonance instability being unaltered by the elastic collisions was also shown in our simulations.

Earlier In PEPNEX2 of Chapter 2 we had also demonstrated that contrary to an existing theory [36] on influence of elastic collisions between electrons and background neutrals, the collisions themselves can not destabilize an otherwise stable electron cloud. This wa shown to be a result of the nature of extraction of potential energy from the cloud by the collisions.Hence through PEPNX2 of Chapter 3, and PNEPNEX2 of this Chapter we have built some understanding of the effects of elastic and excitation collisions of trapped electrons with background neutrals. In the next Chapter we will explore how ionizing collisions of electrons with background neutrals together with elastic and excitation collisions influence the dynamics of a trapped electron cloud [33].

5

Background Ionization by Electron Plasma Numerical EXperiments (BIEPNEX)

In PNEPNEX1 of Chapter 4 the liner model of the ion resonance instability given by Davidson and Uhm [16] was presented. Using the 2D PIC code PEC2PIC the collisionless linear and nonlinear dynamics, and the energetics of the ion-resonance instability was investigated for a range of unstable equilibrium of a 2-component non-neutral plasma [38]. In PNEPNEX2 simulations with the 2D3v PIC-with-MCC code PEC2PIC-3MCC revealed how elastic and excitation collisions of electrons with background neutrals influence the dynamics of an ongoing ion-resonance instability through feedback of collisional relaxation of electron cloud's profile on the instability [32]. Further in Chapter 3 it was demonstrated through PEPNEX2, performed with PEC2PIC-3MCC, that the non-ionizing elastic and excitation collisions of electrons with background neutrals can not be the source of destabilization of the plasma [32]. Such collisions can only influence other destabilization processes like the ion resonance instability. There is still one very crucial collisional mechanism that needs to be investigated when it comes to destabilization of electron plasmas by the ion resonance instability.

Pure electron clouds confined in magnetic traps can get destabilized by the accumulation of ions in the cloud, through the process of electron-impact ionization of background neutrals. Most present day electron plasma traps operate at background pressures below $10^{-8} Torr$ wherein H_2^+ is the predominant background gas [20]. Experiments have also been conducted where an inert neutral species such as He has been injected into the background of an electron plasma trap to produce destabilization of the electron cloud [50]. In cylindrical Penning-Mamlberg traps there is sustained axial motion of electrons through their bouncing at the electrostatic end plugs of the trap and in toroidal traps an electron cloud will be in stable fundamental Diocotron mode orbits about the toroidal axis. Such motion of the trapped electrons can cause ionization of the neutrals that they collide with, along the way. The ionizing collisions will release ions and secondary electrons into the cloud. As the ions accumulate in the potential well of the electron cloud, they gradually form an ion cloud that will have its own

collective motion in the cross sectional plane of the trap in response to the electric field of the grossly nonneutral plasma and trap's magnetic field. The result is always a differential rotation between the electron component and the ion component of the plasma. The differential rotation excites the ion resonance (two-stream) instability described in Chapter 4, on the ion contaminated electron cloud. The ion resonance instability manifests in the form of a growing $l = 1$ (l being the Diocotron mode number) mode on both components of the plasma [16].

While the above described form of instability of an electron cloud caused by contaminant ions is the 2D ion resonance instability [16], ions in electron plasma traps can also get involved in 2-stream instabilities with the electron cloud from other causes. For instance, in cylindrical traps, the electrons and the ions can have different axial profiles which can result in differential rotation between the two components [75], while in toroidal traps the curvature drift can cause differential rotation between electrons and ions [78]. Describing these other forms of 2-stream instabilities between ions and electrons, which are also often referred to as ion resonance instabilities, requires a 3D perspective of the trap. In BIEPNEX we have restricted our investigation using PEC2PIC-3MCC, to axially-averaged 2D differential rotation between the two components of the nonneutral cloud. Speicifically in BIEPNEX we have investigated, through simulation, the process of destabilization of a cylindrically confined electron cloud due to the presence of a single species of neutral atoms, Ar in the background of the trap at a pressure relevant to experiments. The destabilization occurs because of a gradual accumulation of Ar^+ in the cloud by the electron-impact ionization of the background neutrals.

BIEPNEX1 is constituted by two sets of simulations BIEPNEX1 and BIEPNEX2. BIEPNEX1 is a numerical experiment that simulates the evolution of an initial stable trapped electron cloud that is interacting through ionizing and non-ionizing collisions with background Ar maintained at an experimental pressure. The products of ionizing collisions, Ar^+ also undergo elastic and charge exchange collisions with the background neutrals. In BIEPNEX2 the simulation of BIEPNEX1 is repeated with i) the non-ionizing elastic and excitation collisions between electrons and background neutrals turned off, and ii) the elastic and charge exchange collisions between the Ar^+ and background neutrals turned off. The objective of BIEPNEX2 is to investigate the role of the two turned-off collision types on the dynamics of BIEPNEX1. BIEPNEX1 and BIEPNEX2 obviously have same numerical set-up except for the turned off collision types in BIEPNEX2. The common numerical set-up is described in Section 5.1 . Sections 5.2 and 5.3 present the results of BIEPNEX1 and BIEPNEX2 respectively. Conclusions and Discussions on BIEPNEX make up the last section of the Chapter, Section 5.6 .

5.1   Setup of BIEPNEX and its PIC parameters

BIEPNEX was carried out for typical parameters found in experiments of cylindrical traps [20, 58], in particular, a wall radius, $R_w = 0.125\,m$, and axial magnetic field, $B_z = 0.03\,T$. A cylindrical (circular in 2D) pure electron cloud with a uniformly low Brillouin ratio, $f_b = 0.2076$, and a radial

extent $r_p = 0.5 \times R_w$ is loaded symmetrically about the axis of the trap. The background Ar gas is maintained at a pressure, $P_{bg} = 2 \times 10^{-7} \, Torr$ [20, 58], and temperature, $T_{bg} = 300 \, K$. The chosen pressure of the background gas is higher than background pressures in most modern-day traps where background pressures generally vary between $10^{-8} \, Torr$ and $10^{-9} \, Torr$. The higher value of P_{bg} of our simulation is still experimentally relevant, and serves to accelerate the progression of the ion-resonance instability and enhances its effects, which is suitable for our simulation. The same numerical experiment progressing at lower background pressure would show more subdued, and delayed effects of the ion resonance instability.

The pure electron plasma is initially in its slow mode of the rigid rotor equilibrium [1, 34] in the trap, rotating with an angular frequency ω_{re}^-. In the axial direction the electrons are loaded with randomly up or down directed velocities with a common magnitude, $v_z = 1.02727 \times 10^7 \, m/s$. This choice of axial speed of electrons implies that for a typical cylindrical plasma column of length of $60cm$ [58] the bounce frequency of electrons is roughly $8.5 \, MHz$. This value of the axial bounce frequency is higher than the typical experimental bounce frequency (< 0.2 MHz [58]) of a $60cm$ long cylindrical plasma column. By loading the electrons with high axial speeds we have made the electrons more energetic and thereby maintained the average collision cross section of the electrons at moderate values of $\sigma_e = 2.207 \times 10^{-20} \, m^2$, $\sigma_x = 2.741 \times 10^{-21} \, m^2$, $\sigma_i = 1.402 \times 10^{-20} \, m^2$, and $\sigma_t = 3.883 \times 10^{-20} \, m^2$, where σ_e, σ_x, and σ_i, are the elastic, first level excitation, and single ionization collision cross section for $e^- - Ar$ collision (see Fig. 3 of Vahedi and Surendra, 1994 [51]), and $\sigma_t = \sigma_e + \sigma_x + \sigma_i$, is the total collision cross section for $e^- - Ar$ collision. These moderate values of the above collision cross sections is suitable for our simulation. It must be re-emphasized here that the loaded value of the axial velocity of electrons in the simulation serves only to adjust the collisional probabilities and does not partake in any of the 2D PIC dynamics of the plasma.

The PIC simulation time step, $\delta t = 10^{-11} \, s$ is chosen much smaller than the cyclotron time period of electron, $T_{ce} = 1.191 \times 10^{-9} sec$, such that the code can well resolve the cyclotron motion of both the electrons, and the collision generated Argon ions. A common collision time step, $\Delta t_c = 6 \times 10^{-7} s$ is maintained for both $e^- - Ar$ and $Ar^+ - Ar$ collisions in the simulation. This value of Δt_c satisfies the required criteria for collision time step [32] for the numerical experiment of Section III.

PIC-parameters used in BIEPNEX1 and BIEPNEX2 are 87834 pseudo particles initially representing the loaded electron cloud, on a 70×70 grid. $e^- - Ar$ collisions create an additional 35713 e^- pseudo particles and $35713 \times 4 = 142852$ Ar^+ pseudo particles in course of simulation. The mass of Ar atom and Ar^+ ion is taken as 72820.77 times the mass of an electron. The numerical experiments BIEPNEX1 and BIEPNEX2 is carried out till time, $t = 2.88 \times 10^{-4} \, s$ which is roughly $2.42 \times 10^5 \, T_{ce}$.

(a) τ = 0.0   (b) τ = 9069.589   (c) τ = 18139.179   (d) τ = 27208.768   (e) τ = 39301.554   (f) τ = 48371.144

(g) τ = 57440.733   (h) τ = 69533.519   (i) τ = 78603.109   (j) τ = 87672.698   (k) τ = 99765.484   (l) τ = 108835.073

(m) τ = 117904.663   (n) τ = 129997.449   (o) τ = 139067.038   (p) τ = 148136.628   (q) τ = 160229.414   (r) τ = 169299.003

(s) τ = 178368.593   (t) τ = 190461.379   (u) τ = 199530.968   (v) τ = 208600.558   (w) τ = 220693.343   (x) τ = 226739.736

(y) τ = 228251.335   (z) τ = 233541.929   (aa) τ = 236565.125   (bb) τ = 237320.924   (cc) τ = 238832.522   (dd) τ = 241855.719
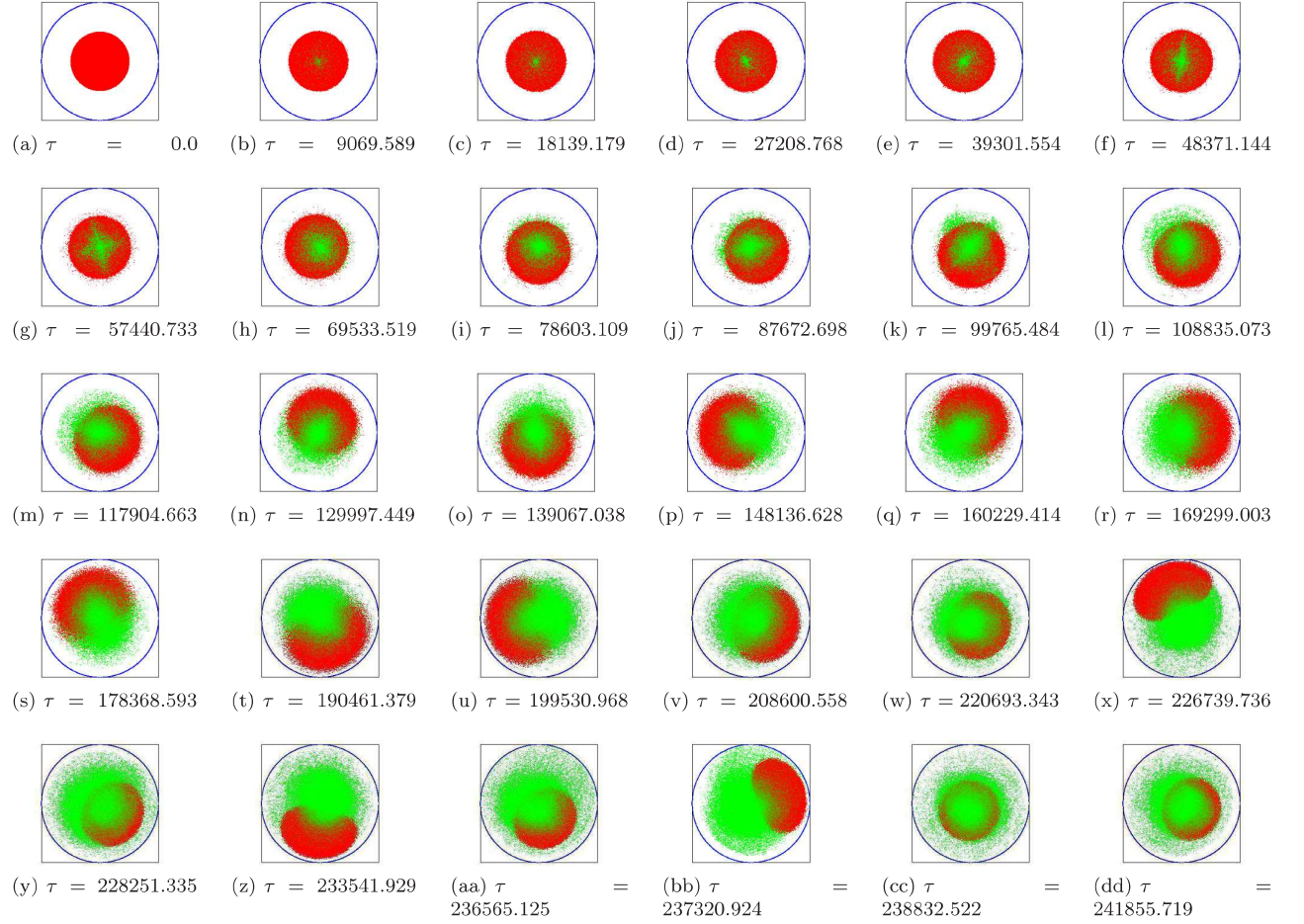
Figure 5.1: Plasma profile evolution in BIEPNEX1: Snapshots of pseudo particles (electrons in red below, and Ar^+ in green on top) showing evolution of the equilibrium load of a $f_b = 0.2076$ pure electron plasma, in the presence background Ar atoms at pressure $P_{bg} = 2 \times 10^{-7} Torr$ and temperature $T_{bg} = 300K$. The electrons undergo elastic, excitation, and ionizing collisions with the Ar atoms. The ions undergo elastic, and charge exchange collisions with the Ar atoms.Below each snap, the time elapsed is mentioned in normalised units of electron cyclotron time, *i.e.* $\tau = t/T_{ce}$.

5.2 BIEPNEX1: PIC-with-MCC simulation of the destabilization of a pure electron cloud

The initial condition for BIEPNEX1 is an electron cloud of moderately low Brillouin ratio, $f_b = 0.2076$, rotating rigidly with angular frequency ω_{re}^- in its slow mode of rigid rotor equilbrium [34]. The evolution of the plasma profile thereafter till the end of the simulation in depicted in the snapshots of Fig. 5.1. We observe from Fig. 5.1 that the Ar^+ ions formed by impact ionizations of the background Argon neutrals initially accumulate in the cross-sectional potential well formed by the electron cloud (Fig. 5.1a-g). As the ion cloud grows in size, it starts engaging in an ion-resonance (2-stream) instability with the electron cloud. The result is the excitation of an $l = 1$ dioctron mode on both components of the plasma (Fig. 5.1h-l). With nonlinear growth of the fundamental mode, a gradual radial separation between the centres of mass of the electron cloud, and the ion cloud, is observed (Fig 5.1m-u). Newly formed ions from electron impact ionization of neutrals still continue to accumulate at the centre of the electron cloud's profile, but they remain connected to the radially transported ions, so that all the ions collectively form a single cloud without any discontinuity in its profile (Fig. 5.1m-u). The electron cloud takes up a higher radial position than the ion cloud in their expanding $l = 1$ orbits (Fig. 5.1m-u). The electron cloud's profile also becomes more and more elliptical in shape as it moves closer to the grounded wall [79] (Fig. 5.1m-u). In Fig. 5.1v-dd, the mode has saturated and there is no further increase in the $l = 1$ orbital radius of the 2-component plasma profile. The elliptical electron cloud has now moved very close to the grounded wall (Fig. 5.1v-dd). The 2-component non-neutral plasma continues to make stable $l = 1$ orbits in this configurations. But there are distinctly observable fluctuations in the radial separation between the electron cloud and ion cloud happening alongside the saturated $l = 1$ orbital motion at this stage (Fig. 5.1v-dd).

The dynamics of the instability was investigated with the help of several numerical diagnostics as shown in Fig. 5.2. Fig. 5.2a is a plot of the radial location of the centre of mass of the electron cloud (composed of the loaded electron population and the additional electrons generated from ionizing collision) as a function of time. The dynamics of the fundamental mode on the electron component can be directly followed from this plot. In Fig. 5.2a the vertical lines at $\tau = 54000$ and $\tau = 206000$ (τ here being the normalised time, t/T_{ce}) approximately divide the evolution of the electron cloud's profile into 3 phases: i) the initial quiet phase ii) the middle nonlinear growth phase and iii) the final saturation phase.

The initial phase from $\tau = 0$ to $\tau = 54000$ (Fig. 5.1a-g) is the quiet phase in which the electron cloud continues to be in a symmetric configuration about the central axis as the collision generated ions accumulate in its cross sectional potential well. The centre of mass of the electron cloud remains very close to the centre of the trap's cross section in this phase (Fig. 5.2a). Between $\tau = 54000$ to $\tau = 206000$ (Fig. 5.1h-u) the radial location of the centre of mass increases from nearly zero to about 0.375 times the wall radius, R_W (Fig. 5.2a). Hence this period is the nonlinear growth phase of the $l = 1$ mode on the electron cloud. From $\tau = 206000$ till the end of the simulation at $\tau = 242000$
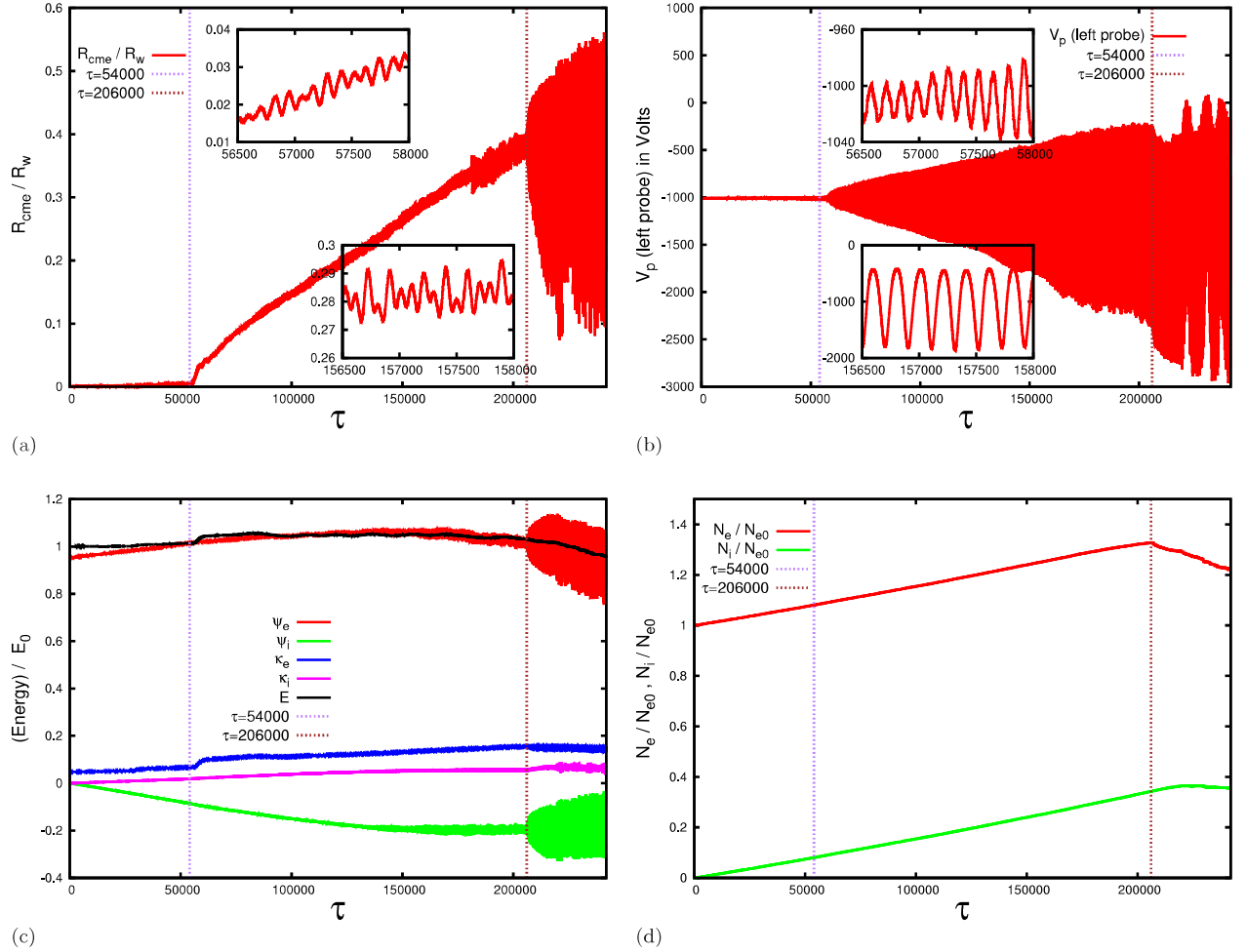
Figure 5.2: Diagnostic readings of BIEPNEX1.: Readings of different probes and plasma parameters are plotted as a function of time. The time axes in the all 4 plots are normalised by the electron cyclotron time, *i.e.* $\tau = t/T_{ce}$. The vertical lines at $\tau = 54000$ and $\tau = 206000$ demarcate the initial rigid rotation phase, the middle growth phase, and the final saturation phase of the dynamics. The top inset, and bottom inset of (a) and (b) are zoomed in versions of (a) and (b) between $\tau = 56500$ to $\tau = 58000$, and $\tau = 156500$ to $\tau = 158000$ respectively. (a) Radial location of the centre-of-mass of the electrons (primary as well as secondary electrons that are trapped in the system), R_{cme} is plotted as a function of time. The y-axis is normalised by the wall radius R_w. (b) Potential reading of the left potential probe V_p is plotted as a function of time. (c) The total energy E of the plasma, and its components viz., potential energy of electrons, ψ_e and ions, ψ_i, and kinetic energy of electrons, κ_e and ions, κ_i are plotted as a function of time. The y-axis is normalised by the initial value of total energy E_0. (d) The total number of trapped electrons, N_e and total number of trapped ions, N_i are plotted as a function of time. The y-axis is normalised by the initial population of trapped electrons, N_{e0}.

(Fig. 5.1v-dd), the expansion of the $l = 1$ orbits of the electron cloud attains an average saturation, although there are now very high amplitude fluctuations in the radial location of the electron cloud (saturation phase of Fig. 5.2a). This period is the saturation phase. The radius of the electron cloud fluctuates between values of 0.05 R_W and 0.55 R_W in the saturation phase (Fig. 5.2a). The high amplitude radial fluctuations of the orbiting electron in the saturation phase, can be associated with the observed fluctuations in the radial separation between the electron cloud and ion cloud in the snapshots of Fig. 5.1v-dd.

In fact a close inspection of the curve of Fig. 5.2a (see insets of Fig. 5.2a) reveals that the radial fluctuations in the electron cloud's position begin with very small amplitude in the growth phase itself. The radial fluctuations steadily gain amplitude through the growth phase, and then suddenly burst into very high amplitude in the saturation phase (Fig. 5.2a). Although some degree of fluctuations is expected in any nonlinear growth and saturation process, the fact that there is a steady increase in the amplitude of these fluctuations in the growth phase and then a sustained burst in their amplitude in the saturation phase (Fig. 5.2a), indicate that these fluctuations are the response of the nonlinearly growing $l = 1$ mode to the changing population of trapped electrons and ions in these two phases. We will come back to this explanation for the radial fluctuations in the positions of the orbiting electron cloud (Fig. 5.2a and Fig. 5.1v-dd), and ion cloud (Fig. 5.1v-dd) later in this discussion.

Fig. 5.2b is a plot of the signal of the left potential probe through the simulation period. The signals of the other 3 potential probes that are not shown here, also echo the same information about the dynamics of the instability. The potential probe signal of Fig. 5.2b aided by the dotted vertical lines at $\tau = 54000$ to $\tau = 206000$ in the figure, clearly captures exactly the same three phases of the dynamics of the plasma as the radius of the centre of mass of electrons in Fig. 5.2a. We will later show how we used Fig. 5.2a and Fig. 5.2b to estimate average growth rates of the nonlinear $l = 1$ mode, at different time intervals in its evolution. The potential probe signal of Fig. 5.2b also holds information about the frequencies dynamically attained by the $l = 1$ mode in course of its growth and saturation. This information will also be extracted from the potential probe reading of Fig. 5.2b. The insets of Fig. 5.2b, are zoomed-in portions of the left potential probe's signal at different time-segments in its growth phase. A comparison of the number of crests of the signal in the two zoomed-in time segments of equal lengths of time, indicate that there must be a chirping of $l = 1$ mode's frequency occurring with the nonlinear progress of the instability.

Now the pair of zoomed-in plots within Fig. 5.2a are at the same intervals of time as those within Fig. 5.2b. A comparison of the corresponding zoomed in time-segments between Fig. 5.2a and 5.2b reveal an interesting correlation between the two diagnostic readings: Although the oscillations in the radial location of the electron cloud are fluctuations, while the potential probe has a pure signal originating from the ongoing $l = 1$ motion of the plasma, the most dominant frequency of the radial fluctuations is nearly equal to the frequency of the potential probe's signal in the corresponding time segments (insets of Fig. 5.2a and 5.2b). Infact, as will be verified later, the close correlation between the dominant frequencies of Fig. 5.2a and 5.2b (the correlation being their nearly equal values) exists

throughout the simulation. The implications of this close correlation between the two diagnostic readings will also be discussed later.

Fig. 5.2c and 5.2d depict the energy components of the plasma, and the trapped particle population respectively, as a functions of time. The vertical lines at $\tau = 54000$ to $\tau = 206000$ in these two figures again divide these curves into the above mentioned three phases. Now consider the potential energy curves of the electron component, ψ_e, and ion component, ψ_i in Fig. 5.2c. The electron/ion cloud's potential energy will directly depend on the temporal evolutions of i) the spatial electrostatic potential function, ii) the net population of trapped electrons/ions in the system which is shown in Fig. 5.2d. In the quiet phase the electron cloud continues to remain nearly in the loaded symmetric configuration about the axis, as equal number of ions, and secondary electrons accumulate within it, conserving the net charge of the cloud. So it can be assumed that the spatial electrostatic potential function will not vary much during this phase. So an almost unchanging electrostatic potential function with linearly increasing electron and ion population (Fig. 5.2d) results in an approximately linear increase of the positive quantity ψ_e and a linear decrease of the negative quantity ψ_i in the quiet phase (quiet phase of Fig. 5.2c). In the growth phase, as typical of the ion-resonance instability [32, 38], there is a potential energy transfer from the electron component to the ion component (Fig. 5.2c) in correspondence to the dynamics of the instability in this phase (Fig. 5.1h-u). In other words the spatial electrostatic potential is so modified by the instability in the growth phase, that part of the electron component's potential energy gets transferred to the potential energy of the ion component [32, 38]. This instability driven potential energy transfer, curbs the linear increase/decrease of ψ_e/ψ_i due to increasing population of electrons/ions and brings about a saturation of the ψ_e/ψ_i curve. (growth phase of Fig. 5.2c). Again as typical of an ion resonance instability [32, 38], part of the potential energy of electrons is also used up by instability for collisionless heating of the plasma components, especially the electrons as evident from the sudden rise in the net kinetic energy of electrons, κ_e, in the growth phase over and above its regular steady increase form the addition of electrons to the system (growth phase of Fig. 5.2c).

In the saturation phase the potential energy curves of both electrons, and ions in Fig. 5.2c, show large amplitude fluctuations, similar to the fluctuations of the saturation phase observed in the radial location of the centre of mass of electrons (saturation phase of Fig. 5.2a) as well as the potential probe signal (saturation phase of Fig. 5.2b). The saturation-phase fluctuations in the diagnostic signals of Fig. 5.2a-c are commonly linked to the radial fluctuations in the positions of the orbiting electron, and ion clouds observed in the saturation phase (Fig. 1v-dd).

We have earlier shown that these radial fluctuations actually originate with much smaller amplitude in the growth phase (insets of Fig. 5.2a), and hinted that the radial fluctuations are the response of the $l = 1$ mode's dynamics in the growth, and saturation phases, to the changing populations of electrons and ions in these phases (Fig. 5.2d). Now Fig. 5.2d shows that there is a steady increase in the electron and ion population in the growth phase. Corresponding to this steady increase in trapped particle population, are the small amplitude radial fluctuations of the expanding orbits of the electron, and ion clouds in the growth phase, which are diagnostically picked up by the radial trace of centre of

mass of the electron cloud (growth phase of Fig. 5.2a). From the diagnostic readings of Fig. 5.2a and Fig. 5.2d we can decipher that during the growth phase, as the orbits of the electron cloud become larger (growth phase of Fig. 5.2a), the amplitude of the radial fluctuations also gradually increase (growth phase of Fig. 2a), in response to the steadily increasing electron and ion populations in this phase (growth phase of Fig. 5.2d).

In the saturation phase we observe a dip in the electron population curve and a saturation of the ion population curve (saturation phase of Fig. 5.2d). It must be understood that the sudden variation of the progress of the trapped particle population curves in the saturation phase is the result of radial transport, and loss of particles from the orbiting plasma to the grounded wall, which is in very close proximity to the plasma in this phase (Fig. 5.1v-dd). So there are electrons and ions being created from ionizing collisions, as well as electrons and ions getting radially untrapped in the saturation phase. The two competing processes of trapping, and untrapping of particles in the saturation phase cause the saturated $l = 1$ mode to respond with high amplitude radial fluctuations observable in Fig. 5.1v-dd, and the region beyond $\tau = 20600$ in Fig. 5.2a-c.

Next, in Fig. 5.3 we have estimated the frequencies that are dynamically, and nonlinearly attained by the $l = 1$ mode in course of the instability. We utilized the left potential probe signal of Fig. 5.2 for the frequency analysis procedure. The signals of the other three potential probes also convey the same information regarding the frequency of the mode.

First, to get an idea of the progressive changes in frequency, ω_s, of the $l = 1$ mode, we sampled different segments of potential probe signal of Fig. 5.2b and performed a piece-wise FFT on each segment to estimate the frequency of the fundamental mode in that segment of time. As an example we have shown in Fig. 5.3a, an FFT performed on the potential probe signal (Fig. 5.2b) in the time-segment between $\tau = 83977.68$ and $\tau = 125966.520$. In this particular time-segment of the potential probe signal (Fig. 5.2b) we obtain a frequency $\omega_s = 2.953 \times 10^7 \, rad/sec$, of the $l = 1$ mode. The progressive change in the value of ω_s, sampled at different time-segments of Fig. 5.2b, is shown in Fig. 5.3b. The rectangular bins in Fig. 5.3b represent the segment of time for which the potential probe signal (Fig. 5.2b) was Fourier analysed to obtain each plotted value of ω_s. We can see from Fig. 5.3b that the initially the value ω_s is nearly equal to the natural $l = 1$ mode frequency, $\omega_{a0} = 6.848 \times 10^7 \, rad/sec$, of the initial pure electron cloud [1]. As the instability progresses, the value of ω_s shows a decreasing trend which saturates at a value of about $0.4 \, \omega_{a0}$ in the saturation phase of the instability. As depicted by the time-segment bins of Fig. 5.3b, FFT analysis were performed for narrower time-segments of Fig. 5.2b in the quiet phase, in order to trace the rapid fall in the value of ω_s in this phase. It is to be noted that although there are sharp fundamental mode frequencies obtained in the quiet phase (Fig. 5.3b), from an amplitude perspective the mode is still negligibly weak in this phase (see quiet phase of Fig. 5.2b) indicating that the plasma is still in a symmetric configuration about the trap's axis with the ions and electrons accumulating within the cloud in a net charge conserving manner (Fig. 5.1a-g). Yet there is a rapid fall in the value of ω_s in the quiet phase!

(a)

(b)

(c)

(d)
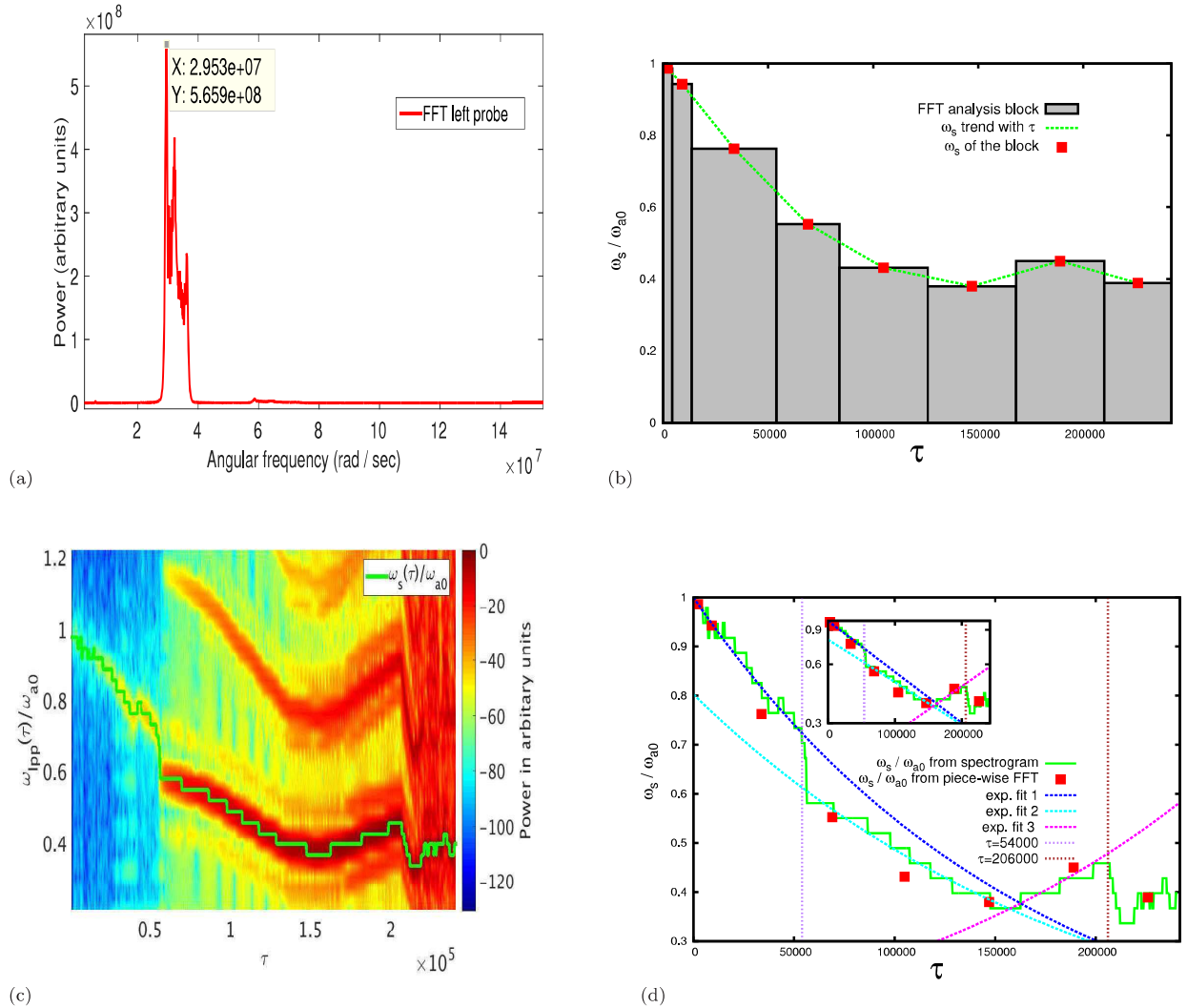
Figure 5.3: Frequency analysis of the left potential probe reading from BIEPNEX1: (a) A FFT is
performed on the left potential probe's readings between $\tau = 83977.68$ and $\tau = 125966.520$ (where
$\tau = t/T_{ce}$) to find the fundamental mode frequency, ω_s in that interval of time. (b) ω_s values obtained
from different time-segments of the left potential probe's reading through FFT analysis, are plotted as a
function of time and also as histogram showing the intervals on which the FFTs were performed. The
y-axis is normalised by $\omega_{a0} = 6.848 \times 10^7 \, rad/sec$, the natural $l = 1$ mode frequency of the loaded
$f_b = 0.2076$ pure electron cloud. (c) The time evolution of the frequency spectrum, ω_{lpp}, of the left
potential probe signal is plotted as spectrogram. Only the most relevant range of ω_{lpp} values which
include ω_s have been plotted in the spectrogram for better resolution. The ω_s frequency has been
identified within the spectrogram and its time evolution has also been traced. (d) ω_s values obtained from
the spectrogram, (c) and the piece-wise FFT analysis, (b), have been plotted as functions of time.
Exponential fits have been made on different regions of the curve. The exponential fits 1, 2, and 3, yield
values $-5.039 \times 10^3 \, rad/sec$, $-4.199 \times 10^3 \, rad/sec$, and $4.619 \times 10^3 \, rad/sec$ respectively, of α_{ω_s}, the
growth rates of ω_s. The vertical lines at $\tau = 54000$ and $\tau = 206000$ demarcate the initial rigid rotation
phase, the middle growth phase, and the final saturation phase of the dynamics. (Inset) A replot of (d)
with the y-axis in logscale used in the exponential fitting of the curve.

To verify the correctness of our our piece-wise FFT analysis in Fig. 5.3b and gain more insight into the time evolution of the fundamental mode's frequency, we also performed a spectrogram analysis of the left potential probe's signal (Fig. 5.2b). The spectrogram method performs Short-Time-Fourier-Transforms (STFT) on consecutive overlapped time-segments of the signal and hence gives a much more continuous scan of the signal's frequency components over time. The resultant spectrogram, zoomed in on a relevant range of the frequency spectrum of the signal, ω_{lpp}, is shown in Fig. 5.3c. A branch of frequencies corresponding to the fundamental mode frequency, ω_s, is clearly distinguishable in Fig. 3c. The exact frequency values at the peaks of this fundamental mode branch have also been traced out with a line in Fig. 5.3c. Frequency branches corresponding to the first two harmonics of ω_s are also distinguishable in Fig. 5.3c. The two harmonic frequency branches are detectable in the spectrogram (Fig. 5.3c) only after the potential probe signal (Fig. 5.2b) has transitioned into the growth phase. This indicates that harmonics of the fundamental mode's frequency, ω_s, come into the signal's frequency spectrum due to nonlinear growth of amplitude of the signal (growth phase of Fig. 5.2b).

In Fig. 5.3d we have plotted the ω_s versus time curve as extracted form the spectrogram (Fig. 5.3c). The ω_s values obtained from piece-wise FFT analysis of Fig. 5.3b have also been plotted with points in Fig. 5.3d. As expected, these two sets of data for ω_s versus time are in very good agreement with each other. The vertical lines in Fig. 5.3d at $\tau = 54000$ and $\tau = 206000$ divide the plot into the quiet phase, growth phase, and saturation phase. Three exponential fits for the growth rate, α_{ω_s} of ω_s, in three time-segments of the ω_s versus time curve (extracted from the spectrogram of Fig. 5.3c) are also shown in Fig. 5.3d. The inset of Fig. 5.3d is a replot of Fig. 5.3d with its y-axis in logscale which was utilized for the exponential fitting of the curve.

Fig. 5.3d shows that there is a rapid fall in the value of ω_s in the quiet phase of the instability. Its value decreases from ω_{a0} at $\tau = 0$ to $0.7\,\omega_{a0}$ at $\tau = 54000$, which marks the end of the quiet phase. The exponential fit 1 (Fig. 5.3d) of the quiet phase shows that ω_s has decayed with growth rate, $\alpha_{\omega_s} = -5.039 \times 10^3\,rad/sec$ in this phase. The rapid fall in the fundamental mode's frequency in the quiet phase can only be due to increasing inertia of the plasma, caused the accumulation of collisions generated Ar^+ ions in an electron cloud. This is because the plasma maintains its shape (Fig. 5.1a-g), net charge (quiet phase of Fig. 5.2d), and near symmetric distribution about the trap's axis (quiet phase of Fig. 5.2a) in this phase. The only influential parameter that changes in the quiet phase is the inertia of the plasma.

Just after the transition from the quiet phase to the growth phase there is downward jump in the value of ω_s. The sudden jump takes the value of ω_s form $\omega_s = 0.7\,\omega_{a0}$ at $\tau = 54000$ to $\omega_s = 0.58\,\omega_{a0}$ at $\tau = 56435$. This jump corresponds to the initial burst in the amplitude of the potential probe's signal (Fig. 5.2b) observed around the same time. Thereafter the nonlinear dynamics of the instability in the growth phase counteracts the effect of the increasing inertia of the plasma on the time evolution of ω_s. The instability dynamics first relaxes the decay in the value of ω_s caused by the building inertia of the plasma. This is evident from the exponential fit 2 (Fig. 5.3d) which yields $\alpha_{\omega_s} = -4.199 \times 10^3\,rad/sec$.

## 5. BACKGROUND IONIZATION BY ELECTRON PLASMA NUMERICAL EXPERIMENTS (BIEPNEX)

Falling at this modified rate from $\tau = 56435$, ω_s reaches a minimum value of $0.37\,\omega_{a0}$ at $\tau = 147635$. Beyond this point the balance tips over in favour of instability dynamics causing an exponential rise of ω_s at $\alpha_{\omega_s} = 4.619 \times 10^3\,rad/sec$ (exponential fit 3 of Fig. 5.3d) up to $\tau = 206000$ which marks the end of the growth phase.

In the saturation phase ω_s also saturates at an average value of about $0.4\,\omega_{a0}$, with fluctuations between values of $0.34\,\omega_{a0}$ and $0.46\,\omega_{a0}$. The fluctuations of ω_s in the saturation phase can be linked to the radial fluctuations in the saturated orbits of the two components in this phase (Fig. 5.1v-dd and saturation phase of Fig. 5.2a), and its underlying cause (saturation phase of Fig. 5.2d) that has been explained earlier.

Turning our attention back to the spectrogram of Fig. 5.3c, it must be mentioned that a similar spectrogram analysis was performed for diagnostic reading of Fig. 5.2a. The purpose here was to check if the dominant frequency of the radial fluctuations in Fig. 5.2a remains close to the evolving values of ω_s throughout the simulation, as indicated by the insets of Fig. 5.2a and Fig. 5.2b. Interestingly the spectrogram analysis of the diagnostic readings of Fig. 5.2a also showed a more diffused ω_s branch, as well as diffused branches of the first two harmonics of ω_s. Now the radial fluctuations are themselves a consequence of changing populations of trapped electrons and ions. Hence it may be possible to develop a linear theoretical model for an ion-resonance-instability-driven, linearly-growing $l = 1$ mode, that connects the evolving frequency of the mode, to the evolving frequency of orbital-radius oscillations (or fluctuations), via a net-charge-conserving, linear-algebraic increase of electron and ion populations. This proposed model is however, beyond the scope of this paper.

As the radial fluctuations are driven by the changing populations of electrons and ions (Fig. 5.2d), it is also necessary to verify that these fluctuations are not completely or partially numerical effects, arising from the discrete collision-steps in which collision generated particles are added to the plasma. This was verified by searching for a $(\Delta t_c)^{-1}$ frequency (Δt_c being the collision time step) in the spectrogram of the radial trace of the centre of mass of the electron cloud (Fig. 5.2a). The radial fluctuations did not have any tell-tale signature of the $(\Delta t_c)^{-1}$ frequency in their spectrogram, which proves beyond doubt that the fluctuations are indeed a physical phenomenon and not numerical effects. In fact, as discussed earlier, the dominant frequency of the radial fluctuations dynamically emulates the chirping frequency of the $l = 1$ mode all through the simulation.

In Fig. 5.4 we have estimated the growth rate, α_s, of the excited $l = 1$ mode at various stages its growth phase, using the left potential probe signal of Fig. 2b, as well as the radial trace of the centre of mass of electrons of Fig. 5.2a. Fig. 5.4a and Fig. 5.4b have exponential fits on logscaled plots of the squared left potential probe signal (original signal in Fig. 2b), and the radial trace of the centre of mass of the electron cloud (original curve in Fig. 5.2a) respectively. The three exponential fits on both Fig. 5.4a and Fig. 5.4b have been made at the exact same time-segments of these readings. The three exponentially fitted time-segments of Fig. 5.4a and Fig. 5.4b have distinguishable temporal variation in the growth trend of these two curves. The exponential fits Fig.5.4a yield growth rates $2\alpha_s$ while those on Fig.5.4b yield growth rates α_s. It turns out that the exponential fits on the two diagnostic
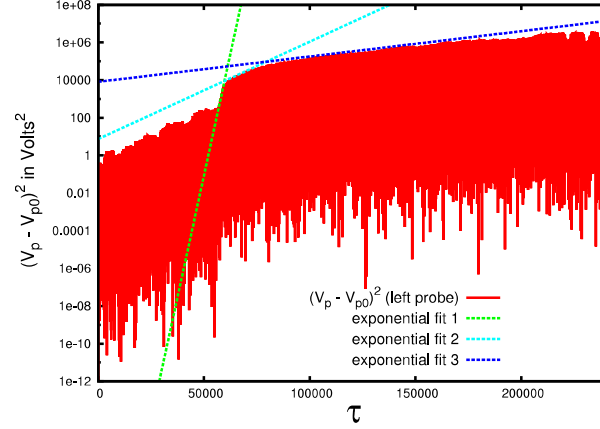
(a)
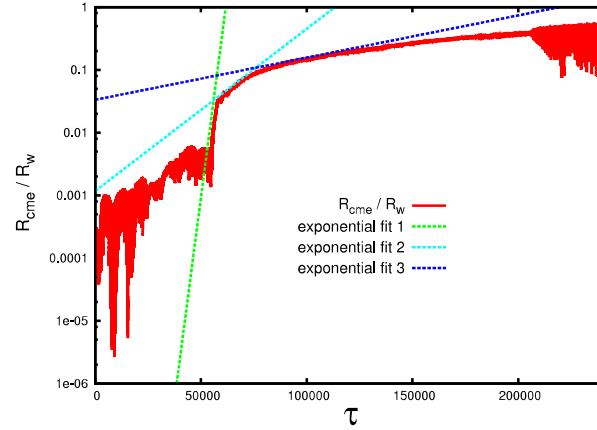
(b)

Figure 5.4: Estimation of dynamic growth rates of the fundamental mode from BIEPNEX1: (a) $(V_p - V_{p0})^2$ is plotted as a function of time, τ where $\tau = t/T_{ce}$, V_p represents the left potential probe reading, and V_{p0} is the initial value of V_p. The y-axis is in logscale. The three straight lines represent the exponential fits in different stages of the growth phase. Each exponential fit has a growth rates $2 \times \alpha_s$ from which the α_s for that stage of the growth phase can be obtained. (b) Radial location of the centre-of-mass of the electrons, R_{cme} is plotted as a function of time. The y-axis is in logscale and is normalised by the wall radius R_w. The three straight lines represent the exponential fits in different stages of the growth phase. Each exponential fit has the growth rates α_s for that stage of the growth phase. These α_s values come out to be same as those obtained from the exponential fits of (a). Obtained α_s values are, $5.0 \times 10^5 rad/sec$, $5.0 \times 10^4 rad/sec$, and $1.3 \times 10^4 rad/sec$ from exponential fits 1, 2, and 3 respectively.
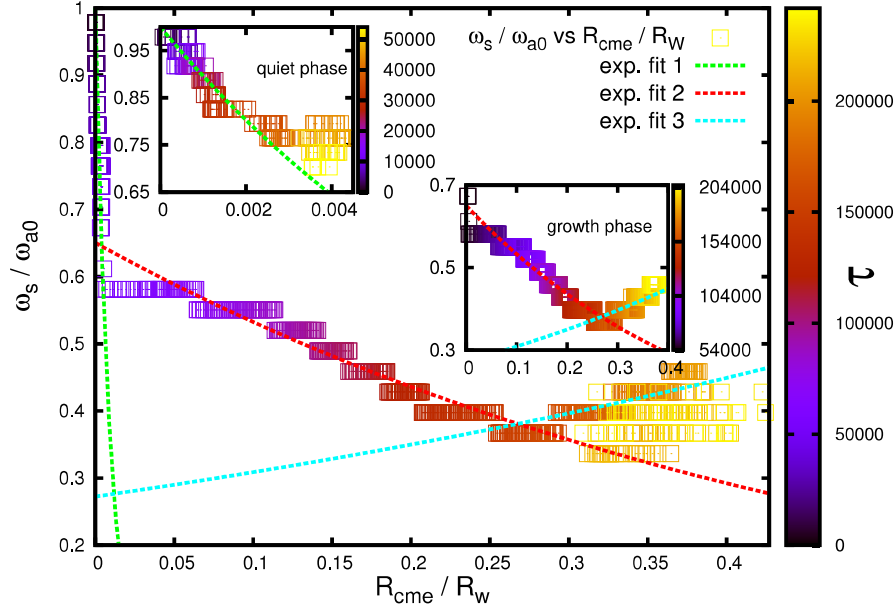
Figure 5.5: Fundamental mode's frequency as a function of orbital radius of the electron cloud: This is a scatter plot of $\omega_s(\tau)/\omega_{a0}$ versus $R_{cme}(\tau)/R_W$, where ω_s is the frequency of the fundamental mode and R_{cme} is the radius of centre of mass of electrons. The normalizing constants ω_{a0} and R_W are the natural $l = 1$ mode frequency of the initial pure electron cloud, and the wall radius respectively. $\tau = t/T_{ce}$ where T_{ce} is the electron cyclotron time. The time co-ordinate of the scatter points have been incorporated in the colorbar. Exponential fits have been made on different sections of the scatter plot. The exponential fits 1,2,3 yield values $-880\,rad/m$, $-16\,rad/m$, $10\,rad/m$ respectively, of γ_{ω_s}, the exponential growth rate of the fitted ω_s versus R_{cme} curve. (Insets) The left and the right insets show the same scatter points restricted to the quiet phase, and the growth phase respectively. The insets have their own colour code of their constrained time axes represented as adjacent colorbars.

readings actually yield the exact same values of α_s for the identified three stages of the growth phase. These values α_s, are obtained as $5.0 \times 10^5\,rad/sec$, $5.0 \times 10^4\,rad/sec$, and $1.3 \times 10^4\,rad/sec$ for the first, second, and third stage of growth respectively.

We have analysed the evolutions of ω_s with time in Fig.5.3d, and R_{cme} with time in Fig.5.4b. Now Fig.5.5 is a scatter plot of ω_s versus R_{cme} that depicts the dynamic dependence of the frequency of the fundamental mode on the orbital radius gained by the electron cloud in the course of the mode's growth. A scatter plot has been preferred over a line plot because R_{cme} has considerable fluctuations with time (Fig.5.2a). The time co-ordinate of the plotted scatter points are incorporated in the color scheme, depicted in the colorbar. Scatter-points constrained to the quiet phase, and growth phase are plotted as insets on the left and right, respectively inside Fig.5.5. Each inset figure has its own color scheme of its constrained time axes, depicted as adjacent colorbars. Exponential fits have been made on the scatter plot of Fig.5.5 to quantify the dependence of ω_s on R_{cme} at different stages of the simulation.

We know that in the quiet phase ω_s rapidly falls with time (Fig.5.3d) while R_{cme} remains almost

stationary very near to zero (Fig.5.2a). Hence ω_s is a very steeply falling function of R_{cme} in the quiet phase (quiet phase inset of Fig. 5.5). The exponential fit 1 (Fig.5.5) in the quiet phase yields a growth rate, $\gamma_{\omega_s} = -880\,rad/m$. In the growth phase ω_s has qualitatively a similar dependence on R_{cme} (growth phase inset of Fig.5.5) as it has with time (growth phase of Fig.5.3d). It first decreases to a minimum value of $0.37\,\omega_{a0}$ at $R_{cme} = 0.24\,R_W$. The associated growth rate of this fall is $\gamma_{\omega_s} = -16\,rad/m$ (exponential fit 2 of Fig.5.5). Note that this minimum value attained by ω_s is the same minimum that was observed in the ω_s versus time curve (Fig.5.3d) at $\tau = 147635$. Thereafter ω_s increases to a value of $0.37\,\omega_{a0}$ at $R_{cme} = 0.4\,R_W$ with a growth rate $\gamma_{\omega_s} = 10\,rad/m$ (exponential fit 3 of Fig.5.5). In the saturation phase there are fluctuations of ω_s about a average value of $0.4\,\omega_{a0}$, while R_{cme} fluctuates about an average value of $0.35\,R_w$. These fluctuations are seen as scattering of points around the point, $(0.35\,R_w\ ,\ 0.4\,\omega_{a0})$, in the saturation phase of Fig.5.5.

The evolution of the growing fundamental mode's frequency with time (Fig.5.3d) and its dependence on the $l = 1$ orbital radius of the electron cloud (Fig.5.5), in this numerical experiment is very unique to chosen pressure, $P_{bg} = 2 \times 10^{-7}\,Torr$ of the Argon background. In fact at the regular background pressures, $10^{-9}\,Torr$, found in experimental traps [50] there is much less contamination of the electron cloud by impact ionization of neutrals. When a growing $l = 1$ mode is excited on such an almost pure electron cloud, by say, a resistive wall instability [80], then the frequency of the mode shows an algebraic increase with increase in orbital radius of the cloud [79, 80, 81]. Hence the unique evolution of ω_s in our numerical experiment is the result of setting the background gas pressure to a higher value, $P_{bg} = 2 \times 10^{-7}\,Torr$.

5.3 BIEPNEX2: Influence of the non-ionizing $e^- - Ar$ collisions on the instability

Now we turn our attention to the role played by the elastic, and excitation collisions between electrons and Ar atoms, on the instability dynamics of the plasma in Expt.1. In our previous work [32] we had established that such non-ionizing collisions can not, solely by themselves, be responsible for the destabilization of trapped electron clouds. However by virtue of the relaxation of the electron cloud's profile caused by these collisions, they can influence the dynamics of collisionless instabilities of the electron cloud [32]. In BIEPNEX1 the electron cloud is involved in an ion resonance instability which is influenced by the non-ionizing $e^- - Ar$ collisions taking place in the background. In order to distinguish the effects of the non-ionizing collisions on the complex dynamics of the plasma in this simulation, we had to re-simulate the numerical experiment with one modification in its set-up, viz. elastic and excitation collisions between electrons and background Argon atoms were turned off in the new modified simulation, BIEPNEX2. The resultant changes in the evolution of the plasma were then compared with the earlier experiment to understand the role played by non-ionizing $e^- - Ar$ collisions in the former experiment.
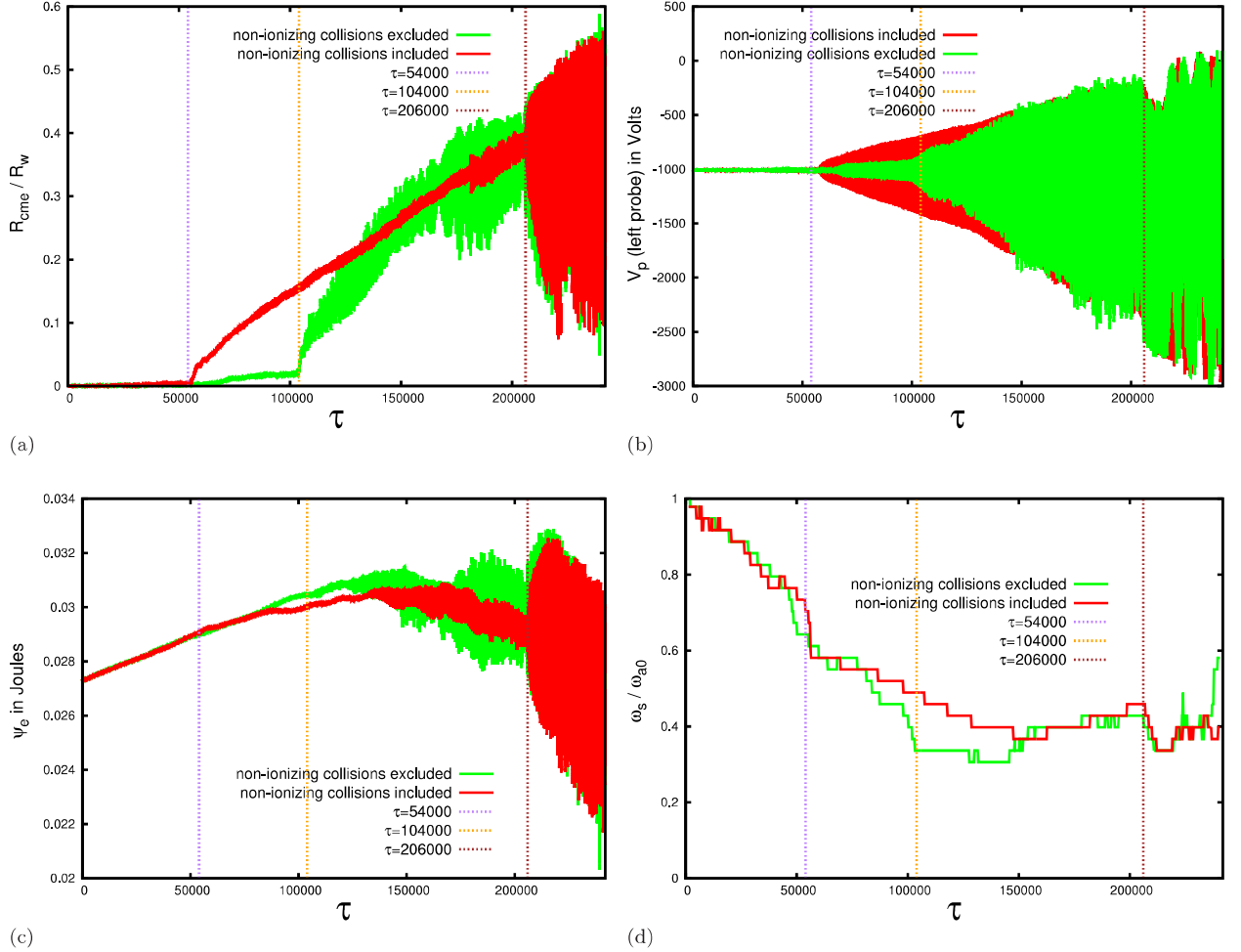
Figure 5.6: Comparison of diagnostic readings of BIEPNEX1 (shown in red) with corresponding diagnostic readings of the modified simulation wherein BIEPNEX1 is repeated with the exclusion of the non ionizing $e^- - Ar$ collisions (shown in green). The 4 pairs comparative diagnostic readings are plotted as a function of time, τ, where $\tau = t/T_{ce}$. The vertical lines at $\tau = 54000$ and $\tau = 206000$ demarcate the initial rigid rotation phase, the middle growth phase, and the final saturation phase of BIEPNEX1 while the vertical lines at $\tau = 104000$ and $\tau = 206000$ demarcate the initial rigid rotation phase, the middle growth phase, and the final saturation phase of the modified experiment .(a) Radial location of the centre-of-mass of the electrons, R_{cme}, from the two experiments, are plotted as a function of time. The y-axis is normalised by the wall radius R_w. (b) Potential reading of the left potential probe, V_p, from the two experiments are plotted as a function of time. (c) The Potential Energy of the electron component of the plasma, ψ_e, from the two experiments are plotted as a function of time. (d) The fundamental mode frequency, ω_s, from the two experiments, are plotted as a function of time. The y axis is normalized by the natural fundamental mode frequency, $\omega_{a0} = 6.848 \times 10^7 \ rad/sec$ of the initial pure electron cloud.

Fig. 5.6 shows a comparison of relevant diagnostic readings between the earlier simulation BIEP-NEX1 and the modified simulation BIEPNEX2 with the non-ionizing $e^- - Ar$ collisions turned off. The radial trace of the centre of mass of the electron cloud, the left potential probe signal, the potential energy of the electron component, and the variation of the fundamental mode's frequency with time are compared between the two experiments in Fig. 5.6a-d respectively. The first striking difference between the two sets of diagnostic data (Fig. 5.6a-c) is observed in the time of onset of the growth phase in the two sets of plots. Transition from the quiet phase to the growth phase happens around $\tau = 54000$ in BIEPNEX1, and around $\tau = 104000$ in the modified experiment. A second distinct difference between the two simulations is observed specifically in the compared radial traces of the centre of mass of the electron cloud in Fig. 5.6a. BIEPNEX1 has more subdued radial fluctuations of the orbiting electron cloud in the growth phase as compared to the modified simulation. Again Fig. 5.6d shows that the exclusion of the non-ionizing collisions from the simulation results in ω_s acquiring slightly lower values in the growth phase of the instability. This can be attributed to the fact that excluding the non-ionizing collisions delays the onset of the nonlinear dynamics of the growth phase that tends to raise the value of ω_s, as explained in Sec 5.2.

Hence we can conclude that non-ionizing $e^- - Ar$ collisions, by virtue of their feedback on the ion resonance instability through the collisional relaxation of the electron cloud's profile, cause an early transition of the plasma dynamics from the quiet phase to the growth phase. The non-ionizing $e^- - Ar$ collisions also make the growing $l = 1$ orbital motion of the electron cloud profile in the growth phase a less noisy (in terms of radial fluctuations), and a slightly higher frequency (in terms of the $l = 1$ mode's frequency), process. We must emphasize here that we are making these observations about the effects of the non-ionizing $e^- - Ar$ collisions as specific to the present set of plasma, and background gas parameters and not drawing any generalized conclusions about their influence in any other experimental condition. We had, in fact, shown in our previous work [32] how the influence of non-ionizing $e^- - Ar$ collisions on evolution of the plasma, is too dynamic, and too nonlinear a process for any such generalized deductions about their effects.

Another similar modified simulation was carried out eliminating only the elastic and charge exchange collisions between Argon ions and Argon atoms from the original simulation BIEPNEX1. This was done in order to understand the role played $Ar^+ - Ar$ collisions, on the dynamics of the plasma. However this modification didnot make any difference to the outcome of the numerical experiment, indicating that for the present set of plasma, and background gas parameters, $Ar^+ - Ar$ collisions have negligible influence on the evolution of the plasma.

5.4   Conclusions and Discussions

We can sum up the results obtained from BIEPNEX as follows.

In BIEPNEX1 cylindrically confined pure electron cloud, was loaded in the presence of Argon background neutrals at pressures relevant to experiments, and the process of the destabilization of the

electron cloud through collisional interaction with the background atoms was simulated using a 2D3v PIC-with-MCC code, and investigated with an array of numerical diagnostics. We have seen that the Ar^+ ions formed through impact ionization of the background Ar atoms first accumulate in the cross-sectional potential well of the electrons and then gradually start engaging an ion-resonance/two-stream instability with the electron cloud. The instability excites a nonlinear fundamental Diocotron mode on both components, of the mixed non-neutral plasma. Associated with the growth of the fundamental mode is a transfer of potential energy from the electron component to the ion component of the plasma as well as collisonless heating of electrons and ions by the instability at the cost of the potential energy of the electrons.

The growth phase of the fundamental mode is also characterized by small amplitude radial fluctuations in the expanding the orbits of the electron, and ion clouds. These radial fluctuations are the response of the growing fundamental Diocotron mode to the increasing electron and ion populations from impact ionization of neutrals.

The mode finally saturates with the electron cloud orbiting very close to the grounded wall of the trap, and the partially overlapped ion cloud orbiting at a slightly lower radius. In the saturation phase some loss of trapped particles of both species is incurred through their radial transport to the grounded wall. The particle loss process of the saturation phase together with the continued generation of new electrons and ions from impact ionizations, vary the electron, and ion populations of the plasma in such a manner, that the fundamental mode responds with high amplitude radial fluctuations of the saturated orbits of the electron, and ion clouds. These high amplitude radial fluctuations are actually observable in the simulation as fluctuations in the radial separation between the electron and ion cloud in the saturation phase.

Through the three phase of the instability there is a chirping of the excited fundamental mode's frequency with time. In general the fundamental mode's frequency versus time curve falls rapidly in the quiet phase, passes through a minimum in the growth phase, and fluctuates about a certain mean value in the saturation phase. This kind of chirping of the fundamental mode's frequency is unique to the background pressure of the Argon atoms being set at $2 \times 10^{-7} Torr$.

By repeating the simulation with the non-ionizing elastic and excitation collisions between the electrons and Argon atoms turned off, BIEPNEX2, we could understand how these non-ionizing $e^- - Ar$ collisions influenced the dynamics of the plasma in the original simulation. The collisional relaxation of the electron cloud's profile brought about the non-ionizing $e^- - Ar$ collisions cause an early transition from the initial quiet phase to the growth phase of the ion resonance instability and also subdue the radial fluctuations of electron cloud in the growth phase. Similarly repeating the simulation with $Ar^+ - Ar$ elastic, and charge exchange collisions turned off did not result in any significant difference in the outcome of the numerical experiment, indicating that for the present set of plasma, and background gas parameters $Ar^+ - Ar$ collisions are unimportant.

Possible directions in which this work may be extended are i) including the 3D effects of axial untrapping of ions in the simulation of the ion -resonance instability ii) introducing a toroidal aspect

ratio to the simulated trap cross-section (in 2D as well as 3D simulations) and investigating how the ion resonance instability evolves in a toroidal trap, iii) simulating an experiment in a cylindrical or toroidal trap wherein the background pressure varies as a function of time, and understanding its effects on the dynamics of trapped plasmas.

In the next Chapter we will the discuss and conclude the thesis work presented in Chapters 1 to 5.

6

Conclusions

The very simple arrangement of trapping an electron gas in a cylinder, the Penning-Malmberg trap, amazingly produces a plethora of plasma phenomena, that can be experimented with, analysed and modelled, and investigated with computer simulations. A solid understanding of such non-neutral plasma behaviour in cylindrical traps can find application beyond the PM trap, in other other scientific and commercial devices, such as antiproton ion sources and free electron lasers, to name a few. A more direct extension of the physics developed from PM traps is the physics of toroidally trapped nonneutral plasmas.

PIC simulation can be a very useful tool to understand the dynamics of non-neutral plasmas in PM traps, especially since PM trap arrangement allows an 2D approximation of the trap for some selected plasma phenomena in the trap. This thesis was an attempt to investigate open physics problems in cylindrically confined nonneutral plasmas using the method of particle-in-cell simulation. In the endeavour to study non-neutral plasmas using simulations, the first challenge was to develop accurate and efficient electrostatic PIC codes, that could tackle non-neutral plasma dynamics for any given plasma, and PM trap, parameters. Roadblocks such as the problem of inclusion of collisions between plasma and background neutrals in the simulations to study the effect of such collisions, were faced, and overcome with suitable modification and upgradations to the code. Every time we had an efficiently working, benchmarked code, ready, numerical experiments were conducted to study selected open problems in cylindrically trapped nonneutral plasmas with the code. When a planned numerical experiment posed challenges beyond the capability of the code/s at hand, upgradations to the code were developed so that the planned numerical experiment could be undertaken. In this way the studies on nonneutral plasma and development of simulation techniques progressed in an integrative manner to result in this thesis.

The following subsections outline, in bullets, the highlights of results of the thesis, and the scope for future work.

6.1 Highlights of results

The highlights of the thesis are systematically categorized under computational aspect and nonneutral plasma physics aspect.

6.1.1 Computational aspect

- Development of the flexible 2D Electrostatic PIC code, PEC2PIC, that can handle any regular or odd size and shape of the 2D trap boundary because of its inherent Cartesian grid

- parallelization of PEC2PIC, including parallelization of the SOR Poisson Solver

- Benchmark of PEC2PIC by matching simulation results with theoretical calculations

- Development of the parallelized 2D3v PIC-with-MCC code PEC2PIC-3MCC, that along with the 2D PIC dynamics on a Cartesian grid, can also simulate collisional interaction of plasma with an Argon background. Specifically $e^- - Ar$ and $Ar^+ - Ar$ collisions can be handled by the MCC part of the code.

- Validation of the correctness of collisions statistics and collision mechanics of the collisions executed by the MCC scheme of PEC2PIC-3MCC

- Development of the parallelized 1D PIC code PEC1PIC that can handle a moving, reflecting wall system, and also maintain a constant resolving power for a system that changes its length during the simulation.

- Benchmark of the PEC1PIC by matching its results with results from other 1D PIC simulations in a reflecting wall system.

6.1.2 Nonneutral plasma aspect

- Simulations of the inertia driven radial breathing in pure electron plasmas revealed interesting nonlinear dynamics of the radial breathing modes such as spontaneous formation of density voids within the profiles of high f_b electron clouds, which in turn triggered transient azimuthal modes on these clouds.

- The nonlinear phase of the ion resonance instability in partially neutralized electron clouds, was the highlight of these simulations. The nonlinear phase not only revealed a characteristic potential energy pumping form the electrons to the ions, but also displayed an array of nonlinear dynamics such as the radial ballooning of Diocotron mode crests on ion cloud and simultaneous azimuthal pinching of the Diocotron mode crests on the electron cloud, the breaking up of the electron cloud into l daughter clouds, where l is the mode number of the excited Diocotron mode, the re-merging of the daughter electron clouds in a reverse cascade process, and many more.

- Simulation of a stable fundamental Diocotron mode on a electron cloud, in the presence of non-ionizing $e^- - Ar$ collisions revealed that contrary to existing theory the non-ionizing collisions are incapable to drawing energy from the negative energy Diocotron mode of the cloud and hence can not destabilize the stable $l = 1$ mode.

- Simulations of the ion resonance instability in the presence of non-ionizing $e^- - Ar$ collisions, revealed that the non-ionizing background collisions can bring about variation in the path of progression of the ion resonance instability, via the dynamical feedback of the collisional relaxation of the electron cloud's profile on the instability.

- The highlight of the simulation of the destabilization of a trapped electron cloud by impact ionization of background Argon, was the curve of $l = 1$ mode frequency as a function time. The fundamental mode's frequency is observed to fall rapidly in the linear phase of the instability, then decrease at a slow rate, pass through a minimum value, and then increase in the nonlinear growth phase of the instability. Finally in the saturation phase the fundamental mode's frequency oscillates about a mean value. This unique curve traced by the fundamental mode's frequency has been explained to be caused by opposing effects of increasing inertia of the 2-component plasma that tends to bring down the value of the frequency and the nonlinear dynamics of the instability that tends to raise the value of the fundamental mode's frequency.

- Simulation performed with the 1D PIC code demonstrated a new scheme for axially heating single species plasmas without driving them far away from thermal equilibrium. The results of the 1D simulations have further reaching consequences, as the the heating scheme can be applied, in principle, to magnetically heat toroidally confined quasi-neutral plasmas.

6.2 Scope for future work

There are several directions in which the work of this thesis can be taken which fall broadly under computational aspect, non-neutral plasma numerical experiment aspect. These avenues of future research are enlisted under these two categories.

6.2.1 Computational

- Further parallelization of PEC2PIC and PEC2PIC-3MCC by using an OPEN-MP parallelization nested within an MPI parallelization or alternatively the codes may be parallelized on a GPU platform

- With higher parallelization implemented these codes may be upgraded to 3D PIC codes

- Inclusion of background collisions in PEC2PIC-3MCC for an Helium or Hydrogen Background

- Upgrade PEC2PIC and PE2PIC-3MCC so that these codes can also handle toroidal cross sections of arbitrary aspect ration - this may involve switching from a fixed grid size to a varying grid size along the direction of the toroidal major radius and/or using a higher order version of Chin's exponential splitting scheme [44] for particle pushing

- The PEC2PIC and PEC2PIC-3MCC are flexible enough to be used as simulation tools in other devices such as plasma thrusters, and Q-devices.

6.2.2 Numerical Experiments on nonneutral plasmas

- Studies on the effect of loading the plasma at varying temperatures on the dynamics of radial breathing would be in line with the kinetic model of Bernstein modes [17]. It could also be interesting to study the influence of elastic collisions of the electrons with background neutrals, on the dynamics of radial breathing modes, using the 2D3v PIC-with-MCC code PEC2PIC-3MCC.

- It could be an interesting pure electron plasma numerical experiment to study the influence of electron-background non-ionizing collisions on the dynamics of the Kelvin-Helmholtz instability in an annular cylindrical electron cloud.

- The heating scheme demonstrated by PEC1PIC simulations may be tweaked so that it produces preferential heating of the heavier of the two components of the quasi-neutral plasma. Numerical experiments demonstrating such a preferential heating scheme could have interesting applications.

- A complete 3D simulations of a PM trap, investigating the destabilization of an electron cloud by impact ionization of background neutrals would be very interesting. 3D effects such as the instability caused by differences in the axial profiles of the electron density and the ion density, and the axial untrapping of ions could then be simulated.

- Destabilization of electron clouds by impact ionization of background Helium or Hydrogen could also be interesting numerical experiments.

- The simulation based investigation of nonneutral plasma phenomena may be extended to finite aspect ratio traps, using a 2D/3D PIC code.

References

[1] R. C. Davidson. *Physics of Nonneutral Plasmas*. Imperial College Press, 1990.

[2] L. Tonks and I. Langmuir. *Phys. Rev.*, **33**:195, 1929.

[3] D. A. Schecter, D. H. E. Dubin, K. S. Fine, and C. F. Driscoll. *Phys. Fluids*, **11**:905, 1999.

[4] R. Ganesh and J. K. Lee. *Phys. Plasmas*, **9**:4551, 2002.

[5] Jérôme Pétri. *AIP Conf. Proc.*, **1114**:191, 2009.

[6] Peter Horak, Aurélien Dantan, and Michael Drewsen. *Phys. Rev. A*, **86**:043435, 2012.

[7] L. Schmöger *et al. Science*, **347**:1233, 2015.

[8] D. H. E. Dubin and T. M. O' Neil. *Phys. Rev. Lett.*, **60**:511, 1988.

[9] Carl Ekdahl *et al.* **Electron beam dynamics in the DARHT-II linear induction accelerator**. http://accelconf.web.cern.ch/accelconf/linac08/papers/mop102.pdf. Proc. of LINAC08, Victoria, BC, Canada (2008), pages 311-313.

[10] J. J. Deng *et al.* **Design of the DRAGON-I linear induction accelerator**. http://accelconf.web.cern.ch/AccelConf/l02/PAPERS/MO403.PDF. Proc. of LINAC2002, Gyeongju, Korea, (2002), pages 40-42.

[11] M. Ahmadi *et al. Nature*, **529**:373, 2016.

[12] Yasunori Yamazaki. *Hyperfine Interactions*, **138**:141, 2001.

[13] Tetsuya Ishikawa *et al. Nature Photonics*, **6**:540, 2012.

[14] A. A. Lutman *et al. PRL*, **110**:134801, 2013.

[15] Ronald C. Davidson and Gian Marco Felice. *Phys. Plasmas*, **5**:3497, 1998.

[16] R. C. Davidson and Hwansup Uhm. *Phys. Fluids*, **20**:1938, 1977.

[17] Grant W. Hart and Ross L. Spencer. *Phys. Plasmas*, **20**:102101, 2013.

[18] J. H. Malmberg and J.S. deGrassie. *Phys. Rev. Lett.*, **35**:577, 1975.

[19] B. P. Cluggish and C. F. Driscoll. *Phys. Plasmas*, **3**:1813, 1996.

[20] A. A. Kabantsev and C. F. Driscoll. *Trans. Fus. Sci. and Tech.*, **51**:96, 2007.

[21] G. Maero, S. Chen, R. Pozzoli, and M. Romé. *J. Plasma Phys.*, **81**:495810503, 2015.

REFERENCES

[22] B.Paroli, G.Maero, R.Pozzoli, and M. Romé. *Phys. Plasmas*, **21**:122102, 2014.

[23] G. Maero, R. Pozzoli, M. Romé, S. Chen, and M. Ikram. *J. Inst.*, **11**:C09007, 2016.

[24] J. P. Marler and M. R. Stoneking. *J. Phys.: Conf. Ser.*, **71**:012003, 2007.

[25] Lavkesh Lachvani, Sambaran Pahari, and Y. C. Saxena. *J. Phys.: Conf. Ser.*, **390**:012047, 2012.

[26] M. R. Stoneking, P. W. Fontana, R. L. Sampson, and D. J. Theucks. *Phys. Plasmas*, **9**:766, 2002.

[27] Q. R. Marksteiner, T. Sunn Pedersen, J. W. Berkery, M. S. Hahn, J. M. Mendez, B. Durand de Gevigney, and H. Himura. *PRL*, **100**:065002, 2008.

[28] H. Himura, Y. Yamamoto, A. Sanpei, , and S. Masamune. *Plasma Fusion Res.*, **2**:S1089, 2007.

[29] M. D. Tinkle, R. G. Greaves, and C. M. Surko. *Phys. Plasmas*, **3**:749, 1995.

[30] B. P. Cluggish, C. F. Driscoll, K. Avinash, and J. A. Helffrich. *Phys. Plasmas*, **4**:2062, 1997.

[31] J. Fajans. *Phys. Fluids B*, **5**:3127, 1993.

[32] M. Sengupta and R. Ganesh. *Phys. Plasmas*, **23**:102111, 2016.

[33] M. Sengupta and R. Ganesh. *Phys. Plasmas*, **24**:032105, 2017.

[34] M. Sengupta and R. Ganesh. *Phys. Plasmas*, **21**:022116, 2014.

[35] M. Sengupta and R. Ganesh. *AIP Conf. Proc.*, **1668**:020005, 2015.

[36] Ronald C. Davidson and Edward H. Chao. *Phys. Plasmas*, **3**:3279, 1996.

[37] K. Avinash, M. Sengupta, and R. Ganesh. *Phys. Plasmas*, **23**:062514, 2016.

[38] M. Sengupta and R. Ganesh. *Phys. Plasmas*, **22**:072112, 2015.

[39] C. K. Birdsall and A. B. Langdon. *Plasma Pysics Via Computer Simulation*. Taylor and Francis Group, 2004.

[40] Dirk P. Kroese, Thomas Taimre, and Zdravko I. Botev. *Handbook of Monte Carlo Methods*. Wiley, 2011.

[41] Louise Olsen-Kettle. **Numerical Solution of partial differential equation**. http://espace.library.uq.edu.au/view/UQ:239427. Lecture notes at University of Queensland, Australia, 2011.

[42] Chaoyang Zhang, Hong Lan, Yang Ye, and Brett D. Estrade. **Parallel SOR Iterative Algorithms and Performance Evaluation on a Linux Cluster**. http://www.ntis.gov/search/product.aspx?ABBR=ADA449212. Proceedings of the International Conference on Parallel and Distributed Processing Techniques and Applications, PDPTA 2005, Las Vegas, Nevada, USA, June 27-30, 2005, Vol 1.

[43] C. C. Lalescu. **Implementation of Splitting-Composition Schemes for the Numerical Study of Charged Particles**. http://www.researchgate.net/profile/Cristian_Lalescu/publications/?pubType=article, 2008.

[44] Siu A. Chin. *Phys. Rev. E*, **77**:066401, 2008.

[45] Shiming Yang and Matthias K. Gobbert. **The Optimal Relaxation Parameter for the SOR Method Applied to a Classical Model Problem**. http://userpages.umbc.edu/~gobbert/papers/YangGobbert2007SOR.pdf, 2007.

[46] Etienne Forest and Ronald D. Ruth. *Physica D*, **43**:105, 1990.

[47] Haruo Yoshida. *Physics Letter A*, **150, number 5,6,7**:262, 1990.

[48] Hong Qin and Xiaoyin Guan. *PRL*, **100**:035006, 2008.

[49] C. A. Kapetanakos and A. W. Trivelpiece. *J. Appl. Phys.*, **42**:4841, 1971.

[50] Edward H. Chao, Ronald C. Davidson, Stephen F. Paul, and Kyle A. Morrison. *Phys. Plasmas*, **7**:831, 2000.

[51] V. Vahedi and M. Surendra. *Computer Physics Communications*, **87**:179–198, 1995.

[52] C. K. Birdsall. *IEEE Transactions on Plasma Science*, **19, issue 2**:65–85, 1991.

[53] M. Frignani and G. Grasso. **Argon cross sections for PIC-MCC codes**. http://www.afs.enea.it/ggrasso/files/reports/LIN-R01.2006.pdf, 2006.

[54] K. Nanbu and S. Uchida. *Jpn. J. Appl. Phys.*, **33**:4752–4753, 1994.

[55] K. Nanbu and S. Uchida. *Proc. 19th Int. Symp. Rarefied Gas Dynamics*, **1**:601–610, 1994.

[56] A. Okhrimovskyy, A. Bogaerts, and R. Gijbels. *Phys. Rev. E*, **65**:037402.

[57] Kenichi Nanbu and Yoshinori Kitatani. *J. Phys. D: Appl. Phys.*, **28**:324, 1995.

[58] C. F. Driscoll and J. H. Malmberg. *Phys. Rev. Lett.*, **50**:167, 1983.

[59] P. F. Schmit, I. Y. Dodin, , and N. J. Fisch. *Phys. Plasmas*, **18**:042103, 2011.

[60] D. A. Schecter, D. H. E. Dubin, A. C. Cass, C. F. Driscoll, and et al. *Phys. Fluids*, **12**:2397, 2000.

[61] S. N. Bhattacharyya. *Phys. Plasmas*, **2**:1077, 1995.

[62] Priyanka Goswami, S. N. Bhattacharyya, A. Sen, and K. P. Maheshwari. *Phys. Plasmas*, **5**:895, 1998.

[63] D. C. Barnes, T. B. Mitchell, , and M. M. Schauer. *Phys. Plasmas*, **4**:1745, 1997.

[64] M. M. Schauer, T. B. Mitchell, M. H. Holzcheiter, and D. C. Barnes. *Rev. Sci. Instrum.*, **68**:3340, 1997.

[65] A. J. Peurrung and J. Fajans. *Phys. Fluids B*, **5**:4295, 1993.

[66] W. D. White, J. H. Malmberg, and C. F. Driscoll. *Phys. Rev. Lett.*, **49**:1822, 1982.

[67] G. Bettega, F. Cavaliere, B. Paroli, R. Pozzoli, M. Romé, and M. Cavenago. *Phys. Plasmas*, **15**:032102, 2008.

[68] Ronald C. Davidson. *Phys. Fluids*, **27**:1804, 1984.

REFERENCES

[69] J. R. DANIELSON, D. H. E. DUBIN, R. G. GREAVES, AND C. M. SURKO. *Rev. Mod. Phys.*, **87**:247, 2015.

[70] R. H. LEVY, J. D. DAUGHERTY, AND O. BUNEMAN. *Phys. Fluids*, **12**:2616, 1969.

[71] R. C. DAVIDSON AND HWAN SUP UHM. *Phys. Fluids*, **21**:60, 1978.

[72] H. C. CHEN. *J. Plasma Physics*, **54**:173, 1995.

[73] HAN S UHM AND RONALD C. DAVIDSON. *Phys. Fluids*, **25**:2334, 1982.

[74] S. ECKHOUSE, A. FISHER, AND N. ROSTOKER. *Applied Physics Letters*, **38**:318, 1981.

[75] A. J. PERRUNG, J. NOTTE, AND J. FAJANS. *PRL*, **70**:295, 1993.

[76] G. BETTEGA, F. CAVALIERE, M. CAVENAGO, A. ILLIBERI, R. POZZOLI, AND M. ROMÉ. *Plasma Phys. Control. Fusion*, **47**:1697, 2005.

[77] G. BETTEGA, F. CAVALIERE, M. CAVENAGO, F. DE LUCA, A. ILLIBERI, R. POZZOLI, AND M. ROMÉ. *Phys. Plasmas*, **13**:112102, 2006.

[78] M. R. STONEKING, P. W. FONTANA, R. L. SAMPSON, AND D. J. THUECKS. *Phys. Plasmas*, **9**:766, 2002.

[79] K. S. FINE. *Phys. Fluids B*, **4**:3981, 1992.

[80] THOMAS G. JENKINS, KYLE A. MORRISON, RONALD C. DAVIDSON, AND STEPHEN F. PAUL. **Large Amplitude m = 1 Diocotron Mode Measurements in the Electron Diffusion Gauge Experiment**. http://www.dtic.mil/dtic/tr/fulltext/u2/p012523.pdf. part of the following report: Non-Neutral Plasma Physics 4. Workshop on Non-Neutral Plasmas [2001] Held in San Diego, California on 30 July-2 August 2001, pages 298-304.

[81] K. S. FINE, C. F. DRISCOLL, AND J. H. MALMBERG. *Phys. Rev. Lett*, **63**:2232, 1989.